Fall 2009

CFD prediction of ship capsize: parametric rolling, broaching, surf-riding, and periodic motions

Seyed Hamid Sadat Hosseini
University of Iowa

CFD PREDICTION OF SHIP CAPSIZE: PARAMETRIC ROLLING, BROACHING, SURF-RIDING, AND PERIODIC MOTIONS

by

Seyed Hamid Sadat Hosseini

An Abstract

Of a thesis submitted in partial fulfillment of the
requirements for the Doctor of Philosophy degree
in Mechanical Engineering in
the Graduate College of
The University of Iowa

December 2009

Thesis Supervisors: Professor Frederick Stern
Associate Professor Pablo M. Carrica

ABSTRACT

Stability against capsizing is one of the most fundamental requirements to design a ship. In this research, for the first time, CFD is performed to predict main modes of capsizing. CFD first is conducted to predict parametric rolling for a naval ship. Then CFD study of parametric rolling is extended for prediction of broaching both by using CFD as input to NDA model of broaching in replacement of EFD inputs or by using CFD for complete simulation of broaching. The CFD resistance, static heel and drift in calm water and static heel in following wave simulations are conducted to estimate inputs for NDA and 6DOF simulation in following waves are conducted for complete modeling of broaching.

CFD parametric rolling simulations show remarkably close agreement with EFD. The CFD stabilized roll angle is very close to those of EFD but CFD predicts larger instability zones. The CFD and EFD results are analyzed with consideration ship theory and compared with NDA. NDA predictions are in qualitative agreement with CFD and EFD.

CFD and EFD full Fr curve resistance, static heel and drift in calm water, and static heel in following waves results show fairly close agreement. CFD shows reasonable agreement for static heel and drift linear maneuvering derivatives, whereas large errors are indicated for nonlinear derivatives. The CFD and EFD results are analyzed with consideration ship theory and compared with NDA models. The surge force in following wave is also estimated from Potential Theory and compared with CFD and EFD. It is shown that CFD reproduces the decrease of the surge force near the Fr of 0.2 whereas Potential Theory fails.

The CFD broaching simulations are performed for series of heading and Fr and results are compared with the predictions of NDA based on CFD, EFD, and Potential Theory inputs. CFD free model simulations show promising results predicting the instability boundary accurately. CFD calculation of wave and rudders yaw moment explains the

processes of surf-riding, broaching, and periodic motion. The NDA simulation using CFD and Potential Flow inputs suggests that CFD/ Potential Flow can be considered as replacement for EFD inputs.

Abstract Approved:

_____
Thesis Supervisor

_____
Title and Department

_____
Date

_____
Thesis Supervisor

_____
Title and Department

_____
Date

CFD PREDICTION OF SHIP CAPSIZE: PARAMETRIC ROLLING, BROACHING, SURF-RIDING, AND PERIODIC MOTIONS

by

Seyed Hamid Sadat Hosseini

A thesis submitted in partial fulfillment of the
requirements for the Doctor of Philosophy degree
in Mechanical Engineering in
the Graduate College of
The University of Iowa

December 2009

Thesis Supervisors: Professor Frederick Stern
Associate Professor Pablo M. Carrica

Graduate College
The University of Iowa
Iowa City, Iowa

CERTIFICATE OF APPROVAL

PH.D. THESIS

This is to certify that the Ph.D. thesis of

Seyed Hamid Sadat Hosseini

has been approved by the Examining Committee for the thesis requirement for the Doctor of Philosophy degree in Mechanical Engineering at the December 2009 graduation.

Thesis Committee:

Frederick Stern, Thesis Supervisor

Pablo M. Carrica, Thesis Supervisor

Larry J. Weber

Shaoping Xiao

James Buchholz

To my lovely wife and my family

ACKNOWLEDGMENTS

The Office of Naval Research under contract/grant N00014-01-1-0073, N00014-04-1-0288, and N00014-06-1-0646 for IIHR, INSEAN, and Osaka University, respectively, administered by Dr. Patrick Purtell, sponsored this research. Partial support was provided by the Italian Minister of Transport for INSEAN and by Japan Society for Promotion of Science for OU under contract 18360415.

I would like to acknowledge the help and interest put my advisors in this research. I would also like to thank the members of the CFD group at IIHR, the EFD group at INSEAN especially Angelo and Emilio, and Prof. Hirotada Hashimoto from Osaka University for always finding time to answer my questions and helping me during the research. This help is highly appreciated.

TABLE OF CONTENTS

LIST OF TABLES

LIST OF FIGURES

LIST OF SYMBOLS

Alphabetical Symbols

A	Wave amplitude
a_H	Interaction factor between hull and rudder
Ak	Wave slope (=A*k)
A_R	Rudder area
A_{WP}	Water plane area
B	Beam
c	Wave speed
D	(1) Derivative gain of controller (2) Benchmark data
D_p	Propeller diameter (=$2r_p$)
E%D	Comparison error (=(D-S)/D)
E_{RSS}%D	Root Summed Square Error (=$1/N\sqrt{\sum\{(D_i - S_i)/D_i\}^2}$)
Fr	Froude number (=$U_0/\sqrt{Lg}$)
g	Gravity
GM	Transverse metacentric height
GM_a	Amplitude of GM variation in waves
GM_L	Longitudinal metacentric height
GM_m	Mean value of GM variation in waves
GZ	Roll restoring moment arm
H	(1) Water depth (2) Wave height (=2*A)
I	Integral gain of controller
I_x, I_y, I_z	Moment of Inertia
I_{xy}, I_{yz}, I_{xz}	Product of Inertia
J	Advance ratio

k	(1) Turbulent kinetic energy (2) Wave number (=$2\pi/\lambda$)
K, M, N	Total Roll, Pitch, and Yaw moment
KG	Vertical position of center of gravity respect to the keel
K_Q (J)	Torque coefficient of propeller
K_T (J)	Thrust coefficient of propeller
k_{xx}, k_{yy}, k_{zz}	Radius of gyration (= $\sqrt{I_x/m}$, $\sqrt{I_y/m}$, $\sqrt{I_z/m}$)
L	Ship Length
l_1, l_3, l_5, …	Roll restoring moment arm coefficients
LC_G	Longitudinal position of center of gravity respect to the bow
m	Mass
n	(1) Propeller RPS (2) Roll decay coefficient
N	Number of data
p	Pressure
P	Proportional gain of controller
p,q,r	Ship angular velocities perturbation in body fixed frame
p_T,q_T,r_T	Ship total angular velocities in body fixed frame
Q_{ij}	Restoring moment variation coefficients
Re	Reynolds number (=$\rho U_0 L/\mu$)
r_h	Hub radius of propeller
t	Time
T	Draft
T_e	Encounter wave period
t_p	Thrust deduction factor
T_w	Wave period
T_ϕ	Natural roll period
u,v,w	Ship linear velocities perturbation in body fixed frame

U'_1,U'_2,U'_3	Fluid velocities in relative inertial coordinate system
U_0	Steady axial velocity of ship
U_1,U_2,U_3	Fluid velocities in earth fixed coordinate system
U_g	(1) Grid velocity in earth fixed coordinate system (2) Grid uncertainty
$\overline{u_i u_j}$	Reynolds stress
u_T,v_T,w_T	Ship total linear velocities in body fixed coordinate system
w_p	Effective propeller wake factor
X, Y, Z	(1) Total Surge, Sway, and Heave force (2) Earth fixed coordinate system
x, y, z	(1) Translation displacement in body fixed coordinate system (2) Body fixed coordinate system
X', Y', Z'	Relative inertial coordinate system
X_c, Y_c, Z_c, K_c, M_c, N_c	Control surface (Rudder) forces and moments
x_{CF}	x of flotation center
x_g, y_g, z_g	Coordinates of center of gravity of ship
x_H	Longitudinal position of hull and rudder interaction factor
X_p, Y_p, Z_p, K_p, M_p, N_p	Propeller forces and moments
x_R	Longitudinal position of rudder force
X_v, X_{vv}, $X_{\phi\phi}$,Y_{qqq},…	Derivative of forces and moments respect to u,v,w,p,q,r,ϕ,δ
X_w, Y_w, Z_w, K_w, M_w, N_w	Wave forces and moments
z_H	Vertical coordinate of acting point of hydrodynamic forces
z_{HR}	Vertical position of rudder force

Greek Symbols

Λ	Rudder aspect ratio
α	Linear damping coefficient
α_e	Equivalent linear damping coefficient

β	Drift angle
δ	Logarithmic decrement
δ_{ij}	Kronecker delta
δ_{max}	Maximum rudder deflection
δ_R	Rudder deflection angle
ε	(1) Wave phase (2) Ship response phase
ε_R	Wake ratio between propeller and hull
φ	Potential of fluid velocity
ϕ	Potential of fluid velocity
ϕ, θ, ψ	Ship angular displacement in body fixed coordinate system
ϕ_0	Initial roll angle
ϕ_C	Critical roll angle causing capsize
ϕ_m	Mean roll angle
γ	(1) Nonlinear (cubic) damping coefficient (2) Specific density
κ_p	Interaction factor between propeller and rudder
λ	(1) Wave length (2) Scale factor of the model
μ	(1) Viscosity of water (2) Wave heading
ρ	Density of water
σ	Sinkage of ship
τ	Trim of ship
ω	Wave frequency
ω_e	Wave encounter frequency ($=2\pi f_e$)
ω_ϕ	Natural roll frequency ($=2\pi f_\phi$)
$\omega_{\phi d}$	Damped roll frequency ($=2\pi f_{\phi d}$)

$\omega_{\phi h}$	Hydrostatic roll frequency ($=\sqrt{gGM}/k_{xx}$)
ξ_G	Longitudinal position of ship respect to wave
ξ,η,ζ	Non-orthogonal curvilinear coordinates
ψ_c	Target heading

CHAPTER 1. INTRODUCTION

Stability against capsizing in heavy waves is one of the most fundamental requirements considered by naval architects when designing a ship. The purpose of studying capsizing is to establish an understanding of ship behavior in extreme waves and to relate this to the geometric and operational characteristics of the ship. Research based on Experimental Fluid Dynamics (EFD), in which scale models are used in realistic wave conditions, has led to improved understanding and insight on the nature of the capsize process. The experience gained from EFD enabled researchers to develop representative mathematical models using Nonlinear Dynamics Approaches (NDA) to describe different modes of capsizing in extreme waves. On the other hands, the use of Computational Fluid Dynamics (CFD) in Naval Architecture has been common for some decades now. CFD simulations use RANS and URANS coupled with 6 DOF rigid body equations of motion to obtain a highly detailed prediction of flow and body motions. Herein, detailed definitions of various modes of capsizing, literature reviews covering EFD, NDA, and CFD, and lastly the objective and approach of the presented study are provided.

1.1 Modes of Capsizing

In the ITTC classification of capsizing, the pioneering work reported by Oakley et al. (1974) is used to make a fundamental understanding of intact ship capsizing and a basis for subsequent research in this area. As a consequence, research efforts have focused mainly on three modes of capsize which are static loss of stability, dynamic loss of stability, and broaching described in this section in some detail (De Kat and Thomas, 1998a,b). Also, water on deck, deck edge submergence, winds, and ship loading distribution can cause capsize in conjunction with three main modes of capsize.

1.1.1 Static Loss of Stability

Loss of static stability refers to the quasi-static loss of transverse stability (associated with an excessive righting arm reduction) in the wave crest. The wave length is usually the same as ship length and ship surges with high Fr number.

1.1.2 Dynamic Loss of Stability

A ship can lose stability dynamically in conjunction with extreme rolling motions and lack of righting energy under a variety of conditions. This major capsize mode may be associated with dynamic rolling, resonant excitation, impact excitation, bifurcation, and parametric rolling.

1.1.2.1 Dynamic Rolling

This mode of motion occurs at forward speed in stern quartering seas, which can be of regular or irregular nature. Here all six degrees of freedom are coupled, where in addition to roll, surge, sway and yaw can exhibit large amplitude fluctuations. Due to surging behavior, the ship spends more time in the wave crest than in the trough, resulting in a periodic but asymmetric reduction and restoring of the righting arm. This changing in righting arm builds asymmetric roll motion. Large roll motion typically builds up over a number of wave encounters to a critical level, and the ship will usually capsize to leeward.

1.1.2.2 Resonant Excitation

In principle large amplitude roll motions can result when a ship is excited at or close to its natural roll frequency. Roll resonance conditions are determined by the combination of GZ curve characteristics, weight distribution, roll damping, heading angle (e.g., beam seas), ship speed, wavelength and height.

1.1.2.3 Impact Excitation

Steep breaking waves can cause severe roll motions and may overwhelm a vessel. The impact due to a breaking wave that hits a vessel from the side will affect the ship dynamics and may cause extreme rolling and capsizing. This capsize mode is relevant especially to smaller vessels in steep seas.

1.1.2.4 Bifurcation

In laboratory conditions, the roll response may jump from one steady state to another (larger amplitude) steady-state condition at the same frequency following a sudden disturbance known as bifurcation.

1.1.2.5 Parametric Rolling

Parametric rolling results from the time-varying roll restoring characteristics of a ship typically found in longitudinal waves. The periodic changes in static righting arm during the repeated passage of a wave crest followed by the trough can cause large amplitude roll motions. Roll motions occurring at approximately the natural roll period and simultaneously at twice the encounter period (encounter frequency equals half of natural roll frequency) characterize this mode of motion. The roll motion is of a symmetric nature and the maximum roll angles to port and starboard occur when a crest passes the midship area. The wavelength must be of the order of the ship length. In such circumstances, parametric rolling - also referred to as low cycle resonance - can result in capsizing.

1.1.3 Broaching

Broaching is related to course keeping in waves. Although there is no uniformly accepted mathematical definition of a broach, it represents the wave-induced undesired, large amplitude change in heading angle. A variety of broaching modes exist in regular

and irregular waves. Broaching due to successive overtaking waves may occur at low speeds if the waves are very steep. Broaching due to low frequency and large amplitude yaw motions is a gradual oscillatory-type build-up of yaw as successive waves impinge on the ship from behind. In moderate sea states a ship is more likely to broach-to if it runs with a high speed and is slowly overtaken by the waves. Lastly, broaching caused by a single wave (surf-riding). Broaching is manifested as a sudden divergent yaw, which peaks within a single wave length. Control is lost when the middle of the ship lies somewhere on the down-slope and nearer to the trough.

1.1.4 Other Factors

Water on deck can occur in conjunction with (and hence influence) the capsize modes discussed above. Large amplitude relative motions and breaking waves can result in the temporary flooding of the deck (bow-diving), which from a stability viewpoint is relevant especially to vessels with bulwarks, such as fishing vessels. Free surface effects and sloshing can influence the ship motions. Furthermore, deck edge submergence results in loss of water-plane area and righting arm. If a bulwark is present, its submergence will influence the forces acting on the vessel. Wind does not necessarily influence wave induced capsizing in astern seas. In beam waves, however, it may be important.

1.2 Literature Review on EFD, NDA and CFD

The proceeding of the 22nd, 23rd, 24th, and 25th ITTC seakeeping committee is be the base of this section, since they review the current state and the most important recent contributions to EFD, CFD, and NDA in the field of ship hydrodynamics.

1.2.1 Literature Review on EFD

Experiments have been done for many modes of capsize. Static loss of stability in regular waves has been studied experimentally by De Kat and Thomas (1998a) and

Umeda et al. (1999). They showed that static loss of stability occurs at high speed (Fr ≈ 0.4) and short waves (λ/L ≈ 1), such that the ship speed matches the phase speed of the wave, and the static stability of the ship is reduced to the point that the ship capsizes. Dynamic rolling is studied by Lilienthal et al. (2007). They conducted free model experiments and showed that this mode of capsize is characterized by asymmetric rolling. The ship rolls heavily to the leeward side in phase with the wave crest (approximately) amidships and rolls back to the windward side in the wave trough, albeit with a shorter half period and smaller amplitude. Olivieri et al. (2006a) conducted 2DOF heave and roll experiment in beam waves for several wave heights to study resonant excitation. It is concluded that resonance excitation makes large roll angle causing existence of higher harmonics in forces and moments. Ishida and Takaishi (1990) and Ishida (1993) carried out experiment to show evidence of impact excitation and concluded that wave impacts on ships can cause extreme roll motion and capsize. For parametric rolling, Skomedal (1982) conducted the experiment with towed model in head waves and showed that the variation of the roll restoring moment in waves plays an important role in addition to the coupling between roll and vertical motions. Consequently, if a towed model is used, special attention should be paid to the towing arrangements to ensure that there is no interference with the vertical motions. Burcher (1990), Neves et al. (2002), Francescutto (2001), and Olivieri et al. (2006b, 2008) described the towing arrangement for parametric rolling. Neves et al. (2002) used two auxiliary lines respectively fixed to the bow and stern of the model at calm water level and tied to the towing wire. The resulting elasticity of the set was found in all cases to be appropriate in order to secure free evolution of the different symmetric and anti-symmetric modes of motion at a controlled speed. Neves et al. (2002) conducted a series of experiments on parametric rolling undertaken for two fishing vessels with different stern shape in head waves. One was a typical round stern vessel while the other one was a transom stern fishing vessel. Several parameters such as wave steepness, metacentric heights, and Fr number effects were studied. It was

concluded that effect of speed on parametric resonance is strongly dependent on stern shape. A transom stern, incorporating longitudinal asymmetry in flare, may exert a significant influence in establishing the tendency of a fishing vessel hull to display strong parametric amplification in head seas, particularly in a condition of low metacentric height. Francescutto (2001) conducted experiment for a destroyer model using a tethering system based on pairs of elastic mooring lines symmetric about the centre line of the model, to attach the model to the towing carriage while the model is free to roll, pitch and heave. This system ensures the model remains on a straight course, while it is sufficiently loose to avoid significant interference with the roll and vertical motions. The results clearly indicated that there is a speed window where the roll motion can be sustained in head waves. The width of the window and the amplitude of steady rolling depend on wave steepness. In particular, the roll amplitude increases with the wave steepness, and in some cases leads to ship capsize. Olivieri et al. (2006b, 2008) conducted the experiment where the model was connected to the carriage by means of a joint specifically designed for 3 DOF heave-roll-pitch parametric rolling. Model motions were measured using both an optical motion tracker and gyroscopic platform. Hashimoto et al. (2006) and France et al. (2003) performed free model tests to improve parametric rolling test results in irregular waves. It is noted that comparative studies between free running and towed model experiments have shown acceptable agreement (IMO, 2006). Broaching experiments were carried out by De Kat and Thomas (1998b), Hamamoto et al. (1996), Umeda (1998), Umeda et al. (1995, 1999, and 2008), and Lilienthal et al. (2007). De Kat and Thomas (1998b) and Hamamoto et al. (1996) observed broaching caused by large amplitude yaw motion due to wave impinge on the ship from behind and broaching caused by singe wave. Umeda (1998) and Umeda et al. (1995, 1999) proposed systematic method to assess ship stability in quartering/following waves executing free running test. First, the model metacentric height and gyro radius were aligned. Then propeller rate (RPS) for specified Fr number was obtained using open water tests. Propeller was also

estimated by running the ship appended with propeller in still water and changing RPS to reach the ship velocity to specified Fr number. Later, free running experiments were conducted at the Marine Dynamic Basin at NRIFE (National Research Institute of Fisheries Engineering). Umeda et al. (2008) performed free running experiment for a surface combatant (ONR Tumblehome) and observed ONR tumblehome vessel can suffer extreme roll angle up to 71 degrees when her nominal Froude number is larger than the surf-riding threshold. Typical broaching was recorded but did not result in capsizing because the angle of vanishing stability was 180 degrees. It was concluded that for more accurate modelling, effect of the emergence of rudder and three-dimensional wave pattern should be investigated for this kind of unconventional vessel. Lilienthal et al. (2007) executed free running model tests in regular following waves at discrete KGs. Tests were carried out at NRIFE and different modes of broaching were observed. It was demonstrated that there was minimal influence of wavelength ratio on capsize behaviour. It was also found that a reduction in vessel speed results in a small decrease in the likelihood to capsize. Matsuda et al. (2006) conducted free running model experiments at NRIFE for a purse-seiner vessel at several Froude numbers to study other factors on capsizing such as bow-diving. It was shown that the model capsized due to bow-diving in the severe following seas at intermediate speeds. The model also experienced stable surf-riding at higher speeds and broaching at lower speeds.

In conclusion, experiments have been used as first and most reliable procedure to study many different modes of capsize. However, they are not able to catch details to insight on the nature of the capsize process. Consequently, NDA and CFD simulations are carried out to investigate the details of capsize procedure.

1.2.2 Literature Review on NDA

NDA has been used to study many aspects of different modes of capsizing. Resonant excitation simulation is carried out by Surendran and Reddy (2002, 2003) using 1DOF

roll equation in frequency domain. They studied the roll responses and resonance excitation of a ship in beam seas and investigated the effect of wave height on it. Das and Das (2004) studied the harmonic response of a floating body by developing a mathematical model for coupled sway, roll and yaw motions. They simplified their method for coupled roll and yaw motions to study roll resonance excitation in beam waves (Das and Das, 2005). Bifurcation is studied by Eissa and EI-Bassiouny (2003) applying method of multiple time scales to study rolling response of a ship in regular beam seas. Kamel (2007) and Zhou and Chena (2008) studied response of a coupled roll and pitch system under a modulated amplitude sinusoidal excitation and obtained the bifurcation response equation near the combination resonance case in the presence of internal resonance of this system. Paulling and Rosenberg (1959) and Shin et al. (2004) modeled parametric roll neglecting nonlinear damping and restoring moment in 1DOF roll equation and considered wave effects and pitch-heave coupling only through a time varying restoring coefficient, which can be transformed into the Mathieu equation. Francescutto et al. (2004) and Umeda et al. (2004) used more advanced theory for parametric rolling in which damping consists of contributions from cubic terms of roll velocity estimated from roll decay towing tank test. Umeda et al. (2004) and Bulian (2004, 2005) applied the restoring term described by higher order functions of roll angle. The time dependent restoring term due to waves was expressed by higher order polynomial function of roll angle with time dependent coefficients expressed as Fourier series (Bulian and Francescutto, 2008; Hashimoto and Umeda, 2004; Umeda and Hashimoto, 2006). In order to consider coupling effects for parametric rolling prediction, Bulian et al. (2003) used a 1.5 DOF to implement roll-pitch-heave coupling in his model. Neves et al. (2009) introduced a 3DOF roll-pitch-heave including linear added mass and wave damping terms, linear and quadratic roll damping, and nonlinear coupling terms up to 3rd order. Another alternative approach to improve coupling terms is to use a fully coupled nonlinear time domain potential code such as LAMP developed by Lin and Yue

(1991) or FREDYN developed by De Kat and Thomas (1989a). NDA has been also used for broaching simulation. Well known theoretical studies on broaching were carried out in Japan by Umeda (1998, 1999) and Umeda et al. (2000). It was mentioned that heave and pitch natural frequencies are very large due to their large restoring moment. Therefore, when the ship runs with relatively high speed in following and quartering seas, the encounter frequency is much smaller than those natural frequencies and heave and pitch can be reasonably approximated by simply tracing their static equilibrium. This outcome indicated that a surge-sway-yaw-roll mathematical model is suitable for investigating broaching. Moreover, they concluded that required maneuvering parameters in their model can be estimated from appropriate captive tests. Later, they implemented more terms in their mathematical model to improve broaching prediction. Nonlinear maneuvering forces in calm water (Hashimoto and Umeda, 2002), wave effect on linear maneuvering forces and wave effect on roll restoring moment (Umeda et al., 2003), nonlinear wave induced forces including mean values (Hashimoto et al., 2004a), nonlinear sway-yaw coupling in calm water (Hashimoto et al., 2004a), wave effect on propeller thrust (Hashimoto et al., 2004a), hydrodynamic forces due to large heel angle in calm water (Hashimoto et al., 2004a), and wave effect on hydrodynamic forces due to large heel angle were studied and essential terms were added to their NDA model (Hashimoto et al., 2004b). Lastly, Umeda et al. (2006) extend the previous model to a model for twin propeller and twin rudders high speed slender ship.

In conclusion, NDA uses many empirical factors as input such as hydrodynamic coefficients, damping coefficients, restoring coefficients, coupling term coefficients and maneuvering coefficients. This makes the main limitation for NDA and results in opening position for CFD which models with no requirement of such inputs.

1.2.3 Literature Review on CFD

URANS CFD codes for ship hydrodynamics offers possibility of providing a complete rational-mechanics based prediction capability of capsizing for improved safety criteria and increased physical understanding. To apply CFD for capsizing, fluid equation has to be coupled with motions equations. Most previous CFD simulations are done for predicting of pitch and heave motions for ships in regular head waves demonstrated for the Wigley hull and Series 60 cargo ships using density function free surface modeling (Sato et al., 1999); a container ship using overlapping structured grids and density function free surface modeling (Orihara and Myata, 2003); a container ship using level-set free surface modeling (Houchbaum and Vogt, 2002); the Wigley hull using overlapping grids and level-set for free surface (Weymouth et al., 2005); and a surface combatant ship using overlapping structured grids and level-set free surface modeling (Wilson et al., 2005; Carrica et al., 2007a,b). Recently, CFD is developed to be capable of simulating maneuvering and seakeeping problems. Mulvihill and Yang (2007) presented numerical simulations of steady pure yaw maneuvers of a submarine, showing the capabilities of the steady overlapping grid approach. Also Benson and Fureby (2007) presented some numerical simulations of a submarine in steady yaw maneuver. They employed an LES approach with a wall model and showed that the model was able to predict some peculiarities of the flow field such as unsteadiness, cross flow separation and presence of horseshoe vortices. Good agreement with experiments, in terms of skin friction coefficient along cross sections in steady yaw maneuver, was observed. Xing et al. (2007) performed numerical simulations of the DTMB 5415 and KVLCC2 in steady drift motion. Numerical tests were performed at 0, 12, 30 and 60 degrees of incidence. These tests were considered to analyze different turbulent models: an isotropic blended $\kappa-\varepsilon/\kappa-\omega$ model (BKW), a Reynolds Stress model (RSM). Steady and unsteady analyses of the flow were performed, the latter within a Detached Eddy Simulation (DES). With

both turbulence models, BKW and RSM, the RANS simulations yielded a better prediction of resistance, axial velocity and turbulent kinetic energy distribution at the propeller plane than the DES. At higher drift angles, the DES approach allowed for capturing the unsteadiness of the flow field. Similar work has also been performed by Bhushan et al. (2007) including simulations at model and full scale Reynolds number for the Athena R/V. Hyman et al. (2006) performed simulations for steady straight ahead and steady turn maneuvers of a fully appended model of the R/V Athena taking into account the transport of bubbles due to air entrainment at the free surface. Simulations were carried out with CFDSHIP-IOWA using a two phase level set algorithm coupled with a gas phase solver called CFDShipM. Propeller effects were taken into account by a non-interactive body force model. Results from unsteady RANS simulation and Detached Eddy Simulation (DES) showed that the method was able to predict the bubbly flow around the vessel. However, some input parameters such as a bubble size distribution and bubble source intensity at the entrainment location had to be specified. Queutey and Visonneau (2007) presented and applied an interface capturing method for simulating the flow around the Series 60 model in steady straight ahead and pure drift motion. The results showed good agreement with experimental data. The use of an unstructured solver for the computation of forces on a surface piercing hull with enforced PMM motion can be seen in Wilson et al. (2007) where simulations of dynamic maneuvers of a surface combatant are presented. Pure sway and pure yaw tests are analyzed; results showed good agreement with experimental data in terms of both global quantities (forces and moments) and local quantities (velocity components on different cross sections with PIV measurements). In Carrica et al. (2006) the capability of the CFDShip-IOWA version 4 in dealing with various problems of the marine hydrodynamics, including the prediction of motion in waves are presented. Dynamic overlapping grids as described in Carrica et al. (2007b) were used. Examples are presented for the steady drift motion of the DTMB 5512 model and the KVLCC2 model in deep and shallow water. The KVLCC2 at high

drift angle was also simulated with the EASM/DES turbulence model. Steady turn computations were performed for the DTMB 5512 model. Dynamical PMM computations (i.e. pure yaw and pure sway) were performed for the HSSL trimaran and for the DTMB 5512 model. For the pure sway motion of the DTMB 5512 model, the agreement in terms of predicted forces and moments with measurements was very satisfactory while some discrepancies were observed when comparing velocity fields. In Sadat-Hosseini et al. (2007) 3DOF heave-roll-pitch parametric rolling was simulated for the first time in the world and analyzed using Mathieu equation showing that the damping caused by bilge keels is larger than the threshold value and prevents parametric rolling. In Carrica et al. (2008a,b,c) and Huang et al. (2008) full 6DOF simulations were used for actual full time domain simulation with a steered rudder with body force propeller and actual rotating propeller. The computations were intended to demonstrate the simulation capability, and no validation or verification was presented at that paper.

In conclusion, a great improvement has been achieved in CFD simulations taking into account the body force/rotating propeller and steering rudder(s) within the computational grid for many maneuvering and seakeeping problems. However, CFD studies of ship stability in waves are still few steps behind the mature state and developments are being made at very fast pace.

1.3 Objective and Approach

For the first time, CFD is performed to predict main modes of capsizing using CFDShip-Iowa v.4 with implementation capsize prediction in it. CFD first is conducted to predict parametric rolling in head waves for an unconventional naval ship, i.e., ONR tumblehome (OT). Then CFD study of parametric rolling is extended for prediction of broaching both by using CFD as input to NDA model of broaching in replacement of input achieved from EFD or by using CFD for complete simulation of broaching. The CFD calm water captive resistance test, static heel, and static drift simulations are

conducted to estimate inputs for NDA model of broaching and 6DOF simulation in following/quartering waves are conducted for complete simulation of broaching.

The research is a collaborative project between IIHR, Osaka University in Japan (OU), and INSEAN in Italy whereby OU conducts captive and broaching experiments and NDA studies, INSEAN performs parametric rolling experiments, and IIHR conducts CFD studies for predicting parametric rolling and broaching for the OT. The overall results enable an assessment of both NDA and CFD for capsize prediction and requirements for future EFD benchmark data (Sadat-Hosseini et al., 2009a,b).

The thesis is organized as follows. The NDA for ship stability and capsize is introduced in Chapter 2 with focus on the mathematical models and their inputs for parametric rolling and broaching. Chapter 3 describes CFDSHIP-IOWA (Carrica et al., 2007a,b; Xing et al., 2008; Stern et al., 2008) with focus on its use for both parametric rolling and broaching predictions. Chapter 4 provides a summary of the INSEAN captive experimental methods and conditions used as the EFD benchmark validation data for parametric rolling (Olivieri et al., 2008). Chapter 5 provides a summary of the OU captive and free model experimental methods and conditions used as the EFD benchmark validation data for broaching (Umeda et al., 2008). Chapter 6 covers the CFD verification and validation studies for the parametric rolling including comparisons with NDA predictions. Chapter 7 covers the CFD verification and validation studies for captive tests to assess inputs for NDA model of broaching. Chapter 8 provides CFD verification and validation studies for broaching including comparisons with NDA predictions. Lastly, Chapter 9 provides conclusions and recommendations for future work.

CHAPTER 2. NDA FOR SHIP STABILITY AND CAPSIZE

The Nonlinear Dynamics Approach (NDA) is one the approaches to predict ship stability and capsize by solving a mathematical model developed based on the theory of ship motions. In this chapter, the theory of ship motion is introduced and all applied forces and moments are discussed in detail. The mathematical models are developed based on the presented ship theory and discussed for many applications including roll decay, parametric rolling, and broaching. The necessary inputs - manoeuvring coefficients- to solve mathematical models are listed and the calculation procedures of inputs for roll decay, parametric rolling, and broaching are explained. Later, the solving methodology for roll decay, parametric rolling, and broaching models are described.

2.1 Equations of Motion

The 6DOF rigid body equations of motion can be expressed as 6 nonlinear coupled equations to represent the translational and rotational motions of a ship. In order to take advantage of ship geometry properties, it is desirable to drive the equations of motion in body fixed coordinates frame. It is also convenient to put the body axes parallel with the principal axes of the vessel. Then the equations of motion with respect to body axes with arbitrary origin can be expressed as:

$$
\begin{aligned}
&m\left[\dot{u}_T - v_T r_T + w_T q_T - x_g\left(q_T^2 + r_T^2\right) + y_g\left(p_T q_T - \dot{r}_T\right) + z_g\left(p_T r_T + \dot{q}_T\right)\right] = X \\
&m\left[\dot{v}_T - w_T p_T + u_T r_T - y_g\left(r_T^2 + p_T^2\right) + z_g\left(q_T r_T - \dot{p}_T\right) + x_g\left(q_T p_T + \dot{r}_T\right)\right] = Y \\
&m\left[\dot{w}_T - u_T q_T + v_T p_T - z_g\left(p_T^2 + q_T^2\right) + x_g\left(r_T p_T - \dot{q}_T\right) + y_g\left(r_T q_T + \dot{p}_T\right)\right] = Z \\
&I_x \dot{p}_T + I_{xy}\left(\dot{q}_T - p_T r_T\right) + I_{xz}\left(\dot{r}_T + p_T q_T\right) + I_{yz}\left(q_T^2 - r_T^2\right) + \left(I_z - I_y\right) q_T r_T \\
&+ m\left[y_g\left(\dot{w}_T - u_T q_T + v_T p_T\right) - z_g\left(\dot{v}_T - w_T p_T + u_T r_T\right)\right] = K \\
&I_y \dot{q}_T + I_{yz}\left(\dot{r}_T - q_T p_T\right) + I_{yx}\left(\dot{p}_T + q_T r_T\right) + I_{zx}\left(r_T^2 - p_T^2\right) \\
&+ \left(I_x - I_z\right) r_T p_T + m\left[z_g\left(\dot{u}_T - v_T r_T + w_T q_T\right) - x_g\left(\dot{w}_T - u_T q_T + v_T p_T\right)\right] = M \\
&I_z \dot{r}_T + I_{zx}\left(\dot{p}_T - r_T q_T\right) + I_{zy}\left(\dot{q}_T + r_T p_T\right) + I_{xy}\left(p_T^2 - q_T^2\right) \\
&+ \left(I_y - I_x\right) p_T q_T + m\left[x_g\left(\dot{v}_T - w_T p_T + u_T r_T\right) - y_g\left(\dot{u}_T - v_T r_T + w_T q_T\right)\right] = N
\end{aligned}
\tag{2.1}
$$

Where, $f = [X, Y, Z]^T$ are forces, $g = [K, M, N]^T$ are moments, $V = [u_T, v_T, w_T]^T$ are linear velocity, $\omega = [p_T, q_T, r_T]^T$ are angular velocity, m is mass, $R = [x_g, y_g, z_g]^T$ are coordinates of

center of gravity, and $I=[I_x, I_y, I_z]^T$ and $J=[I_{xy}, I_{xz}, I_{yz}]^T$ are moment of inertia and product of inertia in body coordinates system and can be expressed as:

$$\begin{aligned} I_x &= I_x{}^{cg} + m\left(y_g^2 + z_g^2\right) \\ I_y &= I_y{}^{cg} + m\left(x_g^2 + z_g^2\right) \\ I_z &= I_z{}^{cg} + m\left(x_g^2 + y_g^2\right) \\ I_{xy} &= I_{yx} = I_{xy}{}^{cg} + m x_g y_g \\ I_{xz} &= I_{zx} = I_{xz}{}^{cg} + m x_g z_g \\ I_{yz} &= I_{zy} = I_{yz}{}^{cg} + m y_g z_g \end{aligned} \tag{2.2}$$

Where $I=[I_x{}^{cg}, I_y{}^{cg}, I_z{}^{cg}]^T$ and $J=[I_{xy}{}^{cg}, I_{xz}{}^{cg}, I_{yz}{}^{cg}]^T$ are moments and product of inertia in body coordinates located on the center of gravity.

The equations of motion shown in Eq. (2.1) are the most general form of the equations of motion relative to body-fixed coordinate system, if the mass and mass distribution does not change in time. Solving Eq. (2.1) defines linear and angular velocity of ship. Then the ship motions can be calculated from:

$$\begin{aligned} p_T &= \dot{\phi} \\ q_T &= \dot{\theta} \\ r_T &= \dot{\psi} \\ u_T &= \dot{x} \\ v_T &= \dot{y} \\ w_T &= \dot{z} \end{aligned} \tag{2.3}$$

In application, Eq. (2) can be simplified due to port/starboard symmetry condition of ships which results in zero value for y_g, I_{xy}, and I_{yz}. Additionally I_{xz} can be neglected as small for ships with approximate fore and aft symmetry. Then the equations of motion in body coordinate system located on the center of gravity i.e. $x_g = y_g = z_g = 0$ would be as follow:

$$\begin{aligned} &m\left[\dot{u}_T - v_T r_T + w_T q_T\right] = X \\ &m\left[\dot{v}_T - w_T p_T + u_T r_T\right] = Y \\ &m\left[\dot{w}_T - u_T q_T + v_T p_T\right] = Z \\ &I_x^{cg}\dot{p}_T + \left(I_z^{cg} - I_y^{cg}\right) q_T r_T = K \\ &I_y^{cg}\dot{q}_T + \left(I_x^{cg} - I_z^{cg}\right) r_T p_T = M \\ &I_z^{cg}\dot{r}_T + \left(I_y^{cg} - I_x^{cg}\right) p_T q_T = N \end{aligned} \tag{2.4}$$

The LHS terms include linear, angular, Coriolis, and centripetal accelerations and the RHS are applied forces and moments.

Ship motions and manoeuvring mathematical models are based on perturbed Eq. (2.4) about an equilibrium position (i.e. steady axial velocity U_0 at the dynamic sinkage σ and trim τ):

$$\begin{aligned}
&m[\dot{u} - vr + (-U_0 \sin\tau + w)q] = X \\
&m[\dot{v} - (-U_0 \sin\tau + w)p + (U_0 \cos\tau + u)r] = Y \\
&m[\dot{w} - (U_0 \cos\tau + u)q + vp] = Z \\
&I_x \dot{p} + (I_z - I_y)qr = K \\
&I_y \dot{q} + (I_x - I_z)rp = M \\
&I_z \dot{r} + (I_y - I_x)pq = N
\end{aligned} \tag{2.5}$$

2.2 Forces and Moments

The right hand side of Eq. (2.5) contains total forces and moments. The total forces and moments (X, Y, Z, K, M, N) are functions of accelerations, velocities, and displacements $\pi_T(x, y, z, \phi, \theta, \psi, u, v, w, p, q, r, \dot{u}, \dot{v}, \dot{w}, \dot{p}, \dot{q}, \dot{r})$ and assumed to be linear superposition of hydrostatic (gravity and buoyancy) restoring π_{GB}, hydrodynamic π_h, and wave induced π_w along with control surfaces π_C, propulsion system π_P, and aerodynamic π_A (not considered herein). The hydrostatic restoring terms are functions of displacements including heave, roll, and pitch motion $\pi_{GB}(z, \phi, \theta)$; the hydrodynamic forces and moments are functions of accelerations, velocities, and angular displacements $\pi_h(\phi, \theta, \psi, u, v, w, p, q, r, \dot{u}, \dot{v}, \dot{w}, \dot{p}, \dot{q}, \dot{r})$ but $\psi = \sin^{-1}(-v/u)$ and $\theta = \sin^{-1}(-w/u)$ such that $\pi_h(\phi, u, v, w, p, q, r, \dot{u}, \dot{v}, \dot{w}, \dot{p}, \dot{q}, \dot{r})$.

2.2.1 Gravity-Buoyancy Forces and Moments

The gravity and buoyancy forces can be represented by:

$$\begin{aligned}
&X_{GB} = 0 \\
&Y_{GB} = 0 \\
&Z_{GB} = -\rho g A_{WP} z + \rho g A_{WP} x_{CF} \theta \\
&K_{GB} = -mgGZ(\phi) \\
&M_{GB} = -mgGM_L \theta + \rho g A_{WP} x_{CF} z \\
&N_{GB} = 0
\end{aligned} \tag{2.6}$$

Where A_{WP} is water plane area, x_{CF} is flotation center, m is mass, GM_L is longitudinal metacentric height, and GZ is roll moment arm.

2.2.2 Hull Induced Hydrodynamic Forces

Hydrodynamic forces $\pi_h(\phi,u,v,w,p,q,r,\dot{u},\dot{v},\dot{w},\dot{p},\dot{q},\dot{r})$ can be approximated by 3rd order Taylor series expansion under the following assumptions:

1) No acceleration/velocity coupling
2) Only first order acceleration terms (added mass terms)
3) No third order coupling
4) For port/starboard symmetry:

i. X_h, Z_h, M_h are even function of $(\phi,v,p,r,\dot{v},\dot{p},\dot{r})$ and general function of $(u,w,q,\dot{u},\dot{w},\dot{q})$.

ii. Y_h, K_h, N_h are odd function of $(\phi,v,p,r,\dot{v},\dot{p},\dot{r})$ and even function of $(u,w,q,\dot{u},\dot{w},\dot{q})$.

5) For slender ships, 1st order X derivatives with respect to $(w,q,\dot{w},\dot{q})$ are negligible.

$$\begin{aligned}X_h &= X_{\dot{u}}\dot{u} + X_* + X_{vv}v^2 + X_{ww}w^2 + X_{pp}p^2 + X_{qq}q^2 + X_{rr}r^2 + X_{\phi\phi}\phi^2 + X_{vp}vp + X_{vr}vr + X_{wq}wq \\ &+ X_{pr}pr + X_{v\phi}v\phi + X_{r\phi}r\phi + X_{wwq}w^2q + X_{wqq}wq^2 + X_{wvv}wv^2 + X_{wrr}wr^2 + X_{w\phi\phi}w\phi^2 + X_{wpp}wp^2 \\ &+ X_{qvv}qv^2 + X_{qrr}qr^2 + X_{q\phi\phi}q\phi^2 + X_{qpp}qp^2 + X_{www}w^3 + X_{qqq}q^3\end{aligned} \tag{2.7}$$

$$\begin{aligned}Y_h &= Y_{\dot{v}}\dot{v} + Y_{\dot{p}}\dot{p} + Y_{\dot{r}}\dot{r} + Y_v v + Y_p p + Y_\phi\phi + Y_r r + Y_{vw}vw + Y_{qr}qr + Y_{vq}vq + Y_{wr}wr + Y_{wp}wp + Y_{w\phi}w\phi + Y_{pq}pq \\ &+ Y_{\phi q}\phi q + Y_{vvp}v^2p + Y_{vv\phi}v^2\phi + Y_{wwp}w^2p + Y_{ww\phi}w^2\phi + Y_{vww}vw^2 + Y_{vvr}v^2r + Y_{wwr}w^2r + Y_{vrr}vr^2 + Y_{vqqr}vq^2 \\ &+ Y_{qqr}q^2r + Y_{vpp}vp^2 + Y_{ppr}p^2r + Y_{v\phi\phi}v\phi^2 + Y_{\phi\phi r}\phi^2r + Y_{pqq}pq^2 + Y_{prr}pr^2 + Y_{\phi qq}\phi q^2 + Y_{\phi rr}\phi r^2 + Y_{vvv}v^3 \\ &+ Y_{ppp}p^3 + Y_{rrv}r^3 + Y_{\phi\phi\phi}\phi^3\end{aligned} \tag{2.8}$$

$$\begin{aligned}Z_h &= Z_{\dot{u}}\dot{u} + Z_{\dot{w}}\dot{w} + Z_{\dot{q}}\dot{q} + Z_* + Z_w w + Z_q q + Z_{vv}v^2 + Z_{ww}w^2 + Z_{pp}p^2 + Z_{\phi\phi}\phi^2 + Z_{qq}q^2 + Z_{rr}r^2 \\ &+ Z_{vp}vp + Z_{v\phi}v\phi + Z_{pr}pr + Z_{\phi r}\phi r + Z_{vr}vr + Z_{wq}wq + Z_{vvw}v^2w + Z_{wwq}w^2q + Z_{vvq}v^2q + Z_{wqq}wq^2 \\ &+ Z_{wrr}wr^2 + Z_{qrr}qr^2 + Z_{wpp}wp^2 + Z_{w\phi\phi}w\phi^2 + Z_{ppq}p^2q + Z_{\phi\phi q}\phi^2q + Z_{www}w^3 + Z_{qqq}q^3\end{aligned} \tag{2.9}$$

$$\begin{aligned}K_h &= K_{\dot{v}}\dot{v} + K_{\dot{p}}\dot{p} + K_{\dot{r}}\dot{r} + K_v v + K_p p + K_\phi\phi + K_r r + K_{vw}vw + K_{qr}qr + K_{vq}vq + K_{wr}wr + K_{wp}wp \\ &+ K_{w\phi}w\phi + K_{pq}pq + K_{\phi q}\phi q + K_{vvp}v^2p + K_{vv\phi}v^2\phi + K_{wwp}w^2p + K_{ww\phi}w^2\phi + K_{vww}vw^2 + K_{vvr}v^2r \\ &+ K_{wwr}w^2r + K_{vrr}vr^2 + K_{vqqr}vq^2 + K_{qqr}q^2r + K_{vpp}vp^2 + K_{ppr}p^2r + K_{v\phi\phi}v\phi^2 + K_{\phi\phi r}\phi^2r + K_{pqq}pq^2 \\ &+ K_{prr}pr^2 + K_{\phi qq}\phi q^2 + K_{\phi rr}\phi r^2 + K_{vvv}v^3 + K_{ppp}p^3 + K_{rrrv}r^3 + K_{\phi\phi\phi}\phi^3\end{aligned} \tag{2.10}$$

$$
\begin{aligned}
M_h &= M_{\dot{u}}\dot{u} + M_{\dot{w}}\dot{w} + M_{\dot{q}}\dot{q} + M_* + M_w w + M_q q + M_{vv}v^2 + M_{ww}w^2 + M_{pp}p^2 + M_{\phi\phi}\phi^2 + M_{qq}q^2 + M_{rr}r^2 \\
&+ M_{vp}vp + M_{v\phi}v\phi + M_{pr}pr + M_{\phi r}\phi r + M_{vr}vr + M_{wq}wq + M_{vvw}v^2 w + M_{wwq}w^2 q + M_{vvq}v^2 q + M_{wqq}wq^2 \\
&+ M_{wrr}wr^2 + M_{qrr}qr^2 + M_{wpp}wp^2 + M_{w\phi\phi}w\phi^2 + M_{ppq}p^2 q + M_{\phi\phi q}\phi^2 q + M_{www}w^3 + M_{qqq}q^3
\end{aligned}
\tag{2.11}
$$

$$
\begin{aligned}
N_h &= N_{\dot{v}}\dot{v} + N_{\dot{p}}\dot{p} + N_{\dot{r}}\dot{r} + N_v v + N_P p + N_\phi \phi + N_r r + N_{vw}vw + N_{qr}qr + N_{vq}vq + N_{wr}wr + N_{wp}wp \\
&+ N_{w\phi}w\phi + N_{pq}pq + N_{\phi q}\phi q + N_{vvp}v^2 p + N_{vv\phi}v^2\phi + N_{wwp}w^2 p + N_{ww\phi}w^2\phi + N_{vww}vw^2 + N_{vvr}v^2 r \\
&+ N_{wwr}w^2 r + N_{vrr}vr^2 + N_{vqqr}vq^2 + N_{qqr}q^2 r + N_{vpp}vp^2 + N_{ppr}p^2 r + N_{v\phi\phi}v\phi^2 + N_{\phi\phi r}\phi^2 r + N_{pqq}pq^2 \\
&+ N_{prr}pr^2 + N_{\phi qq}\phi q^2 + N_{\phi rr}\phi r^2 + N_{vvv}v^3 + N_{ppp}p^3 + N_{rrrv}r^3 + N_{\phi\phi\phi}\phi^3
\end{aligned}
\tag{2.12}
$$

As it is explained, only first order added mass terms are considered in Eqs. (2.7) - (2.12). For some applications, it might be necessary to include higher order added mass terms. Equation (2.13) show the linear and higher order added mass terms for port/starboard symmetric slender ship (Fossen, 1999):

$$
\begin{aligned}
X_{AM} &= \underline{X_{\dot{u}}\dot{u}} + \underline{\underline{Z_{\dot{u}}u_T q}} + Z_{\dot{w}}w_T q + Z_{\dot{q}}q^2 - Y_{\dot{v}}vr - Y_{\dot{p}}rp - Y_{\dot{r}}r^2 \\
Y_{AM} &= \underline{Y_{\dot{v}}\dot{v} + Y_{\dot{p}}\dot{p} + Y_{\dot{r}}\dot{r}} + \underline{\underline{X_{\dot{u}}u_T r - Z_{\dot{u}}u_T p}} - Z_{\dot{w}}w_T p - Z_{\dot{q}}pq \\
Z_{AM} &= \underline{Z_{\dot{u}}\dot{u} + Z_{\dot{w}}\dot{w} + Z_{\dot{q}}\dot{q}} - \underline{\underline{X_{\dot{u}}u_T q}} + Y_{\dot{v}}vp + Y_{\dot{r}}rp + Y_{\dot{p}}p^2 \\
K_{AM} &= \underline{K_{\dot{v}}\dot{v} + K_{\dot{p}}\dot{p} + K_{\dot{r}}\dot{r}} - \underline{\underline{M_{\dot{u}}u_T r + Z_{\dot{u}}u_T v}} + \left(N_{\dot{v}} + Z_{\dot{q}}\right)vq + \left(N_{\dot{r}} - M_{\dot{q}}\right)qr - \left(Y_{\dot{r}} + M_{\dot{w}}\right)w_T r + \left(Z_{\dot{w}} - Y_{\dot{v}}\right)vw_T \\
&- Y_{\dot{p}}w_T p + N_{\dot{p}}pq \\
M_{AM} &= \underline{M_{\dot{u}}\dot{u} + M_{\dot{w}}\dot{w} + M_{\dot{q}}\dot{q}} - \underline{\underline{\left(Z_{\dot{w}} - X_{\dot{u}}\right)w_T u_T - Z_{\dot{u}}u_T^2 - Z_{\dot{q}}u_T q}} + \left(K_{\dot{p}} - N_{\dot{r}}\right)rp + K_{\dot{r}}r^2 - N_{\dot{p}}p^2 + K_{\dot{v}}vr - N_{\dot{v}}vp \\
N_{AM} &= \underline{N_{\dot{v}}\dot{v} + N_{\dot{p}}\dot{p} + N_{\dot{r}}\dot{r}} + \underline{\underline{\left(M_{\dot{u}} + Y_{\dot{p}}\right)u_T p - \left(X_{\dot{u}} - Y_{\dot{v}}\right)u_T v + Y_{\dot{r}}u_T r}} - \left(K_{\dot{p}} - M_{\dot{q}}\right)pq + M_{\dot{w}}w_T p - K_{\dot{v}}vq - K_{\dot{r}}qr
\end{aligned}
\tag{2.13}
$$

For small perturbations, several terms are negligible and only underlined terms have to be considered. The terms underlined by (–) are linear added mass terms and those underlined by (=) show nonlinear terms reducing to linear form for small perturbation. For instance, $M_{\dot{u}}u_T r$ reduces to $M_{\dot{u}}(U_0\cos\tau)r$.

2.2.3 Wave Forces

In order to evaluate wave forces and moments, it is usual to consider the system to be linear. Under these assumptions the system of ship and waves is presented as a linear system:

1) Waves are small i.e. waves amplitude is much smaller than wave length: kA<<1

2) The ship is stable so that small disturbances will yield proportionally small responses

3) Nonlinear effects due to viscosity is negligible

Since it is assumed that effect of viscosity is negligible, potential function can be used to express the system of a ship in presence of waves. It is expected the resulting potential of fluid velocities to be contributed from flow caused by wave and body motion:

$$\varphi = \sum_{j=1}^{6} \varphi_{Bj} + \underbrace{\varphi_W}_{\varphi_I + \varphi_D} \tag{2.14}$$

Where φ_{Bj} is the potential of fluid velocities induced by the different mode of ship motions and it does not include any wave influence (φ_{Bj} is also known as radiation part) and φ_W is the potential of flow caused by the wave including incident φ_I and diffracted waves φ_D. Note that the possibility to break potential of fluid velocities as expressed in Eq. (2.14) is result of linear system.

The assumed linearity of the system makes it possible to say that a sinusoidal input to the linear system produces a sinusoidal output at the same frequency. If the wave is assumed to have a form of cosine function:

$$\zeta_W = A\cos(\omega t) = \mathrm{Re}\left\{Ae^{-i\omega t}\right\} \tag{2.15}$$

Where A is wave amplitude and ω is wave frequency.

Then:

$$\varphi_{Bj} = \mathrm{Re}\left\{\varphi_j e^{-i\omega t}\right\} \tag{2.16}$$

$$\varphi_W = \varphi_I + \varphi_D = \mathrm{Re}\left\{\left(\varphi_{Is} + \varphi_{Ds}\right)e^{-i\omega t}\right\} \tag{2.17}$$

Here φ_j is fluid velocity potential amplitude caused by the j-th component of body motion and φ_{Is} and φ_{Ds} are fluid velocity potential amplitude expressing influence of incident and diffracted waves, respectively.

Re-writing Eq. (2.14) using Eqs. (2.15) – (2.17) yields:

$$\varphi = \mathrm{Re}\left\{\left[\sum_{j=1}^{6} \varphi_j + \left(\varphi_{Is} + \varphi_{Ds}\right)\right]e^{-i\omega t}\right\} \tag{2.18}$$

Bernoulli's equation allows expressing pressure through fluid velocity potential:

$$p = -\rho\left(\frac{\partial \varphi}{\partial t} + \rho g(z+\zeta)\right) \tag{2.19}$$

Here ζ represents the free surface elevation.

Substituting Eq. (2.18) in Eq. (2.19) yields to the pressure formula:

$$p = -\rho\left\{\mathrm{Re}\left[-i\omega e^{-i\omega t}\left(\sum_{j=1}^{6}\varphi_j + (\varphi_{Is}+\varphi_{Ds})\right)\right] + \rho g(z+\zeta)\right\} \tag{2.20}$$

Integration of these pressures over the surface of the ship hull produces wave forces and moments:

$$\begin{aligned}
\vec{F}_{Wave} &= \underbrace{-\rho g\iint_{S_B}(z+\zeta)\vec{n}dS}_{F^{H}_{Wave}} && -\textit{Hydrostatics}\\
&\underbrace{-\rho\iint_{S_B}\mathrm{Re}\left[-i\omega e^{-i\omega t}\left(\sum_{j=1}^{6}\varphi_j\right)\right]\vec{n}dS}_{F^{R}_{Wave}} && -\textit{Radiation Forces}\\
&\underbrace{-\rho\iint_{S_B}\mathrm{Re}\left[-i\omega e^{-i\omega t}(\varphi_{Is}+\varphi_{Ds})\right]\vec{n}dS}_{F^{FK\&D}_{Wave}} && -\textit{Wave Exciiting Forces}\,(FK\ \&\ Diffraction)
\end{aligned} \tag{2.21}$$

$$\begin{aligned}
\vec{M}_{Wave} &= \underbrace{-\rho g\iint_{S_B}(z+\zeta)(r\times\vec{n})dS}_{M^{H}_{Wave}} && -\textit{Hydrostatics}\\
&\underbrace{-\rho\iint_{S_B}\mathrm{Re}\left[-i\omega e^{-i\omega t}\left(\sum_{j=1}^{6}\varphi_j\right)\right](r\times\vec{n})dS}_{M^{R}_{Wave}} && -\textit{Radiation Moments}\\
&\underbrace{-\rho\iint_{S_B}\mathrm{Re}\left[-i\omega e^{-i\omega t}(\varphi_{Is}+\varphi_{Ds})\right](r\times\vec{n})dS}_{M^{FK\&D}_{Wave}} && -\textit{Wave Exciiting Moments}(FK\ \&\ Diffraction)
\end{aligned} \tag{2.22}$$

Here $F_{Wave} = [X_{Wave}, Y_{Wave}, Z_{Wave}]^T$ are wave forces, $M_{Wave} = [K_{Wave}, M_{Wave}, N_{Wave}]^T$ are wave moments, and S_B is the hull surface.

The forces and moments shown in Eqs. (2.21) and (2.22) classify the contribution of each potential as hydrostatics, radiation or wave exciting forces and moments. *Wave-exciting forces* are due to the wave system only, with the body assumed to be fixed. There are two components present in wave-exciting force. One is the result of pressure related with incident wave and another one with diffracted wave. The first component could be considered as wave force acting on a ship in waves, but calculated with assumption that

the ship does not affect fluid velocities by her presence. This assumption is known as Froude-Krylov hypothesis and this kind of force is called Froude-Krylov force. The second component represents the disturbance that a ship makes to the fluid velocities in an incident wave by her presence. This force is called diffraction force. *Radiation forces* are the forces generated by the motion of the body in calm water. *Hydrostatic forces of waves* are the hydrostatic forces and moments in the water with elevated free surface.

In order to calculate radiation and wave exciting forces and moments, having fluid velocity potentials are essential. These fluid velocity potentials have to be found such that they satisfy continuity, the free surface, ship hull and far-field conditions (Newman, 1977). For incident wave:

$$\begin{aligned} \nabla^2 \varphi_{Is} &= 0 \quad - Continuity \\ \omega^2 \varphi_{Is} + g \frac{\partial \varphi_{Is}}{\partial z} &= 0 \; - Free\,surface \\ \frac{\partial \varphi_{Is}}{\partial z} &= 0 \; - Bottom \end{aligned} \tag{2.23}$$

As shown in Eq. (2.23), the incident potential is considered without knowledge of the presence of the ship. This makes it possible to have analytical solution for φ_{Is}. For instance, for a two-dimensional wave:

$$\varphi_{Is} = \frac{i\omega}{k} \frac{\cosh(k[z+H])}{\sinh(kH)} e^{-ikx} \tag{2.24}$$

Here H is the depth of the water.

For diffraction part, the conditions are:

$$\begin{aligned} \nabla^2 \varphi_{Ds} &= 0 \quad - Continuity \\ \omega^2 \varphi_{Ds} + g \frac{\partial \varphi_{Ds}}{\partial z} &= 0 \; - Free\,surface \\ \frac{\partial \varphi_{Ds}}{\partial z} &= 0 \; - Bottom \\ \frac{\partial \varphi_{Ds}}{\partial n} &= -\frac{\partial \varphi_{Is}}{\partial n} \; - Body \end{aligned} \tag{2.25}$$

Here, the solution for φ_{Ds} is dependent on the ship geometry. Since the ship geometry is usually complicated, there is no analytical solution for diffraction part unless it is assumed that the ship is a slender body.

For radiation part, the conditions are:

$$\begin{aligned} \nabla^2\varphi_j &= 0 \quad - Continuity \\ \omega^2\varphi_j + g\frac{\partial\varphi_j}{\partial z} &= 0 \quad - Free\,surface \\ \frac{\partial\varphi_j}{\partial z} &= 0 \quad - Bottom \\ \frac{\partial\varphi_j}{\partial n} &= -i\omega\nabla\varphi_j.\vec{n} \quad - Body \end{aligned} \tag{2.26}$$

Since the geometry of a ship is complicated, there is no analytical solution for radiation part unless the ship is assumed to be a slender body.

Unlike the wave exciting forces and radiation forces, the calculation of hydrostatic force in presence of wave is not function of those fluid velocity potentials and can be calculated directly by integration of hydrostatic pressure. As shown in Eqs. (2.25) and (2.26), hydrostatic forces and moments have two components. One component is the hydrostatic forces in calm water and the second component is added hydrostatic forces and moments due to the waves. The first component is already taken into account in Eq. (2.6) and it would be redundant considering it here. The second component is fairly negligible except for roll moment K:

$$\begin{aligned} X^H_{Wave} &= 0 \\ Y^H_{Wave} &= 0 \\ Z^H_{Wave} &= 0 \\ K^H_{Wave} &= -mg\Delta GZ^{wave} \\ M^H_{Wave} &= 0 \\ N^H_{Wave} &= 0 \end{aligned} \tag{2.27}$$

Substituting Eq. (2.27) in Eqs. (2.21) and (2.22) yields to:

$$\begin{aligned} X_{Wave} &= \underbrace{X^R_{Wave} + X^{FK\&D}_{Wave}}_{X_W} \\ Y_{Wave} &= \underbrace{Y^R_{Wave} + Y^{FK\&D}_{Wave}}_{Y_W} \\ Z_{Wave} &= \underbrace{Z^R_{Wave} + Z^{FK\&D}_{Wave}}_{Z_W} \\ K_{Wave} &= \underbrace{K^R_{Wave} + K^{FK\&D}_{Wave}}_{K_W} - mg\Delta GZ^{wave} \\ M_{Wave} &= \underbrace{M^R_{Wave} + M^{FK\&D}_{Wave}}_{M_W} \\ N_{Wave} &= \underbrace{N^R_{Wave} + N^{FK\&D}_{Wave}}_{N_W} \end{aligned} \tag{2.28}$$

Where subscript "wave" indicates waves forces including Froude-Krylov, diffraction, and radiation components.

2.2.4 Propulsion Forces and Moments of Propellers

The hydrodynamic forces and moments due to twin propellers included in LHS of Eq. (2.5) can be written as Eq. (2.29) under the assumption that both propellers have the same property and the distribution of torque around the propellers due to oblique flow i.e. when the ship is at an attack angle is negligible:

$$\begin{aligned} X_p &= 2(1-t_p)\rho n^2 D_p^4 K_T(J) \\ Y_p &= 0 \\ Z_p &= 0 \\ K_p &= 0 \\ M_p &= 2(1-t_p)\rho n^2 D_p^4 K_T(J) z_p \\ N_p &= 0 \end{aligned} \tag{2.29}$$

Here, t_p is thrust deduction factor, n is propeller revolution, D_p is propeller diameter, K_T is thrust coefficient measured by POT, z_p is the vertical coordinates of the propellers, and J is advance ratio defined as:

$$J = \frac{(1-w_p)U_A}{nD_p} \tag{2.30}$$

Where w_p is known as effective propeller wake fraction, and U_A is the advanced velocity.

2.2.5 Control Surface Forces and Moments of Rudders

The hydrodynamic forces and moments for control surface such as rudders are expressed as:

$$\begin{aligned} X_C &= 0 \\ Y_C &= Y_\delta \delta_R \\ Z_C &= 0 \\ K_C &= K_\delta \delta_R \\ M_C &= 0 \\ N_C &= N_\delta \delta_R \end{aligned} \tag{2.31}$$

In which:

$$
\begin{aligned}
Y_\delta &= -(1+a_H)\frac{1}{2}\rho A_R f_\alpha \varepsilon_R^2 \times (1-w_P)^2\left(1+\kappa_P\frac{8K_T}{\pi J^2}\right)^2 u^2 \\
K_\delta &= -(1+a_H)z_{HR}\frac{1}{2}\rho A_R f_\alpha \varepsilon_R^2 \times (1-w_P)^2\left(1+\kappa_P\frac{8K_T}{\pi J^2}\right)^2 u^2 \\
N_\delta &= -(x_R+a_H x_H)\frac{1}{2}\rho A_R f_\alpha \varepsilon_R^2 \times (1-w_P)^2\left(1+\kappa_P\frac{8K_T}{\pi J^2}\right)^2 u^2
\end{aligned}
\tag{2.32}
$$

Here, a_H is interaction factor between hull and rudder, x_H is the longitudinal position of interaction factor between hull and rudder, z_{HR} is the vertical position of center of effective rudder force, x_R is the longitudinal position of the rudder force, κ_P is interaction factor between propeller and rudder, ε_R is wake ratio between propeller and hull, w_p is effective propeller wake, A_R is the rudder area, and:

$$
f_\alpha = \frac{6.13\Lambda}{2.25+\Lambda} \tag{2.33}
$$

where Λ is rudder aspect ratio.

2.3 Perturbed Equations of Motion for Ship

The general form of body-fixed perturbed equations of motion for a port-starboard symmetric ship can be reached by substituting hydrostatic forces, hull induced hydrodynamic forces, wave forces, propeller forces, and lastly rudder forces in Eq. (2.5):

$$
\begin{aligned}
&m[\dot{u}-vr+(-U_0\sin\tau+w)q] = X_{\dot{u}}\dot{u}+X_*+X_{vv}v^2+X_{ww}w^2+X_{pp}p^2+X_{qq}q^2+X_{rr}r^2+X_{\phi\phi}\phi^2+X_{vp}vp \\
&+X_{vr}vr+X_{wq}wq+X_{pr}pr+X_{v\phi}v\phi+X_{r\phi}r\phi+X_{wwq}w^2q+X_{wqq}wq^2+X_{wvv}wv^2+X_{wrr}wr^2+X_{w\phi\phi}w\phi^2 \\
&+X_{wpp}wp^2+X_{qvv}qv^2+X_{qrr}qr^2+X_{q\phi\phi}q\phi^2+X_{qpp}qp^2+X_{www}w^3+X_{qqq}q^3+X_W+2(1-t_p)\rho n^2 D_p^4 K_T(J)
\end{aligned}
\tag{2.34}
$$

$$
\begin{aligned}
&m[\dot{v}-(-U_0\sin\tau+w)p+(U_0\cos\tau+u)r] = Y_v\dot{v}+Y_{\dot{p}}\dot{p}+Y_{\dot{r}}\dot{r}+Y_v v+Y_P p+Y_\phi\phi+Y_r r+Y_{vw}vw+Y_{qr}qr+Y_{vq}vq \\
&+Y_{wr}wr+Y_{wp}wp+Y_{w\phi}w\phi+Y_{pq}pq+Y_{\phi q}\phi q+Y_{vvp}v^2p+Y_{vv\phi}v^2\phi+Y_{wwp}w^2p+Y_{ww\phi}w^2\phi+Y_{vww}vw^2+Y_{vvr}v^2r \\
&+Y_{wwr}w^2r+Y_{vrr}vr^2+Y_{vqr}vq^2+Y_{qqr}q^2r+Y_{vpp}vp^2+Y_{ppr}p^2r+Y_{v\phi\phi}v\phi^2+Y_{\phi\phi r}\phi^2r+Y_{pqq}pq^2+Y_{prr}pr^2+Y_{\phi qq}\phi q^2 \\
&+Y_{\phi rr}\phi r^2+Y_{vvv}v^3+Y_{ppp}p^3+Y_{rrv}r^3+Y_{\phi\phi\phi}\phi^3+Y_W+Y_\delta\delta_R
\end{aligned}
\tag{2.35}
$$

$$
\begin{aligned}
&m[\dot{w}-(U_0\cos\tau+u)q+vp] = -\rho g A_{WP}z+\rho g A_{WP}x_{CF}\theta+Z_{\dot{u}}\dot{u}+Z_{\dot{w}}\dot{w}+Z_{\dot{q}}\dot{q}+Z_*+Z_w w+Z_q q+Z_{vv}v^2+Z_{ww}w^2 \\
&+Z_{pp}p^2+Z_{\phi\phi}\phi^2+Z_{qq}q^2+Z_{rr}r^2+Z_{vp}vp+Z_{v\phi}v\phi+Z_{pr}pr+Z_{\phi r}\phi r+Z_{vr}vr+Z_{wq}wq+Z_{vvw}v^2w+Z_{wwq}w^2q \\
&+Z_{vvq}v^2q+Z_{wqq}wq^2+Z_{wrr}wr^2+Z_{qrr}qr^2+Z_{wpp}wp^2+Z_{w\phi\phi}w\phi^2+Z_{ppq}p^2q+Z_{\phi\phi q}\phi^2q+Z_{www}w^3+Z_{qqq}q^3+Z_W
\end{aligned}
\tag{2.36}
$$

$$
\begin{aligned}
&I_x^{cg}\dot{p}+\left(I_z^{cg}-I_y^{cg}\right)qr=-mgGZ(\phi)+K_{\dot{v}}\dot{v}+K_{\dot{p}}\dot{p}+K_{\dot{r}}\dot{r}+K_v v+K_P p+K_\phi\phi+K_r r+K_{vw}vw\\
&+K_{qr}qr+K_{vq}vq+K_{wr}wr+K_{wp}wp+K_{w\phi}w\phi+K_{pq}pq+K_{\phi q}\phi q+K_{vvp}v^2p+K_{vv\phi}v^2\phi+K_{wwp}w^2p+K_{ww\phi}w^2\phi\\
&+K_{vww}vw^2+K_{vvr}v^2r+K_{wwr}w^2r+K_{vrr}vr^2+K_{vqqr}vq^2+K_{qqr}q^2r+K_{vpp}vp^2+K_{ppr}p^2r+K_{v\phi\phi}v\phi^2+K_{\phi\phi r}\phi^2r\\
&+K_{pqq}pq^2+K_{prr}pr^2+K_{\phi qq}\phi q^2+K_{\phi rr}\phi r^2+K_{vvv}v^3+K_{ppp}p^3+K_{rrrv}r^3+K_{\phi\phi\phi}\phi^3+K_W-mg\Delta GZ^{Wave}+K_\delta\delta_R
\end{aligned}
\tag{2.37}
$$

$$
\begin{aligned}
&I_y^{cg}\dot{q}+\left(I_x^{cg}-I_z^{cg}\right)rp=-mgGM_L\theta+\rho gA_{WP}x_{CF}z+M_{\dot{u}}\dot{u}+M_{\dot{w}}\dot{w}+M_{\dot{q}}\dot{q}+M_*+M_w w+M_q q+M_{vv}v^2+M_{ww}w^2\\
&+M_{pp}p^2+M_{\phi\phi}\phi^2+M_{qq}q^2+M_{rr}r^2+M_{vp}vp+M_{v\phi}v\phi+M_{pr}pr+M_{\phi r}\phi r+M_{vr}vr+M_{wq}wq+M_{vvw}v^2w\\
&+M_{wwq}w^2q+M_{vvq}v^2q+M_{wqq}wq^2+M_{wrr}wr^2+M_{qrr}qr^2+M_{wpp}wp^2+M_{w\phi\phi}w\phi^2+M_{ppq}p^2q\\
&+M_{\phi\phi q}\phi^2q+M_{www}w^3+M_{qqq}q^3+M_W+2(1-t_p)\rho n^2D_p^4K_T(J)z_p
\end{aligned}
\tag{2.38}
$$

$$
\begin{aligned}
&I_z^{cg}\dot{r}+\left(I_y^{cg}-I_x^{cg}\right)pq=N_{\dot{v}}\dot{v}+N_{\dot{p}}\dot{p}+N_{\dot{r}}\dot{r}+N_v v+N_P p+N_\phi\phi+N_r r+N_{vw}vw\\
&+N_{qr}qr+N_{vq}vq+N_{wr}wr+N_{wp}wp+N_{w\phi}w\phi+N_{pq}pq+N_{\phi q}\phi q+N_{vvp}v^2p+N_{vv\phi}v^2\phi+N_{wwp}w^2p+N_{ww\phi}w^2\phi\\
&+N_{vww}vw^2+N_{vvr}v^2r+N_{wwr}w^2r+N_{vrr}vr^2+N_{vqqr}vq^2+N_{qqr}q^2r+N_{vpp}vp^2+N_{ppr}p^2r+N_{v\phi\phi}v\phi^2+N_{\phi\phi r}\phi^2r\\
&+N_{pqq}pq^2+N_{prr}pr^2+N_{\phi qq}\phi q^2+N_{\phi rr}\phi r^2+N_{vvv}v^3+N_{ppp}p^3+N_{rrrv}r^3+N_{\phi\phi\phi}\phi^3+N_W+N_\delta\delta_R
\end{aligned}
\tag{2.39}
$$

For U_0=0 and zero perturbation velocities and non zero perturbation motions Eqs. (2.34)-(2.39) reduce to Eq. (2.6). For $U_0\neq0$ and zero perturbation velocities and non zero perturbation motions, which is resistance test in calm water, Eqs. (2.34)-(2.39) reduce to $X_{Measured}=X^*$, $\rho gA_{WP}(z_0-x_{CF}\theta_0)=Z_*$, and $mgGM_L\theta_0-\rho gA_{WP}x_{CF}z_0=M_*$ where X* is resistance in calm water, z_0 and θ_0 are dynamic sinkage σ and trim τ.

For small steady state sinkage and trim and small perturbation motions, the linear equations are uncoupled vertical x, z, θ and horizontal y, ϕ, ψ plane motions. The slender ship assumption additionally uncouples x from z and θ since the equations are written with respect to the centre of gravity. Standard seakeeping prediction methods solve linear z and θ equations and 2nd order x equation using potential-flow slender-body theory to predict heave and pitch motions and added resistance for regular and irregular head waves. Standard 4DOF maneuvering prediction methods solve 3rd order x, y, ϕ, ψ equations neglecting z and θ using captive model test data to predict horizontal plane trajectories such as turning circles and zig-zag maneuvers.

2.4 Mathematical Models

The mathematical models for different application can be developed based on the theory shown in Eqs. (2.34)-(2.39) and then can be considered in simulation analysis.

2.4.1 1 DOF Roll Decay in Calm Water

For 1DOF roll decay test in calm water without rudders and propellers, Eqs. (2.34)-(2.39) are simplified as:

$$\begin{aligned}
0 &= X_* + X_{pp}p^2 + X_{\phi\phi}\phi^2 - X_{Measured} \\
0 &= Y_P p + Y_\phi \phi + Y_{ppp}p^3 + Y_{\phi\phi\phi}\phi^3 - Y_{Measured} \\
0 &= Z_* + Z_{pp}p^2 + Z_{\phi\phi}\phi^2 - Z_{Measured} \\
I_x^{cg}\dot{p} &= -mgGZ(\phi) + K_{\dot{p}}\dot{p} + K_P p + K_\phi \phi + K_{ppp}p^3 + K_{\phi\phi\phi}\phi^3 \\
0 &= M_* + M_{pp}p^2 + M_{\phi\phi}\phi^2 - M_{Measured} \\
0 &= N_P p + N_\phi \phi + N_{ppp}p^3 + N_{\phi\phi\phi}\phi^3 - N_{Measured}
\end{aligned} \tag{2.40}$$

Herein, $GZ(\phi)$ usually is considered as a higher order polynomial function of ϕ:

$$mgGZ(\phi) = mg\left(l_1\phi + l_3\phi^3 + l_5\phi^5 + \ldots\right) \tag{2.41}$$

Where l_i are roll restoring moment arm coefficients.

The equation for roll motion, shown in Eq. (2.41), can be rewritten as following form:

$$\ddot{\phi} + \underbrace{\frac{-K_{\dot{\phi}}}{\left(I_x^{cg} - K_{\ddot{\phi}}\right)}}_{\alpha}\dot{\phi} + \underbrace{\frac{-K_{\dot{\phi}\dot{\phi}\dot{\phi}}}{\left(I_x^{cg} - K_{\ddot{\phi}}\right)}}_{\gamma}\dot{\phi}^3 + \underbrace{\frac{mgGM}{\left(I_x^{cg} - K_{\ddot{\phi}}\right)}}_{\omega_\phi^2}\underbrace{\frac{1}{GM}\left[GZ(\phi) + K_\phi\phi + K_{\phi\phi\phi}\phi^3\right]}_{\sum_{n=1,3,5,\ldots,N} l'_n\phi^n} = 0 \tag{2.42}$$

Here, $\alpha$and γ are damping coefficients, ω_ϕ is natural roll frequency, GM is metacentric height in calm water, l'_n is restoring moment coefficients in calm water.

For 1 DOF roll decay in calm water, heave and pitch motions are negligible and roll response is under damped harmonic oscillations at $f_{\phi d}$. X indicates 2nd order/harmonic amplitudes due to roll motion, whereas Y and N indicate 1st and 3rd order/harmonic amplitudes due to roll motion. Z and M indicate 2nd order/harmonic amplitudes due to roll motion.

2.4.2 3 DOF Roll Decay in Calm Water

For 3DOF roll decay test free to roll, sink, and trim, Eqs. (2.34)-(2.39) reduce to the following form:

$$
\begin{aligned}
&m\left[(-U_0\sin\tau+w)q\right]=X_*+X_{ww}w^2+X_{pp}p^2+X_{qq}q^2+X_{\phi\phi}\phi^2+X_{wq}wq+X_{wwq}w^2q+X_{wqq}wq^2\\
&+X_{w\phi\phi}w\phi^2+X_{wpp}wp^2+X_{q\phi\phi}q\phi^2+X_{qpp}qp^2+X_{www}w^3+X_{qqq}q^3-X_{Measured}\\
&m\left[(U_0\sin\tau-w)p\right]=Y_Pp+Y_\phi\phi+Y_{wp}wp+Y_{w\phi}w\phi+Y_{pq}pq+Y_{\phi q}\phi q+Y_{wwp}w^2p+Y_{ww\phi}w^2\phi+Y_{pqq}pq^2+Y_{\phi qq}\phi q^2\\
&+Y_{ppp}p^3+Y_{\phi\phi\phi}\phi^3-Y_{Measured}\\
&m\left[\dot w-(U_0\cos\tau+u)q\right]=-\rho gA_{WP}z+\rho gA_{WP}x_{CF}\theta+Z_{\dot w}\dot w+Z_*+Z_ww+Z_qq+Z_{ww}w^2+Z_{pp}p^2+Z_{\phi\phi}\phi^2\\
&+Z_{qq}q^2+Z_{wq}wq+Z_{wwq}w^2q+Z_{wqq}wq^2+Z_{wpp}wp^2+Z_{w\phi\phi}w\phi^2+Z_{ppq}p^2q+Z_{\phi\phi q}\phi^2q+Z_{www}w^3+Z_{qqq}q^3\\
&I_x^{cg}\dot p=-mgGZ(\phi)+K_{\dot p}\dot p+K_Pp+K_\phi\phi+K_{wp}wp+K_{w\phi}w\phi+K_{pq}pq+K_{\phi q}\phi q+K_{wwp}w^2p\\
&+K_{ww\phi}w^2\phi+K_{pqq}pq^2+K_{\phi qq}\phi q^2+K_{ppp}p^3+K_{\phi\phi\phi}\phi^3\\
&I_y^{cg}\dot q=-mgGM_L\theta+\rho gA_{WP}x_{CF}z+M_{\dot q}\dot q+M_*+M_ww+M_qq+M_{ww}w^2+M_{pp}p^2+M_{\phi\phi}\phi^2+M_{qq}q^2+M_{wq}wq\\
&+M_{wwq}w^2q+M_{wqq}wq^2+M_{wpp}wp^2+M_{w\phi\phi}w\phi^2+M_{ppq}p^2q+M_{\phi\phi q}\phi^2q+M_{www}w^3+M_{qqq}q^3\\
&\left(I_y^{cg}-I_x^{cg}\right)pq=N_Pp+N_\phi\phi+N_{wp}wp+N_{w\phi}w\phi+N_{pq}pq+N_{\phi q}\phi q+N_{wwp}w^2p+N_{ww\phi}w^2\phi\\
&+N_{pqq}pq^2+N_{\phi qq}\phi q^2+N_{ppp}p^3+N_{\phi\phi\phi}\phi^3-N_{Measured}
\end{aligned}
\tag{2.43}
$$

Since heave and pitch velocities (or motions) are very small in roll decay test, higher order heave and pitch terms can be neglected. Therefore:

$$
\begin{aligned}
&m\left[(-U_0\sin\tau+w)q\right]=X_*+X_{pp}p^2+X_{\phi\phi}\phi^2+X_{w\phi\phi}w\phi^2+X_{wpp}wp^2+X_{q\phi\phi}q\phi^2+X_{qpp}qp^2-X_{Measured}\\
&m\left[(U_0\sin\tau-w)p\right]=Y_Pp+Y_\phi\phi+Y_{wp}wp+Y_{w\phi}w\phi+Y_{pq}pq+Y_{\phi q}\phi q+Y_{ppp}p^3+Y_{\phi\phi\phi}\phi^3-Y_{Measured}\\
&m\left[\dot w-(U_0\cos\tau+u)q\right]=-\rho gA_{WP}z+\rho gA_{WP}x_{CF}\theta+Z_{\dot w}\dot w+Z_*+Z_ww+Z_qq+Z_{pp}p^2+Z_{\phi\phi}\phi^2\\
&+Z_{wpp}wp^2+Z_{w\phi\phi}w\phi^2+Z_{ppq}p^2q+Z_{\phi\phi q}\phi^2q\\
&I_x^{cg}\dot p=-mgGZ(\phi)+K_{\dot p}\dot p+K_Pp+K_\phi\phi+K_{wp}wp+K_{w\phi}w\phi+K_{pq}pq+K_{\phi q}\phi q+K_{ppp}p^3+K_{\phi\phi\phi}\phi^3\\
&I_y^{cg}\dot q=-mgGM_L\theta+\rho gA_{WP}x_{CF}z+M_{\dot q}\dot q+M_*+M_ww+M_qq+M_{pp}p^2+M_{\phi\phi}\phi^2\\
&+M_{wpp}wp^2+M_{w\phi\phi}w\phi^2+M_{ppq}p^2q+M_{\phi\phi q}\phi^2q\\
&\left(I_y^{cg}-I_x^{cg}\right)pq=N_Pp+N_\phi\phi+N_{wp}wp+N_{w\phi}w\phi+N_{pq}pq+N_{\phi q}\phi q+N_{ppp}p^3+N_{\phi\phi\phi}\phi^3-N_{Measured}
\end{aligned}
\tag{2.44}
$$

Since heave and pitch motions are negligible and roll response is under damped harmonic oscillations at $f_{\phi d}$, X indicates 2nd order/harmonic amplitudes only due to roll motion whereas Y and N indicate 1st and 3rd order/harmonic amplitudes due to roll motion.

2.4.3 1 DOF Roll in Head Waves

For 1DOF roll in head waves, Eqs. (2.34)-(2.39) reduce to the following form:

$$
\begin{aligned}
&0=X_*+X_{pp}p^2+X_{\phi\phi}\phi^2+X_W-X_{Measured}\\
&0=Y_Pp+Y_\phi\phi+Y_{ppp}p^3+Y_{\phi\phi\phi}\phi^3-Y_{Measured}\\
&0=Z_*+Z_{pp}p^2+Z_{\phi\phi}\phi^2+Z_W-Z_{Measured}\\
&I_x^{cg}\dot p=-mgGZ(\phi)+K_{\dot p}\dot p+K_Pp+K_\phi\phi+K_{ppp}p^3+K_{\phi\phi\phi}\phi^3-mg\Delta GZ^{Wave}\\
&0=M_*+M_{pp}p^2+M_{\phi\phi}\phi^2+M_W-M_{Measured}\\
&0=N_Pp+N_\phi\phi+N_{ppp}p^3+N_{\phi\phi\phi}\phi^3-N_{Measured}
\end{aligned}
\tag{2.45}
$$

Herein, $GZ(\phi)$ usually is considered as a higher order polynomial function of ϕ:

$$mgGZ(\phi) = mg\left(l_1\phi + l_3\phi^3 + l_5\phi^5 + \ldots\right) \tag{2.46}$$

Where l_i are roll restoring moment arm coefficients in calm water.

Also, ΔGZ^{Wave} usually is considered as a higher order polynomial function of ϕ and Fourier function of time:

$$mg\Delta GZ^{Wave} = mg\begin{pmatrix}(Q_{01} + Q_{11}\cos(\omega_e t + \varepsilon_{11}) + \ldots + Q_{n1}\cos(n\omega_e t + \varepsilon_{n1}))\phi \\ +(Q_{03} + Q_{13}\cos(\omega_e t + \varepsilon_{13}) + \ldots + Q_{n3}\cos(n\omega_e t + \varepsilon_{n3}))\phi^3 \\ +(Q_{05} + Q_{15}\cos(\omega_e t + \varepsilon_{15}) + \ldots + Q_{n5}\cos(n\omega_e t + \varepsilon_{n5}))\phi^5 \\ +\ldots\end{pmatrix} \tag{2.47}$$

Where $\omega_e = \omega + (\omega^2/g)U_0\cos\mu$ is encounter frequency, and μ is wave heading which is zero for head waves.

The equation for roll motion, shown in Eq. (2.47), can be rewritten as following form:

$$\begin{aligned}&\ddot{\phi} + \underbrace{\frac{-K_{\dot{\phi}}}{\left(I_x^{cg} - K_{\ddot{\phi}}\right)}}_{2\alpha}\dot{\phi} + \underbrace{\frac{-K_{\dot{\phi}\dot{\phi}\dot{\phi}}}{\left(I_x^{cg} - K_{\ddot{\phi}}\right)}}_{\gamma}\dot{\phi}^3 + \underbrace{\frac{mgGM}{\left(I_x^{cg} - K_{\ddot{\phi}}\right)}}_{\omega_\phi^2}\underbrace{\frac{1}{GM}\left[GZ(\phi) + K_\phi\phi + K_{\phi\phi\phi}\phi^3\right]}_{\sum_{n=1,3,5,\ldots,N} l'_n\phi^n} \\ &+ \underbrace{\frac{mg}{\left(I_x^{cg} - K_{\ddot{\phi}}\right)}}_{\omega_\phi^2/GM}\underbrace{\Delta GZ^{Wave}(\phi,t)}_{\sum_{p=1,3,5,\ldots,P}\left(Q_{0p}+Q_{1p}\cos(\omega_e t+\varepsilon_{1p})+Q_{2p}\cos(2\omega_e t+\varepsilon_{2p})+\ldots\right)\phi^p} = 0\end{aligned} \tag{2.48}$$

Equation (2.48) can be rewritten as:

$$\begin{aligned}&\ddot{\phi} + 2\alpha\dot{\phi} + \gamma\dot{\phi}^3 + \omega_\phi^2\sum_{n=1,3,5,\ldots,N} l'_n\phi^n \\ &+ \omega_\phi^2/GM\sum_{p=1,3,5,\ldots,P}\left(Q_{0p} + Q_{1p}\cos(\omega_e t + \varepsilon_{1p}) + Q_{2p}\cos(2\omega_e t + \varepsilon_{2p}) + \ldots\right)\phi^p = 0\end{aligned} \tag{2.49}$$

Here, $\alpha$and γ are damping coefficients, ω_ϕ is natural roll frequency, GM is metacentric height in calm water, l'_n is restoring moment coefficients in calm water, Q_{0p} and $\{Q_{1p}, Q_{2p,..}\}$ indicate restoring moment mean value and amplitude in waves.

Equation (2.45) shows that, for 1 DOF roll decay in regular head waves, roll response is either under damped harmonic oscillations at $f_{\phi d}$ (roll decay) or 1st harmonic dominant oscillations at $f_\phi = f_e/2$ for parametric rolling in first instability zone. X indicates 1st harmonic amplitude due to waves at f_e and 1st, 2nd and 3rd harmonic amplitudes due to roll motion at f_e. Y and N indicate ½ and 3/2 harmonic amplitudes due to roll motion.

2.4.4 3 DOF Heave-Pitch-Roll in Head Waves

For 3DOF model test free to roll, pitch, and heave, Eqs. (2.34)-(2.39) are simplified to the following form:

$$
\begin{aligned}
&m\left[(-U_0\sin\tau+w)q\right]=X_*+X_{ww}w^2+X_{pp}p^2+X_{qq}q^2+X_{\phi\phi}\phi^2+X_{wq}wq+X_{wwq}w^2q+X_{wqq}wq^2\\
&+X_{w\phi\phi}w\phi^2+X_{wpp}wp^2+X_{q\phi\phi}q\phi^2+X_{qpp}qp^2+X_{www}w^3+X_{qqq}q^3+X_W-X_{Measured}\\
&m\left[(U_0\sin\tau-w)p\right]=Y_Pp+Y_\phi\phi+Y_{wp}wp+Y_{w\phi}w\phi+Y_{pq}pq+Y_{\phi q}\phi q+Y_{wwp}w^2p+Y_{ww\phi}w^2\phi+Y_{pqq}pq^2+Y_{\phi qq}\phi q^2\\
&+Y_{ppp}p^3+Y_{\phi\phi\phi}\phi^3-Y_{Measured}\\
&m\left[\dot w-(U_0\cos\tau+u)q\right]=-\rho gA_{WP}z+\rho gA_{WP}x_{CF}\theta+Z_{\dot w}\dot w+Z_*+Z_ww+Z_qq+Z_{ww}w^2+Z_{pp}p^2+Z_{\phi\phi}\phi^2\\
&+Z_{qq}q^2+Z_{wq}wq+Z_{wwq}w^2q+Z_{wqq}wq^2+Z_{wpp}wp^2+Z_{w\phi\phi}w\phi^2+Z_{ppq}p^2q+Z_{\phi\phi q}\phi^2q+Z_{www}w^3+Z_{qqq}q^3+Z_W\\
&I_x^{cg}\dot p=-mgGZ(\phi)+K_{\dot p}\dot p+K_Pp+K_\phi\phi+K_{wp}wp+K_{w\phi}w\phi+K_{pq}pq+K_{\phi q}\phi q+K_{wwp}w^2p\\
&+K_{ww\phi}w^2\phi+K_{pqq}pq^2+K_{\phi qq}\phi q^2+K_{ppp}p^3+K_{\phi\phi\phi}\phi^3-mg\Delta GZ^{Wave}\\
&I_y^{cg}\dot q=-mgGM_L\theta+\rho gA_{WP}x_{CF}z+M_{\dot q}\dot q+M_*+M_ww+M_qq+M_{ww}w^2+M_{pp}p^2+M_{\phi\phi}\phi^2+M_{qq}q^2+M_{wq}wq\\
&+M_{wwq}w^2q+M_{wqq}wq^2+M_{wpp}wp^2+M_{w\phi\phi}w\phi^2+M_{ppq}p^2q+M_{\phi\phi q}\phi^2q+M_{www}w^3+M_{qqq}q^3+M_W\\
&\left(I_y^{cg}-I_x^{cg}\right)pq=N_Pp+N_\phi\phi+N_{wp}wp+N_{w\phi}w\phi+N_{pq}pq+N_{\phi q}\phi q+N_{wwp}w^2p+N_{ww\phi}w^2\phi\\
&+N_{pqq}pq^2+N_{\phi qq}\phi q^2+N_{ppp}p^3+N_{\phi\phi\phi}\phi^3-N_{Measured}
\end{aligned}
\tag{2.50}
$$

As shown in Eq. (2.50), heave and pitch response is 1st harmonic dominant oscillations at f_e and roll response is either under damped harmonic oscillations at $f_{\phi d}$ (roll decay) or 1st harmonic dominant oscillations at $f_\phi=f_e/2$ for parametric rolling in first instability zone. X indicates 1st harmonic amplitude due to waves at f_e, 2nd and 3rd order/harmonic amplitudes due to heave and pitch motions at f_e, and 1st, 2nd and 3rd harmonic amplitudes due to roll motion at f_e. Y and N indicate 2nd order/harmonic amplitudes due to heave and pitch motions and ½ and 3/2 harmonic amplitudes due to roll motion.

2.4.5 2 DOF Static Heel in Calm Water

For 2DOF model test free to sink and trim and heeled at angle ϕ, Eqs. (2.34)-(2.39) reduce to the following form:

$$
\begin{aligned}
&m\left[(-U_0\sin\tau+w)q\right]=X_*+X_{ww}w^2+X_{qq}q^2+X_{\phi\phi}\phi^2+X_{wq}wq+X_{wwq}w^2q+X_{wqq}wq^2\\
&+X_{w\phi\phi}w\phi^2+X_{q\phi\phi}q\phi^2+X_{www}w^3+X_{qqq}q^3-X_{Measured}\\
&0=Y_\phi\phi+Y_{w\phi}w\phi+Y_{\phi q}\phi q+Y_{ww\phi}w^2\phi+Y_{\phi qq}\phi q^2+Y_{\phi\phi\phi}\phi^3-Y_{Measured}\\
&m\left[\dot{w}-(U_0\cos\tau+u)q\right]=-\rho gA_{WP}z+\rho gA_{WP}x_{CF}\theta+Z_{\dot{w}}\dot{w}+Z_*+Z_ww+Z_qq+Z_{ww}w^2+Z_{\phi\phi}\phi^2\\
&+Z_{qq}q^2+Z_{wq}wq+Z_{wwq}w^2q+Z_{wqq}wq^2+Z_{w\phi\phi}w\phi^2+Z_{\phi\phi q}\phi^2q+Z_{www}w^3+Z_{qqq}q^3\\
&0=-mgGZ(\phi)+K_\phi\phi+K_{w\phi}w\phi+K_{\phi q}\phi q+K_{www\phi}w^2\phi+K_{\phi qq}\phi q^2+K_{\phi\phi\phi}\phi^3-K_{Measured}\\
&I_y^{cg}\dot{q}=-mgGM_L\theta+\rho gA_{WP}x_{CF}z+M_{\dot{q}}\dot{q}+M_*+M_ww+M_qq+M_{ww}w^2+M_{\phi\phi}\phi^2+M_{qq}q^2+M_{wq}wq\\
&+M_{wwq}w^2q+M_{wqq}wq^2+M_{w\phi\phi}w\phi^2+M_{\phi\phi q}\phi^2q+M_{www}w^3+M_{qqq}q^3\\
&0=N_\phi\phi+N_{w\phi}w\phi+N_{\phi q}\phi q+N_{www\phi}w^2\phi+N_{\phi qq}\phi q^2+N_{\phi\phi\phi}\phi^3-N_{Measured}
\end{aligned}
\tag{2.51}
$$

Since sinkage and trim motions are negligibly small, Eq. (2.51) is simplified to:

$$
\begin{aligned}
&0=X_*+X_{\phi\phi}\phi^2-X_{Measured}\\
&0=Y_\phi\phi+Y_{\phi\phi\phi}\phi^3-Y_{Measured}\\
&m\left[\dot{w}-(U_0\cos\tau+u)q\right]=-\rho gA_{WP}z+\rho gA_{WP}x_{CF}\theta+Z_{\dot{w}}\dot{w}+Z_*+Z_ww+Z_qq++Z_{\phi\phi}\phi^2+Z_{w\phi\phi}w\phi^2+Z_{\phi\phi q}\phi^2q\\
&0=-mgGZ(\phi)+K_\phi\phi+K_{\phi\phi\phi}\phi^3-K_{Measured}\\
&I_y^{cg}\dot{q}=-mgGM_L\theta+\rho gA_{WP}x_{CF}z+M_{\dot{q}}\dot{q}+M_*+M_ww+M_qq+M_{\phi\phi}\phi^2+M_{w\phi\phi}w\phi^2+M_{\phi\phi q}\phi^2q\\
&0=N_\phi\phi+N_{\phi\phi\phi}\phi^3-N_{Measured}
\end{aligned}
\tag{2.52}
$$

Equation (2.52) shows that X,z,θ have quadratic trend for different heel angle whereas Y,K, and N show cubic trend. This suggests that the heel angle has 1st order effect on Y, K, N and 2nd order effect on X,z,θ.

2.4.6 2 DOF Static Drift in Calm Water

For 2DOF static drift test free to sink and trim, Eqs. (2.34)-(2.39) reduce to the following form:

$$
\begin{aligned}
&m\left[(-U_0\sin\tau+w)q\right]=X_*+X_{vv}v^2+X_{ww}w^2+X_{qq}q^2+X_{wq}wq+X_{wwq}w^2q+X_{wqq}wq^2+X_{wvv}wv^2\\
&+X_{qvv}qv^2+X_{www}w^3+X_{qqq}q^3-X_{Measured}\\
&0=Y_vv+Y_{vw}vw+Y_{vq}vq+Y_{vww}vw^2+Y_{vqq}vq^2+Y_{vvv}v^3-Y_{Measured}\\
&m\left[\dot{w}-(U_0\cos\tau+u)q\right]=-\rho gA_{WP}z+\rho gA_{WP}x_{CF}\theta+Z_{\dot{w}}\dot{w}+Z_{\dot{q}}\dot{q}+Z_*+Z_ww+Z_qq+Z_{vv}v^2+Z_{ww}w^2\\
&+Z_{qq}q^2+Z_{wq}wq+Z_{vvw}v^2w+Z_{wwq}w^2q+Z_{vvq}v^2q+Z_{wqq}wq^2+Z_{www}w^3+Z_{qqq}q^3\\
&0=-mgGZ(\phi)+K_vv+K_{vw}vw+K_{vq}vq+K_{vww}vw^2+K_{vqqr}vq^2+K_{vvv}v^3-K_{Measured}\\
&I_y^{cg}\dot{q}=-mgGM_L\theta+\rho gA_{WP}x_{CF}z+M_{\dot{w}}\dot{w}+M_{\dot{q}}\dot{q}+M_*+M_ww+M_qq+M_{vv}v^2+M_{ww}w^2\\
&+M_{qq}q^2+M_{wq}wq+M_{vvw}v^2w+M_{wwq}w^2q+M_{vvq}v^2q+M_{wqq}wq^2+M_{www}w^3+M_{qqq}q^3\\
&0=N_vv+N_{vw}vw+N_{vq}vq+N_{vww}vw^2+N_{vqqr}vq^2+N_{vvv}v^3-N_{Measured}
\end{aligned}
\tag{2.53}
$$

Since sinkage and trim motions are negligibly small, Eq. (2.53) is simplified to:

$$
\begin{aligned}
0 &= X_* + X_{vv}v^2 - X_{Measured} \\
0 &= Y_v v + Y_{vvv}v^3 - Y_{Measured} \\
m[\dot{w} - (U_0 \cos\tau + u)q] &= -\rho g A_{WP} z + \rho g A_{WP} x_{CF}\theta + Z_{\dot{w}}\dot{w} + Z_{\dot{q}}\dot{q} + Z_* + Z_w w + Z_q q + Z_{vv}v^2 + Z_{vvw}v^2 w + Z_{vvq}v^2 q \\
0 &= -mgGZ(\phi) + K_v v + K_{vvv}v^3 - K_{Measured} \\
I_y^{cg}\dot{q} &= -mgGM_L\theta + \rho g A_{WP} x_{CF} z + M_{\dot{w}}\dot{w} + M_{\dot{q}}\dot{q} + M_* + M_w w + M_q q + M_{vv}v^2 + M_{vvw}v^2 w + M_{vvq}v^2 q \\
0 &= N_v v + N_{vvv}v^3 - N_{Measured}
\end{aligned}
\tag{2.54}
$$

Equation (2.54) shows that X,z,θ have quadratic trend for different drift angle (v velocity) whereas Y,K, and N show cubic trend. This suggests that the drift angle has 1st order effect on Y, K, N and 2nd order effect on X,z,θ.

2.4.7 2 DOF Static Heel in Following Waves

For 2DOF model test in following waves free to pitch and heave and heeled at ϕ, Eqs. (2.34)-(2.39) are simplified to the following form:

$$
\begin{aligned}
m[(-U_0 \sin\tau + w)q] &= X_* + X_{ww}w^2 + X_{qq}q^2 + X_{\phi\phi}\phi^2 + X_{wq}wq + X_{wwq}w^2 q + X_{wqq}wq^2 \\
&+ X_{w\phi\phi}w\phi^2 + X_{q\phi\phi}q\phi^2 + X_{www}w^3 + X_{qqq}q^3 + X_W - X_{Measured} \\
0 &= Y_\phi\phi + Y_{w\phi}w\phi + Y_{\phi q}\phi q + Y_{ww\phi}w^2\phi + Y_{\phi qq}\phi q^2 + Y_{\phi\phi\phi}\phi^3 - Y_{Measured} \\
m[\dot{w} - (U_0 \cos\tau + u)q] &= -\rho g A_{WP} z + \rho g A_{WP} x_{CF}\theta + Z_{\dot{w}}\dot{w} + Z_* + Z_w w + Z_q q + Z_{ww}w^2 + Z_{\phi\phi}\phi^2 \\
&+ Z_{qq}q^2 + Z_{wq}wq + Z_{wwq}w^2 q + Z_{wqq}wq^2 + Z_{w\phi\phi}w\phi^2 + Z_{\phi\phi q}\phi^2 q + Z_{www}w^3 + Z_{qqq}q^3 + Z_W \\
0 &= -mgGZ(\phi) + K_\phi\phi + K_{w\phi}w\phi + K_{\phi q}\phi q + K_{ww\phi}w^2\phi + K_{\phi qq}\phi q^2 + K_{\phi\phi\phi}\phi^3 - mg\Delta GZ^{Wave} \\
I_y^{cg}\dot{q} &= -mgGM_L\theta + \rho g A_{WP} x_{CF} z + M_{\dot{q}}\dot{q} + M_* + M_w w + M_q q + M_{ww}w^2 + M_{\phi\phi}\phi^2 + M_{qq}q^2 + M_{wq}wq \\
&+ M_{wwq}w^2 q + M_{wqq}wq^2 + M_{w\phi\phi}w\phi^2 + M_{\phi\phi q}\phi^2 q + M_{www}w^3 + M_{qqq}q^3 + M_W \\
0 &= N_\phi\phi + N_{w\phi}w\phi + N_{\phi q}\phi q + N_{ww\phi}w^2\phi + N_{\phi qq}\phi q^2 + N_{\phi\phi\phi}\phi^3 - N_{Measured}
\end{aligned}
\tag{2.55}
$$

Heave and pitch response is 1st harmonic dominant oscillations at f_e and roll is fixed at angle ϕ. X indicates 1st harmonic amplitude due to waves at f_e, 2nd and 3rd order/harmonic amplitudes due to heave and pitch motions at f_e. Y and N indicate 2nd order/harmonic amplitudes due to heave and pitch motions. Equation (2.52) shows that X,z,θ have quadratic trend for different heel angle whereas Y,K, and N show cubic trend. This suggests that the heel angle has 1st order effect on Y, K, N and 2nd order effect on X,z,θ.

2.4.8 4DOF Broaching in Quartering/Following Waves

In a particular case such as surf-riding and broaching, heave and pitch motions, which have high natural frequency compare to the other modes of motion, can be neglected due to the fact that ship heading speed is close to wave celerity which produces small

encounter frequency and stimulates the modes of motions with small natural frequency. Thus, broaching model is 4DOF requiring dealing with low frequency surge-sway-yaw-roll motions. The Eqs. (2.34)-(2.39) can reduce to 4DOF model neglecting heave and pitch motions:

$$\begin{aligned} m[\dot{u}-vr] &= X_{\dot{u}}\dot{u} + X_{*} + X_{vv}v^2 + X_{pp}p^2 + X_{rr}r^2 + X_{\phi\phi}\phi^2 + X_{vp}vp + X_{vr}vr + X_{pr}pr \\ &+ X_{v\phi}v\phi + X_{r\phi}r\phi + X_{W} + 2(1-t_p)\rho n^2 D_p^4 K_T(J) \end{aligned} \tag{2.56}$$

$$\begin{aligned} m[\dot{v}+(U_0+u)r] &= Y_{\dot{v}}\dot{v} + Y_{\dot{p}}\dot{p} + Y_{\dot{r}}\dot{r} + Y_v v + Y_P p + Y_\phi \phi + Y_r r + Y_{vvp}v^2 p + Y_{vv\phi}v^2\phi + Y_{vvr}v^2 r \\ &+ Y_{vrr}vr^2 + Y_{vpp}vp^2 + Y_{ppr}p^2 r + Y_{v\phi\phi}v\phi^2 + Y_{\phi\phi r}\phi^2 r + Y_{prr}pr^2 + Y_{\phi rr}\phi r^2 + Y_{vvv}v^3 + Y_{ppp}p^3 \\ &+ Y_{rrv}r^3 + Y_{\phi\phi\phi}\phi^3 + Y_W + Y_\delta \delta_R \end{aligned} \tag{2.57}$$

$$\begin{aligned} I_x^{cg}\dot{p} &= -mgGZ(\phi) + K_{\dot{v}}\dot{v} + K_{\dot{p}}\dot{p} + K_{\dot{r}}\dot{r} + K_v v + K_P p + K_\phi \phi + K_r r + K_{vvp}v^2 p + K_{vv\phi}v^2\phi + K_{vvr}v^2 r \\ &+ K_{vrr}vr^2 + K_{vpp}vp^2 + K_{ppr}p^2 r + K_{v\phi\phi}v\phi^2 + K_{\phi\phi r}\phi^2 r + K_{prr}pr^2 + K_{\phi rr}\phi r^2 + K_{vvv}v^3 + K_{ppp}p^3 \\ &+ K_{rrrv}r^3 + K_{\phi\phi\phi}\phi^3 + K_W - mg\Delta GZ^{Wave} + K_\delta \delta_R \end{aligned} \tag{2.58}$$

$$\begin{aligned} I_z^{cg}\dot{r} &= N_{\dot{v}}\dot{v} + N_{\dot{p}}\dot{p} + N_{\dot{r}}\dot{r} + N_v v + N_P p + N_\phi \phi + N_r r + N_{vvp}v^2 p + N_{vv\phi}v^2\phi + N_{vvr}v^2 r \\ &+ N_{vrr}vr^2 + N_{vpp}vp^2 + N_{ppr}p^2 r + N_{v\phi\phi}v\phi^2 + N_{\phi\phi r}\phi^2 r + N_{prr}pr^2 + N_{\phi rr}\phi r^2 + N_{vvv}v^3 \\ &+ N_{ppp}p^3 + N_{rrrv}r^3 + N_{\phi\phi\phi}\phi^3 + N_W + N_\delta \delta_R \end{aligned} \tag{2.59}$$

Hashimoto and Umeda (2002) and Hashimoto et al. (2004a,b) introduce following simplifications to Eqn. (2.56)-(2.59) to provide an efficient 4DOF model for broaching:

1) The roll velocity effect is significant in roll motion and is negligible for other modes of motion. Thus: $K_p \neq 0; K_{ppp} \neq 0$ and $X_{pp} = Y_p = Y_{ppp} = N_p = N_{ppp} = 0$

2) There is no cross-coupling between ϕ/p and other velocities. For instance: $Y_{\phi vv} = K_{\phi rr} = N_{pvv} = 0$

3) All the acceleration components are negligibly small except $X_{\dot{u}}$, $Y_{\dot{v}}$, $K_{\dot{p}}$, and $N_{\dot{r}}$.

4) Change of GZ due to waves is negligible since encounter frequency is very small.

5) The nonlinear added mass term for roll motion $-M_{\dot{u}}u_T r$ shown in Eq. (2.13) is added to Eq. (2.58) to improve the model. Note that $M_{\dot{u}}$ can be expressed as $z_H X_{\dot{u}}$ where z_H is z coordinate of acting point of $X_{\dot{u}}$.

Consequently the 4DOF Umeda and Hashimoto model of broaching is:

$$m[\dot{u} - vr] = X_{\dot{u}}\dot{u} + X_* + X_{vv}v^2 + X_{rr}r^2 + X_{\phi\phi}\phi^2 + X_{vr}vr + X_W + 2(1-t_p)\rho n^2 D_p^4 K_T(J) \tag{2.60}$$

$$m[\dot{v} + (U_0 + u)r] = Y_{\dot{v}}\dot{v} + Y_v v + Y_\phi \phi + Y_r r + Y_{vvr}v^2 r + Y_{vrr}vr^2 + Y_{vvv}v^3 + Y_{rrv}r^3 + Y_{\phi\phi\phi}\phi^3 + Y_W + Y_\delta \delta_R \tag{2.61}$$

$$\begin{aligned} I_x^{cg}\dot{p} = {} & -mgGZ(\phi) + K_{\dot{p}}\dot{p} + K_v v + K_p p + K_\phi \phi + K_r r + K_{vvr}v^2 r + K_{vrr}vr^2 + K_{vvv}v^3 + K_{ppp}p^3 \\ & + K_{rrrv}r^3 + K_{\phi\phi\phi}\phi^3 - z_H X_{\dot{u}}(U_0 + u)r + K_W + K_\delta \delta_R \end{aligned} \tag{2.62}$$

$$I_z^{cg}\dot{r} = N_{\dot{r}}\dot{r} + N_v v + N_\phi \phi + N_r r + N_{vvr}v^2 r + N_{vrr}vr^2 + N_{vvv}v^3 + N_{rrrv}r^3 + N_{\phi\phi\phi}\phi^3 + N_W + N_\delta \delta_R \tag{2.63}$$

Surge, sway and yaw motion have no restoring forces or moments and their response are not harmonic such that measured forces and moments should include only harmonics due to roll ω_ϕ or/and due to wave at ω_e. Surge motion introduces first order amplitude in X and second order amplitude in Y and K. Sway and yaw motions introduce second order amplitude in X and 1st and 3rd order amplitudes in Y, K, and N. Roll motion causes second order/harmonic amplitude at $2\omega_\phi$ in X, 1st and 3rd order/harmonic amplitude at ω_ϕ and $3\omega_\phi$ in Y, K, and N. Rudder motion causes first order amplitude in Y, K, and N. Lastly, wave forces and moments introduces 1st harmonics in X, Y, K, and N at ω_e.

Since rudders are free to turn for steered ship, the rudder angle is not fixed in Eqs. (2.60)-(2.63) and the equation of autopilot has to be added to find δ_R at each time. The simplest equation of autopilot can be described by the following linear equation:

$$\delta_R = -K_R(\psi - \psi_C) \tag{2.64}$$

Here $-\psi_C$ is desired course. Eq. (2.64) shows very simple action to control the course; rudder deflection is just proportional to deviation from desired course. K_R is a proportional coefficient called "rudder gain constant". This controller is too simple to be applied practically because such an autopilot is only sensitive to course deviation and would always be late. To make it react in advance, reaction on yaw rate can be added too:

$$\delta_R = -K_R(\psi - \psi_C) - K_R T_D r \tag{2.65}$$

Here T_D is a correction for rudder gain, to keep proportionality to yaw rate. Such controller is called "differential controller" and T_D is called "time constant for differential controller".

The last step to get an appropriate equation of autopilot is to take into account the rudder deflection velocity:

$$T_E \dot{\delta}_R + \delta_R = -K_R(\psi - \psi_C) - K_R T_D r \tag{2.66}$$

Here T_E is called "time constant for steering gear". All coefficients KR, TD, and TE are subjects of autopilot tuning.

2.5 Calculation of Hydrodynamic Derivatives

To solve developed mathematical models, the coefficients existed in the models are necessary to evaluated. These coefficients are called "maneuvering coefficients" or "hydrodynamic derivatives". Herein, the methodology of calculation hydrodynamic derivatives for 1 DOF roll decay model, 1 DOF parametric rolling model, and 4 DOF broaching model are discussed.

2.5.1 1DOF Roll Decay and Parametric Rolling Models

For 1 DOF roll decay and parametric rolling models shown in Eqs. (2.42) and (2.49), linear and cubic roll damping coefficients (α and γ), roll natural frequency (ω_ϕ), restoring moment coefficients l'_n, and lastly restoring moment variation parameters in waves (Q_{p0} ,Q_{p1}..,) are necessary to be estimated to solve the 1 DOF mathematical model.

Linear and cubic roll damping coefficients and roll natural frequency are estimated from towing tank forward speed roll decay test. The restoring moment coefficients in calm water are estimated from fitting a polynomial curve of order N to Fr=0.0 hydrostatically computed restoring moment as a function of heel angle. (Q_{0p} ,Q_{1p}..,) are estimated from fitting a polynomial curve of order P with time dependent coefficients to

measured (or hydrostatically computed) restoring moment of a ship with different heel angles in waves.

2.5.2 4 DOF Broaching Model

The hydrodynamic coefficients in Eqs. (2.60)-(2.63) can be found using empirical formula or determined experimentally using the captive model tests such as Static Drift tests, Static Heel tests, Rotating Arm tests (Circular Motion Test), and Planar Motion Mechanism (PMM) tests in calm water.

In Static Drift tests, the model is towed obliquely in towing tank and the sway velocity related hydrodynamic coefficients such as $X_{vv}, Y_v, Y_{vvv}, K_v, K_{vvv}, N_v,$ and N_{vvv} are determined. Also, z_H can be determined from Static Drift tests.

In Static Heel tests, the model is towed with heel angle and the roll related hydrodynamic coefficients such as $X_{\phi\phi}, Y_\phi, Y_{\phi\phi\phi}, K_\phi, K_{\phi\phi\phi}, N_\phi,$ and $N_{\phi\phi\phi}$ are determined.

In Rotating Arm tests, an angular velocity is imposed on the model by fixing it to the end of a radial arm and rotating the arm about a vertical axis fixed in the tank. The model is oriented with its x-axis and z-axis normal to the radial arm and it is attached to the arm preferably at the model's mid-length. As a result of the particular orientation, as the model revolves about the tank axis, rotates at the rate r while its transverse velocity component v is zero and its axial velocity component is identical to its linear speed. The model is rotated at a constant linear speed at various radii R, and the measured X,Y,K, and N acting on the model result in estimating yaw rate related coefficients such as $X_{rr}, Y_r, Y_{rrr}, K_r, K_{rrr}\ N_r, N_{rrr}$.

Herein, the acceleration terms such as $Y_{\dot{v}}, N_{\dot{v}}, Y_{\dot{r}}, N_{\dot{r}}$ are estimated through empirical formula even though they can be estimated from PMM tests.

Cross-coupling terms in Eqs. (2.60)-(2.63) can be measured through a coupled experiment setup. For instance, since yaw rate terms are measured from Rotating Arm tests and sway velocity terms are measured from Static Drift tests, yaw rate and sway

velocity coupling terms such as Y_{rvv}, Y_{rrv} can be determined by Rotating Arm tests in which the model has drift angle.

A summary of the captive model tests and available hydrodynamic coefficients from each test are presented in Table 2.1.

2.5.2.1 Static Drift

For the static drift results, the forces and moments coefficients are only the function of v thus the RHS of Eqs. (2.60)-(2.63) are simplified as:

$$\begin{aligned} X &= X_* + X_{vv}v^2 = A + Bv^2 \\ Y &= Y_v v + Y_{vvv}v^3 = Cv + Dv^3 \\ K &= K_v v + K_{vvv}v^3 = Ev + Fv^3 \\ N &= N_v v + N_{vvv}v^3 = Gv + Hv^3 \end{aligned} \tag{2.67}$$

where $A = X_*, B = X_{vv}, C = Y_v, D = Y_{vvv}, E = K_v, F = K_{vvv}, G = N_v v, H = N_{vvv}.$

The hydrodynamic derivatives shown in Eq. (2.67) are obtained as polynomial coefficients by least-square curve fitting method. The 2nd order polynomial is used to obtain A and B, although A is usually referenced from steady resistance tests. The 3rd polynomial is used to obtain C, D, E, F, G, and H. Also, E and F can be estimated from Y coefficients using z_H in which:

$$K = z_H Y \tag{2.68}$$

Here z_H is estimated from 1st order polynomial curve fitting to K – Y plot.

Consequently:

$$\begin{aligned} E &= z_H C \\ F &= z_H D \end{aligned} \tag{2.69}$$

2.5.2.2 Static Heel

For the static heel results, the forces and moments coefficients are only the function of ϕ thus the RHS Eqs. (2.60)-(2.63) are simplified as:

$$
\begin{aligned}
X &= X_* + X_{\phi\phi}\phi^2 = A + B\phi^2 \\
Y &= Y_\phi\phi + Y_{\phi\phi\phi}\phi^3 = C\phi + D\phi^3 \\
K &= -mgGZ(\phi) + K_\phi\phi + K_{\phi\phi\phi}\phi^3 = \left(K_\phi - l_1\right)\phi + \left(K_{\phi\phi\phi} - l_3\right)\phi^3 = E\phi + F\phi^3 \\
N &= N_\phi\phi + N_{\phi\phi\phi}\phi^3 = G\phi + H\phi^3
\end{aligned}
\tag{2.70}
$$

Herein, $A = X_*, B = X_{\phi\phi}, C = Y_\phi, D = Y_{\phi\phi\phi}, E = K_\phi - l_1, F = K_{\phi\phi\phi} - l_3, G = N_\phi\phi, H = N_{\phi\phi\phi}$ and l_1, l_3 are restoring moment coefficients. The hydrodynamic derivatives shown in Eq. (2.70) are obtained as polynomial coefficients by least-square curve fitting method. The 2nd order polynomial is used to obtain A and B, although A is usually referenced from steady resistance tests. The 3rd polynomial is used to obtain C, D, E, F, G, and H. Also, l_1, l_3 are measured from 3rd order polynomial curve fitting to roll restoring moment, although l_1 is GM and it is known.

2.5.2.3 Rotating Arm + Drift

For the rotating arm test with drift angle, the rotating arm speed is U = rR and side velocity and yaw rate of the vessel are v=-Usinβ and r. As the result the RHS of Eqs. (2.60)-(2.63) can be simplified as:

$$
\begin{aligned}
X &= X_* + X_{vv}v^2 + X_{rr}r^2 + X_{vr}vr + X_{vrr}vr^2 + X_{vvr}v^2r = A_1 + B_1v^2 + C_1r^2 + D_1vr + E_1vr^2 + F_1v^2r \\
Y &= Y_vv + Y_{vvv}v^3 + Y_rr + Y_{rrr}r^3 + Y_{vrr}vr^2 + Y_{vvr}v^2r = A_2v + B_2v^3 + C_2r + D_2r^3 + E_2vr^2 + F_2v^2r \\
K &= K_vv + K_{vvv}v^3 + K_rr + K_{rrr}r^3 + K_{vrr}vr^2 + K_{vvr}v^2r = A_3v + B_3v^3 + C_3r + D_3r^3 + E_3vr^2 + F_3v^2r \\
N &= N_vv + N_{vvv}v^3 + N_rr + N_{rrr}r^3 + N_{vrr}vr^2 + N_{vvr}v^2r = A_4v + B_4v^3 + C_4r + D_4r^3 + E_4vr^2 + F_4v^2r
\end{aligned}
\tag{2.71}
$$

where X,Y,K, and N are the measured forces and moments in which centrifugal force $((m - Y_{\dot{v}})r^2R$ effects are extracted.

The hydrodynamic coefficients of X, Y, and N shown in Eq. (2.71) are obtained as 3rd order polynomial coefficients (A_1-F_1), (A_2-F_2), and (A_4-F_4) respectively, by least-square surface fitting method. The hydrodynamic coefficients of K can be estimated from polynomial coefficients of Y as follow:

$$\begin{aligned} A_3 &= z_H A_2 \\ B_3 &= z_H B_2 \\ C_3 &= z_H C_2 \\ D_3 &= z_H D_2 \\ E_3 &= z_H E_2 \\ F_3 &= z_H F_2 \end{aligned} \tag{2.72}$$

Herein z_H is already known from the Static Drift test.

2.6 Solution of Mathematical Model

2.6.1 1DOF Roll Decay and Parametric Rolling Models

To solve 1DOF nonlinear roll decay model, Runge-Kutta method is used to integrate Eq. (2.42). The initial roll angle and roll rate, which is usually zero, are applied as initial conditions.

For 1DOF parametric rolling model, Poincaré mapping was applied to identify steady states of parametric rolling as a function of Fr by integrating Eq. (2.49) using Runge-Kutta method. Once a steady state for certain Fr is found, the next numerical integration of Eq. (2.49) starts from the obtained steady state but with a slightly larger or smaller Fr which depends on using increasing or decreasing Poincaré method. Both tracing directions of increasing and decreasing Fr are explored to demonstrate dependency of initial condition.

The Poincaré map is useful to identify bifurcation structures of roll motion, but it requires an initial steady state for continuously tracing steady states. Thus there is still the possibility that another stable state exists with the same condition. In addition, numerical simulations for all possible condition parameters, wave height, wave length, ship speed, GM, etc. consume tremendous simulation time. Therefore, an averaging method was used, which is one of the analytical approaches in nonlinear dynamics for solving Eq. (2.49) in an approximate way. For parametric rolling in first instability zone, all steady

states of principal parametric rolling, where roll frequency is a half of the encounter frequency, can be theoretically determined because steady states are solutions of algebraic equations. Assuming the solution of $\phi = A_\phi \cos(\hat{\omega}t - \varepsilon)$ yields:

$$A_\phi = 0$$
$$\{\alpha + \frac{3}{8}\gamma\hat{\omega}^2 A^2\}^2 + \{\frac{\hat{\omega}}{2} - \frac{1}{2}\frac{\omega_\phi^2}{\hat{\omega}}(1 + GM_{mean}/GM + \frac{3}{4}l_3 A^2 + \frac{5}{8}l_5 A^4)\}^2 = (GM_{amp}\frac{\omega_\phi^2}{4\hat{\omega}}/GM)^2 \tag{2.73}$$

A_ϕ=0 indicates a trivial solution at 0 degrees of roll. Steady states of the parametric rolling orbit can be obtained by solving the eighth-degree algebraic equation. If locally these equations are linearized at their steady states, stability of solutions can be examined with their eigenvalues, and their attractor domain can be determined with their eigenvectors.

2.6.2 4DOF Broaching Model

To solve the system of equations shown in Eqs. (2.60)-(2.63) and steering equation shown in Eq. (2.66), the definition of p and r, and the ship position equation have to be added. Then, Eqs. (2.60)-(2.63) and Eq. (2.66) can be presented as a system of differential equations of the first order to solve it numerically:

$$\begin{aligned}
\dot{\xi}_G &= (U_0 + u)\cos\psi - v\sin\psi - c \\
\dot{u} &= \left\{\begin{array}{l} X_* + X_{vv}v^2 + X_{rr}r^2 + X_{\phi\phi}\phi^2 + X_{vr}vr + X_{vrr}vr^2 \\ + X_{vvr}v^2 r + (m - Y_{\dot{v}})vr + 2(1-t_p)\rho n^2 D_p^4 K_T(J) + X_W \end{array}\right\} / (m - X_{\dot{u}}) \\
\dot{v} &= \left\{\begin{array}{l} -(m - X_{\dot{u}})(U_0 + u)r + Y_{\dot{v}}\dot{v} + Y_v v + Y_{vvv}v^3 + Y_r r + Y_{rrr}r^3 \\ + Y_\phi\phi + Y_{\phi\phi\phi}\phi^3 + Y_{vrr}vr^2 + Y_{vvr}v^2 r + Y_\delta\delta_R + Y_W \end{array}\right\} / (m - Y_{\dot{v}}) \\
\dot{\phi} &= p \\
\dot{p} &= \left\{\begin{array}{l} K_v v + K_{vvv}v^3 + K_r r + K_{rrr}r^3 + K_\phi\phi + K_{\phi\phi\phi}\phi^3 + K_p p \\ + K_{vrr}vr^2 + K_{vvr}v^2 r + K_\delta\delta_R + z_H m_x(U_0 + u)r - mgGZ(\phi) + K_W \end{array}\right\} / (I_x^{cg} - K_{\dot{p}}) \\
\dot{r} &= \psi \\
\dot{r} &= \left\{\begin{array}{l} N_v v + N_{vvv}v^3 + N_r r + N_{rrr}r^3 + N_\phi\phi + N_{\phi\phi\phi}\phi^3 \\ + N_{vrr}vr^2 + N_{vvr}v^2 r + N_\delta\delta_R + N_W \end{array}\right\} / (I_z^{cg} - N_{\dot{r}}) \\
\dot{\delta}_R &= \{-\delta_R - K_R(\psi - \psi_C) - K_R T_D r\} / T_E
\end{aligned} \tag{2.74}$$

It would be more convenient to present system Eq. (2.74) in vector form:

$$\dot{\vec{x}} = F(\vec{x}, \vec{b}) \tag{2.75}$$

where $\vec{x}$ is called the state vector:

$$\vec{x} = \{\xi_G, u, v, \psi, r, \phi, p, \delta_R\}^T \tag{2.76}$$

The vector $\vec{b}$ is control vector which consists here just two parameters:

$$\vec{b} = \{\psi_C, n\} \tag{2.77}$$

Here, n is number of propeller revolutions and it has to be included in all terms connected with thrust and rudder action.

Ship motions response in waves can be calculated by solving Eq. (2.75) for certain initial conditions (for motions and controller) and for certain control parameters (number of propeller revolution and desired course). The solution can define the status of ship which can be capsizing, broaching, periodic motion, and surf-riding.

2.6.2.1 Capsizing and Broaching

Capsizing can be defined if:

$$|\phi| < \phi_C \tag{2.78}$$

Here ϕ_C should be sufficiently larger than the angle of vanishing stability which is usually around 90deg.

Based on the definition of broaching, the condition for broaching can be formulated as follows:

$$\begin{cases} \delta = \delta_{\max} & r < 0 \quad \dot{r} < 0 \\ \delta = -\delta_{\max} & r > 0 \quad \dot{r} > 0 \end{cases} \tag{2.79}$$

Equation (2.79) basically means that for broaching case the magnitude of yaw angle is increasing even though rudder has its maximum deflection to keep the course.

2.6.2.2 Periodic Orbits

The steady state solution of Eq. (2.75) is even more important than time history itself in nonlinear dynamics theory. A nonlinear system of equations such as Eq. (2.75) can

have different type of steady solutions described by: equilibrium points (fixed points i.e. surf-riding), limit cycle (periodic orbits or quasiperodic orbits), and chaos. Static periodic motion can be identified if a value of T exists which satisfies the following equation:

$$\begin{aligned} &\cos(2\pi x_1(t)) = \cos(2\pi x_1(t+T)) \\ &x_i(t) = x_i(t+T) \;\; i = 2,3,...8 \end{aligned} \tag{2.80}$$

2.6.2.3 Equilibrium of Steered Ship Equations; Surf-riding

Equilibrium points of system (2.75) correspond to surf-riding which is a prerequisite for broaching. If the ship is in the equilibrium position, then derivative of ship motions are zero.

$$F(\vec{x},\vec{b}) = 0 \tag{2.81}$$

As all derivatives are disappeared, expression (2.81) degrades to a system of nonlinear algebraic equations that can be solved numerically with a simple method such as Newton method. The system (2.81) consists of 8 equations, so the equilibrium is a point in a space of eight dimensions and changing control parameters move this point. Usually, for each equation there are only two equilibrium points. One equilibrium point corresponds to the state that ship is in the wave crest and another one corresponds to wave trough. This is can be checked by studying stability of equilibrium.

2.6.2.4 Stability of Equilibrium (Attractor vs. Repeller)

Stability of equilibrium points (fixed points) can be studied by eigenvalues of Jacobean matrix of F:

$$J(\vec{F}) = \begin{bmatrix} \frac{\partial F_1(\vec{x},\vec{b})}{\partial x_1} & \frac{\partial F_2(\vec{x},\vec{b})}{\partial x_1} & \cdots & \frac{\partial F_8(\vec{x},\vec{b})}{\partial x_1} \\ \frac{\partial F_1(\vec{x},\vec{b})}{\partial x_2} & \frac{\partial F_2(\vec{x},\vec{b})}{\partial x_2} & \cdots & \frac{\partial F_8(\vec{x},\vec{b})}{\partial x_2} \\ \cdots & \cdots & \cdots & \cdots \\ \frac{\partial F_1(\vec{x},\vec{b})}{\partial x_8} & \frac{\partial F_2(\vec{x},\vec{b})}{\partial x_8} & \cdots & \frac{\partial F_8(\vec{x},\vec{b})}{\partial x_8} \end{bmatrix} \tag{2.82}$$

Eigen-values of J(F) can be expressed:

$$\det(J(\vec{F}) - \lambda I) = 0 \tag{2.83}$$

Here I is the identity matrix.

The number of eigenvalues corresponds to the dimension of the matrix, which is the number of equations. Each eigenvalues can be associated with a variable from the model shown in Eq. (2.76). A positive eigenvalue for a certain variable means that the system will escape in the particular direction into an unstable equilibrium points.

Table 2-1: Summary of captive model tests and relevant hydrodynamic derivatives

Test	Conditions	Motion Parameters	Coefficients
Static Drift		v	X_*, X_{vv} Y_v, Y_{vvv} K_v, K_{vvv}, z_H N_v, N_{vvv}
Static Heel		ϕ	$X_*, X_{\phi\phi}$ $Y_\phi, Y_{\phi\phi\phi}$ $K_\phi, K_{\phi\phi\phi}$ $N_\phi, N_{\phi\phi\phi}$
Rotating Arm	With Drift	v, r	$X_*, X_{vv}, X_{rr}, X_{rv}$ $Y_v, Y_{vvv}, Y_r, Y_{rrr}, Y_{vrr}, Y_{vvr}$ $K_v, K_{vvv}, K_r, K_{rrr}, K_{vrr},$ K_{vvr} $N_v, N_{vvv}, N_r, N_{rrr}, N_{vrr},$ N_{vvr}

CHAPTER 3. IMPLEMENTAION CAPSIZE PREDICTION IN CFDSHIP-IOWA V.4

The general-purpose solver CFDShip-Iowa-V.4 solves the unsteady Reynolds averaged Navier-Stokes (RANS) or detached eddy simulation (DES) equations in the liquid phase of a free surface flow. The code utilizes absolute/relative inertial earth-fixed coordinate system and non-inertial ship-fixed coordinate system to describe prescribed/predicted ship motions. The free surface is captured using a single-phase level set method and the turbulence is modeled by isotropic or anisotropic turbulence models. Numerical methods include advanced iterative solvers, second and higher order finite difference schemes with conservative formulations, parallelization based on a domain decomposition approach using the message-passing interface (MPI), and dynamic overset grids for local grid refinement and large-amplitude motions. A succinct review of the code is presented here, paying special attention to its application on capsize prediction.

3.1 Governing Equations

3.1.1 Inertial Earth-Fixed Coordinates (X,Y,Z)

The governing differential equations (GDEs) of motion are derived and solved in absolute inertial earth-fixed coordinates (X,Y,Z) for an arbitrary moving but non-deforming control volume and solution domain, respectively. The governing differential equation for continuity is expressed as follow:

$$\nabla . U = 0 \tag{3.1}$$

where $U = U_1\hat{i} + U_2\hat{j} + U_3\hat{k}$ is the absolute velocity in (X,Y,Z).

Conservation of momentum using the divergence operator expansion, the continuity equation and expressing the body and surface forces per unit volume, give the momentum equation:

$$\rho\left[\frac{\partial U}{\partial t}+(U-U_G).\nabla U\right]=-\nabla(p+\gamma z)+\mu\nabla^2 U \tag{3.2}$$

Where U_G is the local grid velocity. Note that Eq. (3.2) can be non-dimensionalized using a reference velocity U_{Ref} (generally is the speed of the ship U_0), the ship length L, the water density ρ and viscosity μ which introduces $Fr = U_0/\sqrt{Lg}$ and $\mathrm{Re} = \rho U_0 L/\mu$ numbers.

3.1.2 Relative Inertial Coordinates (X′,Y′,Z′)

Eq. (3.2) can be transformed into the relative inertial coordinates (X',Y',Z') translating at a constant velocity U_C relative to (X,Y,Z) by replacing U by $U = U' + U_C$ and U_G by $U_G = U'_G + U_C$, where U' and U'_G are the fluid and grid velocities in (X',Y',Z'), respectively. The time derivatives in the two inertial coordinates are the same. Since the gradient, divergence, and Laplacian operators in Eq. (3.2) are frame invariant, the governing equations in terms of U' in (X',Y',Z') are obtained:

$$\rho\left[\frac{\partial U'}{\partial t}+(U'-U'_G).\nabla U'\right]=-\nabla(p+\gamma z)+\mu\nabla^2 U' \tag{3.3}$$

3.1.3 Non-Inertial Ship-Fixed Coordinates (x,y,z)

Eq. (3.2) can also be transformed into the non-inertial ship-fixed coordinates (x,y,z) located at center of rotation of ship by replacing U in (X,Y,Z) by $U = U_r + U_G$ and U_G by $U_G = \dot{R} + \Omega \times r$; where U_r is fluid velocity in ship coordinate, r is instantaneous position vector of any point in (x,y,z), $\dot{R} = U_X\hat{i} + U_Y\hat{j} + U_Z\hat{k}$ and $\Omega = \Omega_X\hat{i} + \Omega_Y\hat{j} + \Omega_Z\hat{k}$ are the linear and angular velocity of (x,y,z) in (X,Y,Z).

$$\rho\left[\frac{\partial U_r}{\partial t}+U_r.\nabla U_r\right]=-\rho a_r-\nabla(p+\gamma z)+\mu\nabla^2 U_r \tag{3.4}$$

$$a_r = \ddot{R} + 2\Omega \times U_r + \Omega \times (\Omega \times r) + \dot{\Omega} \times r \tag{3.5}$$

3.2 Turbulence Modeling

CFDShip-Iowa uses a linear closure model, in which Reynolds stresses are proportional to the main rate of strain being ν_t, the isotropic eddy viscosity, the proportional factor. In Cartesian coordinates, the expression is:

$$-\overline{u_i u_j} = \nu_t \left(\frac{\partial U_i}{\partial X_j} + \frac{\partial U_j}{\partial X_i} \right) - \frac{2}{3} \delta_{ij} k \tag{3.6}$$

where δ_{ij} is the Kronecker delta and k is the turbulent kinetic energy.

The equations can be closed by calculating the eddy viscosity.

3.2.1 Blended k–ω/k–ε (BKW)

This blending takes benefits from the strength of both k–ω and k–ε models to calculate ν_t. The k–ω model has proven to be robust, applicable to complex geometries and fairly accurate. In addition, it does not require near-wall dumping functions and uses simple Dirichlet boundary conditions. On the other hand, k–ε model does not exhibit sensitively to the level of free-stream turbulence as k–ω does. The governing equation for turbulent kinetic energy k and the turbulent ω are as follows (Menter, 1994).

$$\frac{\partial k}{\partial t} + \left(\mathbf{v} - \sigma_k \nabla \nu_t \right) \cdot \nabla k - \frac{1}{P_k} \nabla^2 k + s_k = 0 \tag{3.7}$$

$$\frac{\partial \omega}{\partial t} + \left(\mathbf{v} - \sigma_\omega \nabla \nu_t \right) \cdot \nabla \omega - \frac{1}{P_\omega} \nabla^2 \omega + s_\omega = 0 \tag{3.8}$$

Where the source terms, turbulent viscosity and the effective Reynolds numbers are:

$$S_k = R_k \left(-G + \beta^* \omega k \right) \tag{3.9}$$

$$S_\omega = R_\omega \left(-\gamma \frac{\omega}{k} G + \beta \omega^2 + 2(1 - F_1) \sigma_{\omega 2} \frac{1}{\omega} \frac{\partial k}{\partial X_j} \frac{\partial \omega}{\partial X_j} \right) \tag{3.10}$$

$$\nu_t = \frac{k}{\omega} \tag{3.11}$$

$$R_{k/\omega} = \frac{1}{1/\mathrm{Re} + \sigma_{k/\omega} \nu_t} \tag{3.12}$$

$$G = \tau_{ij} \frac{\partial U_i}{\partial X_j} \tag{3.13}$$

Here, β, β^*, σ_k, and σ_ω are constants and F_1 is a blending function, designed to take advantage of the strength of either k-w or k–ε model in different position. To accomplish this, F_1 is 1 in the sub-layer and logarithmic regions of boundary layers and gradually switches to zero in the wake region. The model constants, say α, are calculated from the standard k-ω (α1), and k-ε (α2) values using a blending function:

$$\alpha = F_1\alpha_1 + (1 - F_1)\alpha_2 \tag{3.14}$$

3.3 Free Surface Modeling

CFDShip-Iowa-v4 uses single-phase level set method. The 3D level set function, ϕ, is defined in the whole domain and its value is related to the signed distance to the interface. Therefore, the iso-surface ϕ=0 represents the free surface. Since the free surface is considered a material interface, the level set function must satisfy:

$$\frac{\partial \phi}{\partial t} + (U_j - U_{Gj})\frac{\partial \phi}{\partial X_j} = 0 \tag{3.15}$$

Also, given that ϕ is a distance function, the gradient of the level set function points normal to the interface into the water and the water-to-air normal can then be computed as:

$$n_i = -\frac{\partial \phi / \partial X_i}{|\partial \phi / \partial X_i|} \tag{3.16}$$

In the field of ship hydrodynamics, the big difference in density and viscosity between air and water allows to simplify the problem by solving only the equations for the water phase.

Since the equations are only solve for one of the phases, the jump conditions at free surface must be enforced explicitly. The jump condition in any direction tangential to the free surface given by the tangent vector t_i is:

$$\mu\frac{\partial U_i}{\partial X_j}t_i n_j + \mu\frac{\partial U_i}{\partial X_j}n_i t_j = 0 \tag{3.17}$$

After neglecting shear stress in air, it leads to:

$$\left.\frac{\partial U_i}{\partial X_j} n_j \right|_{\text{int}} = 0 \tag{3.18}$$

In the normal direction, the jump condition is expressed as:

$$p_{abs} - 2\mu \frac{\partial U_i}{\partial X_j} n_i n_j = 0 \tag{3.19}$$

Assuming the pressure is constant on the air and neglecting the contribution of the turbulent kinetic energy to the free surface, the non-dimensional piezometric pressure at the interface is:

$$p_{\text{int}} = \frac{z_{\text{int}}}{Fr^2} \tag{3.20}$$

A velocity in air near the free surface is needed to calculate the transport of the level set function and also velocities and turbulent quantities. This extension velocity is calculated using Eq. (3.18), which provides a good approximation satisfying the jump condition at the same time.

In single level set is critical to keep ϕ as a distance function, since this is assumed in the calculation of the normal in Eq.(3.16). To do this, the level set function is reinitialized periodically everywhere but at the interface by solving:

$$\frac{\partial \phi}{\partial X_j} n_j = sign(\phi_0) \tag{3.21}$$

Where ϕ_0 is the level set function prior to reinitializing. The normal vector n_j points into the fluid to be reinitialized, and is given by Eq. (3.16) in air and by the negative of the same equation in water. Thus Eq. (3.21) is an Eikonal equation propagating information outwards the interface.

Also, Eq. (3.21) is nonlinear because n_j is a function of ϕ and it is solved with nonlinear iterations.

3.4 Motions Modeling

3.4.1 6 DOF Rigid Body Equations of Motion

The 6DOF rigid body equations of motion presented in Eq. (2.1) is solved to calculate ship linear and angular motions. In order to solve Eq. (2.1), the total force $f=[X,Y,Z]^T$ and moment $g=[K,M,N]^T$ in the absolute inertial earth-fixed coordinates for the ship are computed by integrating pressure and friction and buoyancy forces on the ship hull and then projected into the non-inertial ship-fixed coordinates (x,y,z) using:

$$f = J_1\left(f_{inertial}\right) \tag{3.22}$$

$$g = J_1\left(g_{inertial}\right) \tag{3.23}$$

The matrix $\underline{J}_1$ transforms any vector in (X,Y,Z) to a vector in (x,y,z):

$$J_1 = \begin{bmatrix} \cos\psi\cos\theta & \sin\psi\cos\theta & -\sin\theta \\ -\sin\psi\cos\theta+\sin\phi\sin\theta\cos\psi & \cos\psi\cos\phi+\sin\phi\sin\theta\sin\psi & \sin\phi\cos\theta \\ \sin\theta\sin\psi+\cos\phi\sin\theta\cos\psi & -\sin\phi\cos\psi+\cos\phi\sin\theta\sin\psi & \cos\theta\cos\psi \end{bmatrix} \tag{3.24}$$

Where ϕ, θ, and ψ are the Euler angles for roll, pitch, and yaw, respectively.

Any number of degrees of freedom can be imposed and the rest is predicted by solving Eq.(2.1), which results in captive, free, or semi-captive motions. Additional governing equations for the constraints (or imposed motions) need to be solved which results in reduced degrees of freedom. As an approximation, CFDShip-Iowa-V.4 only solves rigid body equations for the predicted degrees of freedom using a predictor/corrector implicit approach. The prescribed motions for position, translation velocity, and Euler angles are specified as functions of time in the absolute inertial coordinates and read into CFDShip-Iowa-V.4 as a data file.

3.4.2 Appendages

The ship might have several appendages which move with the ship. The appendages can have relative motion motions respect to the ship such as rudders and propellers. The CFDShip-Iowa-v.4 models appendages using child and parent concept. The child object is connected to the ship but it can have relative motion respect to the ship. The forces and moments are integrated on the child object and 6DOF rigid body equations of motions can be solved for unrestrained modes of motion.

3.4.2.1 Propellers

For self-propulsion simulation, the ship model has propeller on it which produces necessary thrust for ship motion. The CFDShip-Iowa-v.4 models propeller using body force or real rotating propeller. For body force model, a simplified model is used to prescribe axisymmetric body force with axial and tangential components (Stern et al., 1998). The radial distribution of forces is based on the Hough and Ordway circulation distribution, which has zero loading at the root and tip. A vertex-based search algorithm is used to determine which grid-point control volumes are within the actuator cylinder. The propeller model requires the input of thrust, torque and advance coefficient and outputs the torque and thrust force to the shaft and the body forces for the fluid inside the propeller disk. For the real rotating propeller, the simulation of propeller requires no input and outputs the torque and thrust force to the shaft and propeller blades. The force and torque of each propeller are projected into the non-inertial ship-fixed coordinates and used to compute an effective force and torque about the center of rotation, which is usually coincident to the center of gravity. The location of the propeller is defined in the static condition of the ship. When motions are involved, the propeller will move accordingly with the ship's motions and possibly will intersect the background grid if it is finer than grids from other blocks and becomes "active".

3.4.2.2 Rudders

Rudders are modeled as child objects only enable to turn around their axis. The turning angle, velocity, and acceleration of rudders can be prescribed as functions of time in the absolute inertial coordinates and read into CFDShip-Iowa-V.4 as a data file. Also, the turning angle can be predicted using a controller to turn the ship toward the target heading.

3.5 Controllers Modeling

Controllers are recently added to CFDShip-Iowa code which expand the code applications for capsize prediction. The controller attempts to correct the error between a measured process variable and a desired setpoint by calculating and then outputting a corrective action that can adjust the process accordingly. For instance, rudder controllers are responsible to turn rudders to keep the ship in desired direction or propeller controllers are responsible to rotate propellers to keep the ship at desired speed.

3.5.1 PID Controller

A proportional–integral–derivative controller (PID controller) is a generic control loop feedback mechanism widely used in control systems.

The PID controller calculation involves three separate parameters; the Proportional, the Integral and Derivative values. The Proportional value determines the reaction to the current error, the Integral determines the reaction based on the sum of recent errors and the Derivative determines the reaction to the rate at which the error has been changing. The weighted sum of these three actions is used to adjust the process via a controller.

By "tuning" the three constants in the PID controller algorithm, the controller can provide control action designed for specific process requirements. Some applications may require using only one or two modes to provide the appropriate system control. This is

achieved by setting the gain of undesired control outputs to zero. A PID controller will be called a PI, PD, P or I controller in the absence of the respective control actions.

3.5.1.1 Proportional Controller

The proportional term makes a change to the output that is proportional to the current error value. The proportional response can be adjusted by multiplying the error by a constant *P*, called the proportional gain.

The proportional term is given by:

$$\delta(t) = Pe(t) \tag{3.25}$$

Where $\delta(t)$ is output and $e(t)$ is the error which is:

$$e(t) = A_d - A(t) \tag{3.26}$$

Here, A_d is the desired value and $A(t)$ is the current value.

For rudder controllers, $\delta(t)$ is rudder deflection, A_d is target heading, and A(t) is current heading. For propeller controller, $\delta(t)$ is the propeller RPS, A_d is target speed, and A(t) is current speed. A high proportional gain results in a large change in the output for a given change in the error. If the proportional gain is too high, the system can become unstable. In contrast, a small gain results in a small output response to a large input error, and a less responsive (or sensitive) controller. If the proportional gain is too low, the control action may be too small when responding to system disturbances.

3.5.1.2 Integral Controller

The contribution from the integral term is proportional to both the magnitude of the error and the duration of the error. Summing the instantaneous error over time (integrating the error) gives the accumulated offset that should have been corrected previously. The accumulated error is then multiplied by the integral gain and added to the controller output. The magnitude of the contribution of the integral term to the overall control action is determined by the integral gain, *I*.

The integral term is given by:

$$\delta(t) = I\int_0^{\tau} e(\tau)d\tau \tag{3.27}$$

The integral term (when added to the proportional term) accelerates the movement of the process towards setpoint and eliminates the residual steady-state error that occurs with a proportional only controller. However, since the integral term is responding to accumulated errors from the past, it can cause the present value to overshoot the setpoint value (cross over the setpoint and then create a deviation in the other direction).

3.5.1.3 Derivative Controller

The rate of change of the process error is calculated by determining the slope of the error over time (i.e. its first derivative with respect to time) and multiplying this rate of change by the derivative gain *D*. The magnitude of the contribution of the derivative term to the overall control action is termed the derivative gain, *D*.

The derivative term is given by:

$$\delta(t) = D\frac{d(e(t))}{dt} \tag{3.28}$$

The derivative term slows the rate of change of the controller output and this effect is most noticeable close to the controller setpoint. Hence, derivative control is used to reduce the magnitude of the overshoot produced by the integral component and improve the combined controller-process stability. However, differentiation of a signal amplifies noise and thus this term in the controller is highly sensitive to noise in the error term, and can cause a process to become unstable if the noise and the derivative gain are sufficiently large.

Summation of Eq.(3.26), (3.27), and (3.28) leads to general form of PID controller equation:

$$\delta(t) = Pe(t) + I\int_0^{\tau} e(\tau)d\tau + D\frac{d(e(t))}{dt} \tag{3.29}$$

CFDShip-Iowa solves Eq. (2.29) for rudders or propellers controller and predicts rudder deflection or propellers RPS.

3.6 Numerical Details

3.6.1 Coordinate Transformation

The governing differential equations for continuity and momentum in (X,Y,Z) and (X',Y',Z') are transformed from the physical domain in Cartesian coordinates (X,Y,Z,t) to the computational domain in non-orthogonal curvilinear coordinates (ξ, η, ζ, τ) using the chain rule without involving grid velocity for the time derivative transformation. The transformation is partial, since only the independent variables are transformed, leaving the velocity component U_i in the base coordinates:

$$\frac{1}{J}\frac{\partial}{\partial \xi^j}\left(b_i^j U_i\right) = 0 \tag{3.30}$$

$$\frac{\partial U_i}{\partial \tau} + \frac{1}{J} b_j^k \left(U_j - U_{Gj}\right)\frac{\partial U_i}{\partial \xi^k} = -\frac{1}{J} b_i^k \frac{\partial p}{\partial \xi^k} + \frac{1}{J}\frac{\partial}{\partial \xi^j}\left(\frac{b_i^j b_i^k}{J\,\mathrm{Re}_{eff}}\frac{\partial U_i}{\partial \xi^k}\right) + \frac{b_j^k}{J}\frac{\partial \nu_t}{\partial \xi^k}\frac{b_i^l}{J}\frac{\partial U_j}{\partial \xi^l} + S_i \tag{3.31}$$

3.6.2 Discretization Scheme

The time derivatives in the turbulence and momentum equations are discretized using 2nd order finite Euler backward difference. For the general variable ϕ:

$$\frac{\partial \phi}{\partial t} = \frac{1}{\Delta t}\left(1.5\phi^n - 2\phi^{n-1} + 0.5\phi^{n-2}\right) \tag{3.32}$$

Convection terms in the turbulence and momentum equations are discretized with higher order upwind formula:

$$U^k \frac{\partial \phi}{\partial \xi_k} = \frac{1}{2}\left(U^k + \left|U^k\right|\right)\delta^-_{\xi_k}\phi + \frac{1}{2}\left(U^k - \left|U^k\right|\right)\delta^+_{\xi_k}\phi \tag{3.33}$$

Where

$$\begin{aligned}\delta^-_{\xi_k}\phi &= w_{mm}\phi_{i-2} + w_m\phi_{i-1} + w_n\phi_i + w_p\phi_{i+1} + w_{pp}\phi_{i+2}\\ \delta^+_{\xi_k}\phi &= -w_{pp}\phi_{i-2} - w_p\phi_{i-1} - w_n\phi_i + w_m\phi_{i+1} + w_{mm}\phi_{i+2}\end{aligned} \tag{3.34}$$

The value of weighting coefficients depends on the scheme used. In present work, 2nd order was used which means w_{mm}=0.5,w_m=-2, w_n=1.5, and w_p=w_{pp}=0.

The viscous term in Eq. (3.31) and turbulent equations are computed with similar considerations using a second order difference scheme.

The mass conservation is enforced using the pressure Poisson equation:

$$\frac{\partial}{\partial \xi^j}\left(\frac{b_i^j b_i^k}{Ja_{ijk}}\frac{\partial p}{\partial \xi^k}\right)=\frac{\partial}{\partial \xi^j}\frac{b_i^j}{a_{ijk}}\left(\sum_{nb} a_{nb}U_{i,nb}-S_i\right) \tag{3.35}$$

3.6.3 Solution Algorithm

The grids are read and split according to user directives for domain decomposition parallelization. A MPI-based domain decomposition approach is used, where each decomposed block is mapped to one processor. Then, variables are initialized and initial conditions are set or read. Once all the variables are initialized, SUGGAR (Noack, 2005) is called for the first time to obtain the initial overset interpolation information. A non-linear loop is used to converge the flow field and motions within each time step. At the beginning of each nonlinear iteration, the overset information is read from a binary file produced by SUGGAR, the grids are moved according to the motions resulting from the 6DOF predictor/corrector steps, and the transformation metrics and grid velocity are computed. Then, the turbulence equations are solved first. Then the level set transport equation, which upon convergence is reinitialized in two steps. The close points are reinitialized geometrically first and then all other points are reinitialized. Since the equation is nonlinear, a few iterations are needed here to converge. Then the PISO algorithm is solved using the PETSc toolkit (Balay et al., 2002). This step is repeated a few times to enforce the continuity condition which comprises the solution of the pressure matrix and the explicit update of the velocity field. Once the velocity field is obtained, the forces and moments are weighted with coefficients provided as a pre-processing step by USURP (Boger and Dreyer, 2006) used to properly compute area and

forces on overlap regions for a ship hull with appendages. Lastly, the motions are predicted for the next time step and SUGGAR is called to compute the interpolation given the new location of the moving grids.

CHAPTER 4. INSEAN CAPTIVE TESTS

INSEAN captive tests are performed to study resonant excitation and roll decay/parametric rolling of ONR Tumblehome (OT) with and without bilge keels. Resonant excitation tests are conducted with bilge keels in beam waves as building block for parametric rolling studies. Parametric rolling tests are performed initially with bilge keels and then without bilge keels. Herein, the details of ship model, test design, and operational and environmental conditions of tests are presented.

4.1 Ship Model

The tested model is the ONR Tumblehome (INSEAN model 2498), which is a preliminary design a new concept surface combatant (Fig. 4-1). The model is tested in the INSEAN basin n. 2 (220 m long, 9 m wide and 3.5 m deep), which is equipped with a flap wave maker at the basin end. The adopted scale is $\lambda = 46.6$ and the model is equipped with bilge keels for all tests in beam waves and some tests in head waves. The lines of the tested model are shown in Fig. 4-2 and the main model parameters are given in Table 4-1. Different bilge keels are adopted for the beam and head wave tests. The bilge keels profiles and locations for the beam wave cases are shown in Fig. 4-3, while the ones adopted for the head wave cases are shown in Fig. 4-4. The model length between perpendiculars (L_{PP}) is 3.305 m.

4.2 Test design

4.2.1 Cases with Bilge Keels

Preliminary tests are executed for OT with bilge keels in beam waves (resonant excitation) and head waves (parametric rolling) for one loading condition KG=0.165 m in model scale. The model is floated at the static waterline. The vertical position of center of gravity (VCG) is set to KG=0.165 m using ballast weights. The roll radius of gyration

(gyradius) is set to the target value which is k_{xx}=0.38B=0.153 m. As a result, the metacentric height is GM=0.043 m for the preliminary tests.

4.2.1.1 Resonant Excitation in Beam Waves

Beam wave tests are performed at Fr=0.0 in waves with resonant frequency ($f_w = f_\phi$= 0.650 Hz), which is determined by exciting the model with small amplitude waves. The corresponding wave length is λ=1.12L since $\omega^2 = gk = g(2\pi/\lambda)$ for deep water. Three different wave slopes are adopted, corresponding to small amplitude (Ak = 0.034), medium amplitude (Ak = 0.073) and large amplitude waves (Ak = 0.156), in order to evaluate the rising and development of the nonlinearities in the allowed motions and in the measured forces and moments. During the tests the model is placed at the center of the basin in length and width. The model is 2DOF free to roll and heave. For the restrained motions, the forces and moments at the constraint are measured. The wave height is measured by a servo-mechanic probe (Kenek SH) mounted one model length upstream the tested model. The heave and roll motions are measured both by means of optical motion tracker (Krypton) and gyroscopic platform (MOTAN), while the sway and surge forces are measured by load cells lodged inside a joint (Fig. 4-5) fixed to the model in correspondence of the center of gravity (C_G). The pitch moment is measured by a load cell mounted 100 mm upstream the C_G, while the yaw moment is measured by a torque cell. The torque cell connects the joint to a vertical bar, which is free to slide into a cylindrical guide fixed to the carriage. The yaw motion is inhibited by an additional guide that moves parallel to the vertical bar and rigidly fixed to it. The additional guide is mounted with 200 mm arm with respect to a vertical line passing through the C_G. For the cases Ak= 0.073 and Ak = 0.156 the tests have been repeated five times in order to determine the precision index.

4.2.1.2 Parametric Rolling in Head Waves

The head wave tests are performed in the wave with Ak=0.115 and f_w=0.69 Hz, corresponding to λ=L, to have maximum respond for the model. The ship speed is chosen Fr=0.35 based on the fact that the encounter frequency has to be about twice the natural roll frequency f_ϕ=0.65 Hz for parametric rolling.

$$f_e = f_w + f_w^2\left(2\pi Fr\sqrt{L/g}\right)\cos\mu = 2f_\phi \Rightarrow Fr = 0.35 \quad (4.1)$$

Here, f_e is wave encounter frequency and μ is wave heading which is zero for head waves.

The tests have been performed starting with the model in heave and pitch free condition, but fixed at a given initial roll angle. A servo-mechanic wave probe was used in order to measure the incoming waves and to trigger the magnet that fixed the model at the initial roll angle. When the model encounters the incoming waves, the magnet is disconnected by the trigger and the model started to roll. The adopted initial roll angle is 30°.

4.2.2 Cases without Bilge Keels

The cases without bilge keels are performed since the preliminary tests showed no evidence of parametric rolling for OT with bilge keels. The cases without bilge keels include roll decay test in calm water and parametric rolling test in head waves for a range of Fr and three loading condition KG=0.175, 0.170, and 0.165 m corresponding to GM=0.033, 0.038, and 0.043 m, as shown in Table 4-1. The model is floated at the static waterline and then the vertical position of center of gravity (VCG) is set to proper KG for each test using ballast weights. Initially, the roll radius of gyration was reported 0.146 m for all loading condition. More EFD investigations showed that actual k_{xx} are 0.127, 0.125, and 0.123 m for GM=0.033, 0.038, and 0.043m, respectively.

4.2.2.1 Roll Decay in Calm Water

Roll decay tests are conducted in calm water for Fr=0.05, 0.2, and 0.35. The tests are performed starting with the model free to sink and trim, but fixed at ϕ_0=30 deg initial roll angle for GM=0.033, 0.038 m and at ϕ_0=25 deg for GM=0.043 m. A servo-mechanic wave probe was used in order to trigger the magnet that fixed the model at the initial roll angle. When the model reaches to the desired Fr, the magnet is disconnected by the trigger. The adopted initial roll angle is 30°.

Time histories of roll, sinkage, and trim motions, X, Y, and N are recorded. A standard average roll decay coefficient n is computed as:

$$n = \frac{1}{N}\sum_{k=1}^{N}\frac{1}{2\pi}\ln\left|\frac{\phi_k}{\phi_{k+1}}\right| \tag{4.2}$$

where N is the number of roll cycles used in the analysis, ϕ_k is the roll displacement at the k^{th} roll cycle crest or trough, and ϕ_{k+1} is the roll displacement at the k^{th}+1 roll cycle crest or trough. n is usually expressed as a function of mean roll angle ϕ_{mk}

$$\phi_{mk} = \frac{\phi_k + \phi_{k+1}}{2} \tag{4.3}$$

The logarithmic decrement is computed as:

$$\delta_k = \ln\left|\frac{\phi_k}{\phi_{k+1}}\right| \tag{4.4}$$

The averaged logarithmic decrement δ is δ_k computed over N roll cycles i.e. $\delta = 2\pi n$.

The damping ratio ζ is evaluated from Eq. (4.2) by:

$$\zeta = \frac{n}{\sqrt{1+n^2}} \tag{4.5}$$

The damped natural frequency $f_{\phi d}$ ($\omega_{\phi d} / 2\pi$) is computed from roll decay time history as:

$$f_{\phi d} = \frac{1}{N}\sum_{k=1}^{N}\frac{1}{(t_{k+1}-t_k)_{\phi=0}} \tag{4.6}$$

$f_{\phi d}$ is determined by locating successive zero crossings of the ϕ time history through N roll cycles. This yields the roll periods which are inverted and averaged over N cycles to compute $f_{\phi d}$. The natural roll frequency $f_{\phi n}$ ($\omega_{\phi n} / 2\pi$) is:

$$f_{\phi n} = \frac{f_{\phi d}}{\sqrt{1-\zeta^2}} \tag{4.7}$$

The linear damping coefficient α, shown in Eq. (2.42), is computed by Eq. (4.2) and (4.7):

$$\alpha = n(2\pi f_{\phi n}) = n\omega_{\phi d} \tag{4.8}$$

Also, Himeno method (Himeno, 1981) is used to evaluate linear and nonlinear damping coefficient by plotting roll decrement ($\Delta\phi_k = \phi_{k+1} - \phi_k$) versus mean roll angle (ϕ_{mk}) in degree and fitting the following extinction curve to it.

$$\Delta\phi = a\phi_m + c\phi_m^3 \tag{4.9}$$

Consequently, linear and nonlinear dampings are calculated from extinction coefficients a and c:

$$\alpha = \omega_\phi a / \pi \tag{4.10}$$

$$\gamma = \frac{8}{3\pi\omega_\phi}\left(\frac{180}{\pi}\right)^2 c \tag{4.11}$$

The equivalent linear damping is computed from:

$$\alpha_e = \frac{1}{N}\sum_{k=1}^{N}\left[\frac{\omega_\phi}{\pi}\left(a + c\phi_{mk}^2\right)\right] \tag{4.12}$$

4.2.2.2 Parametric Rolling in Head Waves

The head wave tests are performed in the wave with Ak=0.105, 0.115 and f_w=0.69 Hz, corresponding to λ=L, to have maximum respond for the model. The ship speed is changed for the range of 0.02<Fr<0.44 to observe the parametric rolling instability zone. The tests are conducted starting with the model free to heave and pitch, but fixed at 30

deg initial roll angle. The roll motion constraint is removed after the model reaches to the desired Fr. A servo-mechanical (finger) probe Kenek-SH, positioned at the port side and at the same longitudinal position of the fore perpendicular, is used for the incoming wave measurements. The wave signal is also used to control the instant of model release during the head wave tests that was thus completely repeatable. During all the tests, the model is connected to the carriage by means of a joint specifically designed, as explained earlier. Uncertainty analysis is conducted for Ak=0.115, GM=.038 m and Fr=0.2, and GM=0.033 m and Fr=0.1 following standard procedures including five repeat tests. By re-mounting the model at beginning of each run, all the possible causes of bias related to the model mounting are accounted into the precision limit. For the model motions, in order to take into account the errors related to the measurement system, the mean value of the difference between the two measurement system outputs is taken as residual bias limit.

Table 4-1: Principal dimensions of the INSEAN ONR Tumblehome model

ONR Tumblehome				
	W/O BKs			W/ BKs
L_{PP}	3.305 m			3.305 m
Draft (T)	0.1201 m			0.118 m
Beam (B_{WL})	0.403 m			0.403 m
Displ.	84.7 kg			84.7 kg
LC_G	1.708 m Aft of FP			1.708 m Aft of FP
KG	0.175	0.170	0.165 m	0.165 m
GM	0.033	0.038	0.043 m	0.043 m
k_{XX}	0.146 0.127	0.146 0.125	0.146 m 0.123 m	0.153 m=38% B_{WL}
$k_{YY} = k_{ZZ}$	0.826 m =25% LPP 0.737 m =22% LPP			0.826 m =25% LPP
Bilge Keels	Beam Waves			c = 32.2 mm L = 1098 mm
	Head Waves			c = 26.82 mm L = 1098 mm

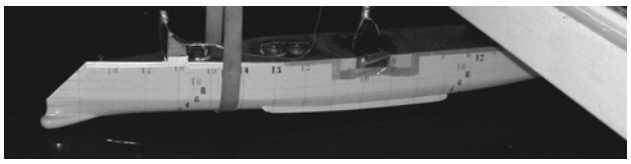

Figure 4-1: ONR Tumblehome (INSEAN model 2498)

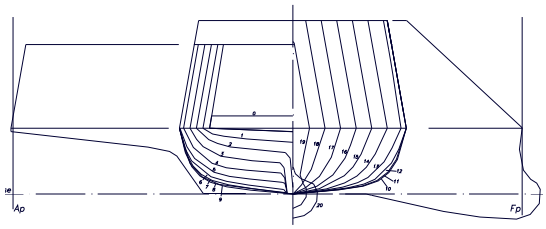

Figure 4-2: ONR Tumblehome lines, bow and stern profiles

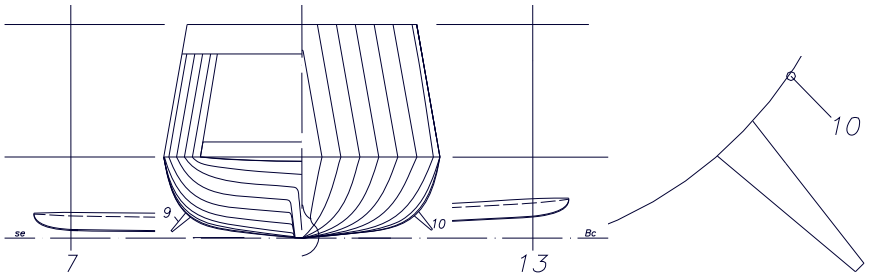

Figure 4-3: ONR Tumblehome bilge keels for the beam wave tests

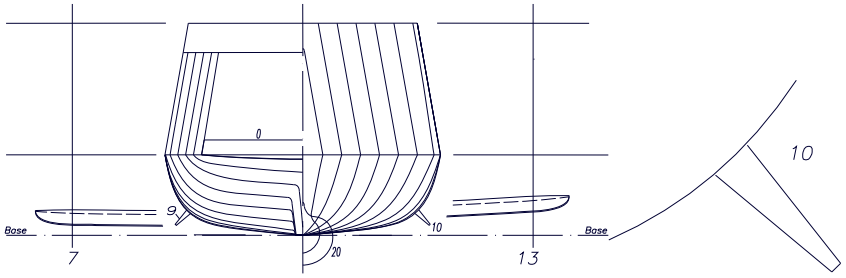

Figure 4-4: ONR Tumblehome bilge keels for the head wave tests

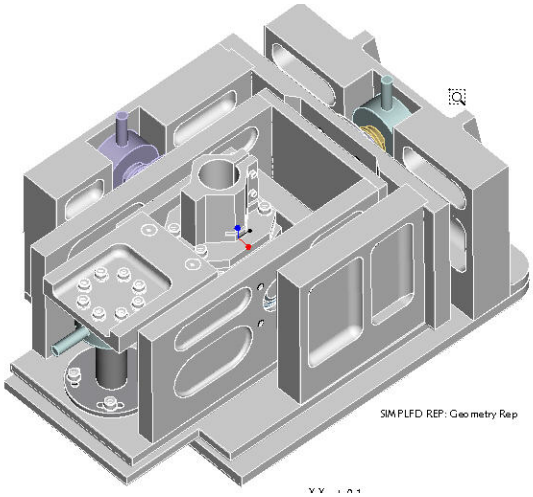

Figure 4-5: Illustration of the joint used for INSEAN towing tank tests; the torque cell is mounted on the top

CHAPTER 5. OU CAPTIVE AND FREE RUNNING TESTS

OU (Osaka University) tests are conducted for captive and free running models. In captive tests the model is restrained in some degrees of freedom while the model is self-propelled in free running tests and free to all vertical and horizontal motions. Captive experiments are designed such that they can collect required data for NDA model of parametric rolling and broaching described in Chapter 2. Free running experiments are designed to study different modes of ship response in following/quartering regular waves such as broaching, surf-riding, and periodic motion.

5.1 Ship Model

The ONR Tumblehome is used for OU captive and free model tests. The captive model is appended with skeg and bilge keels while free running model is appended with superstructure, shaft, strut, twin rudders to steer the model, and propellers. Also, the free model has the superstructure on it. Figure 5-1 and Table 5-1 provide ship model geometry and principles. The scale ratio of the model is 48.9 (L_{pp}=3.147 m) i.e. it is smaller than the model of INSEAN discussed in Chapter 4. The captive tests are conducted for one loading condition GM=2.068 m (GM=0.042 m in model scale) while free model tests are performed for GM=1.78, 2.068 m (GM=0.036, 0.042 in model scale).

5.2 Test design

5.2.1 Captive Test

The captive tests are conducted in the Osaka University towing tank. The tank is 100 m long, 7.8 m wide and 4.35 m deep. It is equipped with drive carriage (7.4m in length, 7.8m in width, and 6.4 m height) running from 0.01 to 3.5 m/s. It is also equipped with plunger-type wave maker generating regular and irregular waves up to 500 mm height

and wave length of 0.5 to 15m. The wave absorber is a small fixed gridiron beach at the basin's end, with movable beaches along its sides.

A right-handed Cartesian coordinate system fixed to the model is used for the tests. The origin is at the longitudinal and vertical center of gravity (LCG, VCG) of the model. The x, y, z axes are directed upstream, transversely to starboard, and downward, respectively.

Model ballasting satisfies three conditions. The first requires model floatation at the static waterline. The second and third conditions impose specific values for *VCG* and roll radius of gyration (gyradius), respectively. The model is ballasted to its design waterline first. Then, the added ballast method is used to set the proper *VCG* which is the distance measured from the keel to a point about which the model rolls. The model and its ballast are suspended in a level orientation from the carriage on a roll axle a distance z above the *VCG* about which the model can roll. Finally, the roll, pitch and yaw radius of gyration are set so that the model's dynamic properties conform to design specifications.

Captive model tests include resistance test, static heel in calm water, static drift in calm water, and static heel in following waves to collect required seakeeping and maneuvering parameters for NDA model of broaching and include static heel in head waves to collect required parameters for NDA model of parametric rolling.

5.2.1.1 Resistance Test

Resistance tests are conducted to measure X_* for NDA model of broaching shown in Eqs. (2.60)-(2.63). The model is free to sink and trim in calm water for a range of speed corresponding to Fr=0.05 up to Fr=0.6. The same experiment is performed at INSEAN for the model without bilge keels for Fr=0.05 up to Fr=0.4.

5.2.1.2 Static Heel in Calm water

Static Heel cases are performed for the model free to sink and trim to measure sinkage and trim, surge and side force, and roll and yaw moment and calculate heel induced hydrodynamic forces and moments terms in NDA model of broaching such as $X_{\phi\phi}, Y_{\phi}, Y_{\phi\phi\phi}, K_{\phi}, K_{\phi\phi\phi}, N_{\phi}$, and $N_{\phi\phi\phi}$. The model is fixed at two heel angles 10 and 20 degree and towed in calm water with a range of forward speed corresponding to Fr=0.05 up to Fr=0.6.

5.2.1.3 Static Drift in Calm water

Static Drift cases are conducted for the model free to sink and trim to measure sinkage and trim, surge and side force, and roll and yaw moment and calculate the sway velocity related hydrodynamic coefficients in NDA model of broaching such as $X_{vv}, Y_{v}, Y_{vvv}, K_{v}, K_{vvv}, N_{v}$, N_{vvv} and K and Y coupling term z_H. The model is fixed at drift angle= {2, 5, 10, 15 , 20} degree and towed in calm water at Fr={0.1,0.2,0.3,0.4}.

5.2.1.4 Static Heel in Following Waves

Static Heel in following waves are performed to measure exciting wave forces and moments X_w, Y_w, K_w, N_w in NDA model of broaching while the model is free to heave and pitch. The experiments are performed for Fr=0.3, H/λ=0.03 and λ/L=1 with ϕ= 10 and 20 degrees and λ/L=1.25, H/λ=0.025 and Fr=0.15,0.25,0.35, and H/λ=0.05 and Fr=0.35 with ϕ= 0.

5.2.1.5 Static Heel in Head Waves

Static Heel in head waves are conducted to measure restoring moment variation terms in NDA model of parametric rolling shown in Eq. (2.49) while the ship is free to heave and pitch. The model is fixed at 10 deg heel and towed with Fr={0.1,0.2,0.3} in head waves with H/λ=0.0366 and λ/L=1. Note that the other terms in NDA model of

parametric rolling such as α and γ are calculated from INSEAN roll decay test described in Chapter 4.

5.2.2 Free Running Test

Free-running model experiments are executed with the scaled model in a seakeeping and manoeuvring basin at National Research Institute of Fisheries Engineering (NRIFE). The basin is 60 m long, 25 m wide and 3.2 m deep, as shown in Fig. 5-2. The basin is equipped with an 80-segment wave maker to generate regular, long-crested irregular and short-crested irregular waves up to the limit of wave breaking. It is also equipped with an X-Y (longitudinally-transversely moving) towing carriage. Two loading conditions are tested: one is critical to the Sarchin and Goldberg (1962) criteria which means GM=1.78 m in full scale and the other is below that (GM=2.068 m). The angles of vanishing stability under these loading conditions are 180 degrees so that capsizing cannot appear. This is because the superstructure of the ONR tumblehome vessel is large enough. The model is propelled with two propellers. Their power is supplied from solid batteries inside the model. A feedback control system is provided to keep the propeller rate constant. The model is equipped with a fibre gyroscope, a computer and steering gears, and a proportional auto pilot for course keeping simulated within the onboard computer by using the yaw angle obtained from the gyroscope. The roll angle, pitch angle, yaw angle, rudder angle and propeller rate are recorded by the onboard computer. Water surface elevation is also measured by a servo needle wave probe attached to the towing carriage of the basin near the wave maker.

The experimental procedure for following and quartering waves is as follows. First, the model is kept near the wave maker without propeller revolution. Next, the wave maker starts to generate regular waves. After a generated water wave train propagates enough, a radio operator suddenly requests the onboard system to increase the propeller revolution up to the specified one and makes the automatic directional control active.

Then the model automatically runs in following and quartering waves to attempt to keep the specified propeller rate and auto pilot course. When the model approaches the side wall or the wave-absorbing beach, the automatic control is interrupted by the radio operator and the propeller is reversed to avoid collision. This is based on the ITTC (International Towing Tank Conference) recommended procedures on model test of intact stability registered as 7.5-02-07-04.1. It should be noted that the specified propeller rate is indicated by running the model in calm water to reach the nominal Froude number.

Two set of free-running test are performed. First set is performed for $\lambda/L=1.25$, $H/\lambda=0.05$, GM=1.78 and 2.068m in full scale, Fr=0.25, 0.3, 0.35, 0.4, 0.45, and autopilot course ψ_c= 5, 15, 30 deg, as shown in Fig. 5-3. The roll, pitch, yaw, and rudder angle and propeller rate are recorded by the onboard computer. The second set is carried out to record more data such as trajectory, initial wave phase respect to the model, and initial surge velocity to collect required parameters for CFD simulation. Second set is performed for $\lambda/L=1.25$, $H/\lambda=0.05$, GM= 2.068m in full scale, Fr=0.25, 0.30, 0.35, 0.40 and 0.45, the auto pilot courses ψ_c= -5, -15, -22.5, -30, -37.5 degrees from the wave direction, as shown in Fig. 5-4.

Table 5-1: Principal particulars of the OU ONR Tumblehome model

Items	*Ship*	*Model*
Length : L	154.0 m	3.147 m
Breadth : B	18.78 m	0.384 m
Depth : D	14.5 m	0.296 m
Draught : T	5.494 m	0.112 m
Displacement : W	8507 ton	72.6 kg
Block coefficient : C_b	0.535	0.535
Longitudinal position of centre of buoyancy from midship	2.587 m aft	0.053 aft
Metacentric height: GM	i) 1.781 m ii) 2.068 m	i) 0.0364 m ii) 0.0423 m
Radius of gyration in pitch/yaw: K_{yy}/L or K_{zz}/L	i) 0.25 ii) 0.25	i) 0.254 ii) 0.246
Radius of gyration in roll: K_{xx}/L	i) 0.056 ii) 0.052	i) 0.056 ii) 0.052
Rudder Area: A_R	28.639 m^2	0.012 m^2
Maximum rudder angle	35°	35°

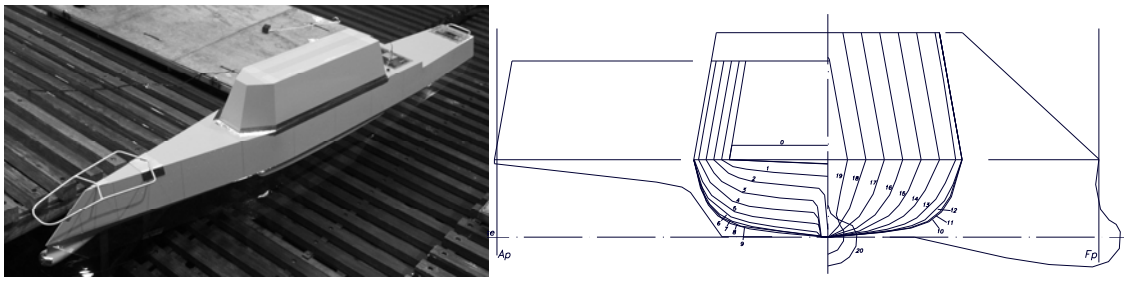

Figure 5-1: ONR Tumblehome (OU model) and body plan

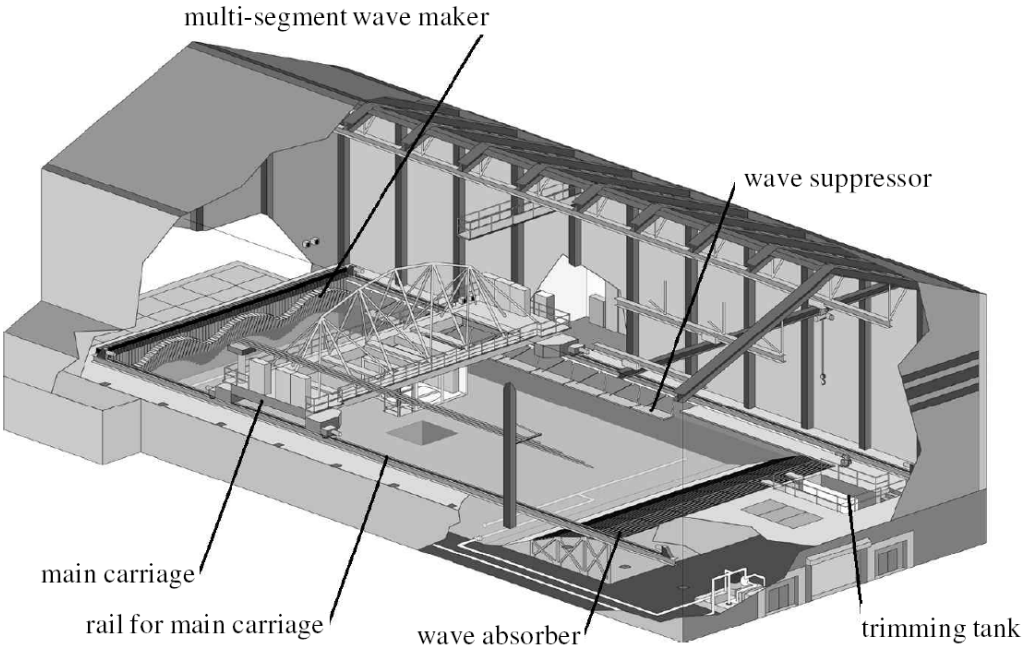

Figure 5-2: Seakeeping and maneuvering basin at NRIFE

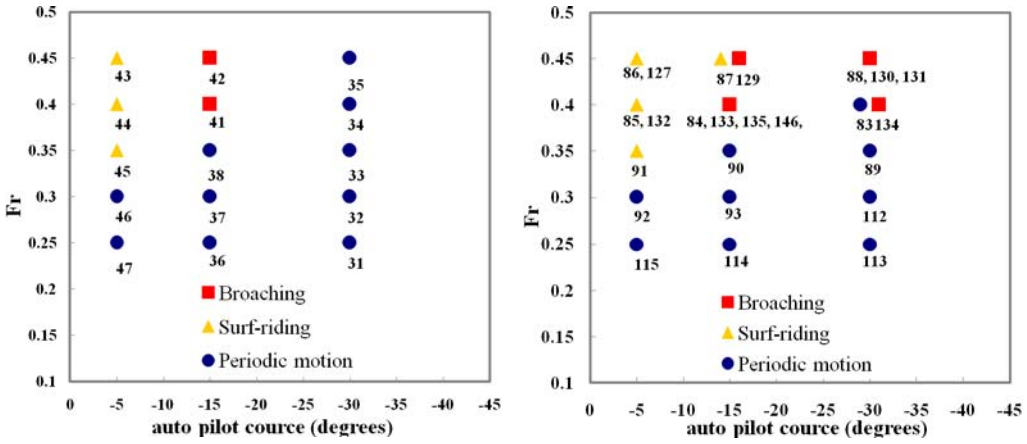

(a) **(b)**

Figure 5-3: EFD free model test program 1: (a) H/λ=1/20, λ/L=1.25 and GM=1.78m; (b) H/λ=1/20, λ/L=1.25 and GM=2.068 m

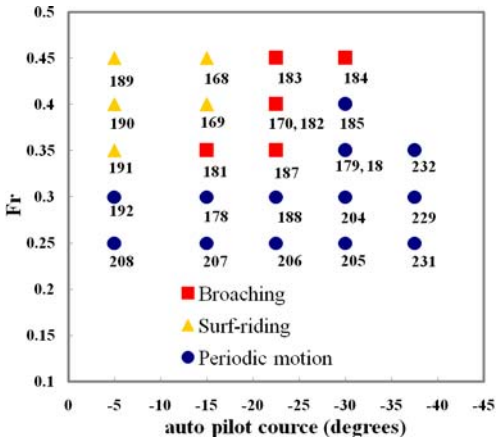

Figure 5-4: EFD free model test program 2 for H/λ=1/20, λ/L=1.25 and GM=2.068m

CHAPTER 6. VALIDATION OF INSEAN CAPTIVE MODEL SIMULATIONS

The INSEAN captive model simulations are performed with the same operational and environmental conditions described in Chapter 4 which include Roll Decay in calm water, resonant excitation in beam waves, and Roll Decay/Parametric Rolling in head waves. The simulations are carried out to validate CFD and compare the results with the outcome of NDA models described in Chapter 2. Herein, the details of CFD simulation including computational domain and boundary conditions, grid, preliminary studies for OT with bilge keels, results for OT without bilge keels including roll decay in calm water and parametric rolling in head waves are presented. Lastly, NDA model of roll decay and parametric rolling described in Chapter 2 (Eq. 2.42 and Eq. 2.49) are solved and compared with EFD and CFD. The CFD and NDA results were blind in that the actual EFD radius of gyration k_{xx} was not known a priori.

6.1 Computational Domain, Boundary Conditions

The computational domains extend from $-0.5 < x < 2, -1 < y < 1, -1 < z < 0.25$ for roll decay and the head wave cases and $-1 < x < 2$, $-1 < y < 2.25$, $-1 < z < 0.25$ for beam wave cases, in dimensionless coordinates based on ship length. The ship axis is aligned with the x-axis with the bow at x = 0 and the stern at x = 1. The free surface at rest lies at z = 0. The ship model is appended with skeg and bilge keels for beam wave and preliminary head wave cases, and appended with only skeg for roll decay and final head wave simulations.

Boundary conditions are shown in Table 6-1. Inlet boundary conditions for cases in calm water waves are different. For calm water, x component velocity at inlet boundary condition is set to be U_0 which is the same as ship velocity in relative coordinate system and zero in earth fixed coordinate system. Other velocity components are imposed to be zero. Normal pressure gradient and level set function are imposed zero and –z(x) for calm

water, respectively. In regular waves, inlet pressure gradient and level set function are imposed such that they follow linear wave theory equations:

$$p = \frac{A}{Fr^2} e^{kz} \cos(kx - 2\pi ft) - \frac{A^2}{2Fr^2 k} e^{2kz} \quad (6.1)$$

$$\phi = A\cos(kx - 2\pi ft) - z(x) \quad (6.2)$$

$$U(x, y, z, t) = U_0 + \frac{A}{Fr}\sqrt{k}e^{kz}\cos(kx - 2\pi ft)(x) \quad (6.3)$$

$$W(x, y, z, t) = \frac{A}{Fr}\sqrt{k}e^{kz}\sin(kx - 2\pi ft) \quad (6.4)$$

Here, U_o would be zero in earth coordinate system. Other boundary conditions are the same for cases in calm water and in waves.

6.2 Grid

As shown in Fig. 6-1, computational grids for the hull and bilge keels are designed to accurately resolve geometric features of the model and the unsteady turbulent boundary layer, wake, and wave fields. The hull boundary layer and bilge keels grids were generated using GRIDGEN. The hull boundary layer and bilge keels grid were fixed to and move with the ship. The hull boundary layer has a double-O topology and extends to cover the deck of the ship and wraps around it, allowing for computations with extreme motions. Grid topology was selected so that two other blocks were responsible to capture the flow near the hull (refinement block) and far from the hull (background block). Since there might be a wave on the free surface, the background block was designed to have enough grid points near free surface. The computational domain for all blocks covers both the port and starboard sides of the ship, since the flow and wave fields are asymmetric during the roll motion.

6.3 Preliminary Study (Cases with Bilge Keels)

Preliminary studies were conducted with bilge keels to investigate large amplitude roll (beam waves) and parametric roll (head waves). The beam wave studies were useful as building block for CFD prior to parametric roll studies. Parametric roll studies indicated bilge keel condition roll damping is excessive, i.e., greater than the threshold value such that parametric roll is not exhibited as discussed later, which motivated the removal of the bilge keels.

2DOF zero-speed heave-roll in beam waves was investigated for $\lambda / L = 1.12$, i.e. wave frequency equal natural frequency roll, and wave steepness Ak=0.156. 3DOF forward-speed heave-roll-pitch in head waves was investigated for $\lambda / L = 1$, Fr=0.35, Ak=(0.115,0.156), and ϕ_0=30 deg. This condition corresponds to the linear theory instability estimate for small excitation and zero damping where the encounter frequency is twice the natural roll frequency.

6.3.1 Resonant Excitation in Beam Waves

Table 6-2 summarizes the 2DOF beam wave response for Ak=0.156. EFD indicates dominant first harmonic a_1 at f_{ϕ} for heave, roll, side force, and yaw moment, whereas surge force and pitch moment indicate dominant second harmonic a_2 with significant 3rd and 4th harmonic amplitudes. The maximum heave and roll amplitudes are large: z_{max}/T=.83 and ϕ_{max}=25 deg. Heave responds at $f_w = f_\phi$ since f_{zh}=1.67 Hz >> f_ϕ. For X and M, large 2nd and 4th harmonic are observed due to roll and heave coupling, whereas small 1st and 3rd harmonic are observed due to heave coupling, as discussed in Chapter 2. For Y and N, large 1st harmonic is due to roll coupling. Hydrostatic restoring force and static drift test results provide estimates for M and Y/N induced maximum pitch and drift angle: θ_{max}=0.5 deg and β_{max}=0.063 deg. Results for smaller and larger Ak show that heave and roll amplitudes increase linearly with A and Ak, respectively. CFD

qualitatively predicts these trends, but with relatively large comparison errors E=(D-S)%D. CFD analysis shows that dominant second harmonic for pitch moment results from equal contributions from hydrostatic and pressure components, which are larger than friction component and 180 deg out of phase.

6.3.2 Parametric Rolling in Head Waves

Table 6-3 summarizes the 3DOF head wave response for Ak=0.115 and 0.156 (CFD only) and ϕ_0=30 deg. EFD indicates dominant first harmonic response at $f_e=2f_\phi$ for heave, pitch, and surge force X, whereas roll, side force Y, and yaw moment N are under damped harmonic oscillations, i.e., response is roll decay in waves and parametric roll is not exhibited. Surge force 2nd, 3rd, 4th, and 5th harmonic amplitudes are also significant. Roll decay first peak, linear and nonlinear damping, and large/small mean roll angle frequency are $0.4\phi_0$, 0.55 and 0.0052, and $0.91f_{\phi h}/f_e$, respectively. The linear damping corresponds to a logarithmic decrement $\delta = \ln(\phi_i / \phi_{i+1})$ of .82 and energy ratio $e^{2\delta}$ of 5.2. Initially, i.e., for large mean roll angles ($t<6T_e=3T_\phi$), roll, side force, and yaw moment respond at roll damped natural frequency and surge, heave, and pitch exhibit effects roll, whereas for small mean roll angles, ϕ, Y, and N respond at f_e with small amplitudes and surge, heave, and pitch that are unaffected by roll motion. Y and N FFT show large peaks at $f_e/2$, $3f_e/2$, $7f_e/2$ and $11f_e/2$. For X, large 1st-5th harmonics are due to both heave/pitch and roll coupling. For Y and N, large ½, 3/2, etc. harmonics are due to roll coupling. CFD qualitatively predicts these trends with relatively small E for heave, pitch, and ϕ, Y decay and large E for surge and N decay. Roll decay first peak $f_{\phi\,1}$, linear α and nonlinear damping γ, and large/small mean roll angle frequency ($f_{\phi dl}/f_{\phi ds}$) are $.5\phi_0$, .4 and .0061, and $.89f_{\phi h}/f_e$, respectively, which are close to EFD. CFD analysis shows that significant 2nd harmonic surge force is due to 180 deg phase difference between weight and hydrostatic forces. CFD shows that increased Ak to 0.156 reduces z/A, θ/Ak first harmonics by 10%, 7%, but increases surge force amplitude by 15%. Roll decay first

peak, linear and nonlinear damping, and large/small mean roll angle frequency are $.33\phi_0$, .68 and .0089, and $.74f_{\phi h}/f_e$, respectively.

6.3.2.1 Instability Analysis

The roll motion neglecting nonlinear damping and restoring moment and considering wave effects and pitch-heave coupling only through a time varying restoring coefficient is modeled as a 1D mass-damper-spring linear system with small damping and periodic restoring coefficient, as described in Chapter 2 (Eq. (2.49)). This 1D model can be transformed into the Mathieu equation (Paulling and Rosenberg, 1959). Bounded/unbounded solutions to the Mathieu equation are delineated in the Ince-Strutt diagram as $q=\omega_a^2/\omega_e^2$ vs. $p=\left(\omega_\phi^2-\alpha^2\right)/\omega_e^2$ curves where $\omega_\phi=\sqrt{gGM_m}/k_{xx}$ is the roll natural frequency in waves, $\omega_a=\sqrt{gGM_a}/k_{xx}$ is the amplitude of parametric excitation in waves expressed in terms of frequency, α is the linear roll damping, and GM_a and GM_m are the amplitude and mean value of GM variation in waves. For q=0.0, instability occurs at $p=n^2/4$ $n=\{1, 2, 3,\ldots\}$. The first parametric resonance region occurs for n=1 meaning p=0.25 or, equivalently, for zero damping. In other words, for small excitation and damping the roll period equals twice the wave encounter/pitch motion period for first parametric resonance region. For q>0.0 instability occurs for increasing ranges of p for increasing q, which can be equivalently expressed as a Froude number (Fr) range. Unbounded solutions to the Mathieu equation may not lead to unbounded roll unless the damping α is less than a threshold value $\alpha_T=\alpha_T(p,q)$ (Shin et al., 2004). CFD analysis of roll moment and GM variation for Ak=.115, provides the mean $GM_m=(GM_{max}+GM_{min})/2=0.033$ (note that GM=0.043 m) and excitation $GM_a=(GM_{max}-GM_{min})/2=0.021$ from which roll frequencies with neglected added mass $\omega_\phi=\sqrt{gGM_m}/k_{xx}$=3.71 (note that $\omega_{\phi h}$=4.24 rad/s) and $\omega_a=\sqrt{gGM_a}/k_{xx}$=2.89 rad/s such that (p,q)= (0.2, 0.12) with instability range 0.17<Fr<0.38 and α_T=0.32.

Consequently, the performed simulation at Fr=0.35 is inside the instability range but $\alpha=0.4>\alpha_T$ which is explanation for with bilge keels study not achieving parametric roll.

6.4 Cases without Bilge Keels

Since the actual EFD K_{xx} was not known a priori, first CFD was conducted for 3DoF forward speed heave-roll-pitch roll decay/parametric roll in head waves for $\lambda/L=1.0$, $0.0 \le Fr \le 0.44$, and different GM with k_{xx}=0.153 m (the same as k_{xx} for cases with bilge keels) and Ak=0.115. For GM=0.043 sensitivity studies were conducted for larger Ak=0.156 for Fr=0.13, 0.15, and 0.2 and for drift angle β=2 and 4 deg for Fr=0.13 with Ak=0.115. Second EFD was conducted for 3DoF forward speed heave-roll-pitch roll decay in calm water for $0.05 \le Fr \le 0.35$ and ϕ_0=30 deg (GM=0.033 m), $0.05 \le Fr \le 0.35$ and ϕ_0=30 deg (GM=0.038 m), and $0.05 \le Fr \le 0.45$ and ϕ_0=25 deg (GM=0.043 m); and 3DoF forward speed heave-roll-pitch roll decay/parametric roll in head waves for $\lambda/L=1.0$, $0.02 \le Fr \le 0.44$, ϕ_0=30 deg, and different GM and Ak, as described in Chapter 4. Third CFD was conducted for 1DoF forward speed roll decay in calm water for Fr=0.2 and ϕ_0=30 deg (GM=0.033 m), Fr=0.05, 0.2, and 0.35 and ϕ_0=30 deg (GM=0.038 m), and Fr=0.2 and ϕ_0=25 deg (GM=0.043 m) and different k_{xx} to find actual k_{xx}, and 3DoF forward speed heave-roll-pitch roll decay/parametric roll in head waves for $\lambda/L=1.0$, $0.02 \le Fr \le 0.44$, ϕ_0=30 deg and different GM and Ak with adjusted k_{xx}. Lastly, additional EFD radii of gyration tests were conducted.

6.4.1 Forward Speed Roll Decay in Calm Water

6.4.1.1 Forces, Moments, and Motions

CFD roll decay simulations are performed for several k_{xx} to find the actual EFD k_{xx} by comparing CFD with EFD. For GM=0.038 m and Fr=0.2, as shown in Table 6-4, CFD roll with k_{xx}=0.146 m show large differences EFD roll with average absolute value error

E_{RSS}=127%ϕ_0 ($E_{RSS} = (1/N)\sqrt{\sum_{i=1}^{N}((\phi(t_i)_{EFD} - \phi(t_i)_{CFD})/\phi_0)^2}$), i.e. CFD under/over predicts large roll angle damping/period. CFD with reduced k_{xx}=0.1246 m indicates much closer agreement EFD, at least for large roll angles, although damping is still under predicted such that E_{RSS}=3.7%ϕ_0. The under prediction is larger for Fr=0.05 and 0.35 with E_{RSS} =7.1 and 9.33%ϕ_o. Similarly for GM=0.033 and 0.043 m and Fr=0.2 reduced values of k_{xx}=0.1388 and 0.1298 m indicate closer agreement EFD, although damping is under and over predicted such that E_{RSS}=11.28 and 5.92%ϕ_0.

Figure 6-2 compares CFD and EFD roll decay time history for GM=0.043 m. EFD is for 3DOF condition with large initial roll and zero initial heave and pitch. Roll is under damped harmonic oscillations at $f_{\phi d}$. Heave and pitch asymptote to their dynamic calm water values for each Fr with small amplitude oscillations mostly at $f_{\phi d,}$ but also at their natural frequencies f_{zh} and $f_{\theta h}$. X shows no discernable harmonic amplitudes, whereas Y and N show large $f_{\phi d}$ and $3f_{\phi d}$ harmonic amplitudes. CFD is 1DOF condition, i.e., same as EFD for roll, but fixed heave and pitch. X shows no discernable harmonic amplitudes, whereas Z and M show $f_{\phi d}/2$, $2f_{\phi d}$ and 4 $f_{\phi d}$ and Y and N show large $f_{\phi d}$ and $3f_{\phi d}$ harmonic amplitudes. Consequently, these harmonics follow the theory explained in Chapter 2. Similar harmonics are observed for GM=0.038 m and GM=0.033 m, as shown in Fig. 6-3,6-4,6-5, and 6-6.

6.4.1.2 Roll Decay Parameters

Figure 6-7 compares CFD and EFD damped natural roll frequency ($f_{\phi d_k} / f_{\phi h}$) vs. mean roll angle (ϕ_{m_k}). For GM=0.043 m, $f_{\phi d_k}$ is close to $f_{\phi h}$=0.84 Hz at small ϕ_{m_k} and decreases for increasing ϕ_{m_k} by about 5/10/15% $f_{\phi h}$ for Fr=0.35/0.2/0.05. $f_{\phi d_k}$ has larger value for larger Fr for some ϕ_{m_k} . For GM=0.038 and 0.033m, $f_{\phi d_k}$ are close to $f_{\phi h}$=0.78 and 0.71 Hz, respectively, at small ϕ_{m_k} and decreases for increasing ϕ_{m_k} by about the same values for GM=0.043 m. It is observed that GM effect on $f_{\phi d_k}$ is small for low Fr but noticeable

for high Fr. For Fr=0.35, $f_{\phi d_k}$ at large ϕ_{m_k} decreases for decreasing GM by about 10% $f_{\phi h}$. CFD simulations show similar results.

CFD and EFD mean roll angle averaged damped natural frequency $f_{\phi d}$ and mean roll angle ϕ_m vs. Fr are shown in Fig. 6-8a, b, respectively. $f_{\phi d}$ increases with Fr about 10% $f_{\phi h}$ in the observed range of speed, whereas the mean roll angle decreases by about half from low to high Fr. Decreasing GM to 0.033m does not change $f_{\phi d}$ significantly but decreases ϕ_m by about half. CFD results show good agreement with EFD for GM=0.043 and GM=0.038 m but show fairly large error for GM=0.033 m. CFD predicts the same effects of Fr on $f_{\phi d}$ and ϕ_m and strong effect of GM on $f_{\phi d}$.

Figure 6-9 shows CFD and EFD logarithmic decrement vs. mean roll angle for GM=0.043, 0.038, and 0.033 m. δ_k increases slightly with increasing ϕ_{m_k} and increases by factor of 2 from low to high Fr and from high to low GM. The largest $\delta_k < 0.7$ such that $\zeta_k \approx \frac{\delta_k}{2\pi} < 0.1$ for all conditions confirming that the roll motion is under damped. CFD prediction of δ_k indicates that CFD predicts δ_k very well for GM=0.043 m and under predicts δ_k for lower GM by about 50%D.

CFD and EFD mean roll angle averaged δ and ER are shown in Fig.6-10a,b, respectively. As discussed with reference to Fig. 6-9, logarithmic decrement δ increases with increasing Fr and is larger for low GM condition. The rate of increase of δ respect to Fr is larger for $0.05 \le Fr \le 0.2$. ER increases about 40% from Fr=0.05 to Fr=0.35 for all GM. CFD shows the same trend for δ and ER with increasing Fr even though both are under predicated by 50%D for GM=0.033 and 0.038 m.

Figure 6-11 compares CFD and EFD linear and nonlinear damping coefficients based on Himeno method (α,γ). The linear damping increases with increasing Fr and is larger for low GM condition. The rate of increase of α respect to Fr is larger for $0.05 \le Fr \le 0.2$. Table 6-5 compares linear damping coefficient α with equivalent damping coefficient α_e estimated based on Himeno method and linear damping coefficient based on $n\omega_{\phi d}$ where

$n=\delta/2\pi$ and damped roll period $\omega_{\phi d}$ are averaged over all mean roll angles. The EFD trends for $n\omega_{\phi d}$ and α_e are similar as for the linear damping coefficient α i.e. $n\omega_{\phi d}$ and α_e increase by factor of 2 from low to high Fr. For GM=0.043 m, the differences between logarithmic decrement and Himeno methods are very small over all Fr. For lower GM, α is smaller than $n\omega_{\phi d}$ and α_e. Notice that linear damping for Fr=0.35 and GM=0.043 m is 0.28 which is about 70% of the damping for the ship with bilge keels at the same Fr and GM discussed in Section 6.3.2. This means that the damping is less than the threshold value for parametric rolling ($\alpha<\alpha_T=0.4$) and there is a chance of parametric rolling for the ship without bilge keels. CFD shows similar values linear damping for GM=0.043 m, but under predicts for lower GM. For both EFD and CFD nonlinear damping increases with Fr and increases significantly from high to low GM. CFD shows good agreement with EFD for GM=0.043 and under predicts for lower GM, especially GM=0.038 m and Fr=0.35.

6.4.1.3 NDA Model of 1DOF Roll Decay

In order to assess the accuracy of damping coefficients estimation, Eq. (2.42) was solved based on Rung Kutta method of order four with linear and nonlinear damping coefficients (Fig.6-11 and Table 6-5) along with nonlinear restoring coefficients estimated from CFD/EFD, shown in Fig. 6-12, to reconstruct roll decay. As shown in Table 6-6, the best results are for nonlinear damping and restoring with E_{RSS}=7.3, 6.8, 4.7%ϕ_o for GM=0.043, 0.038, and 0.033 m, respectively, averaged over Fr. Use of linear restoring increased E_{RSS}=18.4, 16.9, and 13.2%ϕ_o. Use of only linear damping and nonlinear restoring coefficients increased E_{RSS} by only about 1%ϕ_o.

6.4.1.4 OT vs. 5415

EFD data of OT are compared with EFD data for DTMB 5415 (Irvine et al., 2004) for design GM, i.e., previous generation surface combatant. The $\omega_{\phi d_k}$ and δ_k vs. ϕ_{m_k} are

estimated for 5415 and compared with OT, as shown in Fig. 6-13a,b. $\omega_{\phi d_k}$ of 5415 are fairly independent of ϕ_{m_k} whereas $\omega_{\phi d_k}$ of OT decreases for increasing ϕ_{m_k}. δ_k of 5415 is fairly independent of ϕ_{m_k} whereas δ_k of OT increases slightly for increasing ϕ_{m_k}. Also, δ_k of 5415 increases by factor 3 from low to high Fr but OT shows increases by factor of 2. Comparing OT and 5415 gives that $\omega_{\phi d}$ vs. Fr have similar trend for 5415 and OT but ϕ_m against Fr shows decreasing with increasing Fr by about half for OT vs. by 60% for 5415, as shown in Fig. 6-14a. δ for 5415 is smaller for low Fr and the same for both OT and 5415 for $0.2 \le Fr \le 0.35$ as shown in Fig. 6-14b. The similar trend is indicated for ER. The linear and nonlinear damping coefficients are estimated for 5415 and compared with OT, as shown in Fig. 6-15. It is concluded that α, α_e, and $n\omega_{\phi d}$ damping coefficients are very close to each other and are smaller than those for OT for low Fr. Nonlinear damping coefficient is not observed for 5415. For 5415, best reconstruction is for equivalent linear damping without requiring nonlinear restoring coefficients and E_{RSS} about $8\%\phi_0$ whereas best reconstruction for OT requires nonlinear damping and restoring coefficients and E_{RSS} $=7.3\%\phi_0$.

6.4.1.5 Summary of Roll Decay

In conclusion, CFD with adjusted k_{xx} indicates reasonable agreement with EFD, especially for GM=0.043 m and GM=0.038 m. $f_{\phi d_k}$ and δ_k decreasing and increasing with increasing ϕ_{m_k}. $f_{\phi d}$, linear and nonlinear damping coefficients increase with increasing Fr whereas ϕ_m decreases from low to high Fr. Increasing GM decreases ϕ_m and increases linear and nonlinear damping coefficients. OT roll reconstruction requires nonlinear restoring coefficients with linear or nonlinear damping coefficient. Comparing NDA roll decay reconstruction with CFD indicates that E values are similar to those for CFD. Comparing 5415 and OT shows that effects of mean roll angle on roll decay characteristics are stronger for OT vs. 5415. The linear damping of 5415 is smaller than that of OT and the nonlinear damping is not observed for 5415 whereas it is significant

for OT. Lastly, best reconstruction for 5415 is for equivalent linear damping without requiring nonlinear restoring coefficients whereas best reconstruction for OT requires nonlinear damping and restoring coefficients.

6.4.2 Forward Speed Roll Decay/Parametric Roll in Head Waves

6.4.2.1 Parametric Rolling Zone

First CFD simulations for GM=0.043, 0.038, and 0.048 m and k_{xx}=0.153 m (i.e. same value as for with bilge keels conditions), including for GM=0.043 m effects of Ak and β are performed. Figure 6-16a shows the GM=0.043 m results. Parametric roll is predicted for $0.11 \le Fr \le 0.35$ with maximum stabilized roll angle $\phi_{\max} \approx 40$ deg for Fr=0.13. For smaller GM=0.038 m capsize is predicted as shown in Fig. 6-16b, whereas for larger GM=0.048 parametric roll is predicted for $0.11 \le Fr \le 0.35$ with maximum stabilized roll angle $\phi_{\max} \approx 60$ deg for Fr=0.18, as shown in Fig. 6-16c. Wave steepness and drift angle effects are studied for GM=0.043 m and concluded that increased wave steepness increases pitch amplitude, but inhibits parametric roll since over some steepness the ship and the incoming wave are away of resonance tune. Drift angle β=2 deg increases $\phi_{\max} \approx 43$, whereas β=4 deg inhibits parametric roll.

Second EFD for GM=0.043, 0.038, and 0.033 m with Ak=0.115, including Ak effects for GM=0.038 and uncertainty analysis for GM=0.038 m and Fr=0.2, and GM=0.033 m and Fr=0.1 are carried out. For GM=0.38 m, uncertainly analysis for heave and surge force are 6.1% and 10.9 %, respectively while for other parameters are less than 4%, as shown in Table 6-7. Uncertainty for GM=0.033 m shows fairly the same situation even though heave has higher uncertainty for this case, as shown in Table 6-8. Figure 6-16 shows EFD heave, pitch, and roll amplitude for GM=0.043, 0.038, and 0.033 m. For all GM, heave amplitude increases with Fr number and then decreases at high Fr number. Also, it diminishes with decreasing GM. Pitch amplitude increases from low to high Fr to

reach to its maximum around Fr=0.2 and then decreases. Also, pitch amplitude for GM=0.043 and 0.038 have the same order whereas it is smaller for GM=0.033. Roll amplitude indicates no parametric roll for GM=0.043 m (Fig. 6-16a) whereas for GM=0.038 parametric roll is shown for $0.18 \le Fr \le 0.35$ with maximum stabilized roll angle $\phi_{\max} \approx 35$ deg for Fr=0.18, as shown in Fig. 6-16b. For GM=0.033 parametric roll is indicated for $0.07 \le Fr \le 0.28$ with maximum stabilized roll angle $\phi_{\max} \approx 40$ deg for Fr=0.07, as shown in Fig. 6-16d. For GM=038 and smaller Ak=0.105 parametric roll indicated for $0.19 \le Fr \le 0.28$ with maximum stabilized roll angle $\phi_{\max} \approx 33.5$ deg for Fr=0.2, as shown in Fig. 6-16b.

Third CFD simulations are performed for GM=0.043, 0.038, and 0.033 m and k_{xx}=0.1298, 0.1246, and 0.1388 m, respectively, as estimated from the roll decay tests with Ak=0.115. Figure 6-16 shows CFD heave, roll, and pitch amplitude for GM=0.043, 0.038, and 0.033 m. For all GM, CFD heave amplitude is over predicted but it has the same trend as EFD, showing increasing trend with Fr and then decreasing trend at high Fr number. Roll amplitude shows that parametric roll is not indicated for GM=0.043, whereas for GM=0.038 m parametric roll is shown for $0.17 \le Fr \le 0.44$ with maximum stabilized roll angle $\phi_{\max} \approx 45$ deg for Fr=0.17, as shown in Fig. 6-16b, and for GM=0.033 m parametric roll indicated for $0.0 \le Fr \le 0.3$ with maximum stabilized roll angle $\phi_{\max} \approx 50$ deg for Fr=0.02, as shown in Fig. 6-16d. For GM=0.033 m and Fr=0 capsize is predicted. The agreement between CFD and EFD for GM=0.038 and 0.033 m is remarkable, although CFD predicts larger instability zones at high and low Fr, respectively. For pitch amplitude, CFD under predicts at low Fr number and over predicts at high Fr number but it shows the same trend as EFD.

Lastly, additional EFD conducted for revised estimates k_{xx}=0.123, 0.125, and 0.127 m, respectively, for GM=0.043, 0.038, and 0.033 m and k_{yy}=0.737 m. The average k_{xx} difference between EFD and CFD is 5%. The EFD uncertainty in k_{xx} and GM are estimated at 2.5% and 2%, respectively.

6.4.2.2 Forces, Moments, and Motions Time History and FFT

Figure 6-17, 6-18, 6-19 compare EFD and CFD parametric roll for max roll angle condition for GM=0.043 m, 0.038, and 0.033, respectively, including motion, time histories and FFT analysis of X, Y, N. Since for GM=0.043 m parametric roll is not shown, Fig. 6-17a compares EFD and CFD roll decay parameters such as roll angle vs. Fr, damping coefficients vs. Fr, and period vs. mean roll angle in waves. EFD is only available for Fr=0.35. CFD under predicts linear damping coefficients and over predicts cubic term. Current results show that non dimensional damping coefficients are the same as those in calm water at high Fr and larger by factor of 2 at low Fr. The period vs. mean roll angle shows that roll period is close to twice the encounter period only at Fr>0.25. This suggest that parametric roll has not chance to occur at low Fr for GM=0.043m. Fig. 6-17b shows EFD and CFD time history for Fr=0.35. Heave and pitch responses at f_e and are fairly linear and independent of roll angle suggesting roll effects on heave and pitch are second order or higher. Roll response is the same as preliminary studies roll decay in waves but with roll damping frequency for bare hull condition. X,Y, and N show nonlinearity for both large and small roll angle. CFD simulation indicates fairly good agreement with EFD in overall. Heave is over predicted and pitch is under predicted at their minimums and both are predicted to response at f_e. Roll decay is predicted similar to EFD but roll angle is over predicted i.e. damping is under predicted in waves. X and Y are under predicted and N is over predicted by CFD. Fig. 6-17c illustrates CFD and EFD comparison of FFT of restrained forces and moments. As it is explained in Chapter 2, X indicates 1st, 2nd and 3rd harmonic amplitudes due to wave, and heave-pitch-roll coupling. Y indicates 2nd harmonic amplitudes due to heave and pitch motions and ½, 3/2, 5/2 harmonic amplitudes due to roll motion. N responses at ½ and 3/2 harmonics due to roll motion. CFD simulation shows similar harmonics for X, Y, and N but X and Y are under predicted and N is over predicted. Harmonics of cases with GM=0.043m and other Fr are

obtained, as shown in Fig. 6-20a, and concluded that for all Fr, X indicates 1st, 2nd, and 3rd harmonics whereas Y, and N show ½, 3/2, and 5/2 harmonics as expected.

As shown in Fig. 6-18a, for GM=0.038m and Fr=0.2, roll responses at $1/2f_e$ and parametric roll is observed. Heave and pitch response fairly linear at f_e with the amplitude of order of 0.5A and 0.5Ak, respectively. X,Y, and N show harmonic oscillations with some nonlinearity. CFD simulation predicts parametric rolling as observed in EFD. Heave and pitch are predicted to response at f_e and both over predicted whereas roll amplitude prediction agrees with EFD. N is over predicted and X and Y are under predicted. FFT analysis shown in Fig. 11b indicates 1st and 2nd harmonics for X, ½, 3/2, 5/2 harmonic for Y and N, as it is expected. CFD predicts similar harmonics for X, Y, and N even though 1st harmonic of X and 1/2 harmonic of Y are under predicted. Harmonics of cases with GM=0.038m and other Fr are obtained, as shown in Fig. 6-20b, and concluded that X indicates 1st, 2nd, and 3rd harmonics for all Fr whereas Y, and N show ½, 3/2, and 5/2 harmonics as expected.

CFD and EFD comparison for GM=0.033m and Fr=0.1 is shown in Fig. 6-19. EFD observes parametric roll in which roll responses at $1/2f_e$. Heave and pitch response at f_e with the amplitude of order of 0.3A and 0.5Ak, respectively. The parametric rolling zone is moved to lower Fr range compare with the one for GM=0.038 which was expected according to Mathieu equation. The harmonic behaviour of motions results in harmonic oscillations in restrained forces and moments. CFD simulation indicates similar response for roll i.e. parametric rolling. The CFD prediction of roll amplitude is excellent but heave and pitch are over predicted. X and N are predicted very well whereas Y is under predicted by 100% as shown in Fig. 6-19a. FFT analysis shows similar harmonics existed for GM=0.038m. CFD is not able to capture 1/2 harmonic of Y whereas it predicts 1st and 2nd harmonics of X, and 1/2 and 3/2 harmonic of N shown in Fig. 6-19b. This study is performed for all other Fr and similar harmonics are observed as shown in Fig. 6-20d. A snapshot of CFD solution for GM=0.033 m in one period is shown in Fig. 6-21.

6.4.2.3 NDA Model of Parametric Rolling

NDA model of 1DOF parametric rolling described in Eq. (2.49) is solved by OU and UNITS. Linear and cubic roll damping coefficients are estimated from INSEAN towing tank forward speed roll decay test at Fr=0.05, 0.2,and 0.35 using Himeno method, as a function of Fr. However, UNITS uses roll reconstruction to improve damping coefficients estimations for Fr=0.05 due to scattered EFD data at low Fr number. Fig. 6-22a and 6-23b show OU and UNITS damping coefficients. Fairly the same linear damping coefficients are used for OU and UNITS whereas UNITS cubic damping term at high Fr number is much smaller than that used in OU. Also, UNITS and OU cubic damping term versus Fr show opposite trend. The reason for OU and UNITS damping coefficient difference is that OU uses shifted EFD roll decay data to have zero roll angle at $t=\infty$ while UNITS estimates coefficients directly from EFD data. The restoring moment coefficients in calm water l'_n are estimated from fitting a polynomial curve of order N to Fr=0.0 hydrostatically computed restoring moment as a function of heel angle. OU fits 5^{th} order curve and UNITS fits 9^{th} order curve to hydrostatically computed restoring moment for $0 \le \phi \le 50$ deg. Fig. 6-22c shows restoring moment in calm water used for OU and UNITS. Even though UNITS uses higher order polynomial to represent restoring moment, it is close to OU model. Restoring arm in waves estimated from 2DOF heave-pitch for CFD and EFD at Fr=0.1,0.2,0.3, hydrostatic computation for OU at Fr=0.1,0.2,0.3 and 1DOF pitch hydrostatic computation for UNITS for 10 deg heeled ship at Fr=0.0 corrected for Fr=0.2 are shown in Fig. 6-23 as function of time. In order to compare OU and UNITS, the function $(GM_m + GM_a \cos(\omega_e t))\phi$ is fitted to restoring arm shown in Fig. 6-23. As shown in Fig. 6-24, GM_m used by UNITS is smaller than that for OU since UNITS GM_m is for Fr=0.0 and does not have speed effect. In fact, that is why it is constant versus Fr and it is close to GM_m value of EFD/OU at Fr=0.0. For GM_a, UNITS corrects GM_a for Fr=0.0 by using a constant value 1.386 to match it to OU data

for Fr=0.2 to consider speed effect on GM_a. However, it doesn't match GM_a to OU data for other Fr numbers, as shown in Fig. 6-24. CFD prediction of GM_m and GM_a are also shown in Fig. 6-24. CFD under predicts GM_m for Fr=0.1 and Fr=0.2 and under predicts GM_a for Fr=0.1. Lastly, OU uses speed independent ω_ϕ=4.39 rad/sec estimated from best fit to towing tank roll decay test data for Fr=0.05 and GM=0.038 m whereas UNITS applies ω_ϕ=4.062, 4.157, 4.348 rad/sec for Fr=0.05, 0.2, 0.35, respectively, estimated from towing tank roll decay test data for GM=0.038 m. Therefore OU model covers speed effect on total restoring moment through restoring arm in waves but UNITS model covers speed effect on total restoring moment through GM or ω_ϕ.

Nonlinear dynamics solutions of Eq. (2.49) for parametric rolling for OU and UNITS are shown on Fig. 6-25a,b,c. For GM=0.038 m, as shown in Fig. 6-25b, Poincaré mapping parametric roll appears at Fr=0.22 and disappears at Fr=0.37 in increasing direction (i), but it appears at 0.13 and disappear at 0.37 in decreasing direction (d). There is significant difference of roll angle from 0.13 to 0.22 in Fr, and this difference can be explained as a sub-critical bifurcation. This result indicates that initial value dependency of parametric roll of OT is significant and its steady state in sub-critical bifurcation region depends on initial condition significantly. The maximum stabilized roll angle is $\phi_{\max} \approx 30$ deg for Fr=0.2. Calculated region of parametric roll does not agree with EFD result perfectly, but this is expectable due to the approximated nature of the model in Eq. (2.49). Nevertheless the general agreement between instability regions predicted from Eq. (2.49) and results from EFD can be considered satisfactory. It is also to be taken into account that the effect of water on deck has to be accurately implemented in the model particularly in high Fr for quantitative prediction. OU averaging method agreement of roll amplitude in comparison with EFD result is not bad but stability of solutions is not so from 0.18 to 0.34 in Fr. Disagreement in stability of parametric roll between OU averaging and Poincaré mapping based on OU model could suggest that existence of other stable state outside the applicable range of the roll angle in the model. Note that

averaging method unstable solution means that such solution cannot be seen in a real experiment. The maximum stabilized roll angle $\phi_{max} \approx 27$ deg for Fr=0.34. UNITS averaging approach shows a region of instability for the upright position extending approximately from Fr=0.18 to Fr=0.3, with a maximum roll inside this region close to $\phi_{max} \approx 30$. In addition, the presence of a stable rolling motion is predicted also outside the linear instability region for the upright position, and a stable vertical equilibrium coexists with a stable rolling motion between Fr=0.05 and Fr=0.18, with a predicted maximum of about $\phi_{max} \approx 45$ at Fr=0.05. In this region where two stable solutions coexist the final steady state depends on the initial conditions. The comparison with EFD shows that the shape of the response curve (bending towards low Fr) is well predicted by the UNITS model (capturing the softening behaviour of the restoring), but the region of instability of the upright position is slightly shifted to lower Fr. This difference could be associated with the fact that in the UNITS model the restoring moment is speed independent, and the introduction of a speed dependence especially in GM_m following the indications in Fig. 6-24a, could have shifted the response curve to higher Fr. The sudden jump at reduced Fr seen in the EFD response curve can be interpreted as the occurrence of the Hopf bifurcation predicted by the UNITS model. It could be guessed that additional experiments with different initial conditions performed in the range of small Fr could have shown the coexistence of a stable roll motion of large amplitude together with the stable upright position. For GM=0.033 m (Fig. 6-25c), Poincaré mapping parametric roll are indicated for $0.12 \le Fr \le 0.35$ and $0.10 \le Fr \le 0.35$ for increasing and decreasing directions, respectively, with maximum stabilized roll angle $\phi_{max} \approx 22$ deg for Fr=0.2. OU averaging method parametric roll is indicated for $0.26 \le Fr \le 0.35$ with maximum stabilized roll angle $\phi_{max} \approx 25$ deg for Fr=0.26, as shown in Fig. 6-25c. The results from the UNITS model shows a response curve having a stable solution for $0.12 \le Fr \le 0.3$ with $\phi_{max} \approx 30$ and two stable solutions (trivial and nontrivial) along with one unstable solution between Fr=0.0 and Fr=0.12 with $\phi_{max} \approx 45$. The agreement between EFD and analytical predictions for the

UNITS model are, in this case, very satisfactory. The jump at Fr=0.07 seen in EFD seems to be due to the coexistence of two solutions, a trivial stable upright position and a nontrivial resonant roll as predicted by the analytical UNITS model. For GM=0.043 m, as shown in Fig. 6-25a, parametric roll is not indicated by EFD and OU but UNITS averaging method predicts the inception of parametric roll with two stable solutions coexisting with an unstable upright position in the range $0.14 \le Fr \le 0.23$ with $\phi_{\max} \approx 35$ for Fr=0.14, and a stable solution for $0.23 \le Fr \le 0.3$. The discrepancy between the analytical predictions from the UNITS model and the experiments are again to be sought in the fact that the UNITS model incorporates speed effects only partially with a tuning at Fr=0.2 for the amplitude of the GM variation and without any correction on the mean GM, as shown in Fig. 6-24. Tables 6-9 and 6-10 summarize and compare Mathieu equation and CFD and EFD estimates for mean and excitation GM and the instability ranges and stabilized roll angles from EFD, CFD, and NDA.

6.5 Summary of INSEAN Captive Model Simulations

Complementary CFD, towing tank EFD, and nonlinear dynamics approach study of roll decay/parametric roll for the OT surface combatant both with and without bilge keels is presented. The investigations without bilge keels include 2DOF forward speed roll decay in calm water for varying GM; and 3DOF forward speed roll decay/parametric roll in head waves for varying wave steepness Ak, GM, and drift angle. CFD shows fairly close agreement with EFD for forward speed roll decay in calm water, although damping is over/under predicted for largest/smaller GM. Most importantly CFD shows remarkably close agreement with EFD for forward speed roll decay/parametric roll in head waves for GM=0.038 and 0.033 m, although CFD predicts larger instability zones at high and low Fr, respectively. The CFD and EFD results are analyzed with consideration ship motion theory and compared with Mathieu equation and nonlinear dynamics approaches. Nonlinear dynamics approaches are in qualitative agreement with CFD and EFD. The

CFD and nonlinear dynamics approach results were blind in that the actual EFD radius of gyration k_{xx} was not known a priori.

Table 6-1: Boundary conditions for all the variables

	ϕ	p	k	ω	U	V	W
Inlet for waves	$A\cos(kx-2\pi ft)-z(x)$	$\frac{A}{Fr^2}e^{kz}\cos(kx-2\pi ft)-\frac{A^2}{2Fr^2k}e^{2kz}$	$k_{fs}=10^{-7}$	$\omega_{fs}=9$	$U(x,y,z,t)=U_0+\frac{A}{Fr}\sqrt{k}e^{kz}\cos(kx-2\pi f$	$V=0$	$W(x,y,z,t)=\frac{A}{Fr}\sqrt{k}e^{kz}\sin(kx-2\pi ft)$
Inlet for calm water	$-z(x)$	$\frac{\partial p}{\partial n}=0$	$k_{fs}=10^{-7}$	$\omega_{fs}=9$	$U=U_0$	$V=0$	$W=0$
Exit	$\frac{\partial\phi}{\partial n}=0$	$\frac{\partial p}{\partial n}=0$	$\frac{\partial k}{\partial n}=0$	$\frac{\partial\omega}{\partial n}=0$	$\frac{\partial^2 U}{\partial n^2}=0$	$\frac{\partial^2 V}{\partial n^2}=0$	$\frac{\partial^2 W}{\partial n^2}=0$
Sides	$\frac{\partial\phi}{\partial n}=0$	$\frac{\partial p}{\partial n}=0$	$\frac{\partial k}{\partial n}=0$	$\frac{\partial\omega}{\partial n}=0$	$\frac{\partial U}{\partial n}=0$	$\frac{\partial V}{\partial n}=0$	$\frac{\partial W}{\partial n}=0$
Bottom	$\frac{\partial\phi}{\partial n}=1$	$\frac{\partial p}{\partial n}=0$	$\frac{\partial k}{\partial n}=0$	$\frac{\partial\omega}{\partial n}=0$	$U=1$	$V=0$	$W=0$
Top	$\frac{\partial\phi}{\partial n}=-1$	$\frac{\partial p}{\partial n}=0$	$\frac{\partial k}{\partial n}=0$	$\frac{\partial\omega}{\partial n}=0$	$\frac{\partial U}{\partial n}=0$	$\frac{\partial V}{\partial n}=0$	$\frac{\partial W}{\partial n}=0$
Ship hull	$\frac{\partial\phi}{\partial n}=0$	Poisson Eq.	$k=0$	$\omega=\frac{60}{\mathrm{Re}\,\beta y}$	$U=0$	$V=0$	$W=0$

Table 6-2: Summary of 2DOF zero-speed heave-roll in beam waves results for Ak=0.156 and λ/L=1.12

	EFD				CFD				E % D				
	a_1	a_2/a_1	a_3/a_1	a_4/a_1	a_1	a_2/a_1	a_3/a_1	a_4/a_1	a_1	a_2	a_3	a_4	Phase Error for domnant harmonic deg
z/A	1.07	0.07	-	-	1.22	0.05	-	-	-14.02	24.05	-	-	3.08
θ/Ak	2.90	0.08	-	-	1.66	0.07	-	-	42.76	43.44	-	-	6.11
X	1.7E-3	2.25	0.48	1.52	5.6E-4	0.70	0.38	0.20	67.48	89.82	73.80	95.63	24.13
Y	0.067	0.05	-	-	0.053	0.10	-	-	20.89	-52.82	-	-	5.12
M	2.4E-4	1.69	0.17	0.10	1.1E-4	1.58	0.24	-	53.39	56.50	34.20	100	-24.61
N	5.9E-4	0.13	-	-	7.3E-4	0.19	-	-	-23.77	-81.58	-	-	17.42

Table 6-3: Summary of 3DOF forward-speed heave-roll-pitch in head waves results for λ/L=1.0 and Fr=0.35

	EFD Ak=0.115				CFD Ak=0.115 Ak=0.156			
	a_1	a_2/a_1	a_3/a_1	a_4/a_1	a_1	a_2/a_1	a_3/a_1	a_4/a_1
z/A	0.8601	0.06	0.005	0.005	0.8762 0.78	0.04 0.05	0.022 0.019	0.014 0.011
θ/Ak	0.4463	0.06	0.02	0.01	0.4012 0.374	0.07 0.08	0.02 0.03	0.008 0.012
X	0.0087	0.49	0.53	0.24	0.0042 0.0048	1.01 1.21	0.93 0.97	0.02 0.21
	$a_{1/2}$	$a_{3/2}/a_{1/2}$	$a_{5/2}/a_{1/2}$	$a_{7/2}/a_{1/2}$	$a_{1/2}$	$a_{3/2}/a_{1/2}$	$a_{5/2}/a_{1/2}$	$a_{7/2}/a_{1/2}$
Y	0.0004	4.5	0.98	3.25	0.0004 0.0005	0.51 0.53	1.5 1.7	0.25 1.23
N	0.0003	1.01	0.01	0.01	0.0026 0.0032	0.89 1.03	0.27 0.48	0.23 1.41
	ϕ_1	$f_{\phi dl}$& $f_{\phi ds}$	α&γ	δ&ER	ϕ_1	$f_{\phi dl}$& $f_{\phi ds}$	α&γ	δ&ER
ϕ	$.4\phi_0$	$.91f_{\phi h}/f_e$	0.55/0.005	0.82/5.2	$.5\phi_0$ $.33\phi_0$	$.89f_{\phi h}/f_e$ $.74f_{\phi h}/f_e$	0.4/0.006 0.7/0.009	0.6/3.3 0.9/6.0

Table 6-4: CFD roll decay RSS error for all k_{xx}

GM=0.043	**Fr**	**No. of cycles analysis**	**Ave ϕ/ϕ_0 for adjusted k_{xx}**	**E_{RSS}**				
				k_{xx}= 0.1124	**k_{xx}= 0.1246**	**k_{xx}= 0.1269**	**k_{xx}= 0.1298**	**k_{xx}= 0.1322**
Case No. 1	0.2	6	0.16599	15.76%	8.49%	7.21%	5.92%	11.83%
GM=0.038				**k_{xx}= 0.1246**	**k_{xx}= 0.1322**	**k_{xx}= 0.146**		
1	0.05	6	0.25781	7.1%				
2	0.2	6	0.17108	3.7%	11.42%	127%		
3	0.35	6	0.13014	9.33%				
GM=0.033				**k_{xx}= 0.1289**	**k_{xx}= 0.1315**	**k_{xx}= 0.1388**		
1	0.2	4	0.20216	12.76%	12.51%	11.28%		

Table 6-5: Summary of roll decay damping coefficients

		EFD				CFD			
GM	Fr	α	$n\omega_d$	α_e	γ	α	$n\omega_d$	α_e	γ
GM=0.033	0.05	0.23	0.24	0.24	0.14				
	0.2	0.34	0.37	0.36	0.24	0.12	0.20	0.20	0.08
	0.35	0.35	0.59	0.67	1.29				
GM=0.038	0.05	0.19	0.19	0.19	0.04	0.09	0.10	0.10	0.026
	0.2	0.31	0.31	0.32	0.08	0.18	0.19	0.18	0.08
	0.35	0.34	0.40	0.40	0.18	0.25	0.27	0.28	0.11
GM=0.043	0.05	0.14	0.14	0.14	0.03				
	0.2	0.23	0.24	0.23	0.05	0.23	0.24	0.24	0.08
	0.35	0.28	0.28	0.28	0.02				

Table 6-6: Roll reconstruction error for different methods

GM=0.043	Fr	Number of cycles analysis	Ave ϕ/ϕ_0	E_{RSS}			
				α & γ	α_e	$n\omega\phi_d$	α & γ With linear restoring
Case No. 1	0.05	6	0.14623	10.66%	11.15%	11.59%	30.02%
2	0.2	6	0.09326	6.81%	7.39%	7.59%	15.05%
3	0.35	6	0.07692	4.36%	5.17%	5.41%	10.13%
Ave. of 1,2,3	0.2	6	0.105	7.3%	7.9%	8.2%	18.4%
GM=0.038							
1	0.05	6	0.2787	7.28%	7.23%	7.42%	25.18%
2	0.2	6	0.2131	4.77%	4.78%	4.80%	13.49%
3	0.35	6	0.15026	8.35%	8.26%	8.38%	12.03%
Ave. of 1,2,3	0.2	6	0.21402	6.80%	6.75%	6.82%	16.9%
GM=0.033							
1	0.05	4	0.22626	4.90%	6.06%	6.14%	16.88%
2	0.2	4	0.18197	4.13%	4.84%	4.91%	12.24%
3	0.35	4	0.12662	5.07%	5.32%	5.34%	10.49%
Ave. of 1,2,3	0.2	4	0.1783	4.7%	5.41%	5.47%	13.2%

Table 6-7: Uncertainty analysis for GM = 0.038 m, Fr = 0.20, and Ak=0.115

	Average	Amplitude	U	U %
Z (mm)	-1.3	34.5	2.1	6.1%
θ^0	-0.91	4.25	0.15	3.5%
ϕ^0	-0.16	35.9	0.97	2.7%
X (N)	21.15	51.8	5.6	10.9%
Y (N)	-1.53	212.4	4.53	2.1%
N (N.m)	0.01	55.0	1.48	3.0%

Table 6-8: Uncertainty analysis for GM = 0.033 m, Fr = 0.10, and Ak=0.115

	Average	Amplitude	U	U %
Z (mm)	0.6	22.2	2.31	10.4%
θ^0	-0.6	3.77	0.14	3.7%
ϕ^0	0.23	35.9	1.24	3.4%
X (N)	7.28	37.0	2.95	11.5%
Y (N)	0.06	143.8	2.90	2.0%
N (N.m)	0.66	55.6	1.47	2.6%

Table 6-9: CFD, EFD, and hydrostatic estimates for GM_m and GM_a at Fr=0.2

	GM=0.033			GM=0.038			GM=0.043 m		
Method	k_{xx}	GM_m	GM_a	k_{xx}	GM_m	GM_a	k_{xx}	GM_m	GM_a
CFD	0.1388	-0.0051	0.014	0.153 0.1246	-0.0058 -0.0058	0.014 0.014	0.153 0.1298	-0.0066 -0.0066	0.014 0.014
EFD (OU)	0.1330	-0.0039	0.012	0.1330	-0.0045	0.012	0.1330	-0.0051	0.012
Hydrostatic (UNITS)	0.1401	-0.0097	0.0086	0.1468	-0.0111	0.0086	0.1498	-0.0126	0.0086
Hydrostatic (UNITS)-corrected	0.1401	-0.0097	0.012	0.1468	-0.0111	0.012	0.1498	-0.0126	0.012

Table 6-10: Parametric rolling zone and max roll angle predicted by CFD, EFD, NDA, and Mathieu Equation

	GM=0.033 m				GM=0.038 m				GM=0.043 m			
Method	kxx	Fr range Min	Fr range Max	Max roll (deg)	kxx	Fr range Min	Fr range Max	Max roll (deg)	kxx	Fr range Min	Fr range Max	Max roll (deg)
CFD	0.1388	0.0	0.3	50	0.153 0.1246	0.17 0.18	0.44	capsize 45	0.153 0.1298	0.1 No PR	0.35	37 -
EFD	0.127	0.07	0.28	40	0.125	0.18	0.35	35	0.123	No PR		-
NDA_OU: Poincare' Increasing (i) Increasing (d)	0.1330	(i) 0.12 (d) 0.10	0.35 0.35	22	0.1330	(i) 0.22 (d) 0.13	0.37 0.37	30	0.1330	No PR		-
NDA_OU: Ave.	0.1330	0.26	0.35	25	0.1330	0.34	0.37	27	0.1330	No PR		-
NDA_UNITS: Ave.	0.1401	0.0	0.3	45	0.1468	0.05	0.30	45	0.1498	0.14	0.3	35
Mathieu Eq.	0.1388	0.0	0.26	∞	0.1246	0.07	0.41	∞	0.1298	0.07	0.41	∞

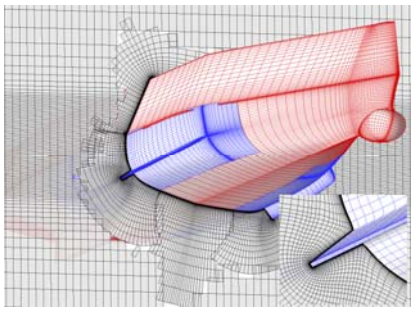

Figure 6-1: Grid for ONR Tumblehome with bilge keels

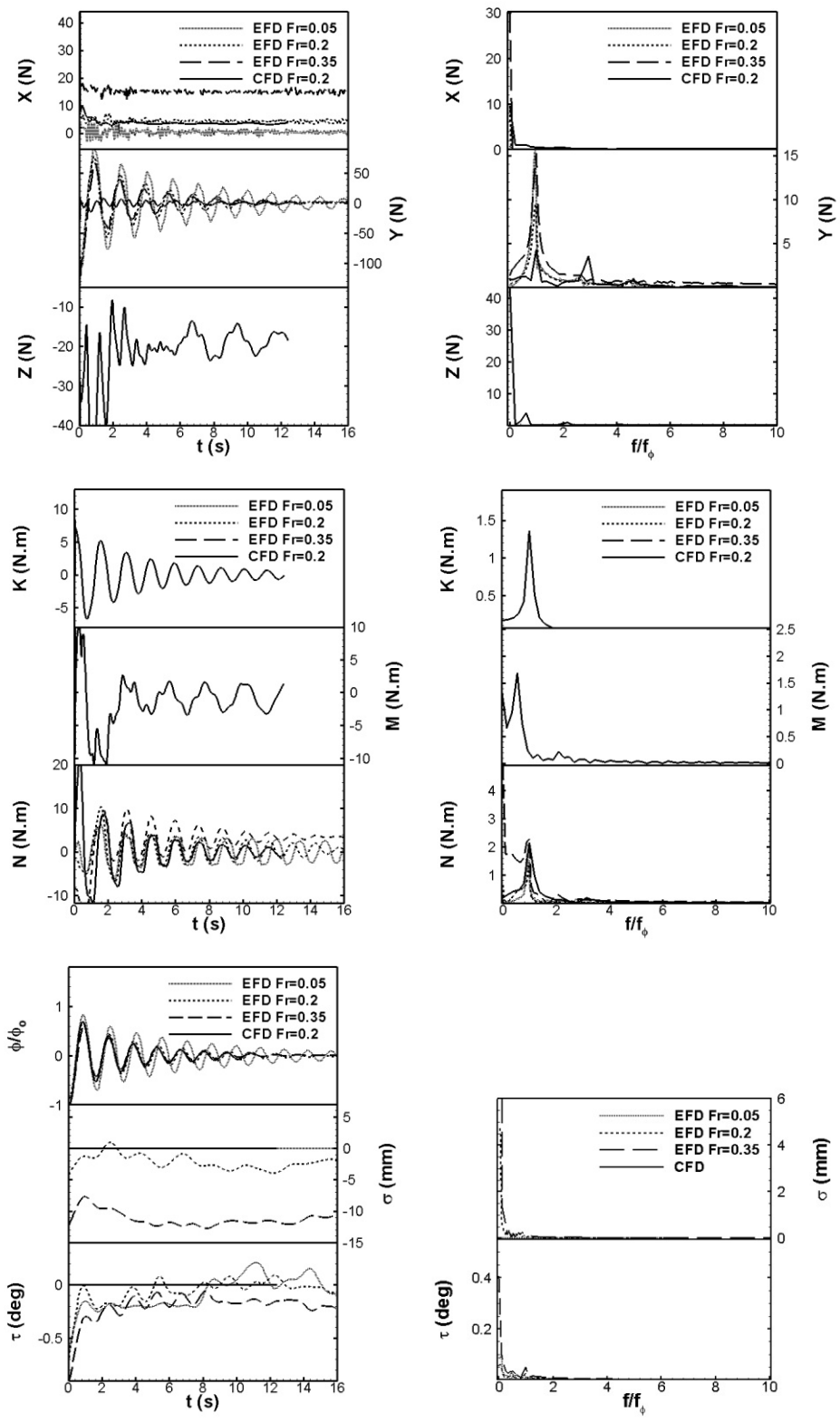

Figure 6-2: CFD (Fr=0.2) and EFD (Fr=0.05, 0.2, 0.35) roll decay comparison for GM=0.043 m: (a) time history; (b) FFT

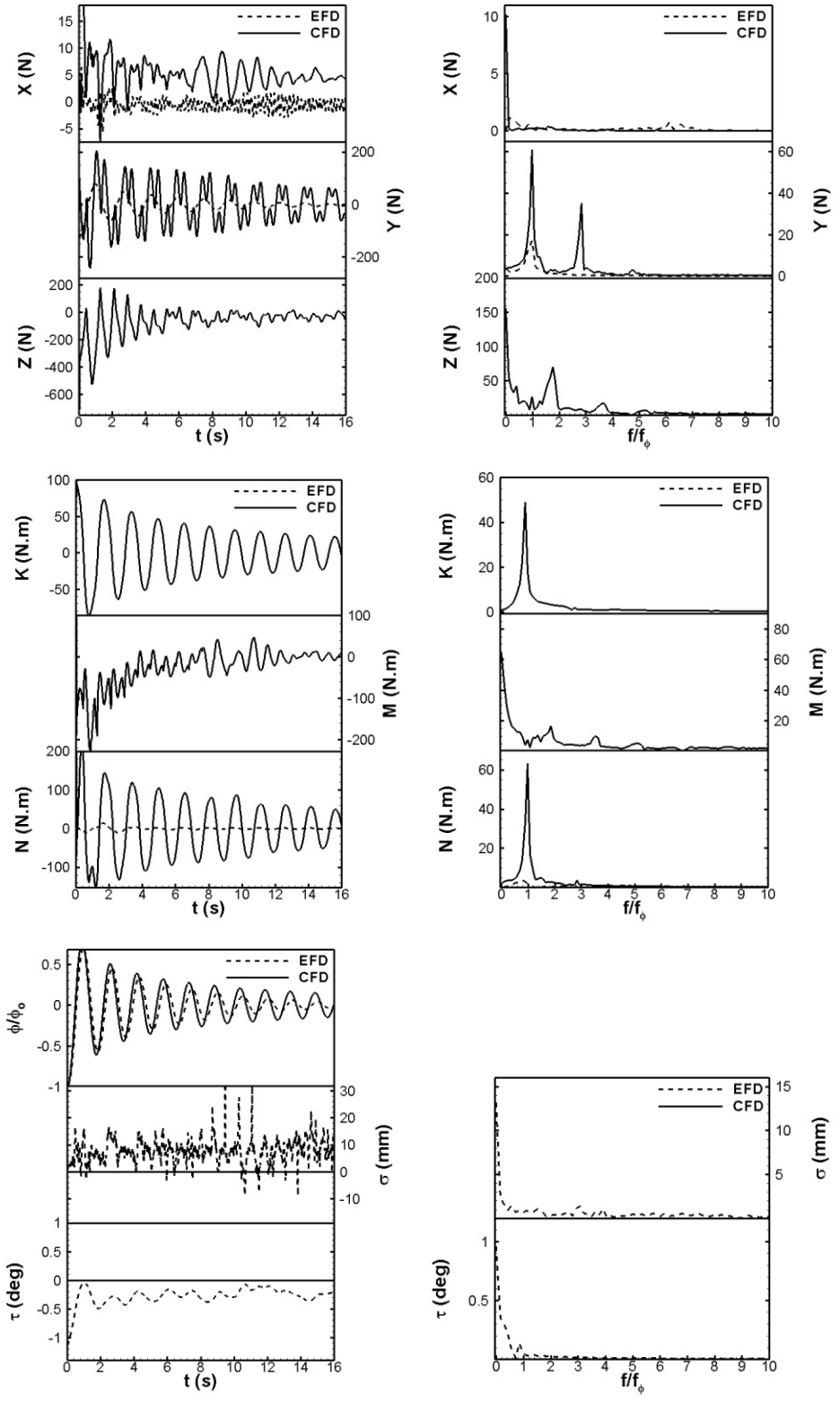

Figure 6-3: CFD and EFD roll decay comparison for GM=0.038 m and Fr=0.05: (a) time history; (b) FFT

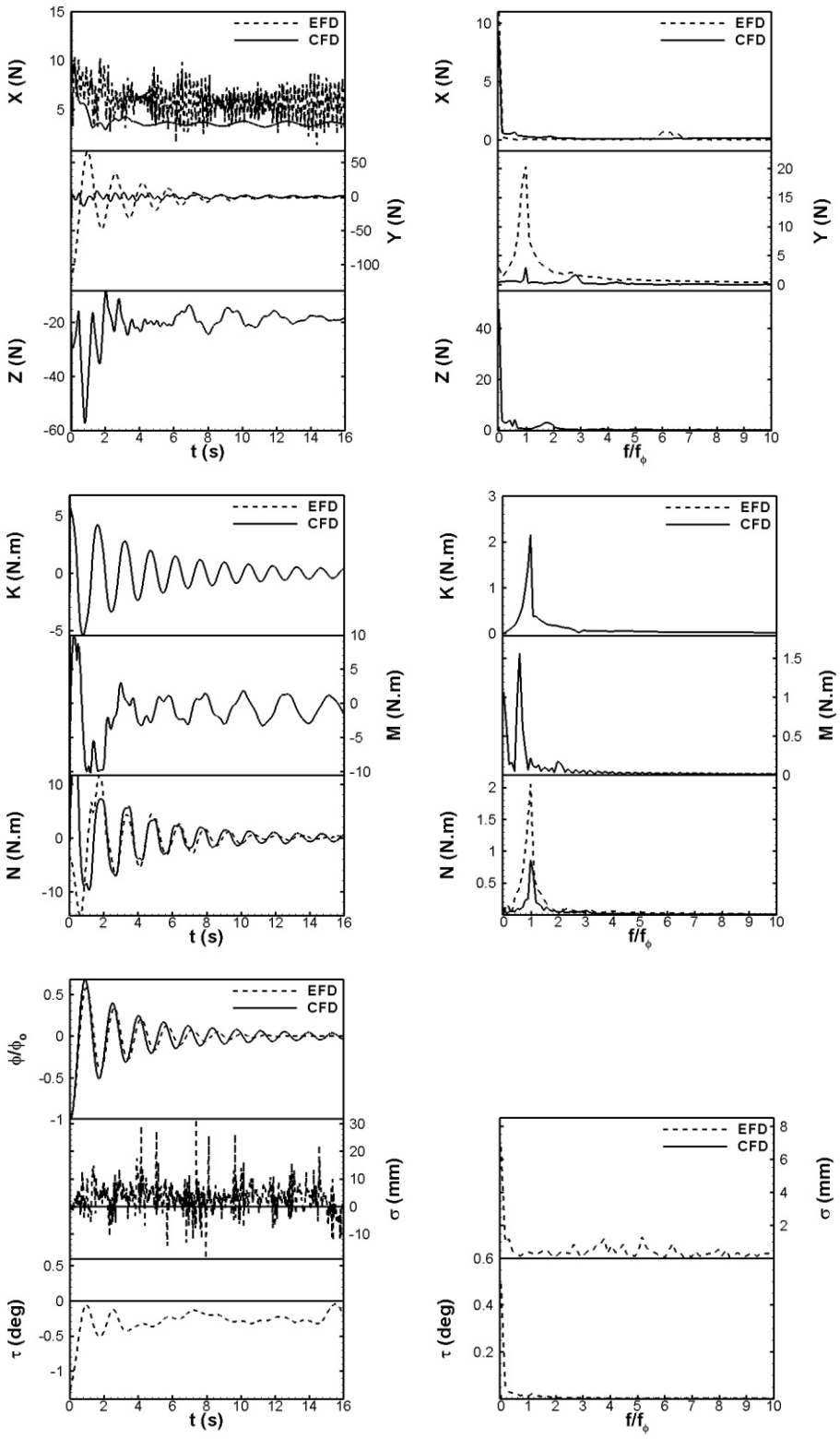

Figure 6-4: CFD and EFD roll decay comparison for GM=0.038 m and Fr=0.2: (a) time history; (b) FFT

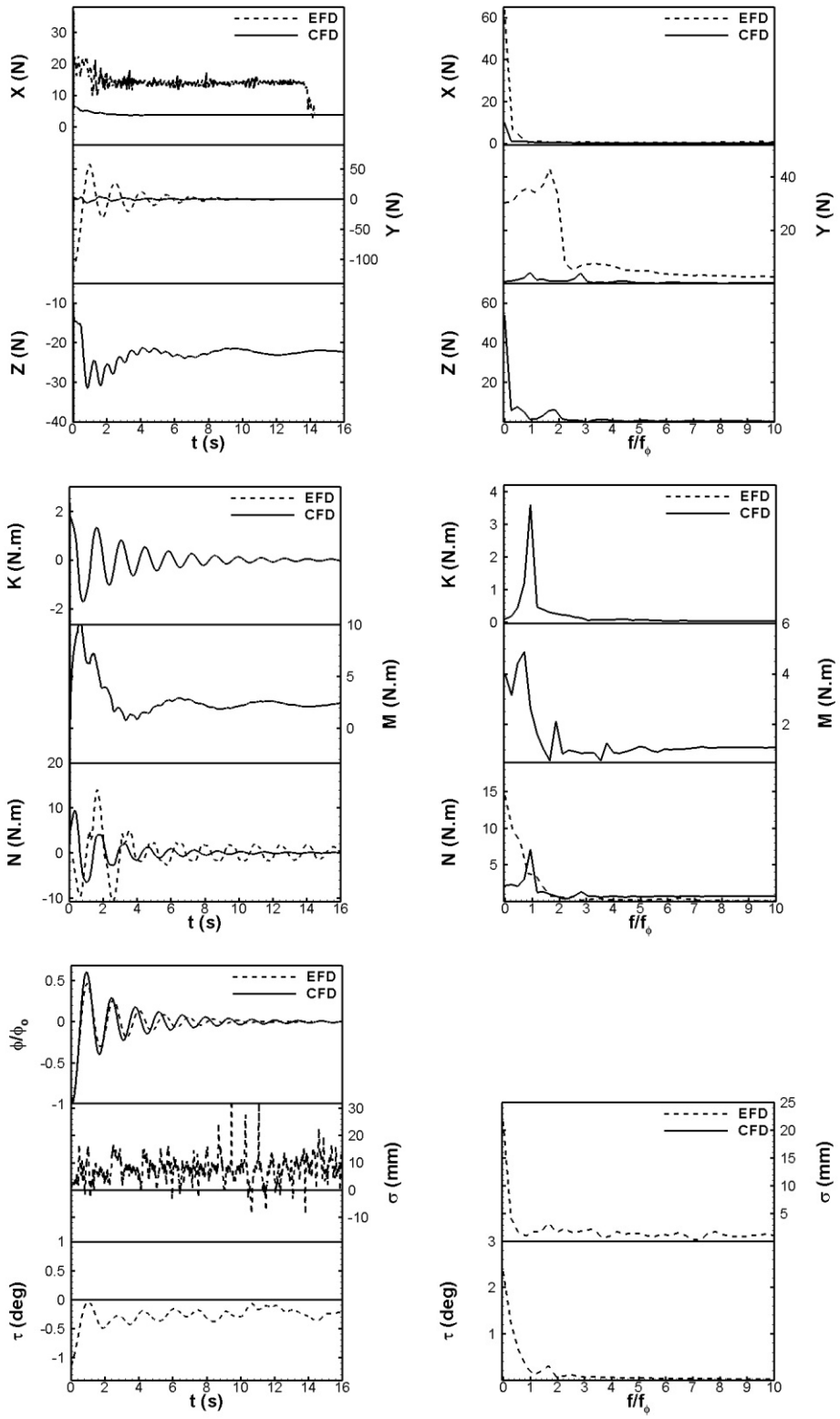

Figure 6-5: CFD and EFD roll decay comparison for GM=0.038 m and Fr=0.35: (a) time history; (b) FFT

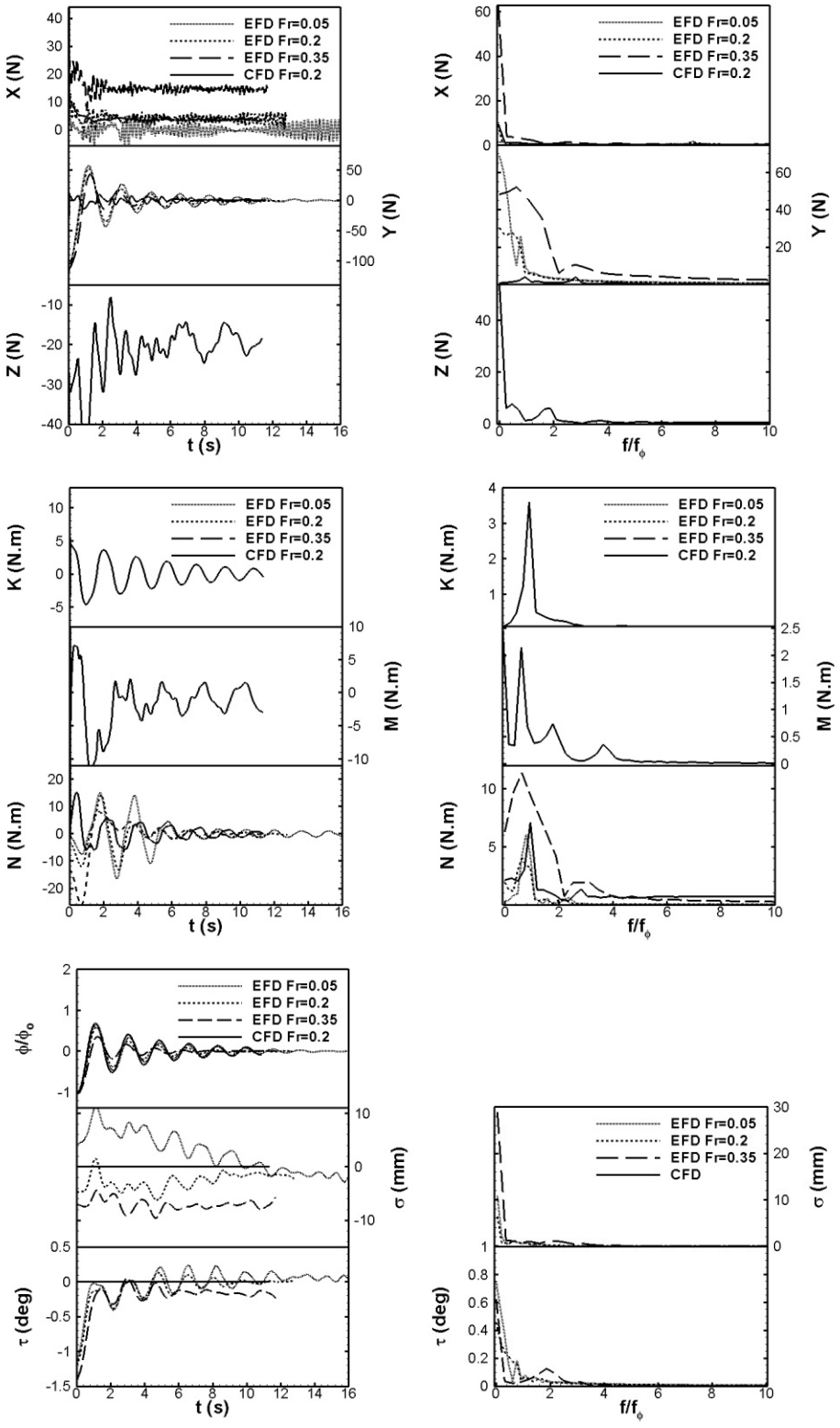

Figure 6-6: CFD (Fr=0.2) and EFD (Fr=0.05, 0.2, 0.35) roll decay comparison for GM=0.033 m: (a) time history; (b) FFT

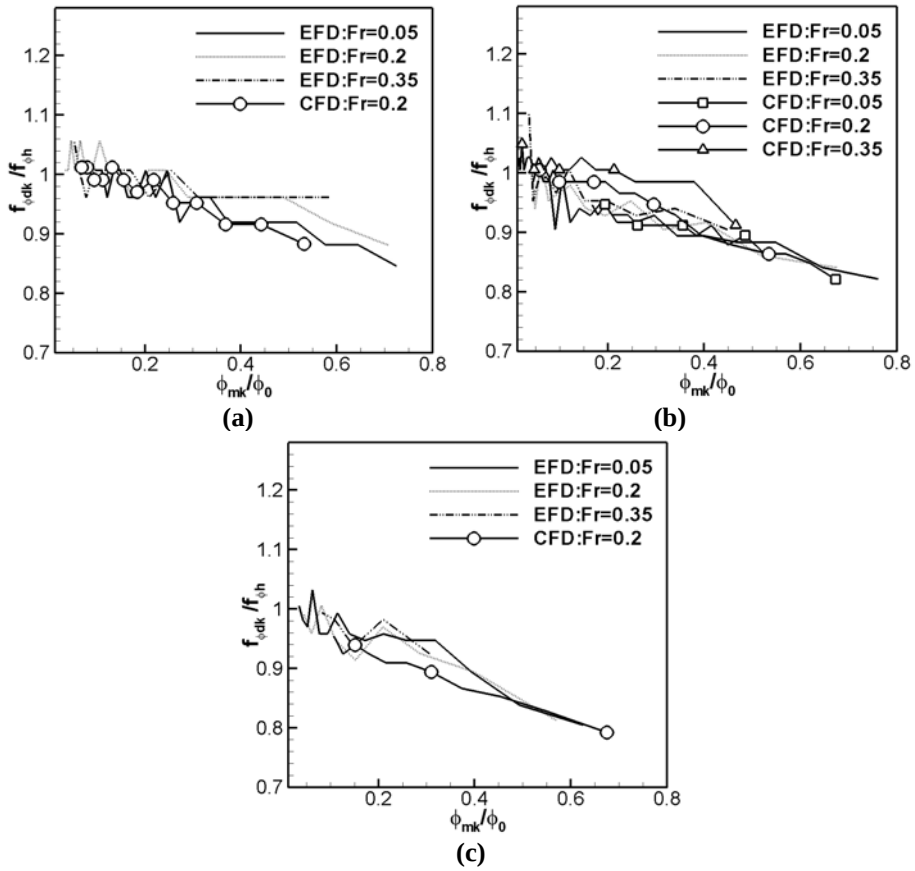

Figure 6-7: CFD and EFD damped natural frequency vs. mean roll angle: (a) GM=0.043 m; (b) GM=0.038 m; (c) GM=0.033 m

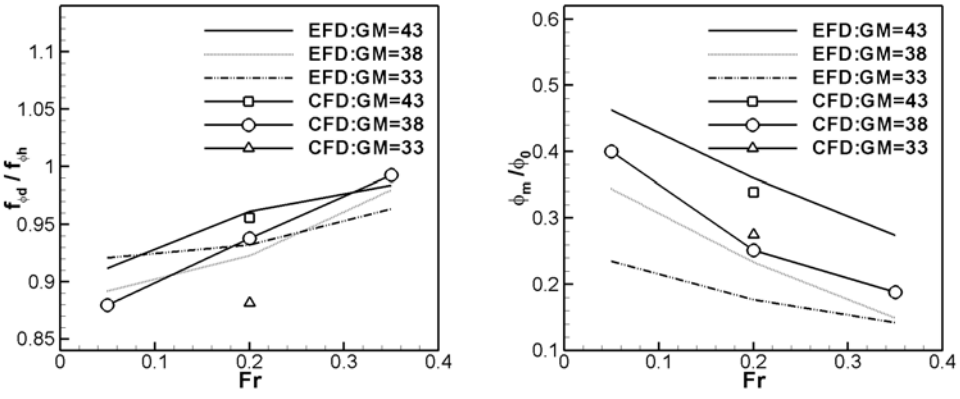

Figure 6-8: CFD and EFD averaged damped natural frequency and mean roll angle vs. Fr: (a) $\omega_{\phi d}$; (b) ϕ_m

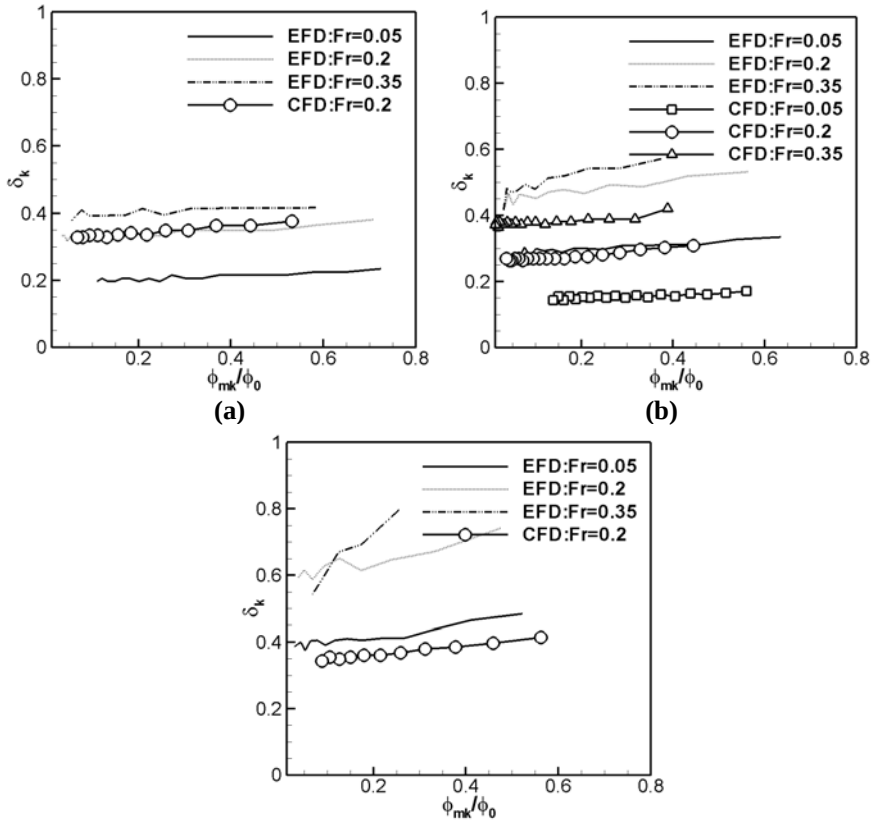

Figure 6-9: CFD and EFD logarithmic decrement vs. mean roll angle: (a) GM=0.043 m; (b) GM=0.038 m; (c) GM=0.033 m

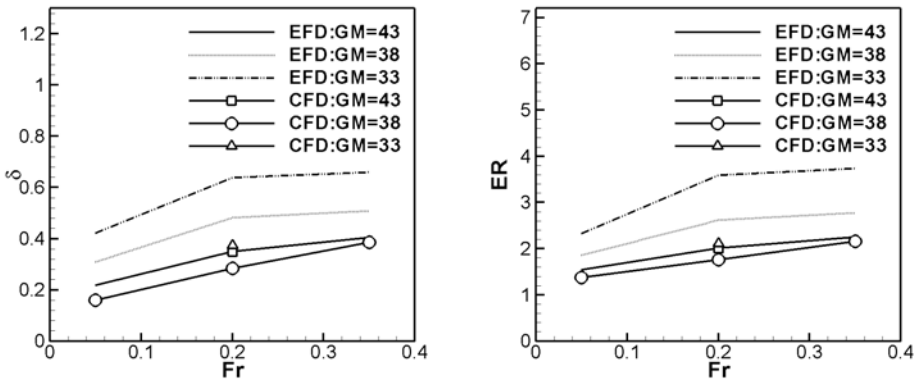

Figure 6-10: CFD and EFD mean roll averaged logarithmic decrement and ER vs. Fr: (a) δ; (b) ER

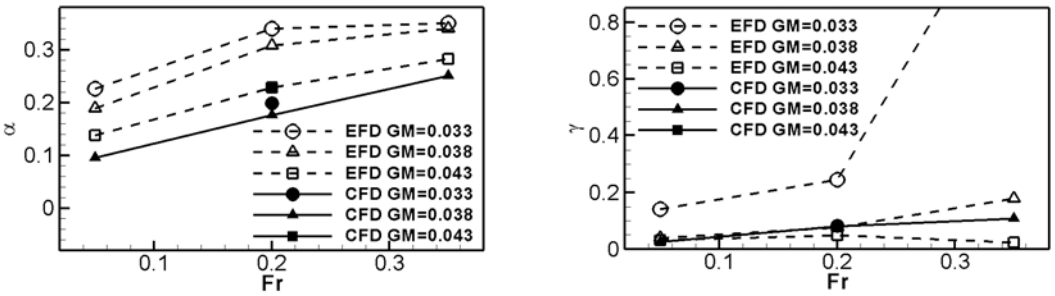

(a) **(b)**

Figure 6-11: CFD and EFD damping coefficients: (a) linear term, (b) cubic term

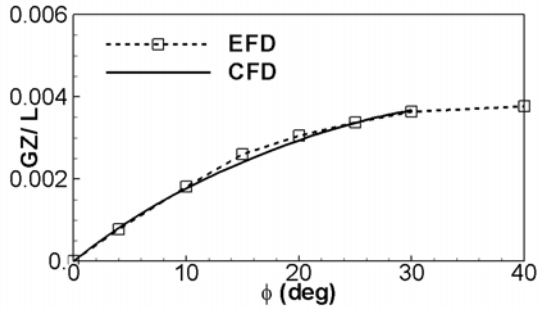

Figure 6-12: CFD and EFD roll restoring moment for GM=0.043 m

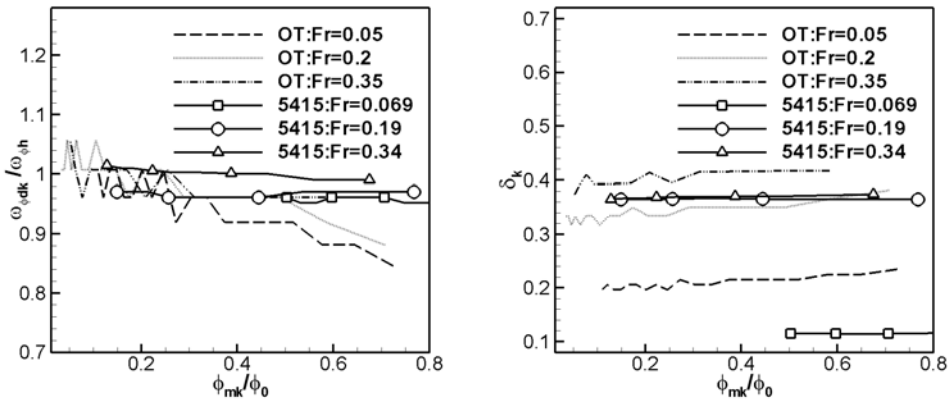

(a) **(b)**

Figure 6-13: OT and 5415 damped natural frequency and logarithmic decrement vs. mean roll angle: (a) $\omega_{\phi dk}$; (b) δ_k

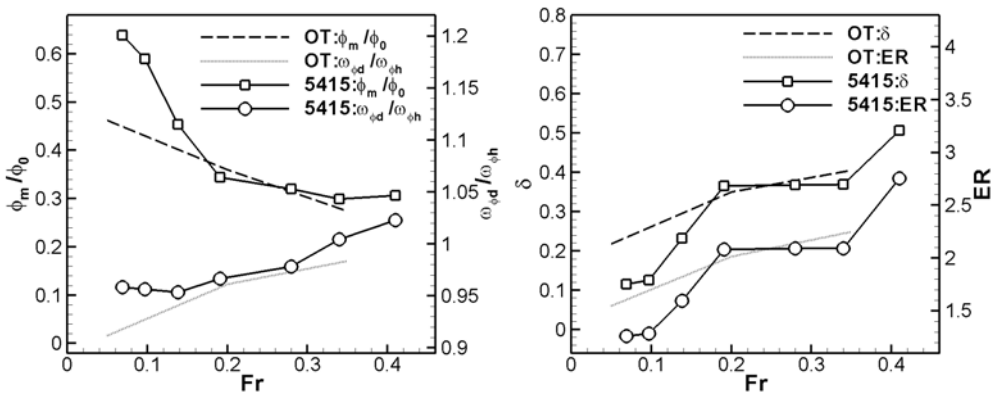

(a) **(b)**

Figure 6-14: OT and 5415 roll decay parameters vs. Fr: (a) ϕ_m and $\omega_{\phi dk}$; (b) δ and ER

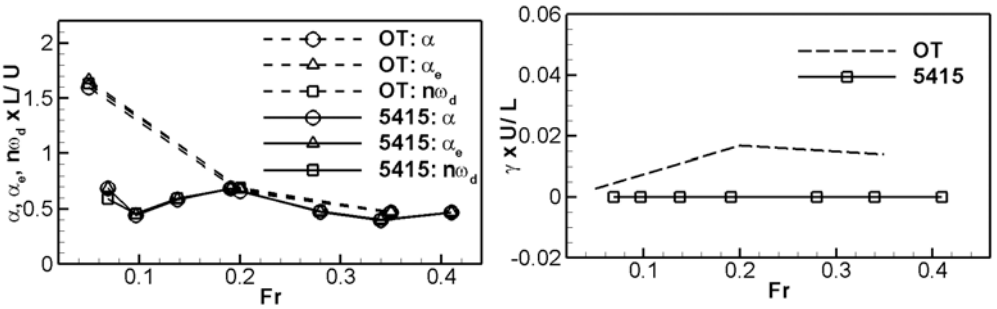

(a) **(b)**

Figure 6-15: OT and 5415 roll decay coefficients vs. Fr: (a) linear damping; (b) cubic damping

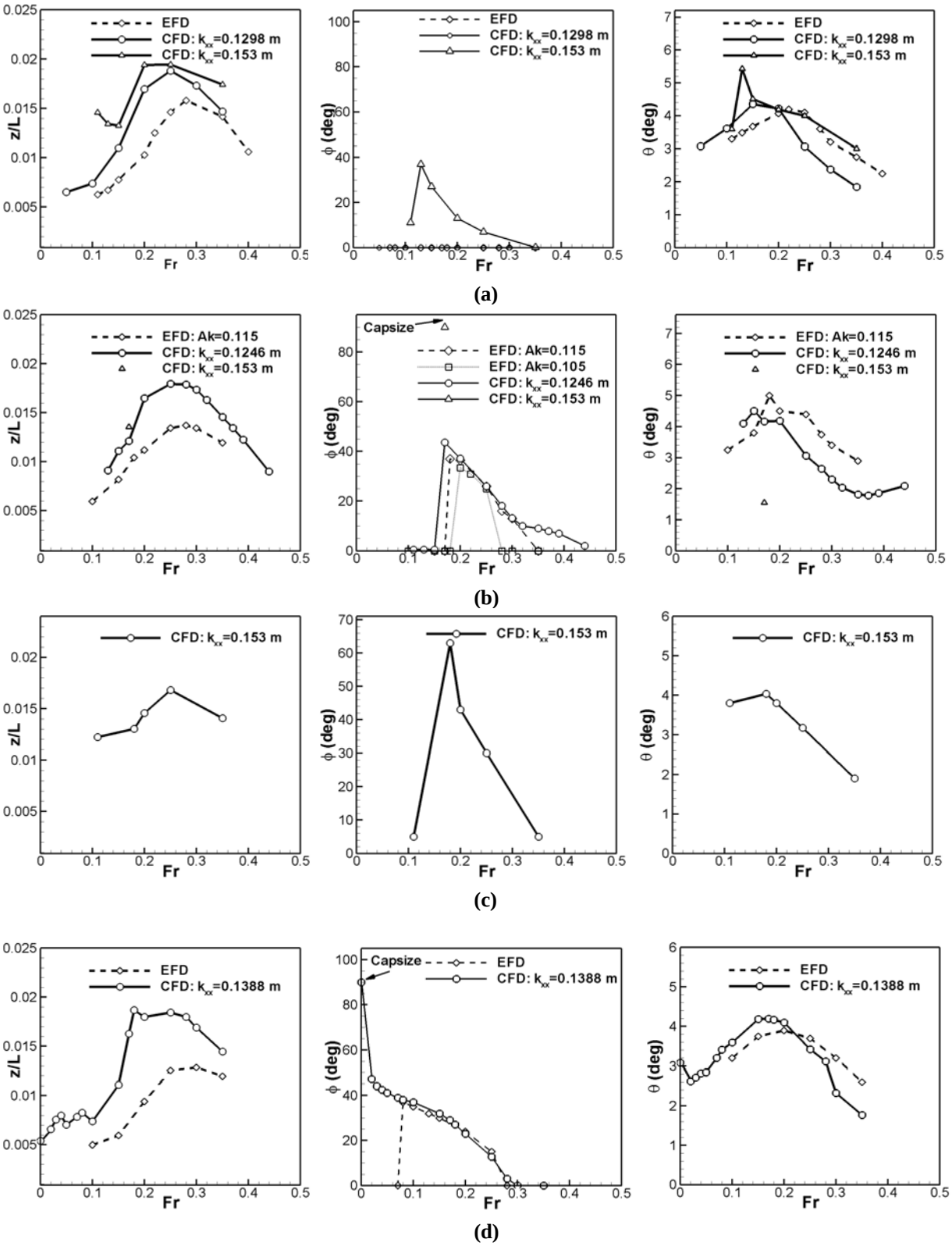

Figure 6-16: CFD and EFD parametric rolling motions for all GM: (a) GM=0.043 m; (b) GM=0.038 m; (c) GM=0.048m; (d) GM=0.033 m

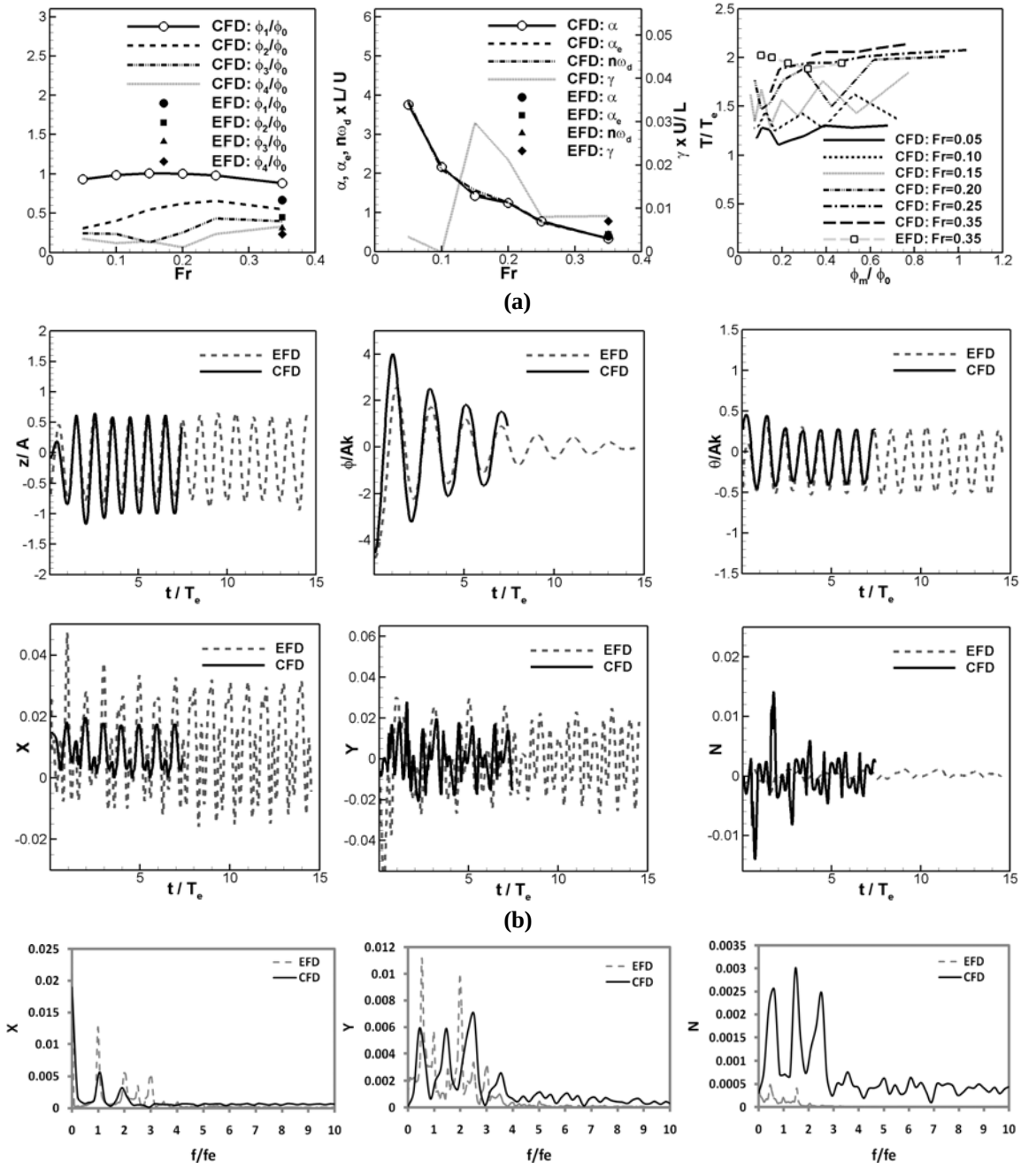

Figure 6-17: EFD and CFD (k_{xx}=0.1298) parametric rolling results for GM=0.043 m: (a) CFD roll decay parameters; (b) time history comparison for Fr=0.35; (c) FFT comparison for Fr=0.35

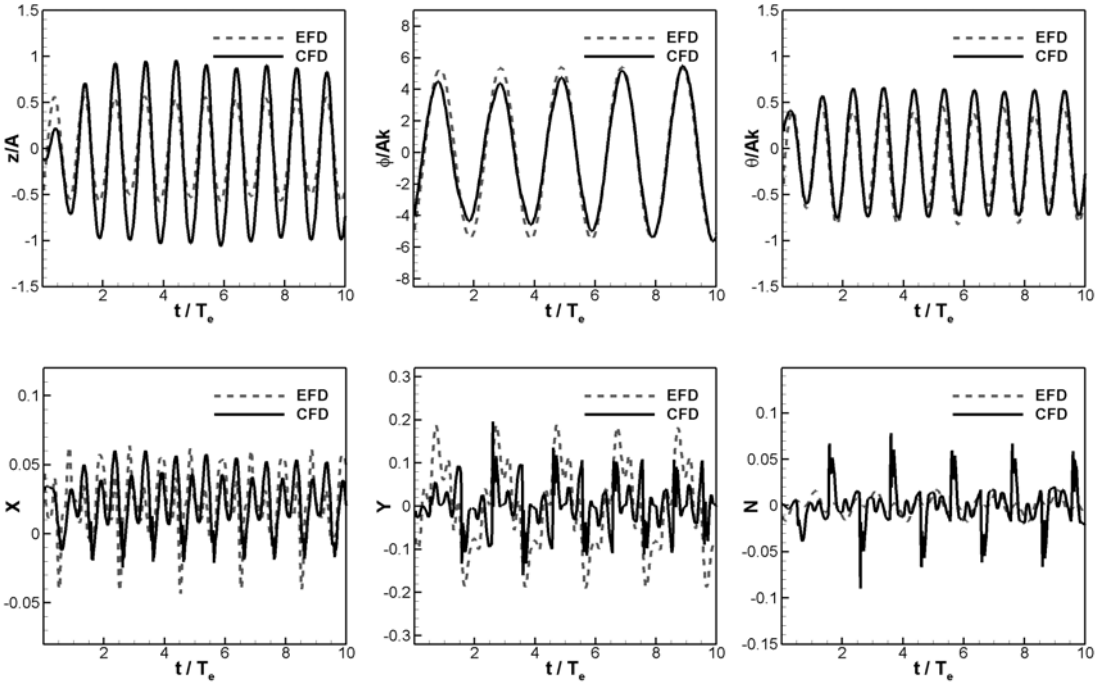

(a)

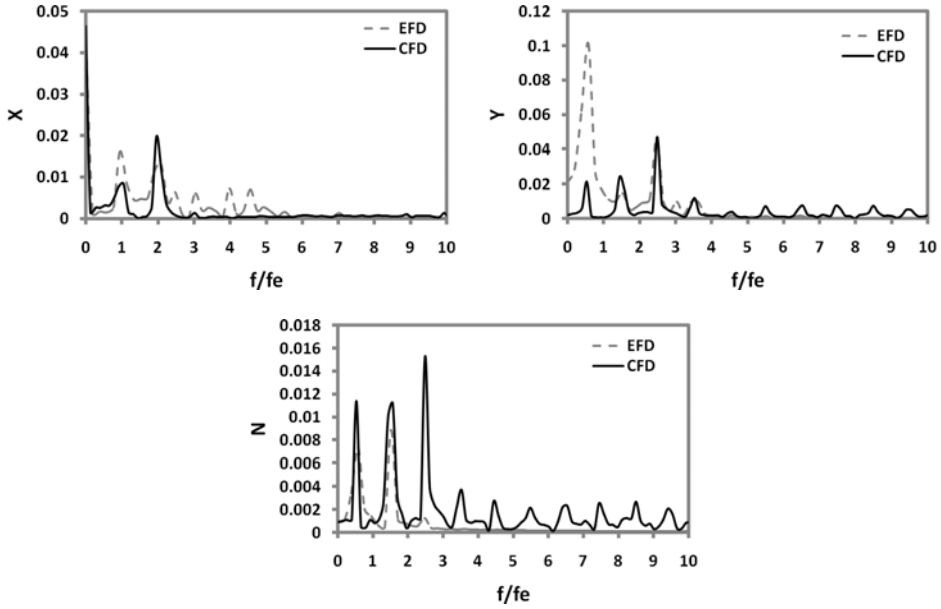

(b)

Figure 6-18: EFD and CFD (k_{xx}=0.1246) parametric rolling results for GM=0.038 m: (a) time history comparison for Fr=0.2; (b) FFT comparison for Fr=0.2

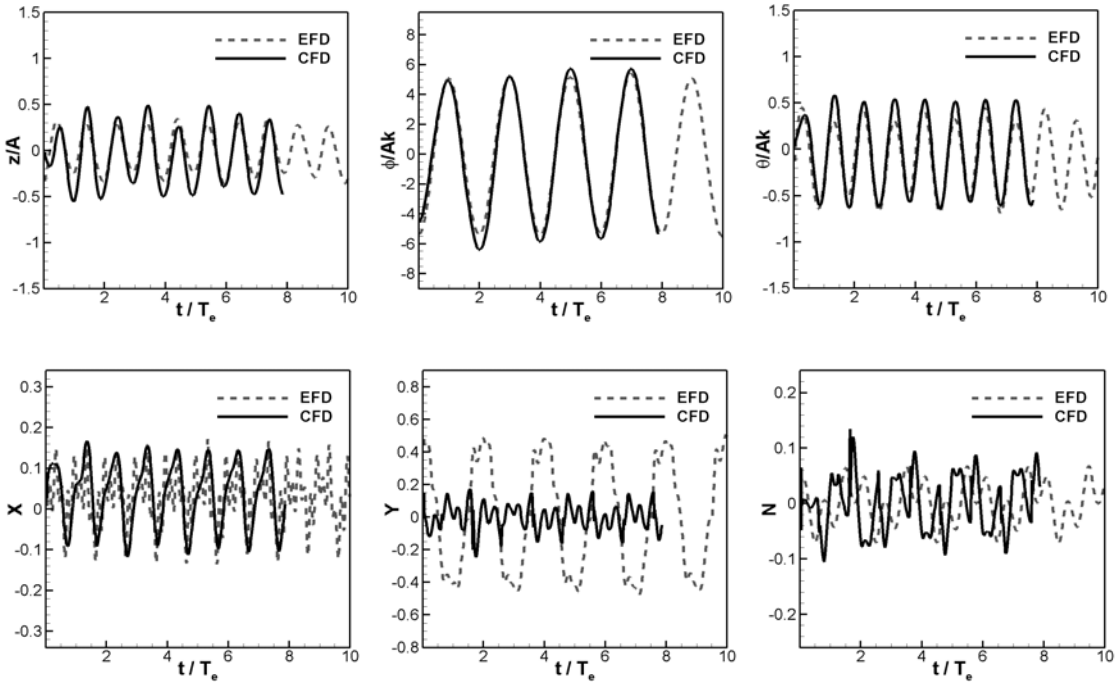

(a)

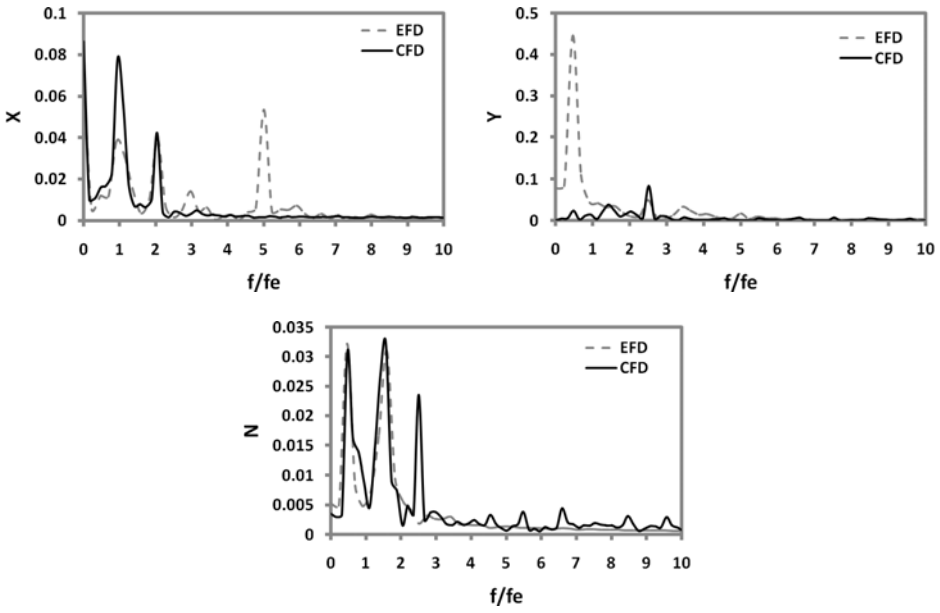

(b)

Figure 6-19: EFD and CFD (k_{xx}=0.1388) parametric rolling results for GM=0.033 m: (a) time history comparison for Fr=0.1; (b) FFT comparison for Fr=0.1

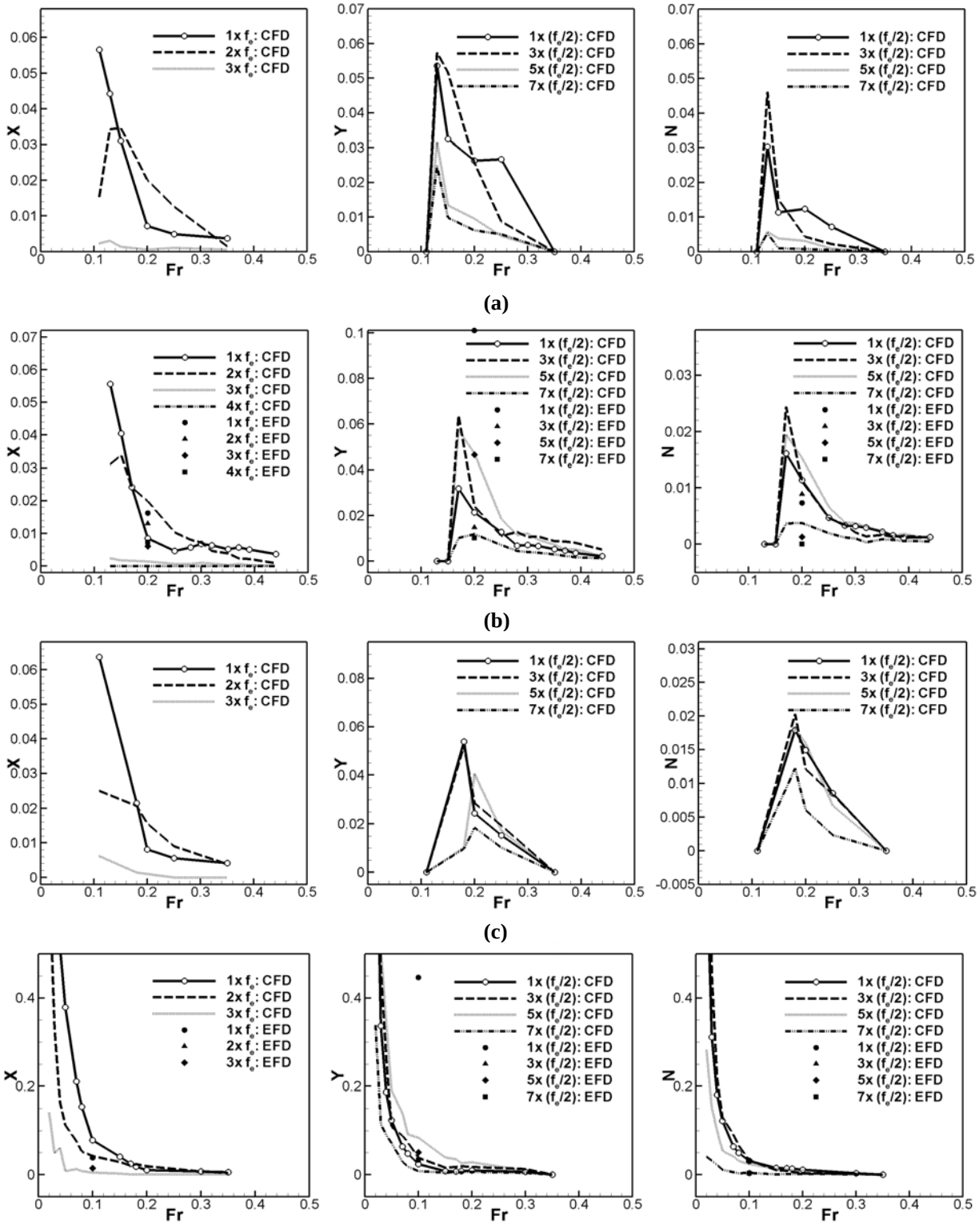

Figure 6-20: FFT analysis for CFD and EFD cases with parametric rolling: (a) GM=0.043 m; (b) GM=0.038 m; (c) GM=0.048 m; (d) GM=0.033 m

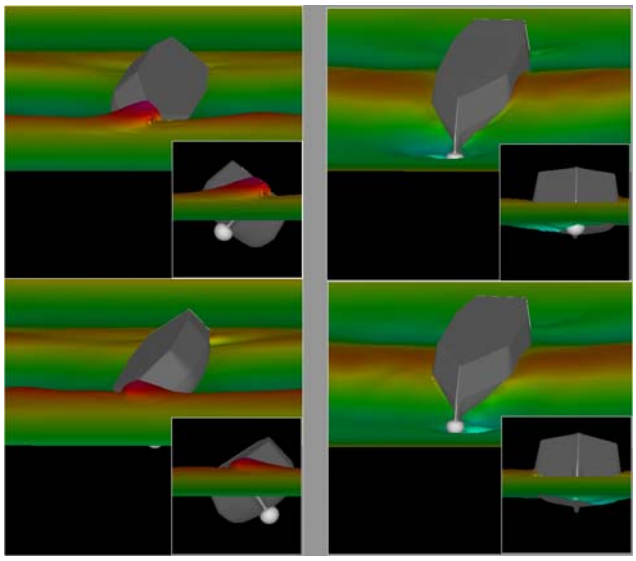

Figure 6-21: A snapshot of CFD solution for GM=0.033 m and Fr=0.1 in one roll period

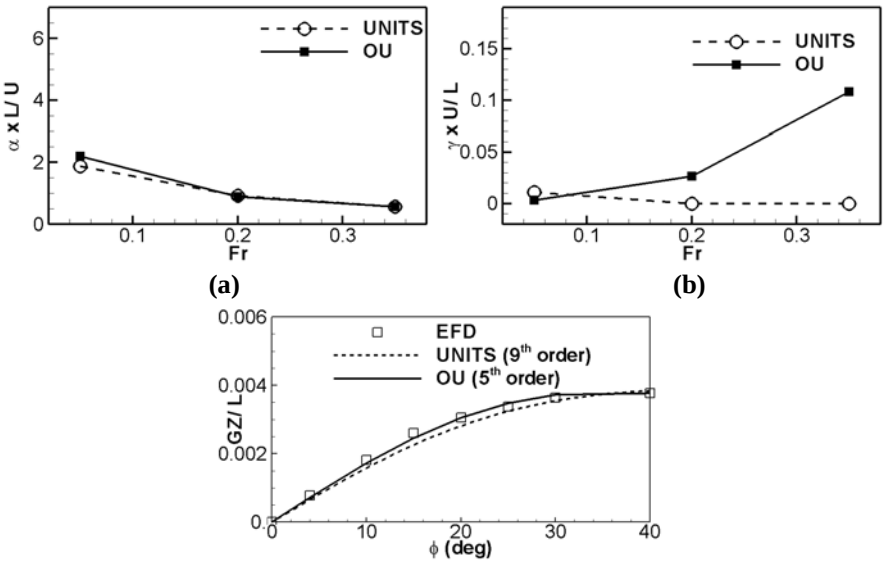

Figure 6-22: OU and UNITS model parameters: (a) linear damping coefficient as a function of Fr; (b) cubic damping coefficient as a function of Fr; (c) calm water restoring moment

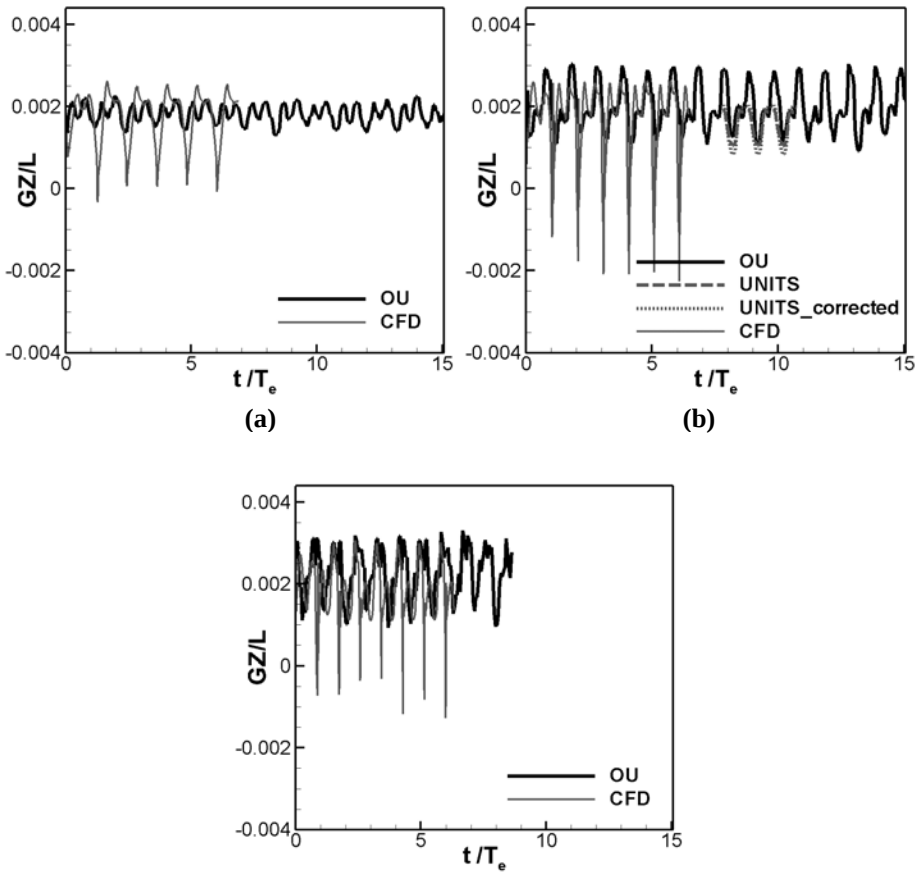

Figure 6-23: GZ variation in head waves for GM=0.043 m and 10 deg heel angle for OU and UNITS model and CFD: (a) Fr=0.1; (b) Fr=0.2; (c) Fr=0.3

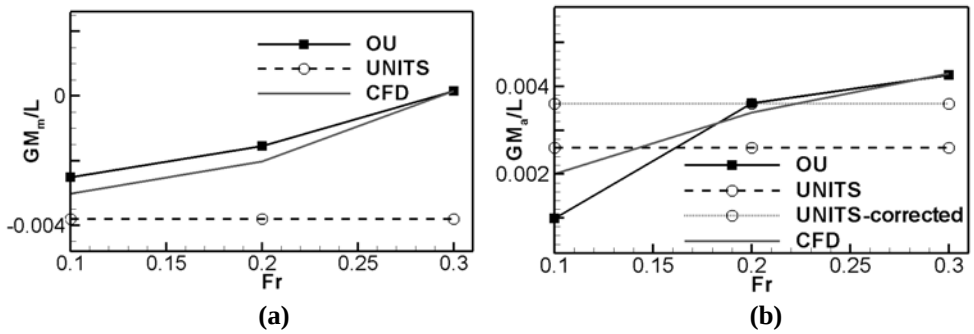

Figure 6-24: GZ parameters in head waves for GM=0.043 m for OU and UNITS model and CFD (10 deg heel angle): (a) nondimensional GM_m versus Fr; (b) nondimensional GM_a versus Fr

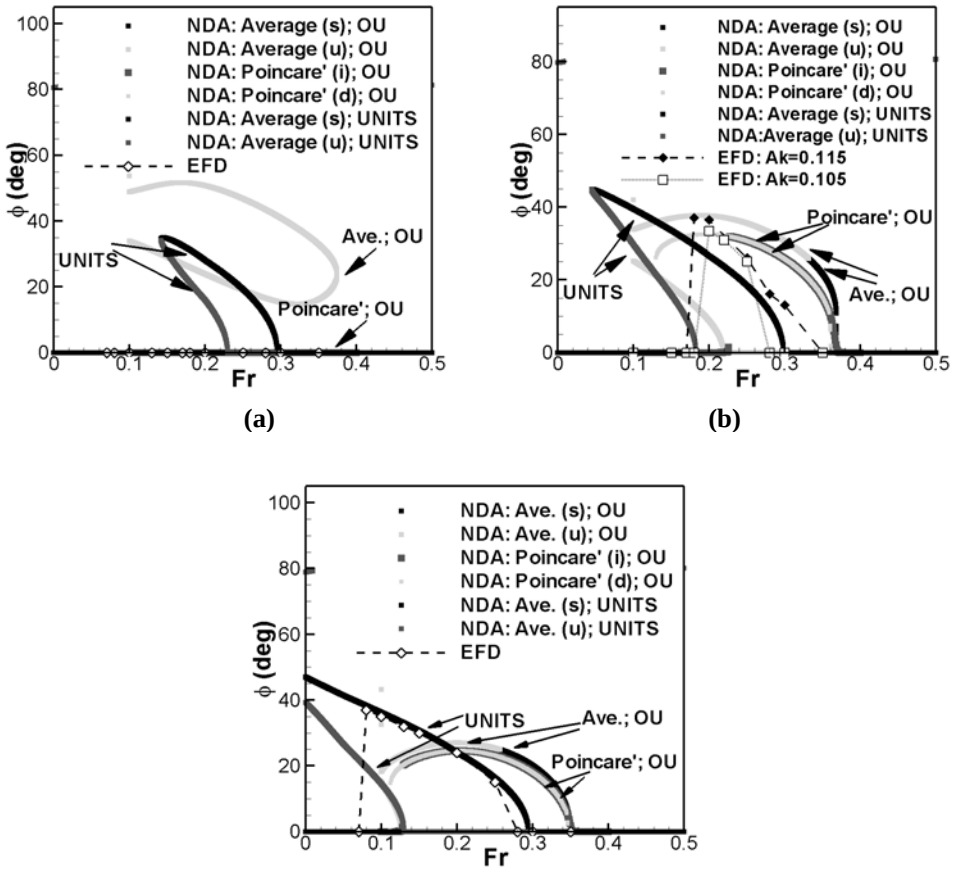

Figure 6-25: OU and UNITS model results for parametric rolling: (a) GM=0.043 m; (b) GM=0.038 m; (c) GM=0.033m

CHAPTER 7. VALIDATION OF OU CAPTIVE MODEL SIMULATIONS

The OU (Osaka University) captive model simulations are performed with the same operational and environmental conditions described in Chapter 5 which include resistance test, static heel in calm water, static drift in calm water, and static heel in following waves. The simulations are carried out to validate CFD and to obtain manoeuvring coefficients as inputs for NDA model of broaching described in Chapter 2. Herein, the details of CFD simulation including computational domain and boundary conditions, grid, and simulation design are presented and lastly the results are discussed and compared with EFD and Potential Theory calculation.

7.1 Computational Domain, Boundary Conditions

The computational domains extend from $-0.5 < x < 2, -1 < y < 1, -1 < z < 0.25$, in dimensionless coordinates based on ship length, as shown in Fig. 7-1. The ship axis is aligned with the x-axis with the bow at x = 0 and the stern at x = 1. The free surface at rest lies at z = 0. The ship model is appended with skeg and bilge keels.

Boundary conditions are shown in Table 7-1. Inlet boundary condition in calm water and waves are different. For calm water, x component velocity at inlet boundary condition is set to be U_0 which is the same as ship velocity in relative coordinate system and zero in earth fixed coordinate system. Other velocity components are imposed to be zero. Normal pressure gradient and level set function are imposed zero and –z(x) for calm water, respectively. In regular waves, inlet pressure gradient and level set function are imposed such that they follow linear wave theory equations:

$$p = \frac{A}{Fr^2} e^{kz} \cos(kx - 2\pi ft) - \frac{A^2}{2Fr^2 k} e^{2kz} \quad (7.1)$$

$$\phi = A\cos(kx - 2\pi ft) - z(x) \quad (7.2)$$

$$U(x, y, z, t) = U_0 + \frac{A}{Fr}\sqrt{k}e^{kz}\cos(kx - 2\pi ft)(x) \quad (7.3)$$

$$W(x, y, z, t) = \frac{A}{Fr}\sqrt{k}e^{kz}\sin(kx - 2\pi ft) \quad (7.4)$$

Here, U_o would be zero in earth coordinate system. Other boundary conditions are the same for cases in calm water and in waves.

7.2 Grid

Two different grids are generated for captive tests as shown in Table 7-2 and 7-3. For both grids, computational grids for the hull, skeg and bilge keels are designed to accurately resolve geometric features of the model and the unsteady turbulent boundary layer, wake, and wave fields. The hull boundary layer and bilge keels grids were generated using GRIDGEN. The hull boundary layer and bilge keels grid were fixed to and move with the ship. The hull boundary layer has a double-O topology and was created with a hyperbolic grid generator, with a grid spacing at the hull designed to yield $y^+ < 1$ for the highest Reynolds number case Fr = 0.6. In this way the same boundary layer grid could be used for all cases. The hull boundary layer grid extends to cover the deck of the ship and wraps around it, allowing for computations with extreme motions. For Grid No.1, grid topology was selected so that two other blocks were responsible to capture the flow near the hull (refinement block) and far from the hull (background block) whereas grid No.2 has only background. Since there is a wave on the free surface for some cases, the background block was designed to have enough grid points near free surface. The computational domain for all blocks covers both the port and starboard sides of the ship, since the flow and wave fields might be asymmetric due to static drift angle or the roll

motion. Table 7-3 summarize the grids matrix used for different captive tests and Figure 7-1 shows grid No.1 for the ship.

For the grid convergence study, a fine grid 10M and a coarse grid 1.2M were generated by refining and coarsening the medium size of grid No.1 using a factor of $\sqrt{2}$ in each direction with a tri-linear interpolation algorithm, so that the grid distribution and shape would be as close as possible to the original grid. This grid study was performed for the ship with 10 deg heel angle towed in calm water, free to sink and trim, and for all Fr numbers in the range of 0-0.6. Figure 5-2 provides Ug for X, Y, K, M, σ, and τ. Y for Fr<0.4 and N/σ for 0.5<Fr<0.55 show relatively poor convergence, i.e., Fr regions with oscillatory convergence or divergence. Table 7-4 provides the grid verification results. Consideration is given to Fr averages U_g in $\%S_2$ (medium grid solution) $\overline{U_g} = \frac{1}{N}\sum_{i=1}^{N}\left|U_g(Fr_i)/S_2(Fr_i)\right|$ and in %DR (Dynamic Range) $\overline{U_g} = \frac{1}{N}\sum_{i=1}^{N}\left|U_g(Fr_i)/DR_{S_2}\right|$ and RSS $\overline{U_{g\,RSS}} = \frac{1}{N}\sqrt{\sum_{i=1}^{N}\left(U_g(Fr_i)/S_2(Fr_i)\right)^2}$ in $\%S_2$. The average RSS U_g seems most representative. The RSS average of Ug over Fr is 0.1, 6.8, 1, 1.5, 2.3, 2.4 $\%S_2$ for X, Y, K, N, σ, and τ, respectively, i.e. the average value is $3\%S_2$. This suggests that the results are fairly insensitive to grid changes for present range of grid sizes.

7.3 Simulation Design

Captive simulations are carried out for single Fr number and a range of Fr number (Full Fr curve). Single Fr number simulations are performed in relative inertial coordinate system in which velocity is not imposed on the ship but it is given to the flow. Simulations are executed at “unsteady mode” and stopped after flow travels at least seven times of ship length.

7.3.1 Full Fr Curve Simulation Design

Full Fr curve simulations are executed in inertial earth fixed coordinate system. The basic assumption of this approach is that at every instant the flow field is in a quasi steady-state, by virtue of imposing a very small acceleration to cover the desired velocity range during the computation. From the mathematical point of view, this means that the time derivatives of the momentum, level set transport, and turbulence model equations are negligible in a time-average sense. Full Fr curve simulation is able to capture unsteady phenomena such as vortex shedding, oscillation of forces and moments, and free surface fluctuation as long as the characteristic times of these phenomena (shedding period, motion period, and free surface fluctuations) are much smaller than the characteristic ship acceleration time. This condition is easy to meet for vortex shedding and the free surface fluctuations, being high-frequency phenomena, but may be difficult for ship motions that have a long period such as ship motion in waves. Therefore, Full Fr curve is applicable for cases in calm water.

The procedure for full Fr curve simulation starts with an appropriate choice of a reference velocity to non-dimensionalize the equations of motion. For convenience ship speed corresponding to the maximum *Fr* to be achieved in the computation is used, thus:

$$V^*(t) = \frac{V(t)}{V_{\max}} = \frac{Fr(t)}{Fr_{\max}} \qquad (7.5)$$

Here V(t) and Fr(t) are instant velocity and Fr, respectively.

Different kind of continues functions such as linear or quadratic function can be used for $V^*(t)$ to change it smoothly and very slowly to have quasi steady-state at each time step. In this study, $V^*(t)$ is changed by linear function.

$$V^* = at \qquad (7.6)$$

Where, *a* is a constant acceleration.

The traveled distance by ship at each time step can be estimated from:

$$\Delta D^* = V_{\max} \int_{t_0-\Delta t}^{t_0} V^*(t)dt = aV_{\max}\left(\frac{-2t_0\Delta t + \Delta t^2}{2}\right) \quad (7.7)$$

The traveled distance reaches to its maximum at the last time step of simulation corresponded to $t_0=t_{max}$, when $Fr=Fr_{max}$. To achieve quasi steady state condition, maximum of traveled distance should be small enough compare with the ship length. This makes a limit for choosing acceleration and time step. Table 7-5 shows parameters applied for full Fr curve simulations in this study.

7.4 Resistance

7.4.1 Forces, Moments, and Motions

CFD resistance tests are performed for full Fr curve Fr=0.0-0.6 and single Fr=0.5 for the model free to sinkage and trim in calm water. Figure 7-3 compares EFD and CFD for C_T, σ, and τ, including with and without bilge keels. Consideration is given to Fr averages based on absolute error in %D $\overline{E} = \frac{1}{N}\sum_{i=1}^{N}\left|E_i / D_i\right|$ and in %DR $\overline{E} = \frac{1}{N}\sum_{i=1}^{N}\left|E_i / DR\right|$ and RSS error $\overline{E_{RSS}} = \frac{1}{N}\sqrt{\sum_{i=1}^{N}\left(E_i / D_i\right)^2}$ in %D, and maximum errors E_{max} in %D and %DR. The average RSS error seems most representative. In general the results indicate expected trends and excellent agreement between CFD and EFD (average RSS error $E_{CT,}$ σ, τ =1.32, 4.32, 2.04 %D), except for C_T for $0.35 \le Fr \le 0.45$, σ for $0.45 \le Fr \le 0.55$ and τ for Fr>0.55 for which CFD under predicts EFD by maximum $E_{CT,}$ σ, τ =4.11, 17.7, 6.43 %D, as shown in Table 7-6. Single Fr=0.5 CFD shows same values as full curve CFD at same Fr. The CFD grid study, explained earlier, indicates relatively small dependency on grids, which suggests large Fr errors are due to free surface, turbulence modeling, and/or requirement of much larger grids than 11M.

7.4.2 Free Surface Elevation and Vortex Structures

Figure 7-4 indicates general view of free surface for several Fr numbers. In overall, increasing Fr washes away waves generated by the ship to the downstream. More details of the free surface have been shown in Fig. 7-5. Free surface fluctuation at y/L=0 indicates bow and stern waves, as shown in Fig. 7-5. The stern wave is pushed away from the aft at high Fr number such that the ship transom comes out of water. This introduces important role of turbulence modelling for low Fr number to model properly wet transom vortices and their effects on the ship resistance and free surface fluctuation. Also, free surface profile at y/L=0 illustrates that pitch angle has to be positive (bow is up) at high Fr and nearly zero at low Fr which can be confirmed by Fig. 7-3. Axial velocity contours indicate several vortex structures around the hull, as shown in Fig. 7-6. The sonar dome, bilge keels, and skeg produce vorticities even though vorticities created by the sonar dome are dominant.

7.5 Static Heel in Calm Water

7.5.1 Forces, Moment, and Motions

CFD static heel tests are performed for full Fr curve Fr=0.0-0.6 with ϕ=10 and 20 degree, and single Fr=0.6 with ϕ=10 degree for the model free to sinkage and trim in calm water. Figures 7-7 and 5-8 show dimensional and non-dimensionalized results comparing CFD and EFD for axial and side force, roll and yaw moment, and heave and pitch motions for ϕ=10 degree. In general, full curve simulation results show fairly large error for Fr<0.2. It is because of the fact that running time was not enough for Fr<0.2 and boundary layer was not developed yet. In order to have enough time to simulate Fr<0.2, very small time step could have been chosen which is very expensive and time consuming. For Fr>0.2, CFD shows acceptable results for motions, forces, and moments. CFD under predicts sinkage and trim by average RSS error 3.62%D and 14.1%D,

respectively, as shown in Table 7-7. Average RSS error for X, Y, K, and N are 2.6, 11, 1.3, and 11%D, respectively. In overall, E=7.3%D. Even though errors are quite large for side force and yaw moment, CFD indicates similar trend as EFD. Comparing roll moment and yaw moment explain that heel to the starboard causes yaw moment pushing the bow to the port. Also, roll moment versus Fr indicates that the roll moment is close to hydrostatic value (roll moment at Fr=0.0) and Fr would not change that significantly unless Fr>0.5. Lastly, single Fr=0.6 CFD shows fairly same values as full curve at same Fr. Figures 7-9, 7-10 represent motions, forces, and moments for ϕ=20 degree. CFD results show fairly small error for all variables for Fr>0.2, except side force which shows reasonable result for Fr>0.4 in which side and axial force have the same order. CFD average RSS errors for sinkage and trim are 2.5 and 10%D, respectively. CFD average RSS error for X, Y, K, and N are 2.5, 14.2, 1.3, 6.7%D, respectively. In overall, E=6.2%D.

7.5.2 Coupling Effects

Figure 7-11 summarizes CFD and EFD X, Y, K, and N for both heel angles and resistance test as a zero heel angle case. It is shown that axial force would not be changed significantly by giving a heel angle to the ship. However, impact of heel angle is huge on Y, K and N. This matches with the theory described in Chapter 2. In fact, roll angle has second order effect on X while it has first order effect on Y, K, and N. More than that, comparing Fig. 7-8 and 7-10 indicates that roll angle would not change trim and sinkage supporting the theory that roll has second order effect on heave and pitch modes.

7.5.3 Maneuvering Coefficients

As shown in Fig. 7-11, $a+b\phi^2$ is fitted to X for each Fr and $a\phi+b\phi^3$ is fitted to Y, K, and N in order to estimate coefficients a and b which are linear and nonlinear maneuvering coefficients as explained in Chapter 2. CFD and EFD reconstructions based

on the fitted curves show exactly similar values to the original CFD and EFD data due to limit number of CFD and EFD data explaining that the CFD and EFD reconstruction errors are zero. The values of CFD and EFD maneuvering coefficients are shown in Table 7-8. The average RSS error of CFD prediction is 7.4%D for linear maneuvering coefficients and 106%D for nonlinear maneuvering coefficients.

7.5.4 Free Surface Elevation and Vortex Structures

Figures 7-12,7-13 illustrate CFD free surface elevation around the ship heeled toward starboard for several Fr number. As expected, the flow stagnates as it collides with the bow of the ship and the free surface becomes higher, forming a bow wave. When both the flows coming from portside and starboard collide at the aft region, the velocity decreases and subsequently the pressure increases. An elevation is then produced, as shown in Fig. 7-14. The boomerang shape of this elevation is consequent with the velocities in the area, higher away from the hull, so from the sides, the small wave is carried away faster. The flow stagnates at bow forming high elevation and then increases its speed as it turns the fore perpendicular. Subsequently, the pressure drops and the free surface dives. After that the flow decreases its speed at the aft and forms high elevation on the free surface again. Even though the ship is heeled to the starboard, the free surface level for the portside and starboard is nearly the same due to same pressure drop for both sides. At high Fr number, the peaks of the free surface at centreline become higher due to high pressure at stagnation. Figures 7-15 and 7-16 show details of free surface near the bow and the aft for the worst case, Fr=0.6 and ϕ=20 deg. Figure 7-15 indicates possibility of wave breaking and overturning at high Fr number near the bow. Figure 7-16 shows the free surface at the transom. It shows clearly that the transom is out of water at high Fr number and there is a wake region after the aft with complex free surface shape. The shape of the hull at the bottom of the bow can be assimilated to a flat plate with no thickness. As the flow turns around the bow hull, a complicated vertical structure is generated. One vortex,

as shown in Fig. 7-17, is generated in the tip of the bow and runs almost parallel to the hull. Another vortex comes from the tip of the bilge keels and again moves parallel to the hull. A final vortex is generated close to the aft region as flow passes the skeg.

7.6 Static Drift in Calm Water

7.6.1 Forces, Moments, and Motions

CFD static drift tests are performed for full Fr curve Fr=0.0-0.6 with β=5, 10, and 15 degrees for the model free to sinkage and trim in calm water. Figures 7-18 and 7-19 show dimensional and non-dimensionalized results comparing CFD and EFD for axial and side force, roll and yaw moment, and heave and pitch motions for β =5 degrees. Similar to static heel cases, full curve simulation results show fairly large error for Fr<0.2 due to insufficient running time to develop boundary layer. For Fr>0.2, CFD predicts absolute value of sinkage and trim by average RSS error 8.9%D and 16.3%D, respectively, as shown in Table 7-9. Average RSS error for X,Y, K, and N are 8.5, 16.8, 43.2, and 6.0%D, respectively. Even though errors are quite large, CFD indicates similar trend as EFD for Fr>0.2. Comparing roll moment and yaw moment explains that turning the bow to the right causes heel to the portside suggesting that yaw angle would produce enough heel moment in free model simulation and cause capsize. Figures 7-20 and 7-21 represent dimensional and non-dimensionalized motions, forces, and moments for β=10 degrees. The trend for all variables versus Fr number for β=5 and β=10 degrees are the same except for trim. For β=10 degrees, trim is always negative but for β=5 degrees trim jumps to positive value for Fr>0.35. CFD predictions for β=10 degrees indicate average RSS error 7.8 and 16.7%D for sinkage and trim, respectively. CFD average error for X, Y, K, and N are 11.5, 11.4, 54.7, 6.5%D, respectively. Figures 7-22 and 7-23 show dimensional and non-dimensionalized results for β=15 degrees. The overall trend versus Fr number is the same as before. Dimensional results clearly show that increasing Fr number would

increase all motions, forces, and moments' magnitude. CFD prediction average RSS errors are 10.8, 7.9, 49, 5.7, 6.4, and 11.5%D for X, Y, K, N, sinkage, and trim, respectively. Comparing CFD prediction errors for all drift angle cases demonstrates that CFD prediction for side force and trim are improved significantly for larger drift cases. However, error for other variables has increased for larger drift cases and amongst them error of roll moment is much bigger than the others. In overall, CFD predicts forces, moments, and motions for a drift angle case by the average error of 10%D excluding K and 19%D including K. Herein, the accuracy of EFD roll moment data is under question and that would be a possibility of large CFD errors for K. Comparing current results of OT with similar type of obliquely towed hull (5415) simulated at non-zero speed with the same level of grid size (Sakamoto, 2009) show that the error of current simulation is acceptable.

7.6.2 Coupling Effects

Figure 7-24 shows the impact of side velocity or drift angle ($v=-u\sin\beta$) on forces and moment. It is observed that drift angle has significant effect on Y, K, and N whereas X would not be changed that much. According to the theory explained in Chapter 2, drift angle has second order effect on X and first order effect on Y, K, and N. Therefore, the results follow the theory. Comparing Fig. 7-19, 7-21, and 7-23 illustrate the effect of drift angle on sinkage and trim. It is observed that drift angle effect is negligible on sinkage whereas its effect is huge on trim especially at high Fr. This suggests that drift angle effect on sinkage is second order as it is expected from the theory. However, drift angle effect on trim is not second order, at least at high Fr.

7.6.3 Maneuvering Coefficients

Figure 7-24 shows the forces and moment used to calculate the v-velocity related hydrodynamic derivatives obtained from EFD and CFD. These figures also include the

reconstructions. $a+bv^2$ is fitted to X for each Fr and $av+bv^3$ is fitted to Y, K, and N in order to estimate coefficients a and b which are linear and nonlinear maneuvering coefficients as explained in Chapter 2. Also, z_H is estimated from 1st order polynomial curve fitting to K–Y plot. The values of CFD and EFD maneuvering coefficients are shown in Table 7-10. The average RSS error of CFD prediction including/excluding K moment and z_H are 28/8.4%D for linear maneuvering coefficients and 30/20.4%D for nonlinear maneuvering coefficients.

7.6.4 Free Surface Elevation and Vortex Structures

Figure 7-25 shows the elevation of the free surface. Stagnation on the windward side of the hull creates a bow wave. As expected, the height of wave is bigger for higher drift angle case. The flow accelerates as it turns the fore perpendicular and the subsequent pressure drop is manifested by the loss of height of the free surface on the leeward side, as Fig. 7-26 shows. The flow stagnates in the windward side of the hull, as shown in Fig. 7-27. As the velocity decreases, the pressure increases, so the wave elevation is higher in this region. For β=15 deg, the free surface elevation indicates bow diving due to large wave height formed around the bow. Figure 7-28 shows a representation of flow at windward side. The stagnation area, easily identified by pressure contour, is near the bow at high pressure area and moves toward the aft a little bit at β=15 deg.

As the flow turns around the bow hull, a complicated vertical structure is generated. Two vortices are generated at keel. One of them starts right at the bottom of the bow and can be considered a tip vortex, as shown in Fig. 7-29.This vortex runs almost parallel to the flow direction. Another keel vortex comes from the sharp shape of the keel at bottom. This vortex extends backward and losses its strength gradually as the curvature of the keel increases. Another vortex structure comes from bilge keels once flow passes the tip of bilge keels and it moves toward the flow direction. A final vortex is generated close to the aft region as flow passes the skeg.

7.7 Static Heel in Following Waves

7.7.1 Forces, Moments, and Motions

CFD static heel tests in following waves are performed for Fr=0.3, H/λ=0.03 and λ/L=1 with ϕ= 10 and 20 degrees and λ/L=1.25, H/λ=0.025 and Fr=0.15,0.25,0.35, and H/λ=0.05 and Fr=0.35 with ϕ= 0 for the model free to heave and pitch. Figures 7-30 and 7-31 show EFD and CFD X,Y,K,N,z,θ vs. time and ξ_g/λ constructed based on averages over 2-5 wave periods and evaluated for Fr=0.3, H/λ=0.03 and λ/L=1 with 10 deg heel angle. CFD results are shown for both grids, as mentioned in Table 7-3. In general, grid 2 achieves better agreement with EFD. Average RSS errors are evaluated as provided in Table 7-11. CFD predicts heave and pitch by average error of 8 and 4.9%D. The average RSS errors of X, Y, K, and N are 35, 45, 4, and 6.7%D, respectively. In overall, trends are predicted by CFD. Figure 7-32 and 7-33 show results for 20 deg heel angle. The average RSS errors of X, Y, K, and N are 27, 23, 3.4, and 3.3%D, respectively. The results indicate better agreement with EFD such that the overall error is 12%D whereas it is 17%D for 10 degree heel angle, as shown in Table 7-11.

Figures 7-34 and 7-35 show comparing CFD and EFD results versus time for zero heel angle, λ/L=1.25, H/λ=0.025 and Fr=0.15,0.25,0.35, and H/λ=0.05 and Fr=0.35. The results versus ξ_g/λ are constructed based on average over 2-5 wave periods and evaluated as shown in Fig. 7-36 and 7-37. CFD simulations are performed for grid 2, as mentioned in Table 7-3. The average RSS errors, shown in Table 7-11, indicates the average error is 15%D with the largest errors for X and θ. The average error increases by factor of 2 for same increase in wave amplitude.

7.7.2 Coupling Effects

FFT analysis is performed to help to understand different harmonics and coupling effects available in CFD or EFD of ship responses in waves. According to the theory

explained in Chapter 2, for static heel in regular following waves, heave response should indicate 1st harmonic at wave encounter frequency f_e, and 1st, 2nd, and 3rd order/harmonics due to pitch motion. The similar harmonics are expected for pitch response due to wave and heave motion. Forces and moments should also show harmonics due to waves and pitch and heave motion. X indicates 1st harmonic amplitude due to waves at f_e, 2nd and 3rd order/harmonic amplitudes due to heave and pitch motions at f_e. Y and N indicate 1st order/harmonic amplitudes due to waves and 2nd and 4th order/harmonic amplitudes due to heave and pitch motions.

Figures 7-38 and 7-39 exhibit FFT analysis of CFD and EFD for Fr=0.3, H/λ=0.03 and λ/L=1 with ϕ= 10 and 20 degrees. Heave response shows 1st and 2nd harmonics and pitch show 1st harmonic. X indicates 1st and 2nd harmonics and Y and N show 1st, 2nd, and 4th harmonics, as expected. In overall, CFD simulations using grid 1 and grid 2 could predict all harmonics, as shown in Fig. 7-38 and 7-39. However, grid 2 shows much better agreement with EFD, as shown in Table 7-12. For 10 degrees heel angle, CFD predicts 1st and 2nd harmonics of heave by error of 2.97/58%D and 1st harmonic of pitch by error of 8%D using grid 2. The errors of 1st and 2nd harmonics of axial force prediction are 76%D and 35%D. CFD sway force FFT analysis shows good agreement with EFD for first harmonic using grid 2 (E=9.3E%D). Yaw moment errors of 1st and 2nd harmonics for grid 2 are about 12.6%D and 9.53%D. For 20 degrees heel angle, CFD errors of 1st / 2nd harmonics of heave are 2.75/48%D using grid 2. CFD predicts 1st harmonic of pitch by error of 5.08%D. The errors of 1st/2nd harmonics of axial force prediction are 99.3/32.4%D. CFD sway force 1st harmonic prediction error is 27%D and yaw moment first/second harmonics predictions provide error about 0.49/31%D using grid 2.

Figures 7-40 and 7-41 illustrate FFT analysis of results for wave induced heave and pitch motions and axial force for Fr=0.05, 0.2, 0.35, H/λ=0.025 and 0.05, and λ/L=1.25 with zero heel angle. For Fr=0.35 and H/λ=0.025, FFT analyses of heave and pitch show only first harmonic in their behaviour. CFD prediction of heave shows error of 1.79%D

for first harmonic while the error of pitch first harmonic prediction is 59%D. FFT analysis of induced axial force indicates only first harmonic which is under predicted by error of 11.6%D. For Fr=0.35 and H/λ=0.05, FFT analysis indicates dominant first harmonic for heave, pitch and induced axial force. The prediction of heave, pitch, and axial force first harmonic has the error of 15.5%D, 64.5%D, and 22.3%D, respectively.

7.7.3 CFD Results vs. Potential Theory Calculation

Since wave-induced surge force is responsible for surf-riding and it is necessary to accurately evaluate for realising a quantitative prediction of ship behaviours in following/quartering waves, the Potential Theory, as an uncomplicated method, is performed to estimate surge force for λ/L=1.25, H/λ=0.025 and several Fr with ϕ= 0. The surge force can be calculated as the linear Froude-Krylov force as the first-order approximation, which well explains the wave-induced surge force for a small trawler up to the wave steepness of Ak=1/10 (H/λ=0.03). The Froude-Krylov calculation is compared with EFD results as shown in Fig. 7-42. The comparison indicates that the linear Froude-Krylov calculation significantly overestimates the experiment when the Fr is smaller than 0.2. The Fr of 0.2 coincides with the Hanaoka parameter $\tau = U\omega_e / g$ of 0.25. Here, in an unsteady potential flow theory with linear free-surface condition, the velocity potential relating to symmetric motions diverges. When the Hanaoka parameter increases by increasing the forward velocity, the Froude-Krylov prediction provides better agreement. Comparing CFD and Froude-Krylov calculation shows that the CFD successfully reproduces the decrease of the wave-induced surge force near the Fr of 0.2 probably because the CFD can capture the 3D wave pattern. In fact, the discrepancy between EFD/CFD and the linear Froude-Krylov calculation in higher speed region could consist of diffraction radiation and higher order Froude-Krylov components.

7.8 Summary of OU Captive Model Simulations

The grid study calm water static heel indicates the average RSS grid uncertainty is 3%D. CFD resistance test full Fr curve simulation in calm water shows close agreement with EFD with average RSS error of 3%D for X, σ, τ. Single Fr=0.5 CFD shows same values as full curve CFD at same Fr. CFD and EFD full Fr curve static heel results show fairly close agreement for σ, τ, X, K for the full Fr range, whereas Y and N were significantly under predicted for large Fr>.4. In overall, CFD prediction average RSS error is 7.3 and 6.2%D for 10 and 20 degrees heel angle. Single Fr=0.6 CFD shows fairly same values as full curve at same Fr. Forces and moment analyses show that heel angle has second order effect on X while it has first order effect on Y, K, and N such that increasing heel angle would change Y, K, and N except X. CFD shows fairly close agreement for static heel linear maneuvering derivatives, whereas large errors are indicated for nonlinear maneuvering derivatives. The average RSS error of CFD prediction of linear and nonlinear maneuvering coefficients is 7.4%D and 106%D, respectively. CFD and EFD static drift show good results of σ, τ, X, Y, N for the full Fr range, whereas K is over predicted for Fr>0.2. In overall, CFD predicts force, moment, and motions for a drift angle case by the average error of 10%D excluding K and 19%D including K. It shows that drift angle has second order effect on X and first order effect on Y, K, and N supporting the theory explained in Chapter 2. CFD predicts linear and nonlinear maneuvering coefficients excluding K by the error of 8.4%D and 20.4%D. CFD non-zero static heel in following waves average errors are 12 and 15%D for 20 and 10 degrees heel angle with the largest errors for surge and sway forces. CFD zero static heel in following waves average errors is 15%D with the largest errors for X and θ. The average error increases by factor of 2 for same increase in wave amplitude. Heave response shows 1^{st} and 2^{nd} harmonics and pitch show 1^{st} harmonic. X indicates 1^{st} and 2^{nd} harmonics and Y and N show 1^{st}, 2^{nd}, and 4^{th} harmonics. In overall, CFD static heel in

following waves simulations using grid 1 and grid 2 could predict all harmonics. However, grid 2 shows much better agreement with EFD. The surge force in following wave is estimated from Potential Theory calculation (Froude-Krylov calculation) and compared with CFD and EFD. It is shown that CFD successfully reproduces the decrease of the wave-induced surge force near the Fr of 0.2 whereas Potential Theory fails probably because it cannot capture the 3D wave pattern.

Table 7-1: Summary of boundary conditions

	ϕ	p	k	ω	U	V	W
Inlet for waves	$A\cos(kx-2\pi ft)-z(x)$	$\frac{A}{Fr^2}e^{kz}\cos(kx-2\pi ft)-\frac{A^2}{2Fr^2k}e^{2kz}$	$k_{fs}=10^{-7}$	$\omega_{fs}=9$	$U(x,y,z,t)=U_0+\frac{A}{Fr}\sqrt{k}e^{kz}\cos(kx-2\pi f$	$V=0$	$W(x,y,z,t)=\frac{A}{Fr}\sqrt{k}e^{kz}\sin(kx-2\pi ft)$
Inlet for calm water	$-z(x)$	$\frac{\partial p}{\partial n}=0$	$k_{fs}=10^{-7}$	$\omega_{fs}=9$	$U=U_0$	$V=0$	$W=0$
Exit	$\frac{\partial\phi}{\partial n}=0$	$\frac{\partial p}{\partial n}=0$	$\frac{\partial k}{\partial n}=0$	$\frac{\partial\omega}{\partial n}=0$	$\frac{\partial^2 U}{\partial n^2}=0$	$\frac{\partial^2 V}{\partial n^2}=0$	$\frac{\partial^2 W}{\partial n^2}=0$
Sides	$\frac{\partial\phi}{\partial n}=0$	$\frac{\partial p}{\partial n}=0$	$\frac{\partial k}{\partial n}=0$	$\frac{\partial\omega}{\partial n}=0$	$\frac{\partial U}{\partial n}=0$	$\frac{\partial V}{\partial n}=0$	$\frac{\partial W}{\partial n}=0$
Bottom	$\frac{\partial\phi}{\partial n}=1$	$\frac{\partial p}{\partial n}=0$	$\frac{\partial k}{\partial n}=0$	$\frac{\partial\omega}{\partial n}=0$	$U=1$	$V=0$	$W=0$
Top	$\frac{\partial\phi}{\partial n}=-1$	$\frac{\partial p}{\partial n}=0$	$\frac{\partial k}{\partial n}=0$	$\frac{\partial\omega}{\partial n}=0$	$\frac{\partial U}{\partial n}=0$	$\frac{\partial V}{\partial n}=0$	$\frac{\partial W}{\partial n}=0$
Ship hull	$\frac{\partial\phi}{\partial n}=0$	Poisson Eq.	$k=0$	$\omega=\frac{60}{\mathrm{Re}\beta y}$	$U=C_g$	$V=0$	$W=0$

Table 7-2: Grid size for CFD tests

	Grid 1 (refinement ratio=√2)			Grid 2
	Coarse	Medium	Fine	Medium
Boundary Layer	0.47 M	1.33 M	3.76 M	1.29 M
Bilge keels	0.22 M	0.63 M	1.78 M	0.24 M
Refinement	0.35 M	1.00 M	2.83 M	-
Background	0.18 M	0.52 M	1.47 M	1.76 M
Total	1.22 M	3.48 M	9.84 M	3.29 M

Table 7-3: Grid matrix for CFD tests

		Grid1 (Medium)	Grid2
Cases in calm water	Resistance	X	
	Static Heel	X	
	Static Drift	X	
Cases in waves	Head Waves	X*	
	Following waves (10 and 20 deg heel)	X	X
	Following waves (zero heel)		X

*: Grid 1 without BKs is used for head waves.

Table 7-4: Verification study for static heel=10 deg

Refinement ratio=!2	X	Y	K	N	σ	τ	$\overline{U_g}$
DR	51.83524 (N)	5.443227 (N)	4.184471 (N.m)	10.19919 (N.m)	12.95431 (mm)	1.648851 (deg)	
Ug_{ave} (%S_2)	1.320523	25.92286	1.352147	20.957	3.232973	5.801962	9.76
Ug_{ave} (%DR)	0.424326	6.567709	1.312601	5.481052	1.552964	1.181102	2.75
$Ug_{ave\text{-}RSS}$(%S_2)	0.1008	6.750302	1.024958	5.112561	2.290736	2.365466	2.94

Table 7-5: Non-dimensional input variables for CFD tests

	Resistance and Static Heel in calm water	Static Drift in calm water	Single run tests in calm water and waves
Time step	0.02	0.02	0.02
Velocity variation at each time step	2e-4	2e-4	-
Fr variation at each time step	2e-4	2e-4	-
Number of iterations	3000	2000	2000
Maximum running time	60	40	40
Maximum Fr variation	2e-4	2e-4	-
Maximum traveled distance variation	0.012002	0.008002	-

Table 7-6: Resistance tests validation

		E_{ave}%D	E_{ave}%DR	$E_{ave\text{-}RSS}$%D	Max E%D
With BK (Fr>0.2)	X	1.5	1.23	1.32	4.11(Fr=0.4)
	σ	5.02	4.15	4.32	17.7(Fr=0.5)
	τ	2.13	2.11	2.04	6.43(Fr=0.6)
w/o BK (Fr>0.2)	X	1.83	1.72	1.68	3.76(Fr=0.4)
	σ	NA	NA	NA	NA
	τ	NA	NA	NA	NA
Single run (Fr=0.5)	X	0.97	-	0.97	-
	σ	16.4	-	16.4	-
	τ	3.96	-	3.96	-

Table 7-7: Static heel validation

Heel		X	Y	K	N	σ	τ	$\overline{E}$
10 deg (Fr>0.2)	E_{ave} %D	6.25	28.54	2.78	29.8	9.63	26.9	**17.32**
	E_{ave} %DR	5.98	18.45	1.88	21.06	7.91	4.20	**9.91**
	$E_{ave\text{-}RSS}$ %D	2.60	11.05	1.33	11.08	3.62	14.15	**7.31**
	Max E%D	10.55 (Fr=0.25)	48.78 (Fr=0.6)	8.28 (Fr=0.6)	51.95 (Fr=0.25)	14.52 (Fr=0.55)	101.70 (Fr=0.35)	
	Max E%DR	10.91 (Fr=0.4)	48.78 (Fr=0.6)	3.42 (Fr=0.6)	26.48 (Fr=0.45)	13.92 (Fr=0.55)	8.72 (Fr=0.5)	
20 deg (Fr>0.2)	E_{ave} %D	6.3	600	2.23	17.43	5.64	19.9	**108.6**
	E_{ave} %DR	6.19	17.84	1.29	11.74	4.98	5.15	**7.86**
	$E_{ave\text{-}RSS}$ %D	2.50	14.23	1.31	6.69	2.47	10.03	**6.21**
	Max E%D	10.62 (Fr=0.35)	4327 (Fr=0.3)	9.12 (Fr=0.6)	35.00 (Fr=0.25)	13.46 (Fr=0.55)	69.78 (Fr=0.35)	
	Max E%DR	10.35 (Fr=0.35)	31.04 (Fr=0.25)	3.88 (Fr=0.6)	15.57 (Fr=0.25)	13.46 (Fr=0.55)	10.37 (Fr=0.5)	
Single run (10 deg, Fr=0.6)	$E_{ave\text{-}RSS}$ %D	1.86	46.69	6.94	30.20	1.18	5.92	**15.46**

Table 7-8: Hydrodynamic derivatives error estimated from static heel

	EFD				CFD				E_{ave} %D	$E_{ave\text{-}RSS}$ %D
Fr	**0.6000**	**0.4000**	**0.2000**	**0.0500**	**0.6000**	**0.4000**	**0.2000**	**0.0500**		
x*'	0.0061	0.0063	0.0051	0.0060	0.0062	0.0056	0.0048	0.0113	13.58	2.66
$X'_{\phi\phi}$	-0.0015	0.0036	0.0012	0.0095	0.0043	0.0085	0.0047	-0.0118	545.41	246.23
Y'_{ϕ}	-0.0328	-0.0200	0.0009	-0.0067	-0.0152	-0.0128	-0.0057	-0.0031	99.15	12.61
$Y'_{\phi\phi\phi}$	0.0897	0.1182	-0.0137	-0.2015	-0.0054	0.0262	0.0229	0.0284	95.10	30.56
K'_{ϕ}	-0.0063	0.0059	-0.0041	-0.0032	-0.0064	0.0062	-0.0041	-0.0053	16.60	1.99
$K'_{\phi\phi\phi}$	0.0294	-0.0276	0.0190	0.0150	0.0312	-0.0631	0.4576	0.0150	1204.54	24.76
N'_{ϕ}	0.0119	0.0090	0.0055	0.0058	0.0091	0.0058	0.0018	-0.0291	95.91	12.43
$N'_{\phi\phi\phi}$	-0.0091	-0.0139	-0.0092	-0.0112	0.0032	0.0014	0.0058	0.0267	328.74	124.48
								$\overline{E}$	299.88	**56.97**
								$\overline{E}_{linear}$	56.31	**7.42**
								$\overline{E}_{Nonlinear}$	543.45	**106.5**

Table 7-9: Static drift validation

Drift		X	Y	K	N	σ	τ	$\overline{E}$	$\overline{E}_{-K}$
5 deg (Fr>0.2)	E_{ave} %D	13.25	27.75	77.60	8.16	13.78	88.03	38.10	**30.19**
	E_{ave} %DR	12.09	27.46	68.18	7.55	7.14	17.67	23.35	**14.38**
	$E_{ave\text{-}RSS}$ %D	8.54	16.80	43.24	5.99	8.88	16.28	25.95	**11.30**
	Max E%D	14.76(Fr=0.3)	31.44(Fr=0.3)	83.53(Fr=0.2)	12.60(Fr=0.3)	15.94(Fr=0.2)	216.34(Fr=0.2)		
10 deg (Fr>0.2)	E_{ave} %D	14.18	12.97	106.34	11.18	8.076	31.14	30.65	**15.51**
	E_{ave} %DR	12.018	11.58	85.80	6.99	4.85	17.74	23.16	**10.64**
	$E_{ave\text{-}RSS}$ %D	11.51	11.42	54.75	6.53	7.80	16.71	18.12	**10.79**
	Max E%D	16.83(Fr=0.4)	19.19(Fr=0.4)	120.36(Fr=0.3)	24.39(Fr=0.2)	9.087(Fr=0.4)	37.24(Fr=0.4)		
15 deg (Fr>0.2)	E_{ave} %D	10.74	8.84	133.7	15.04	13.07	28.44	34.97	**15.23**
	E_{ave} %DR	10.14	7.99	145.5	10.71	4.46	12.71	31.92	**9.20**
	$E_{ave\text{-}RSS}$ %D	10.85	7.89	49.06	5.67	6.36	11.49	15.22	**8.45**
	Max E%D	13.30(Fr=0.3)	9.43(Fr=0.2)	147.8(Fr=0.3)	27.91(Fr=0.2)	24.10(Fr=0.2)	38.92(Fr=0.2)		

Table 7-10: Hydrodynamic derivatives error estimated from static drift

	EFD				CFD				E_{ave} %D	$E_{ave\text{-}RSS}$ %D
Fr	**0.4000**	**0.3000**	**0.2000**	**0.1000**	**0.4000**	**0.3000**	**0.2000**	**0.1000**		
X*'	0.0063	0.0056	0.0054	0.0055	0.0055	0.0049	0.0049	0.0064	12.36	6.27
X'_{vv}	0.2930	0.1803	0.1196	0.1020	0.1595	0.0833	0.0650	0.0862	40.13	21.35
Y'_{v}	0.3740	0.3649	0.3405	0.3006	0.2932	0.2651	0.2691	0.3496	21.57	10.96
Y'_{vvv}	3.7256	2.1744	0.9668	1.3854	2.2757	1.9354	1.7121	1.9435	41.82	23.98
K'_{v}	0.2206	0.1796	0.1717	0.1578	0.3990	0.3327	0.3474	0.3993	105.40	54.61
K'_{vvv}	1.5611	0.7531	1.5467	1.8460	1.5813	2.4280	2.7410	2.4192	83.00	59.37
N'_{v}	-0.1237	-0.1083	-0.0960	-0.0821	-0.1276	0.1106	-0.1034	-0.1071	10.88	7.93
N'_{vvv}	-2.1223	-1.1992	-0.5132	-0.4078	-1.2217	0.7914	-0.5909	-0.2859	30.37	15.97
Z'_{H}	0.5543	0.4566	0.6473	0.6852	1.1633	1.2550	1.3705	1.1657	116.64	61.26
					$\overline{E}/\overline{E}_{-K\&Z_H}$				51.35/ 26.19	**29.08/ 14.41**
					$\overline{E}_{linear}/\overline{E}_{linear-K\&Z_H}$				53.37/ 14.94	**28.21/ 8.39**
					$\overline{E}_{nonlinear}/\overline{E}_{nonlinear-K\&Z_H}$				48.83/ 37.44	**30.17/ 20.43**

Table 7-11: Simulation E_{RSS} of static heel in following waves estimated from results vs. ship position in waves

Heel&Fr	Wave	X	Y	K	N	z	θ	$\overline{E}$
Heel10-Fr=0.3	H/λ=0.03;λ/L=1	35.29011	45.02286	3.93254	6.67891	8.35731	4.87985	16.85
Heel20-Fr=0.3	H/λ=0.03;λ/L=1	27.05689	23.62012	3.38126	3.28103	8.80345	6.56903	12.11
Heel0-Fr=0.35	H/λ=0.025;λ/L=1.25	9.98453				4.69035	30.7823	15.15
Heel0-Fr=0.35	H/λ=0.05;λ/L=1.25	18.54791				9.49351	58.0826	28.70

Table 7-12: FFT of static heel in following waves

			E (%D) First/Second hamonic											
			Grid 1						Grid 2					
Heel	Wave	Fr	X	Y	K	N	σ	τ	X	Y	K	N	σ	τ
10 deg	H/λ=0.03 λ/L=1	0.3	5.73/56	56.1	58.2	30.9/71.9	58.4/62	32.4	76/35	9.3	21	12.6/9.33	2.97/58	8.08
20 deg	H/λ=0.03 λ/L=1	0.3	18.8/53.1	52.8	54.4	30.5/74.2	60.1/51	35.6	99.3/32.4	27	7.25	0.49/31	2.75/48	5.08
0 deg	H/λ=0.025 λ/L=1.25	0.15							NA	-	-	-	NA	NA
0 deg	H/λ=0.025 λ/L=1.25	0.25							NA	-	-	-	NA	NA
0 deg	H/λ=0.025 λ/L=1.25	0.35							11.6	-	-	-	1.76	59
0 deg	H/λ=0.05 λ/L=1.25	0.35							22.3	-	-	-	15.5	64.5

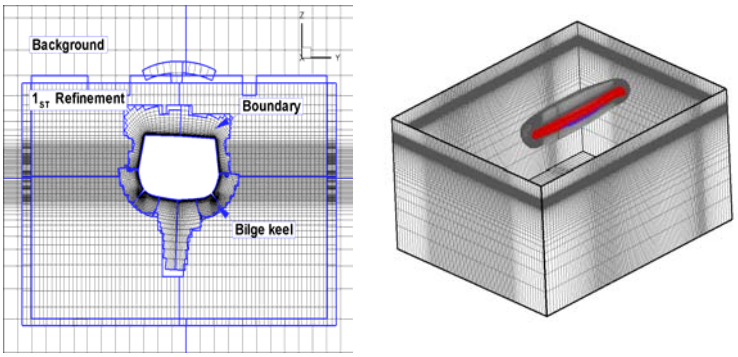

Figure 7-1: Grids and solution domain of captive test simulations

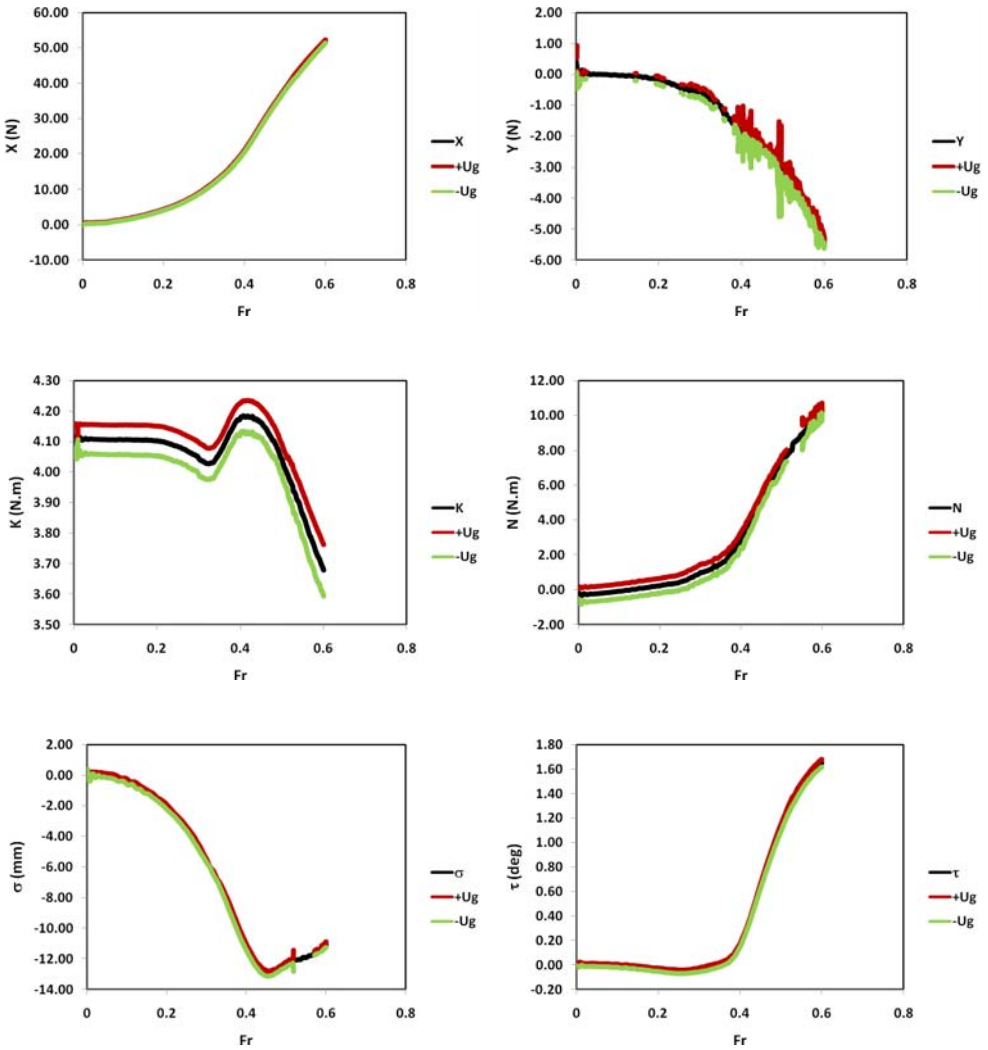

Figure 7-2: Grid uncertainty for 10 deg static heel

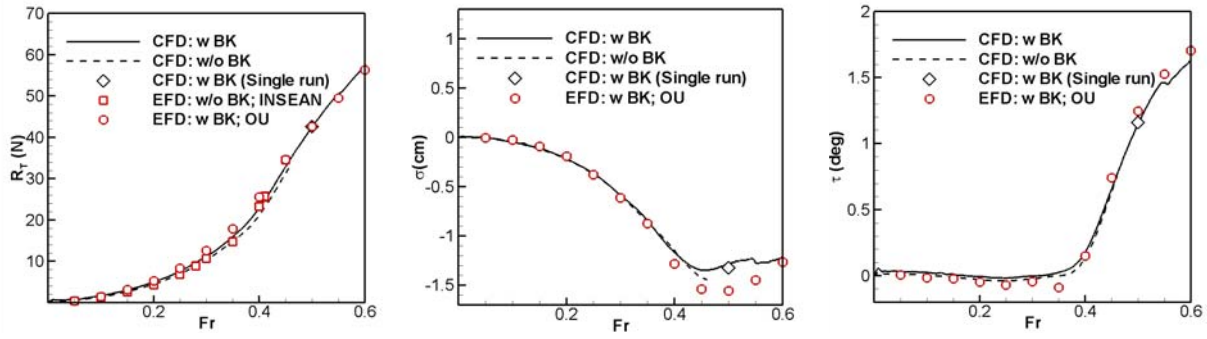

(a) **(b)** **(c)**

Figure 7-3: Resistance test results: (a) resistance; (b) sinkage; (c) trim versus Fr number

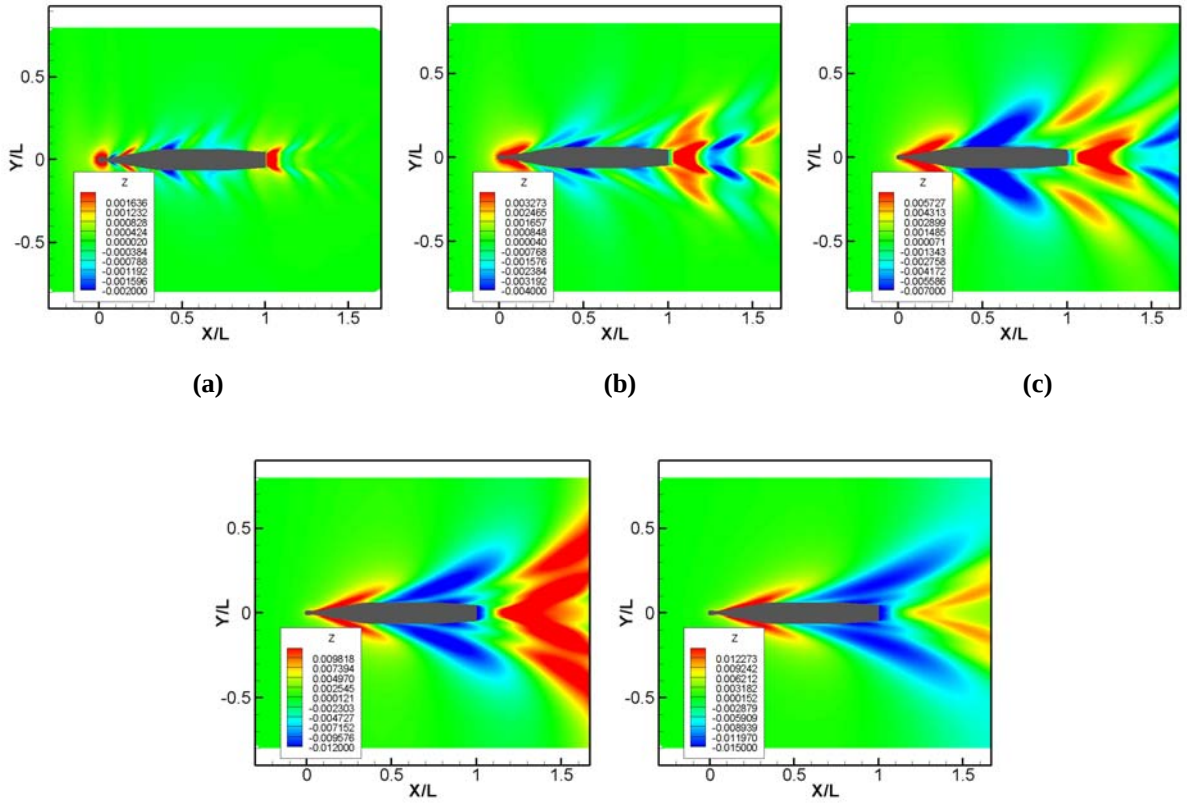

(a) **(b)** **(c)**

(d) **(e)**

Figure 7-4: Free surface elevation for resistance test: (a) Fr=0.2; (b) Fr=0.3; (c) Fr=0.4; (d) Fr=0.5; (e) Fr=0.6

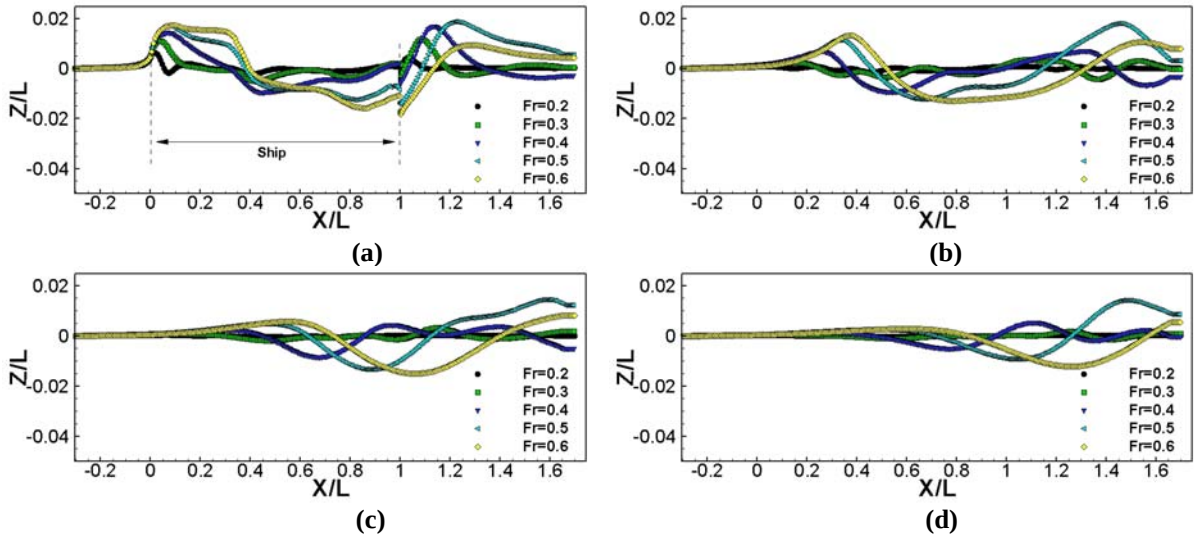

Figure 7-5: Free surface elevation for resistance test at: (a) y/L=0.0; (b) y/L=0.1; (c) y/L=0.2; (d) y/L=0.3

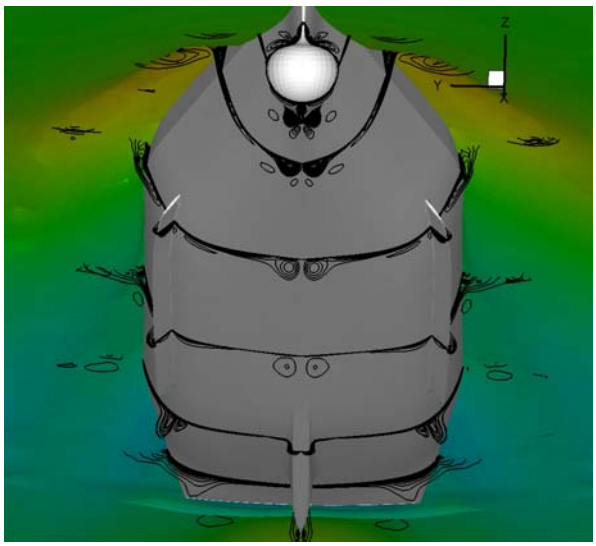

Figure 7-6: Vortex structures for resistance test at Fr=0.6

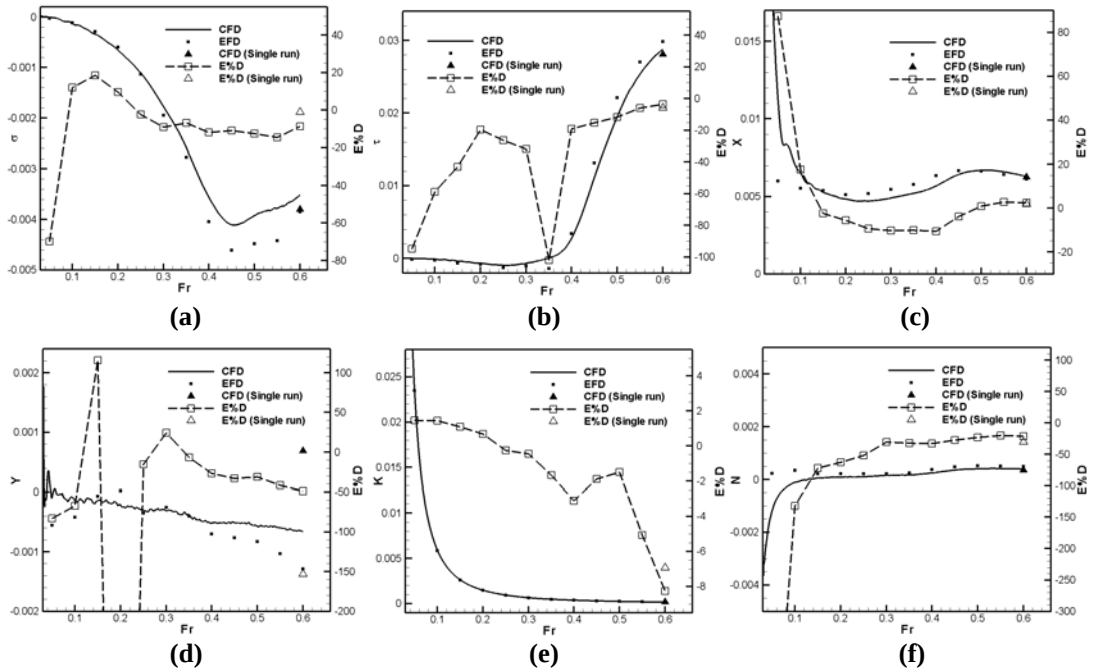

Figure 7-7: Non-dimensionalized results for static heel at ϕ=10: (a) sinkage; (b) trim; (c) axial force; (d) side force; (e) roll moment; (f) yaw moment

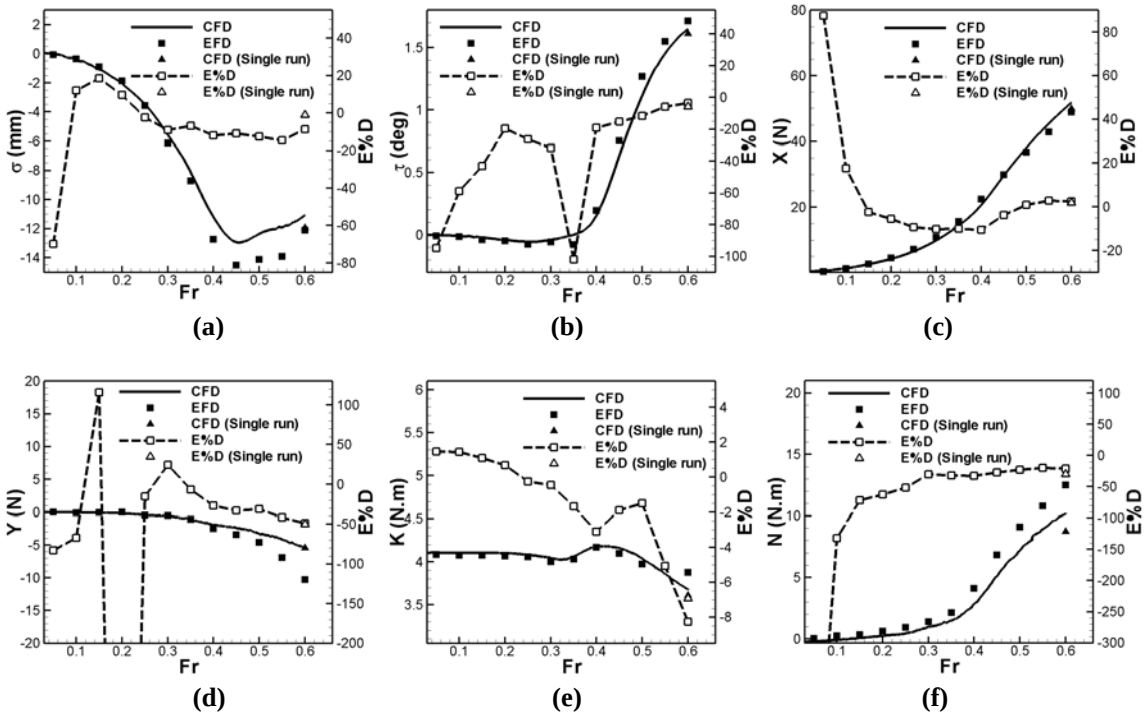

Figure 7-8: Dimensional results for static heel at ϕ=10: (a) sinkage; (b) trim; (c) axial force; (d) side force; (e) roll moment; (f) yaw moment

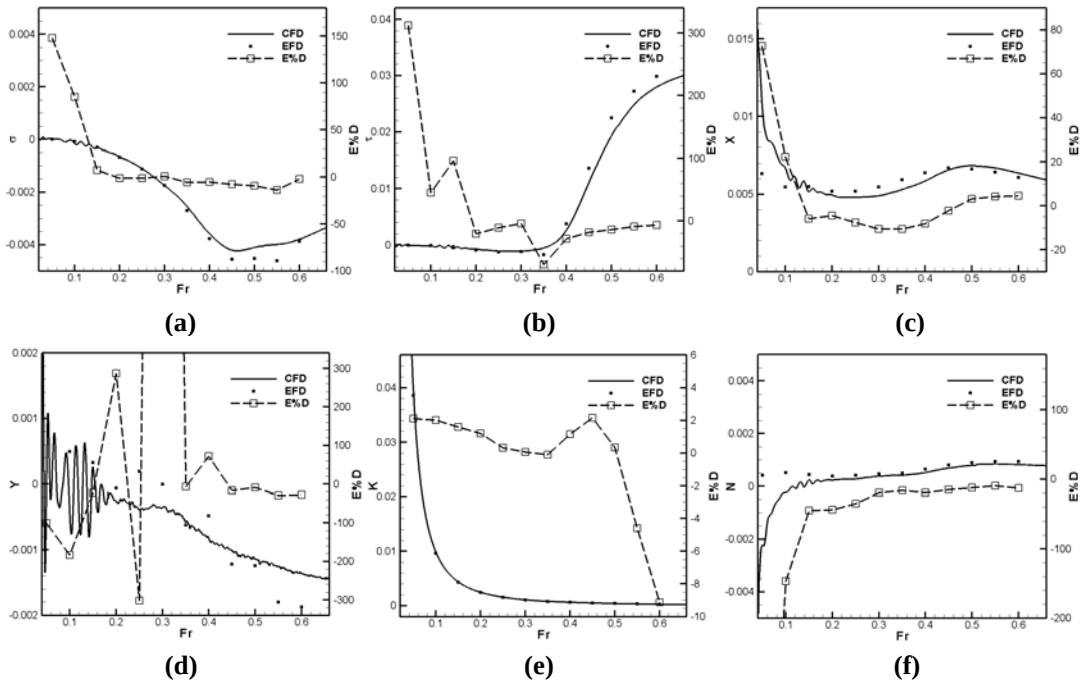

Figure 7-9: Non-dimensionalized results for static heel at ϕ=20: (a) sinkage; (b) trim; (c) axial force; (d) side force; (e) roll moment; (f) yaw moment

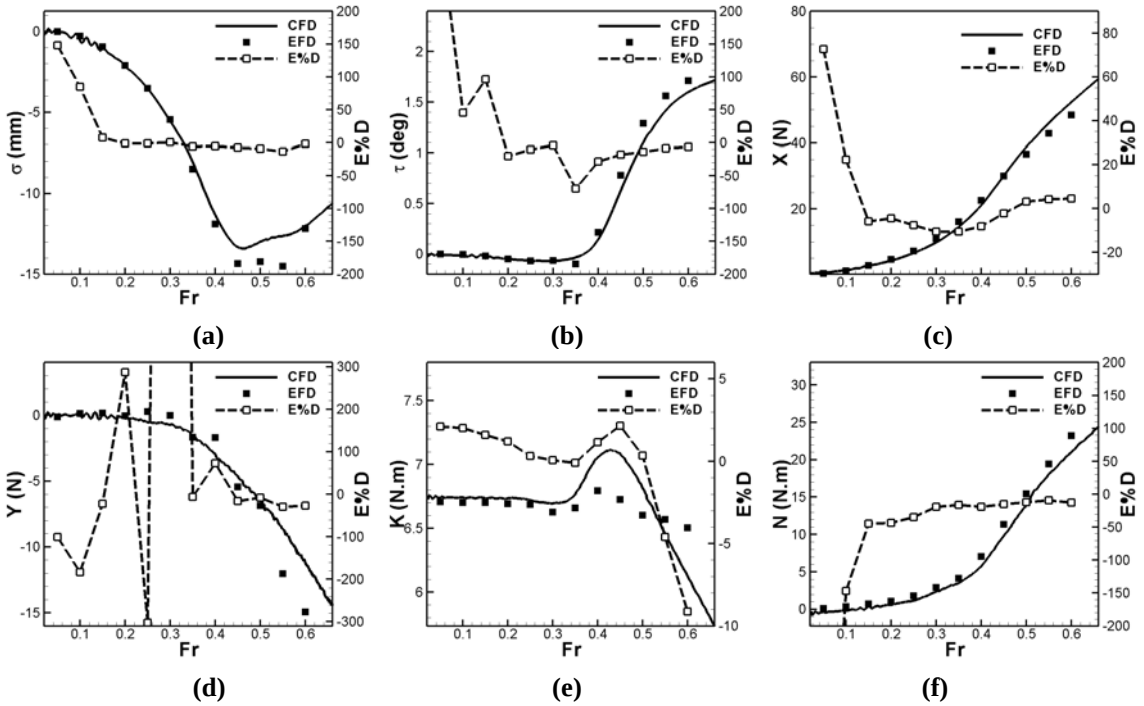

Figure 7-10: Dimensional results for static heel at ϕ=20: (a) sinkage; (b) trim; (c) axial force; (d) side force; (e) roll moment; (f) yaw moment

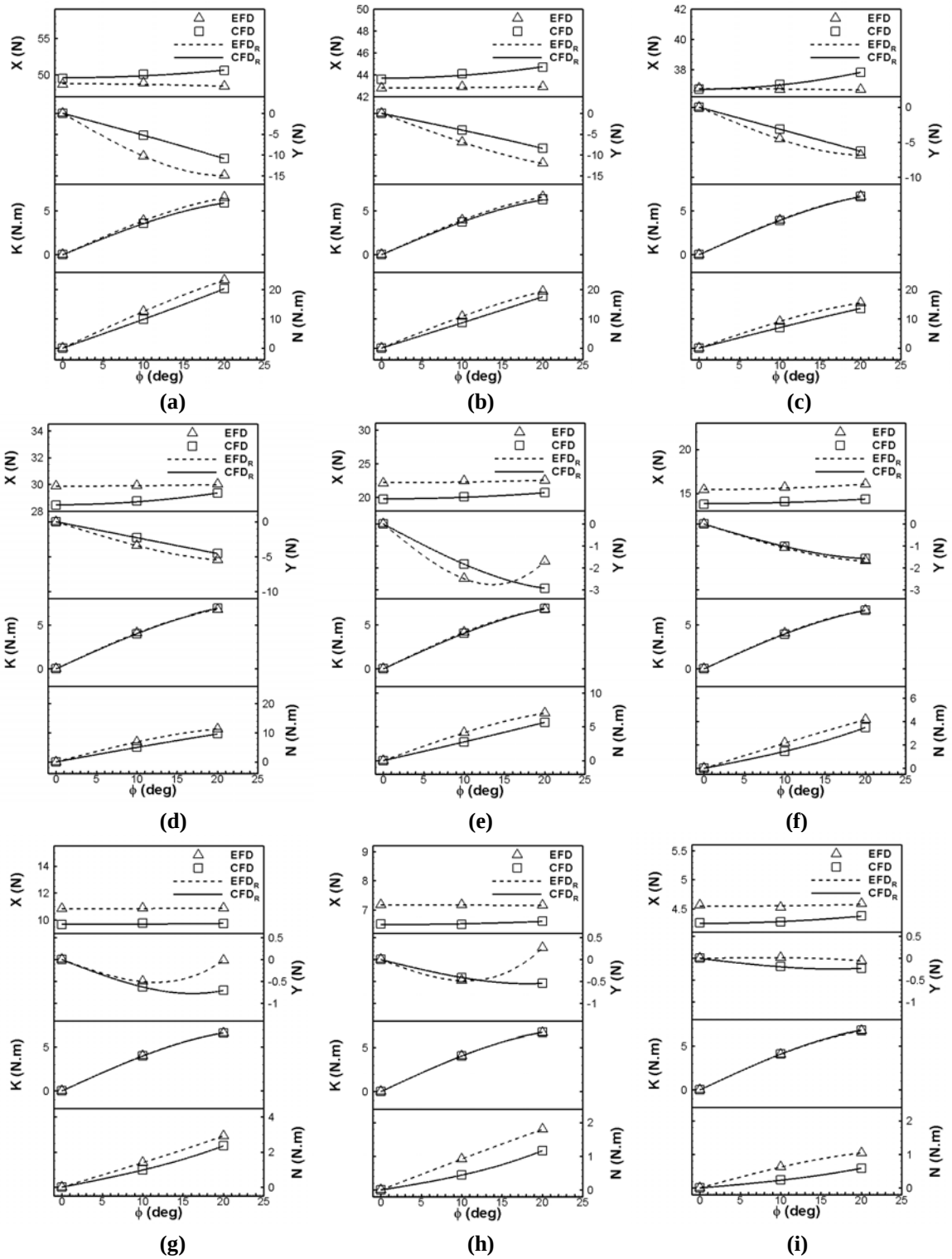

Figure 7-11: CFD and EFD data and their reconstructions using regression method: (a) Fr=0.6; (b) Fr=0.55; (c) Fr=0.5; (d) Fr=0.45; (e) Fr=0.4; (f) Fr=0.35; (g) Fr=0.3; (h) Fr=0.25; (i) Fr=0.2

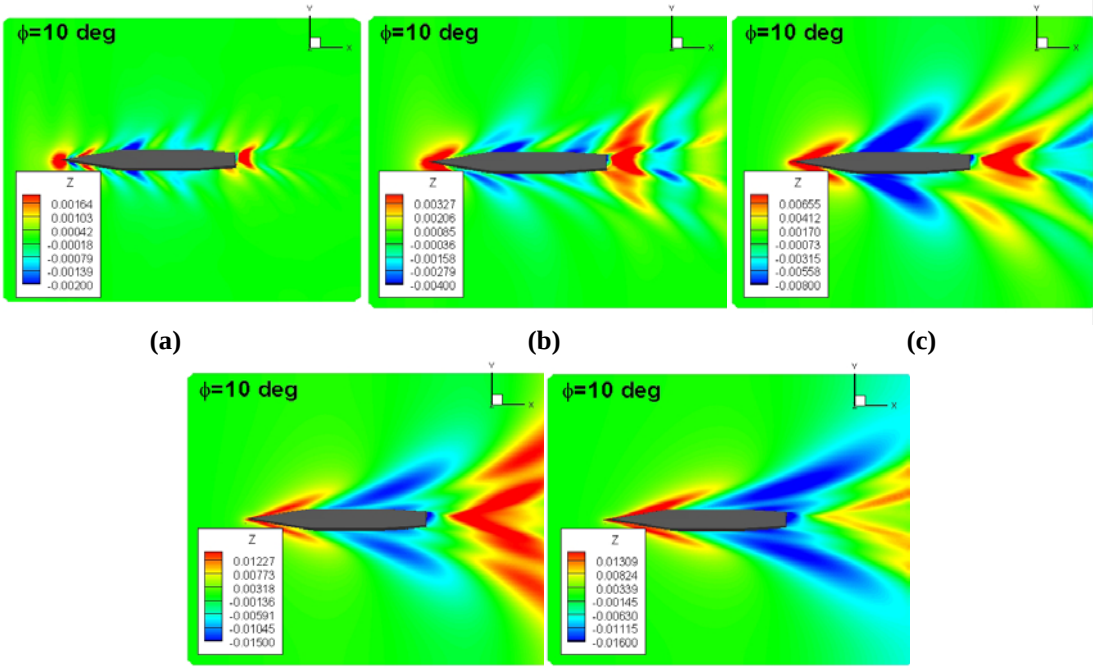

Figure 7-12: Free surface elevation for 10 deg static heel simulation: (a) Fr=0.2; (b) Fr=0.3; (c) Fr=0.4; (d) Fr=0.5; (e) Fr=0.6

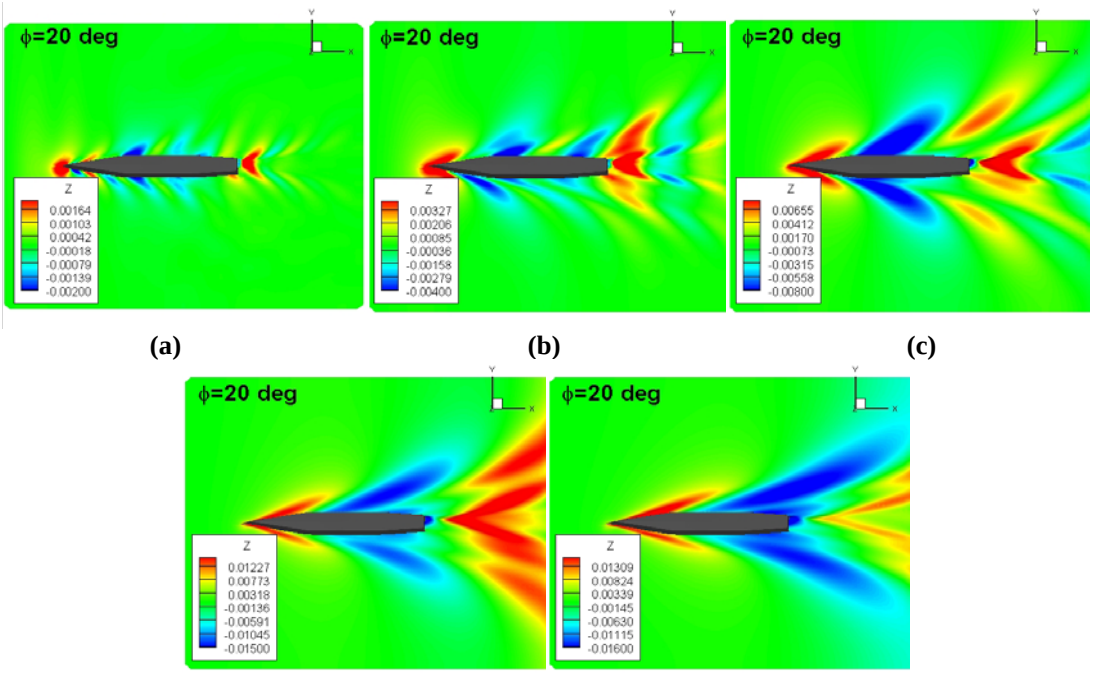

Figure 7-13: Free surface elevation for 20 deg static heel simulation: (a) Fr=0.2; (b) Fr=0.3; (c) Fr=0.4; (d) Fr=0.5; (e) Fr=0.6

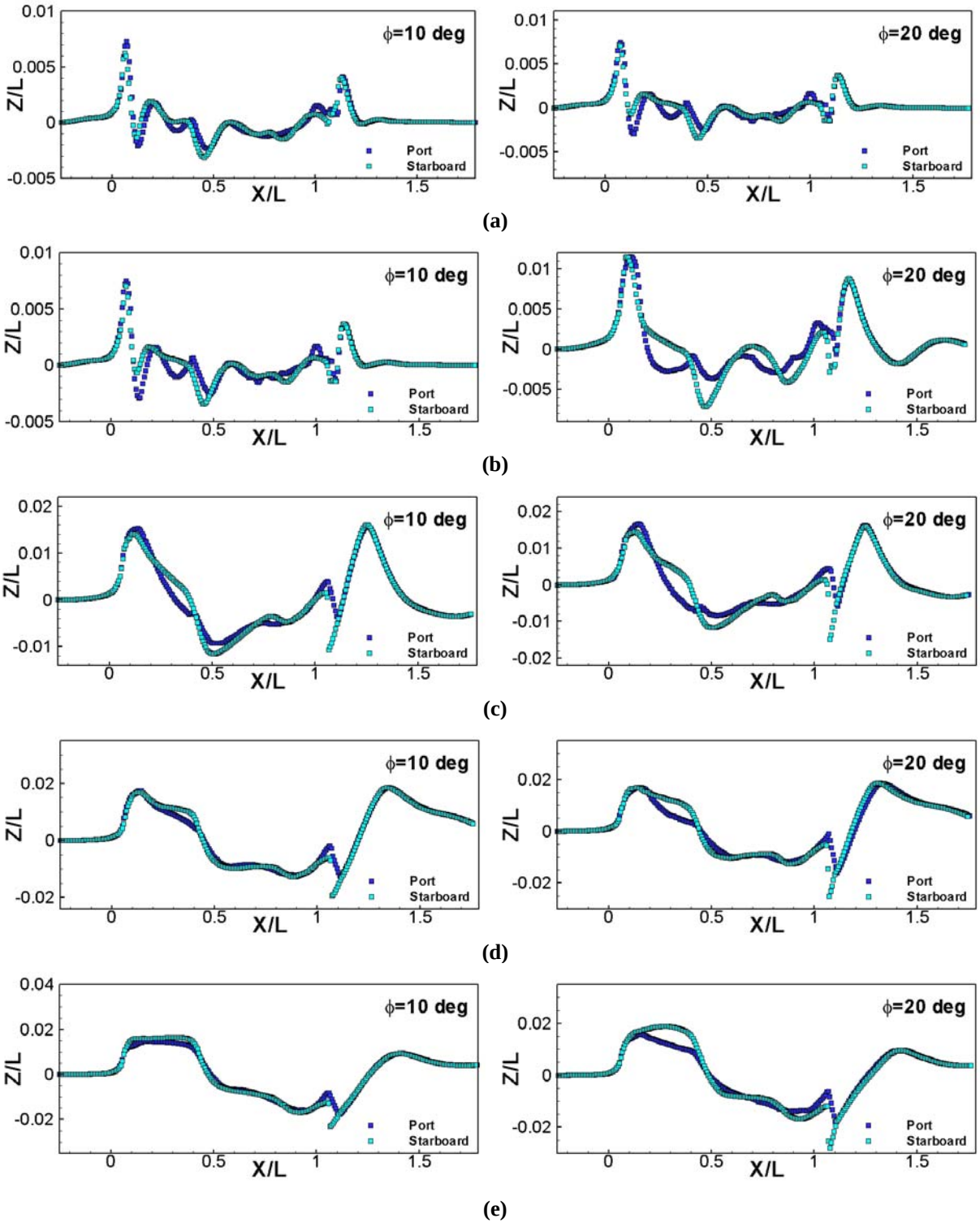

Figure 7-14: Free surface elevation for static heel test at y/L=0.0: (a) Fr=0.2; (b) Fr=0.3; (c) Fr=0.4; (d) Fr=0.5; (e) Fr=0.6

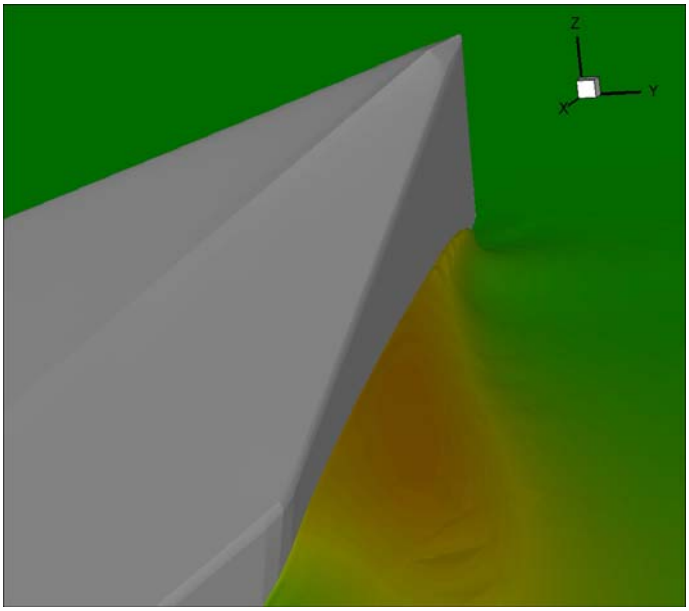

Figure 7-15: Free surface elevation at the bow for static heel test at Fr=0.6 and ϕ=20 deg

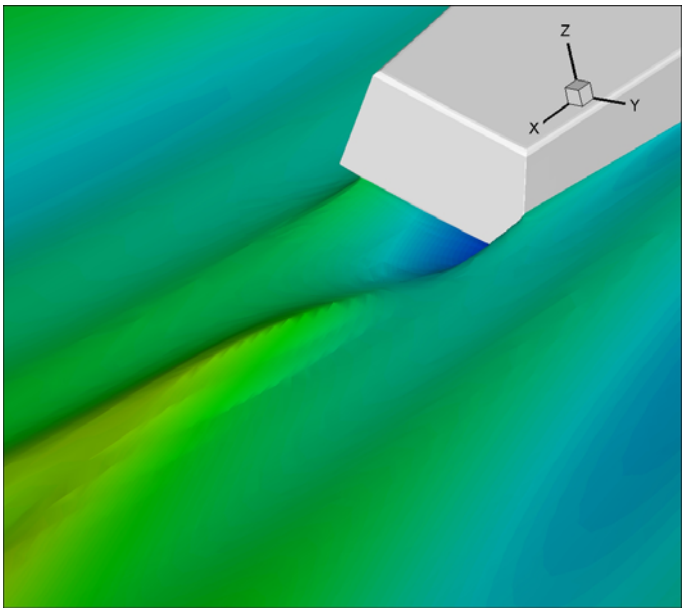

Figure 7-16: Free surface elevation at the aft for static heel test at Fr=0.6 and ϕ=20 deg

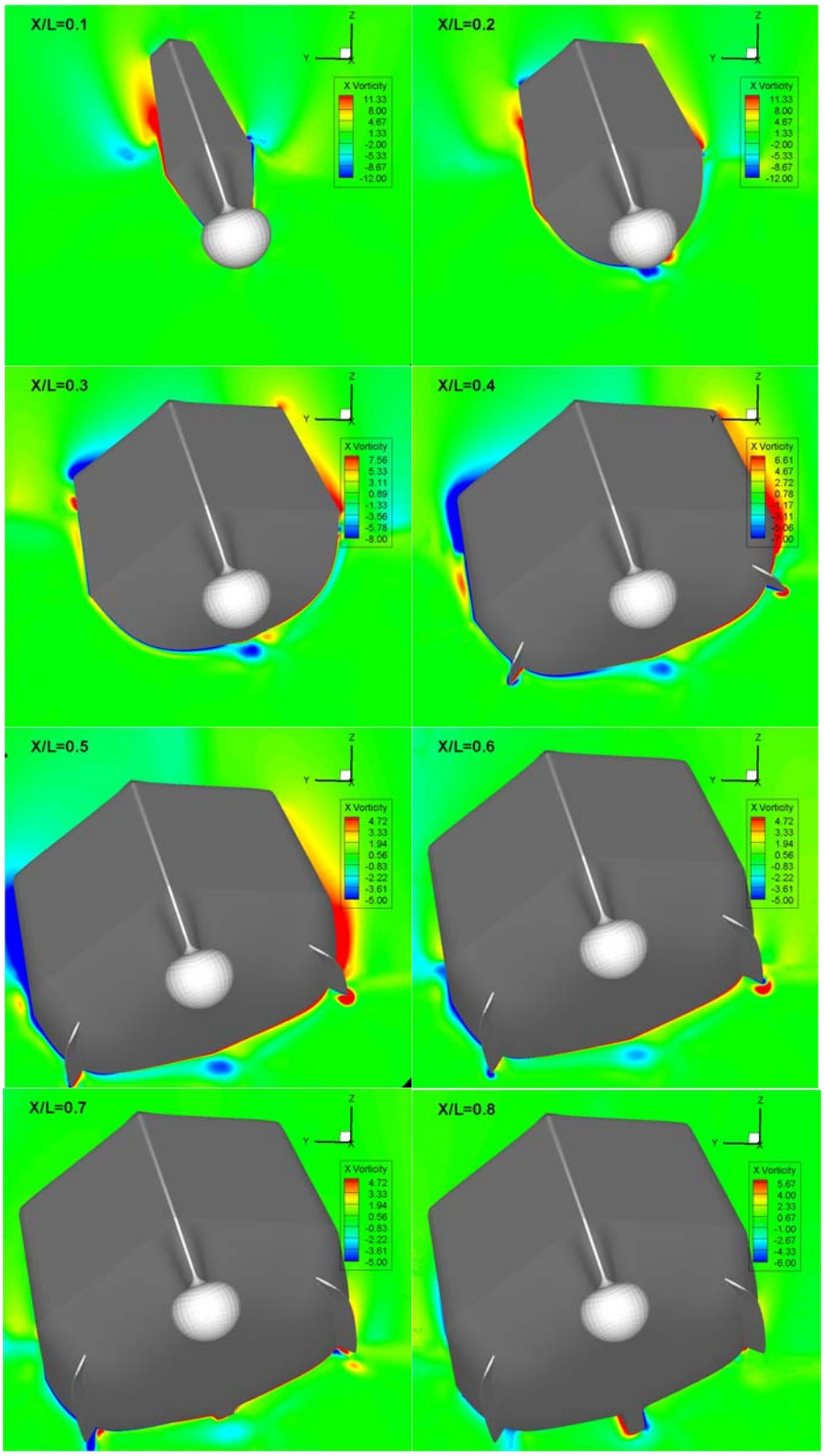

Figure 7-17: Contours of x-vorticity at several sections for static heel test at Fr=0.6 and ϕ=20 deg

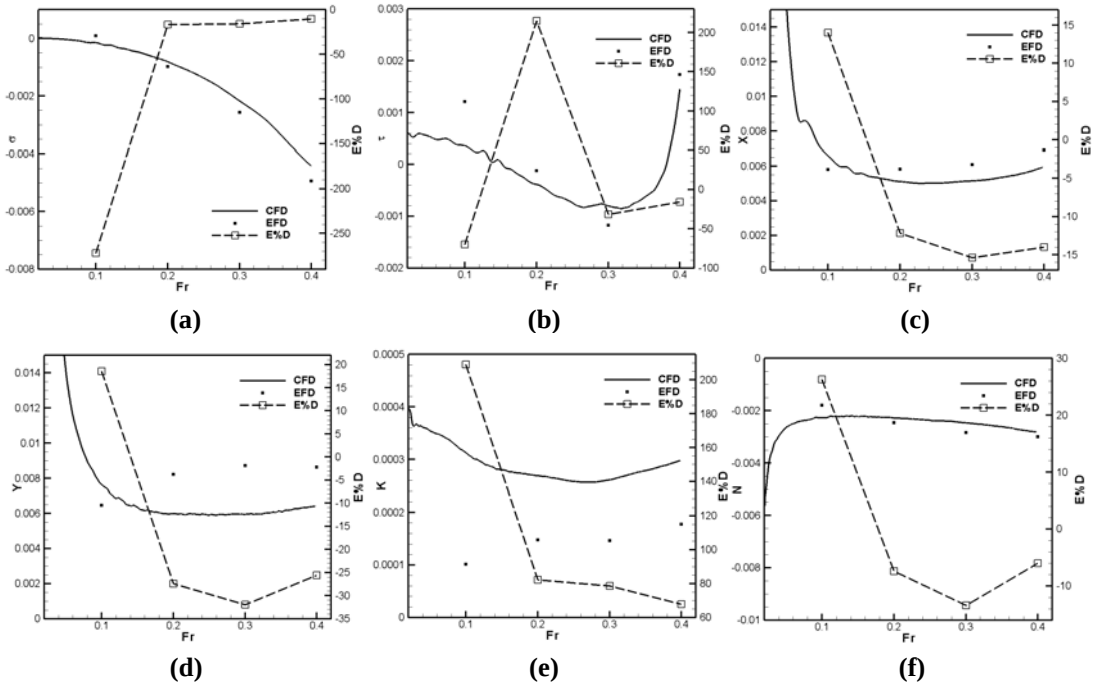

Figure 7-18: Non-dimensionalized results for static drift at β=5: (a) sinkage; (b) trim; (c) axial force; (d) side force; (e) roll moment; (f) yaw moment

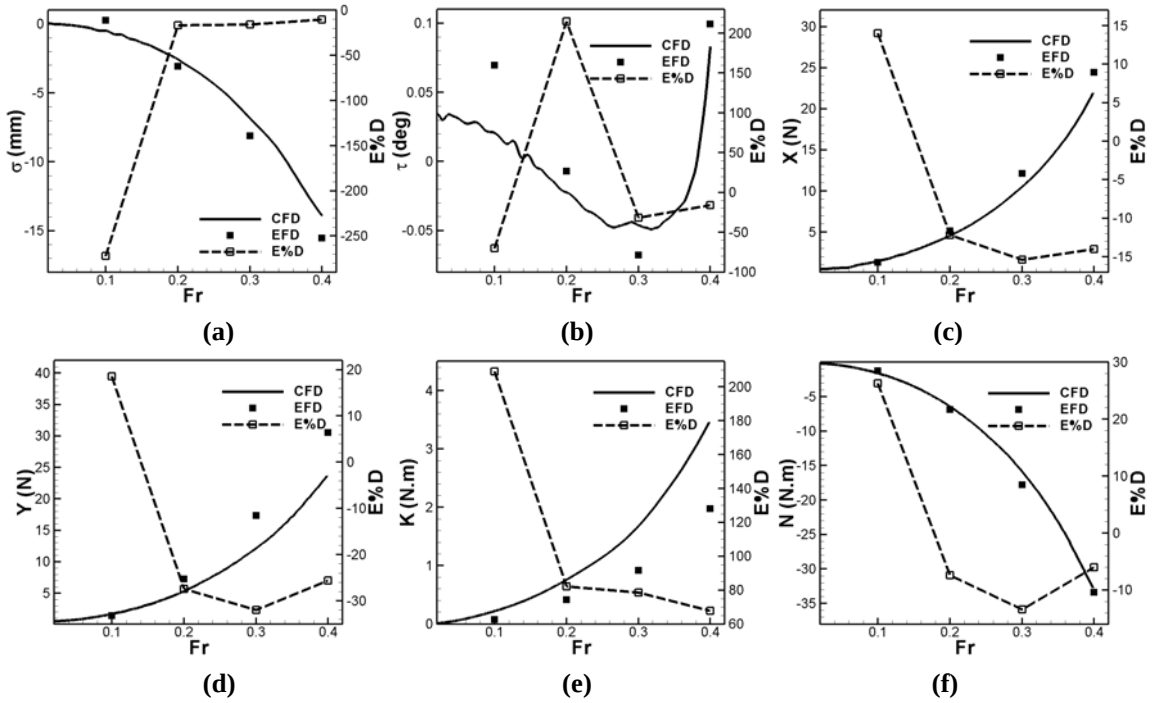

Figure 7-19: Dimensional results for static drift at β=5: (a) sinkage; (b) trim; (c) axial force; (d) side force; (e) roll moment; (f) yaw moment

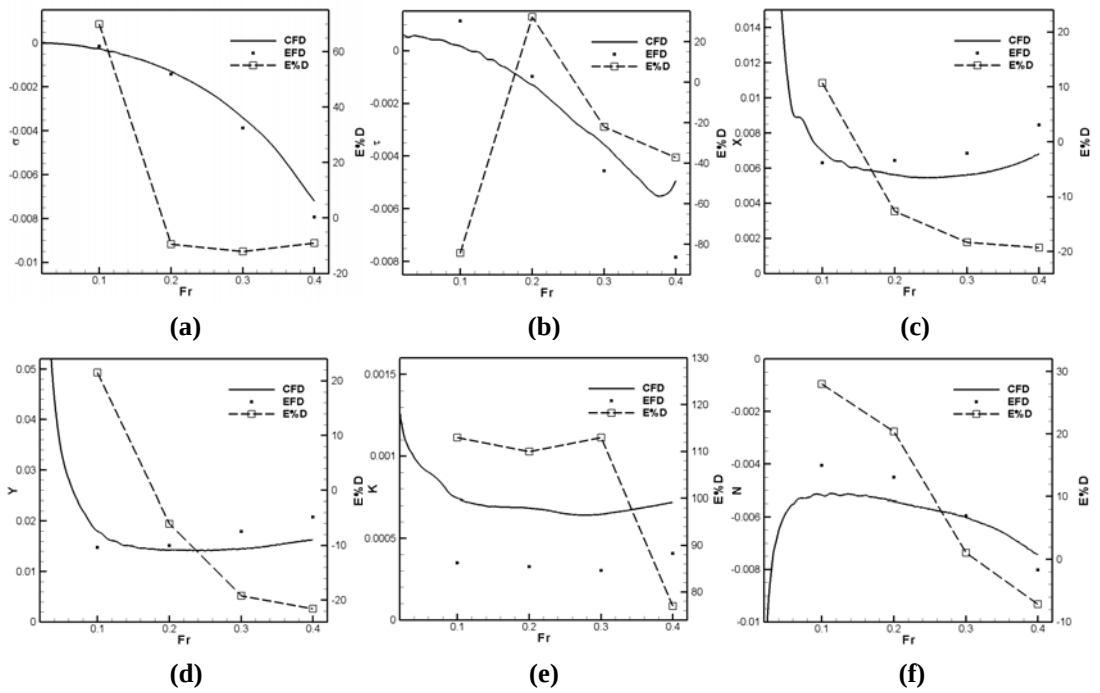

Figure 7-20: Non-dimensionalized results for static drift at β=10: (a) sinkage; (b) trim; (c) axial force; (d) side force; (e) roll moment; (f) yaw moment

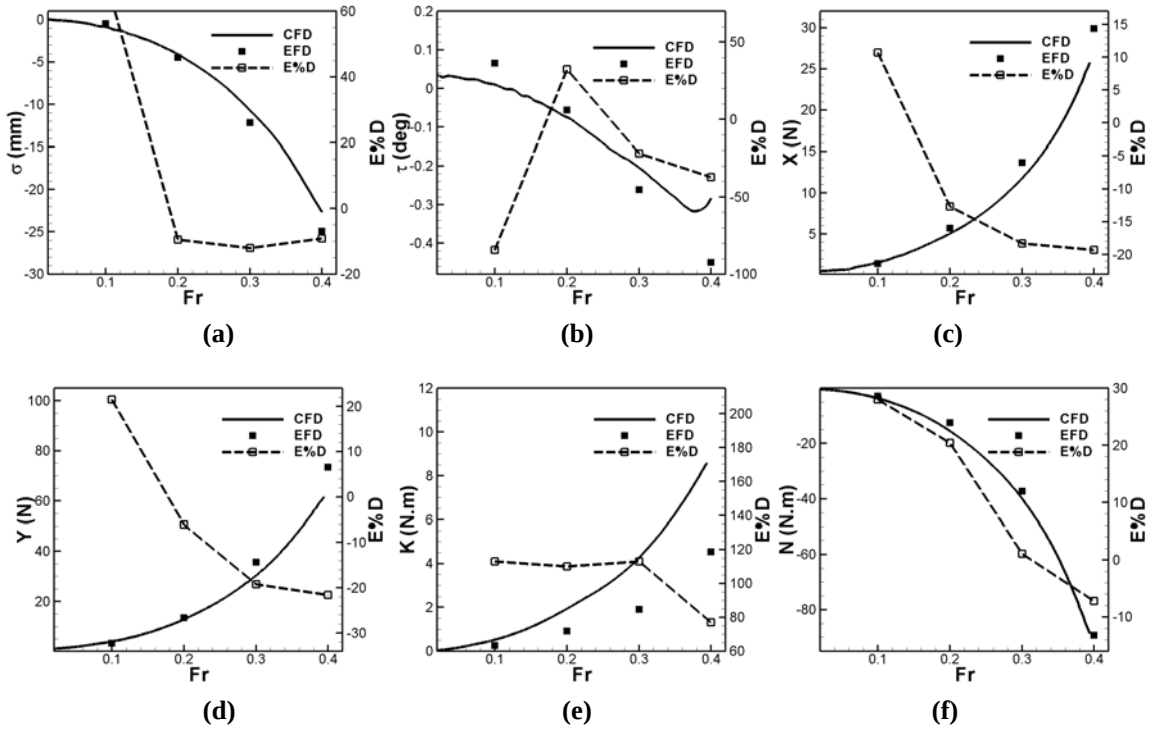

Figure 7-21: Dimensional results for static drift at β=10: (a) sinkage; (b) trim; (c) axial force; (d) side force; (e) roll moment; (f) yaw moment

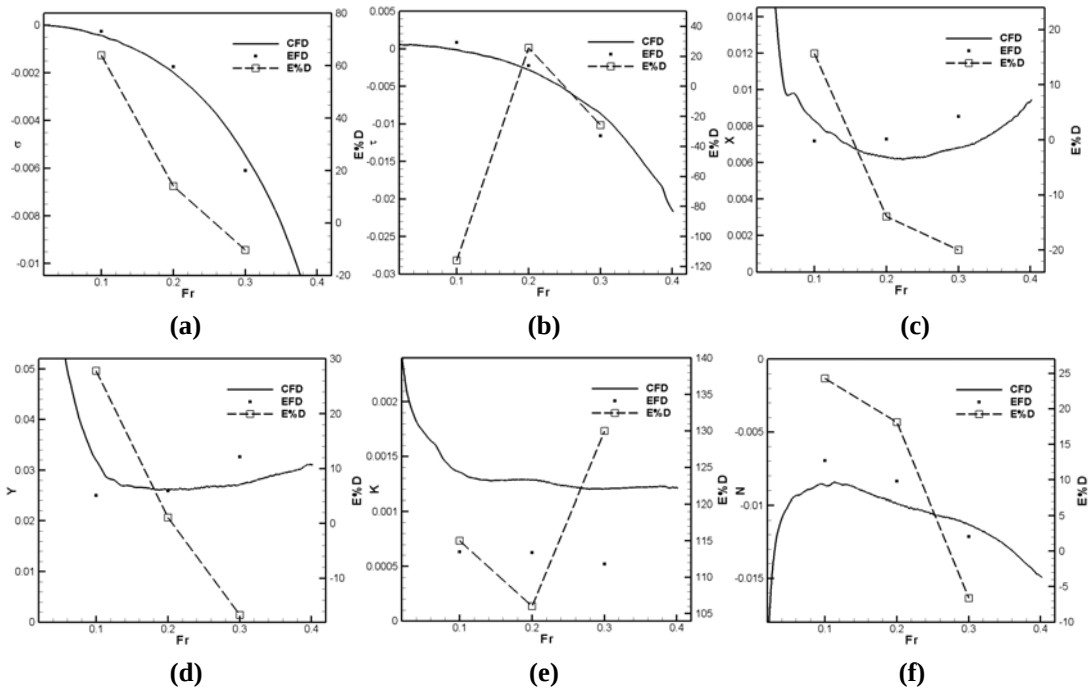

Figure 7-22: Non-dimensionalized results for static drift at β=15: (a) sinkage; (b) trim; (c) axial force; (d) side force; (e) roll moment; (f) yaw moment

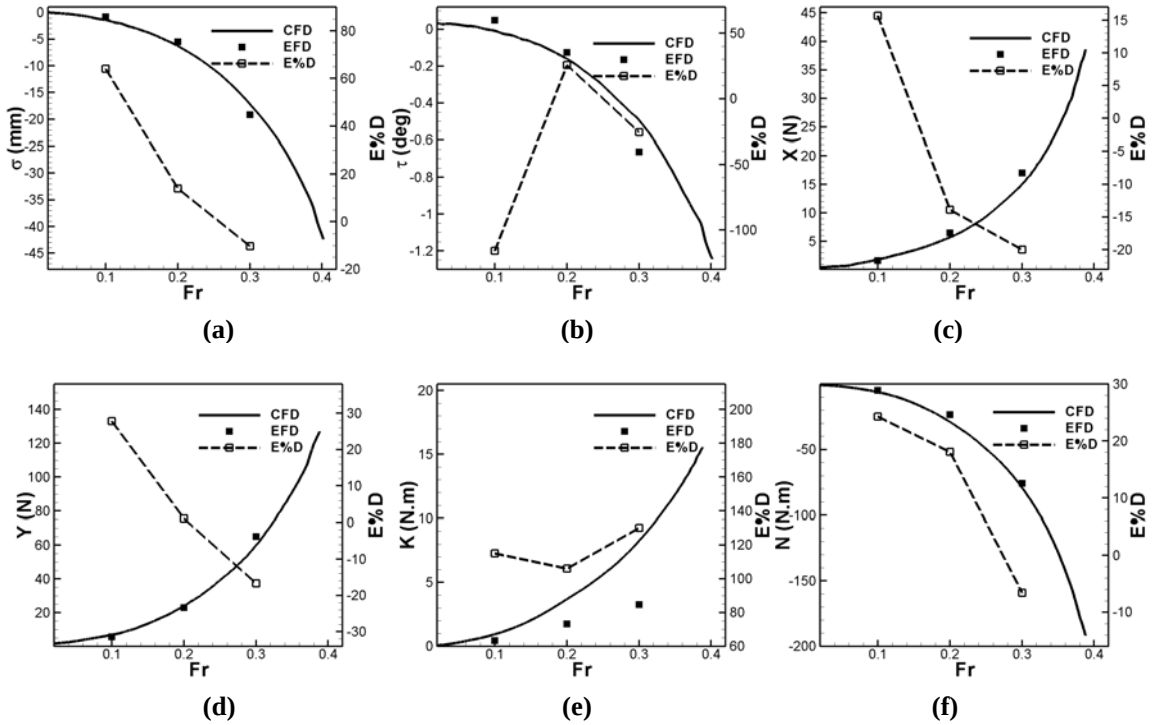

Figure 7-23: Dimensional results for static drift at β=15: (a) sinkage; (b) trim; (c) axial force; (d) side force; (e) roll moment; (f) yaw moment

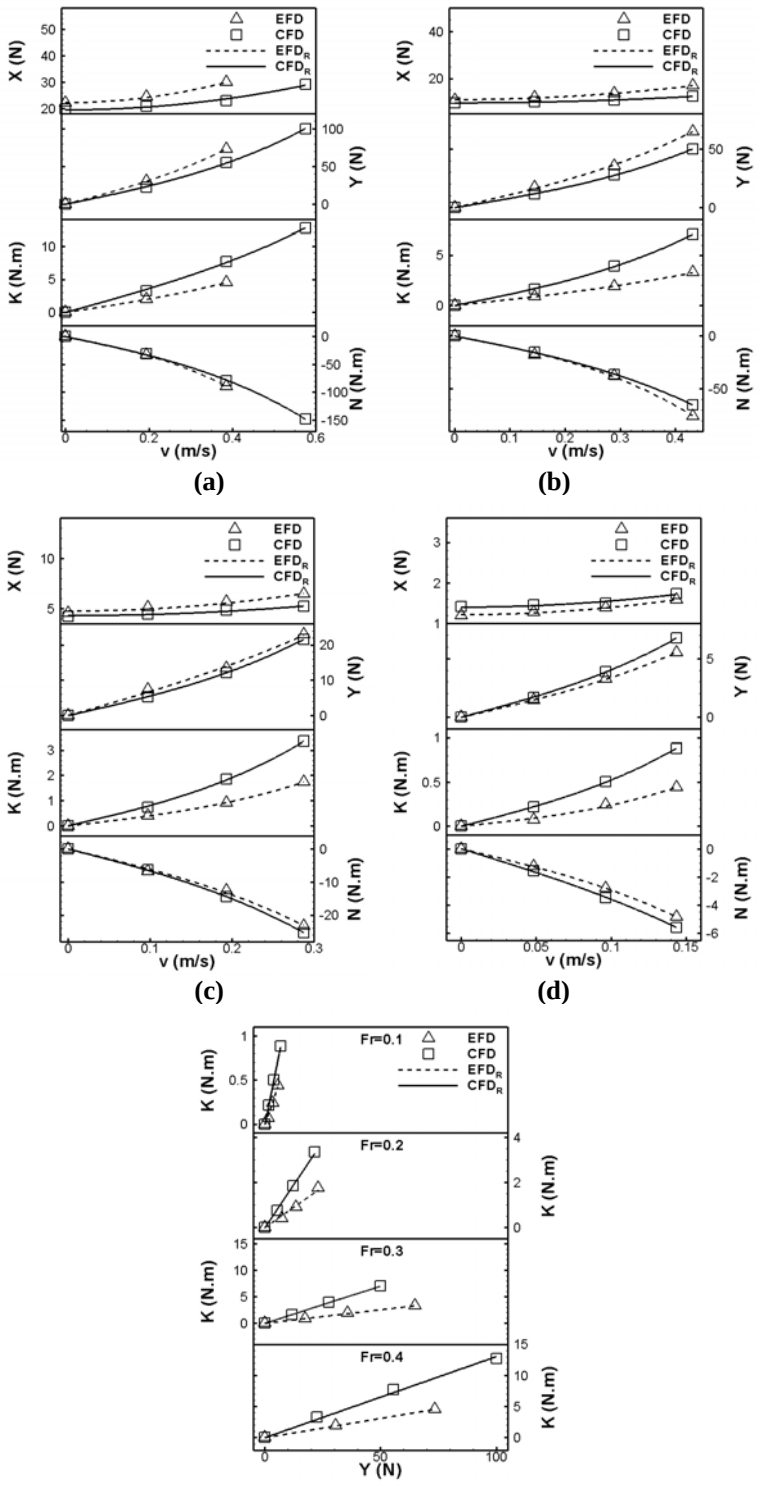

Figure 7-24: CFD and EFD and their reconstructions using regression method: (a) forces and moments vs. side velocity for Fr=0.4; (b) forces and moments vs. side velocity for Fr=0.3; (c) forces and moments vs. side velocity for Fr=0.2; (d) forces and moments vs. side velocity for Fr=0.1; (e) K-Y plot for all Fr

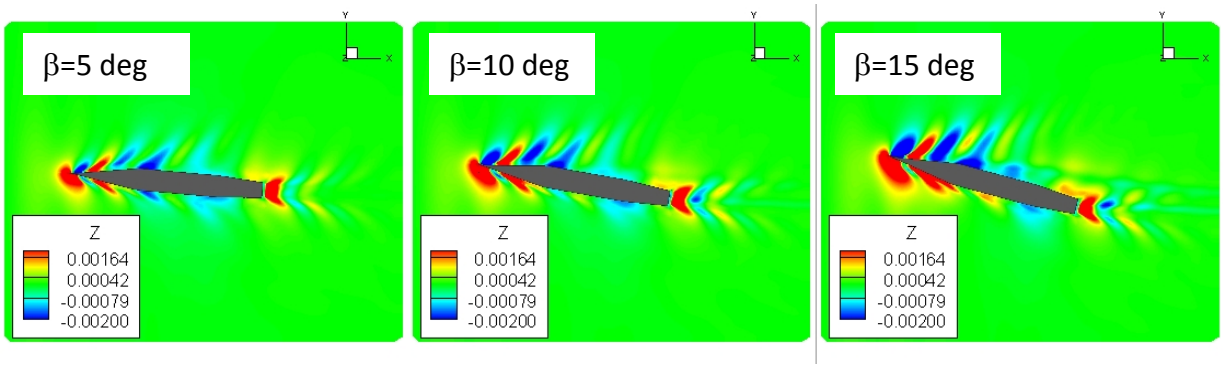

(a)

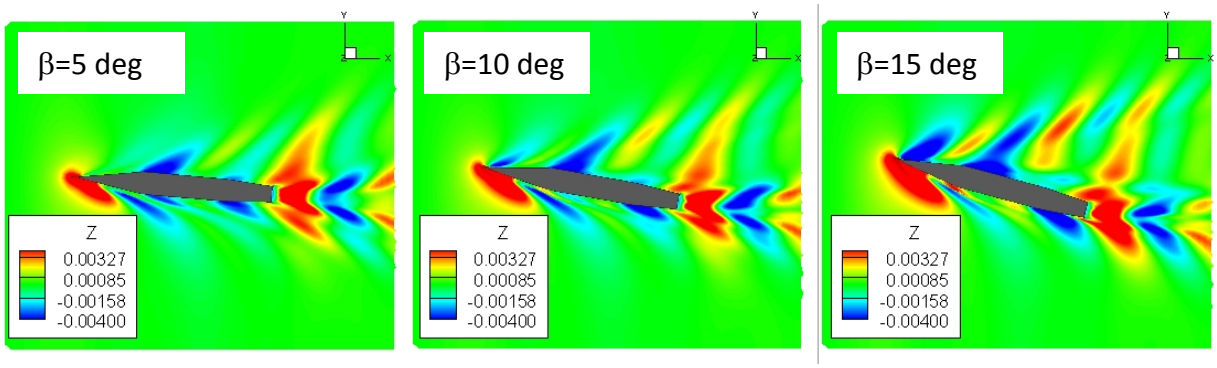

(b)

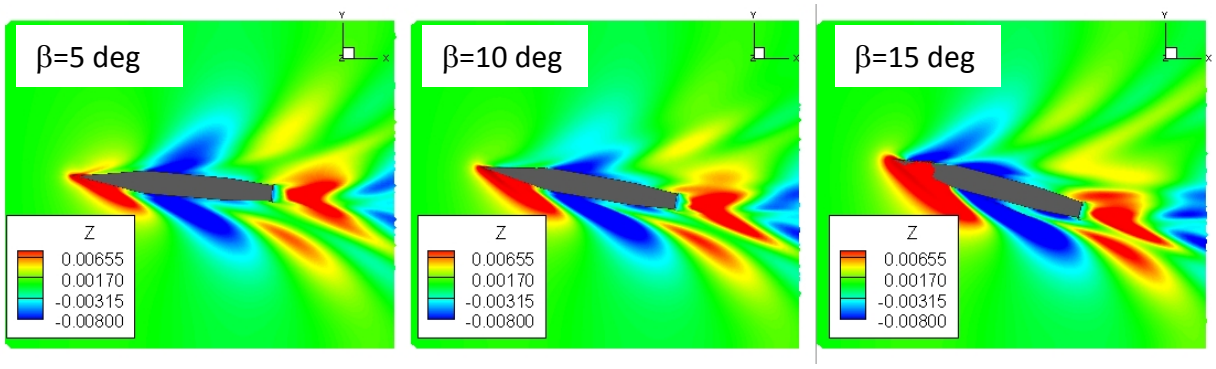

(c)

Figure 7-25: Comparing free surface elevation for static drift angle cases: (a) Fr=0.2; (b) Fr=0.3; (c) Fr=0.4

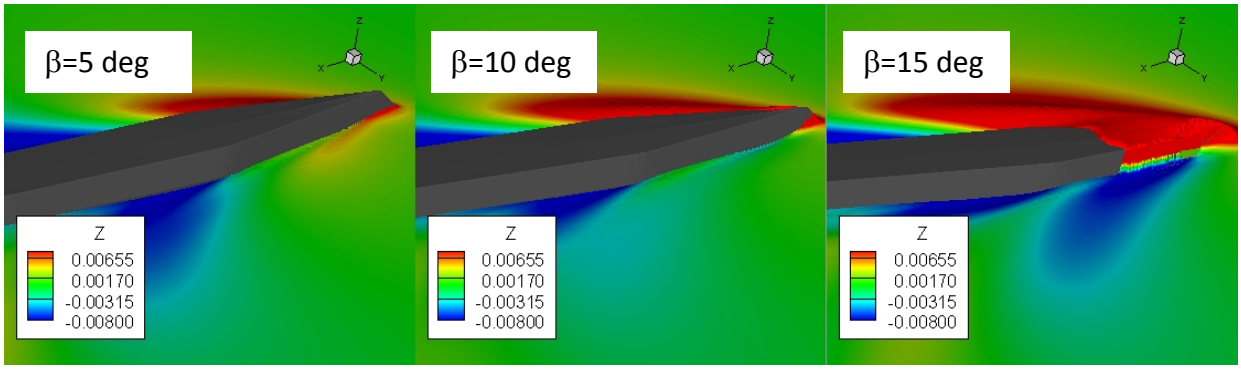

Figure 7-26: Free surface elevation at leeward side for static drift angle cases at Fr=0.4

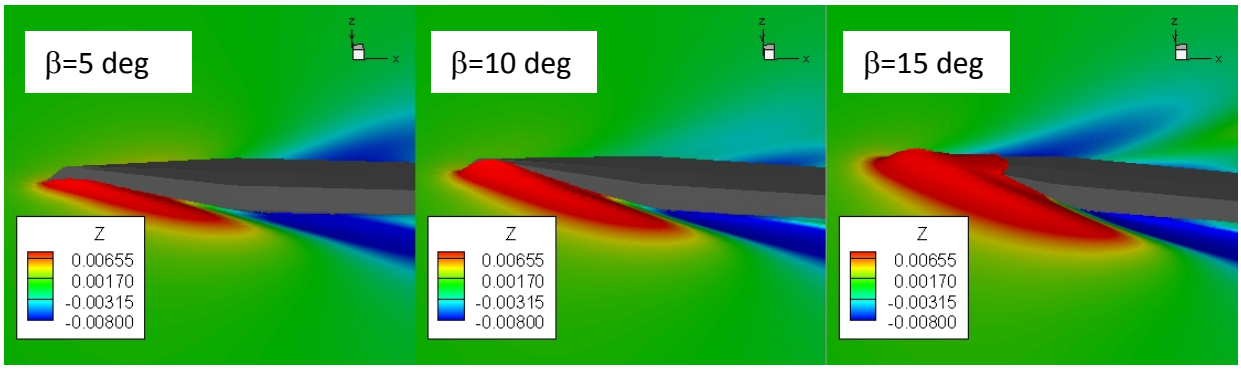

Figure 7-27: Free surface elevation at windward side for static drift angle cases at Fr=0.4

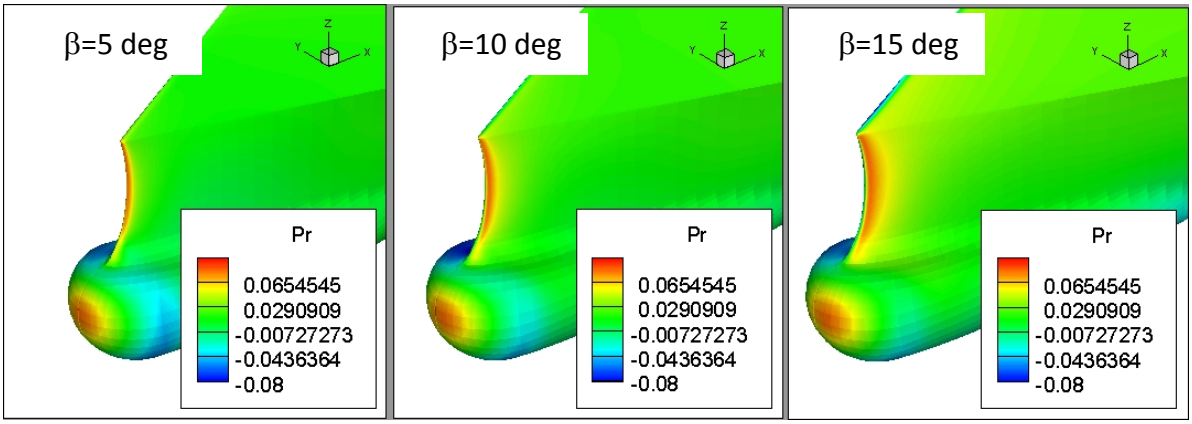

Figure 7-28: Pressure counters on the hull for static drift angle cases at Fr=0.4

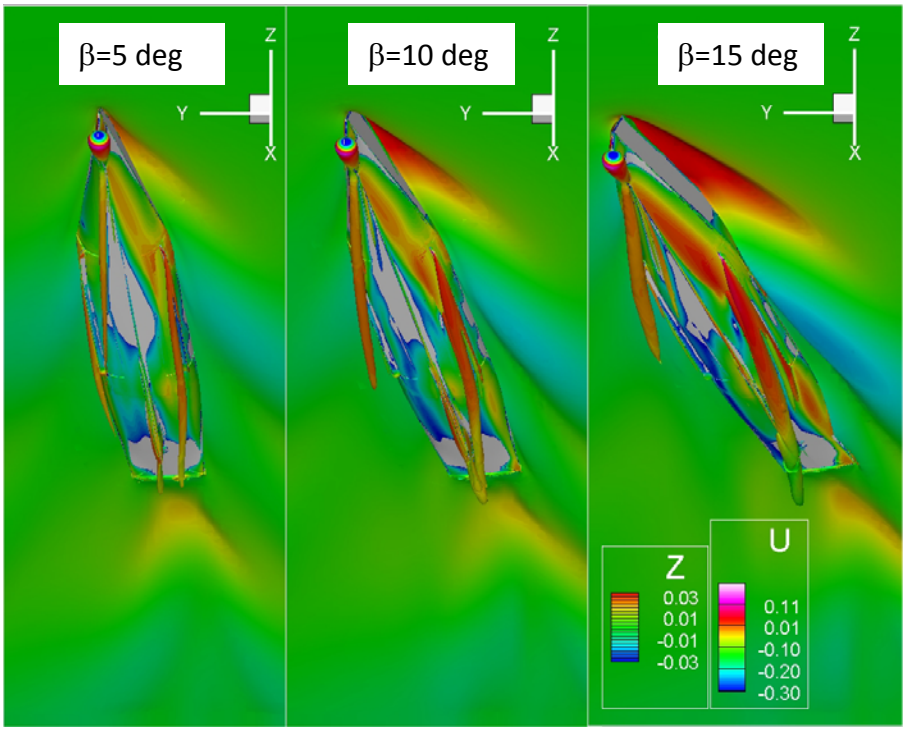

(a)

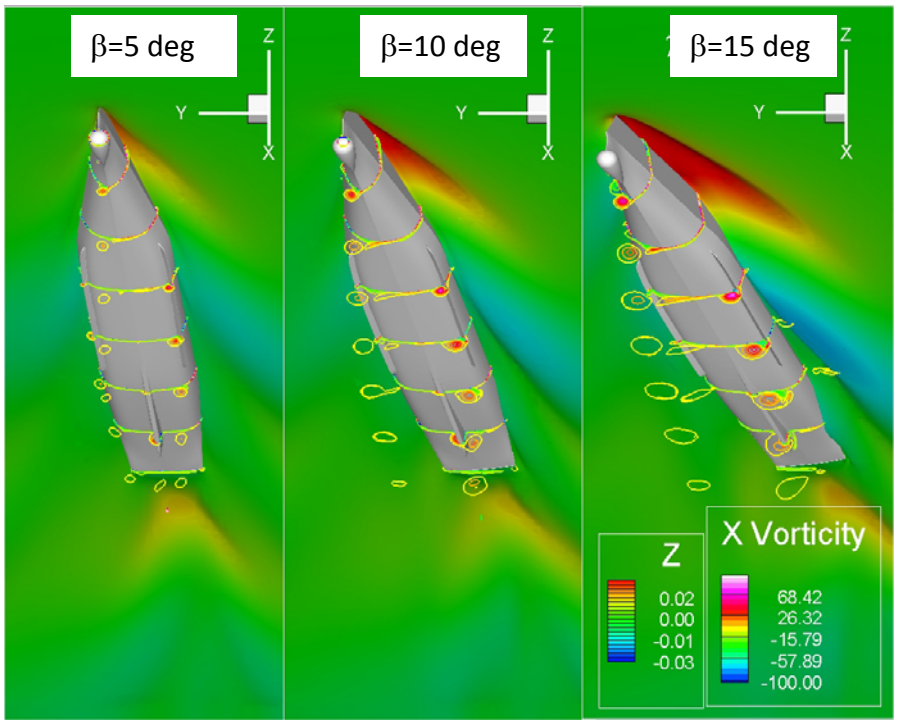

(b)

Figure 7-29: Vortices around the hull for static drift angle cases at Fr=0.4: (a) Iso-surface of q=30 contoured by velocity and free surface contoured by z ; (b) X-vorticity contours at several sections and free surface contoured by z

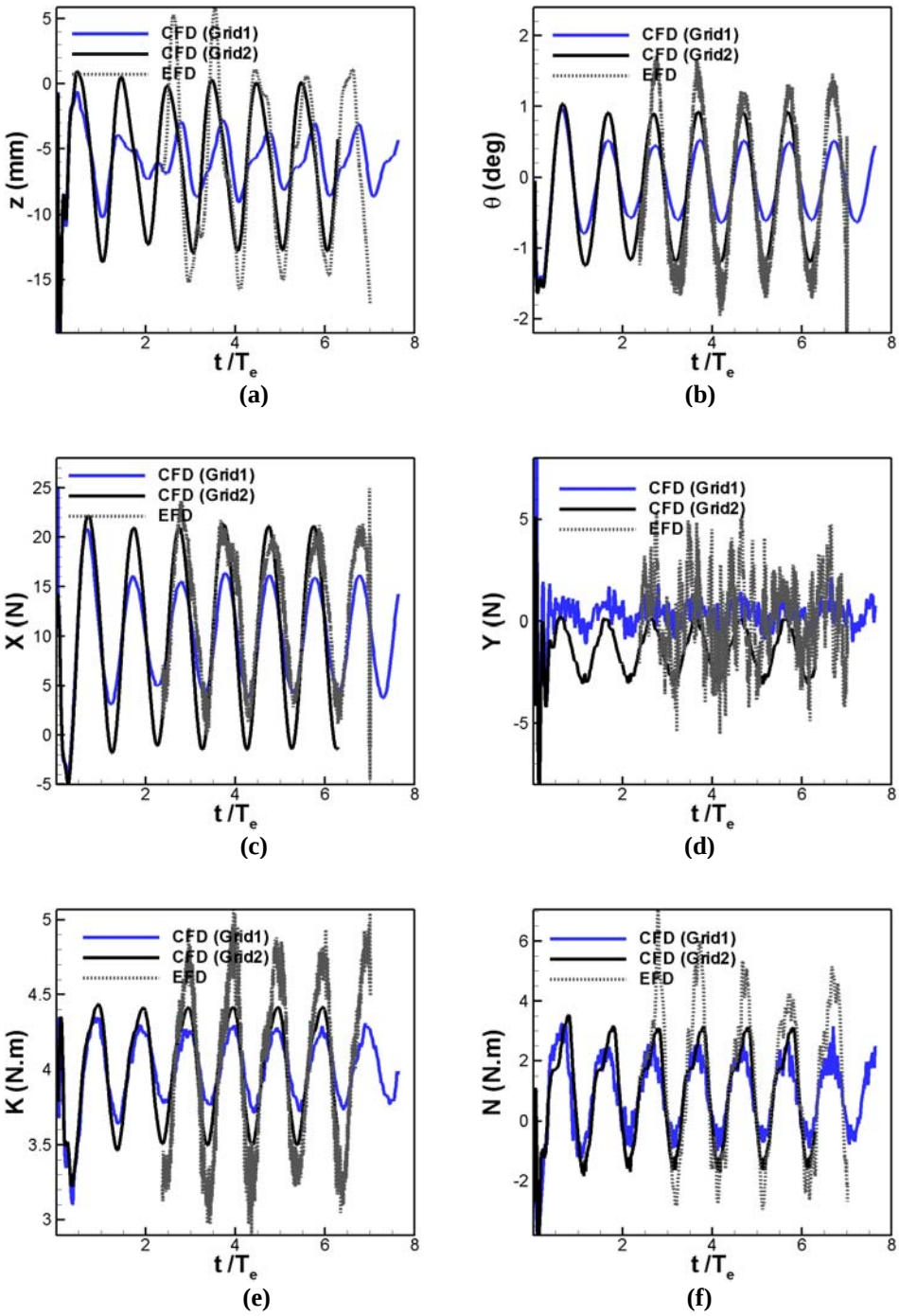

Figure 7-30: CFD and EFD comparison for 10 deg static heel at Fr=0.3 in following waves with H/λ=0.03 and λ/L=1: (a) heave; (b) pitch; (c) axial force; (d) side force; (e) roll moment; (f) yaw moment

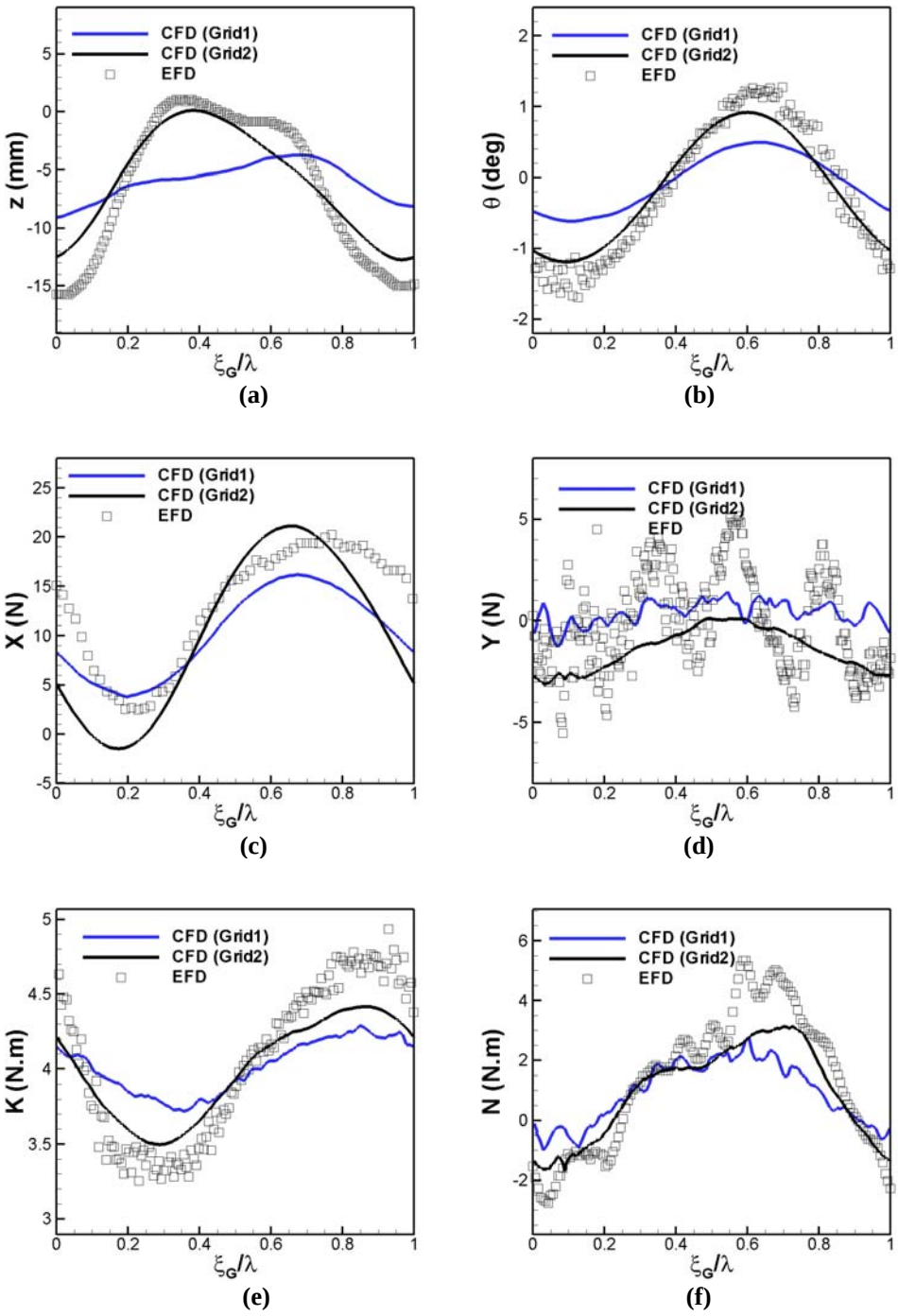

Figure 7-31: CFD and EFD results vs. ship position for 10 deg static heel at Fr=0.3 in following waves with H/λ=0.03 and λ/L=1: (a) heave; (b) pitch; (c) axial force; (d) side force; (e) roll moment; (f) yaw moment

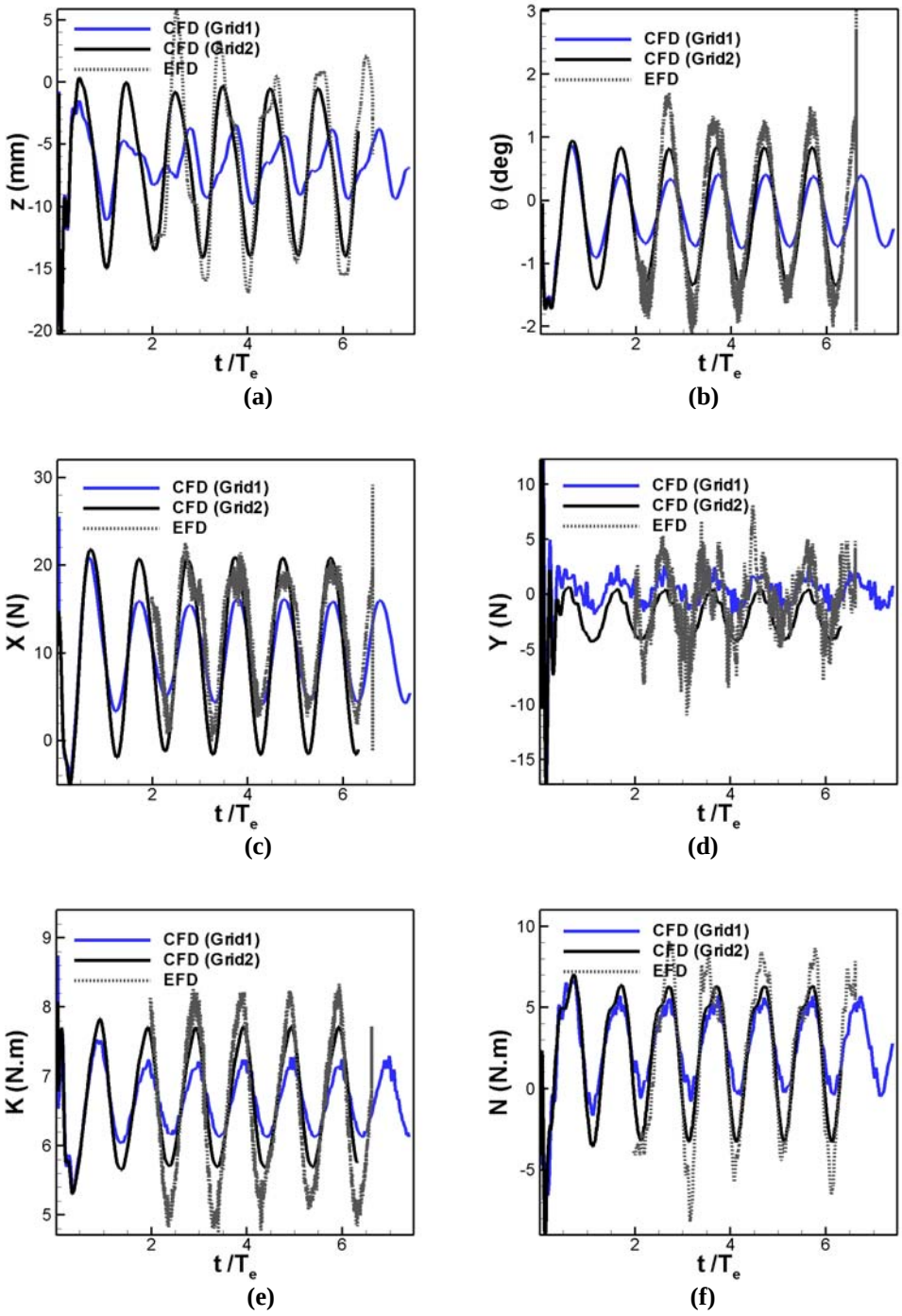

Figure 7-32: CFD and EFD comparison for 20 deg static heel at Fr=0.3 in following waves with H/λ=0.03 and λ/L=1: (a) heave; (b) pitch; (c) axial force; (d) side force; (e) roll moment; (f) yaw moment

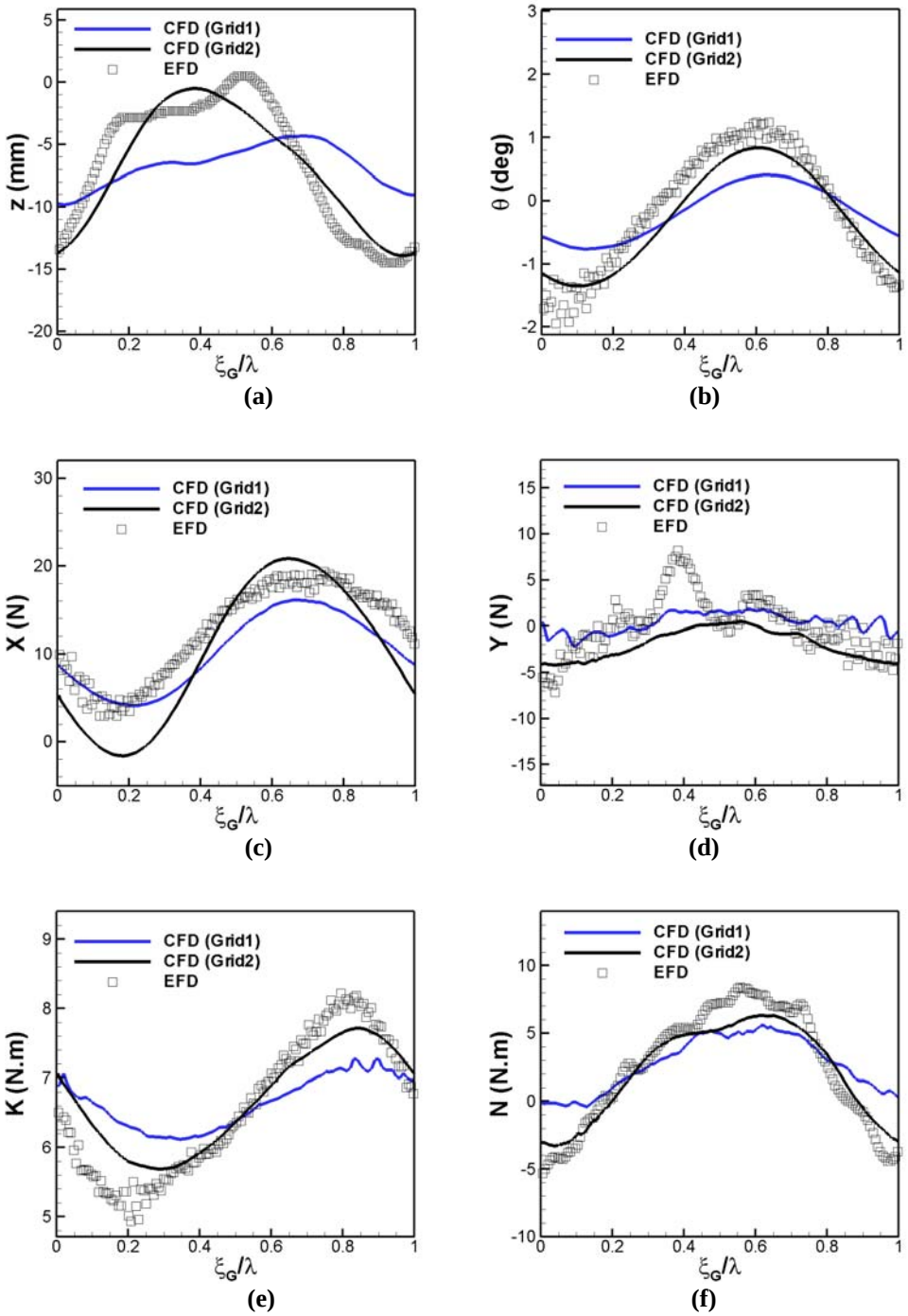

Figure 7-33: CFD and EFD results vs. ship position for 20 deg static heel at Fr=0.3 in following waves with H/λ=0.03 and λ/L=1: (a) heave; (b) pitch; (c) axial force; (d) side force; (e) roll moment; (f) yaw moment

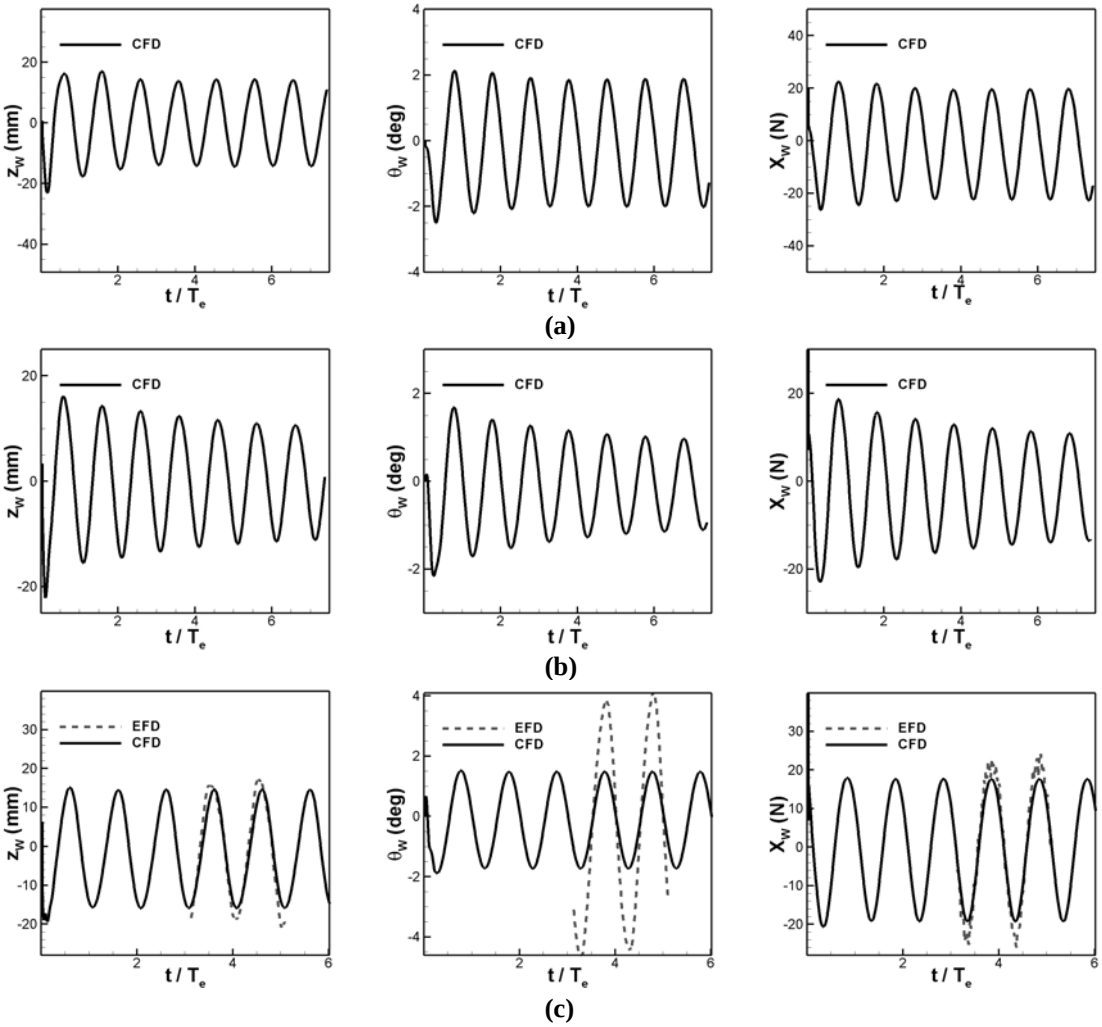

Figure 7-34: CFD and EFD comparison of wave induced heave, pitch, and axial force for zero deg static heel in following waves with H/λ=0.025 and λ/L=1.25: (a) Fr=0.15; (b) Fr=0.25; (c) Fr=0.35

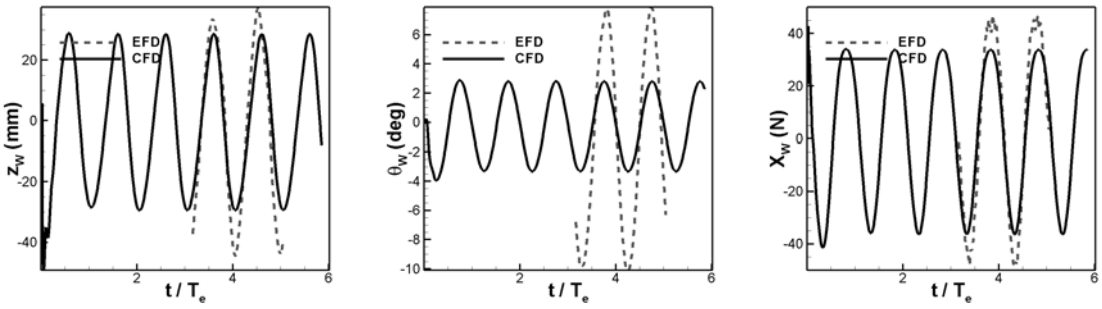

Figure 7-35: CFD and EFD comparison of wave induced heave, pitch, and axial force for zero deg static heel at Fr=0.35 in following waves with H/λ=0.025 and λ/L=1.25

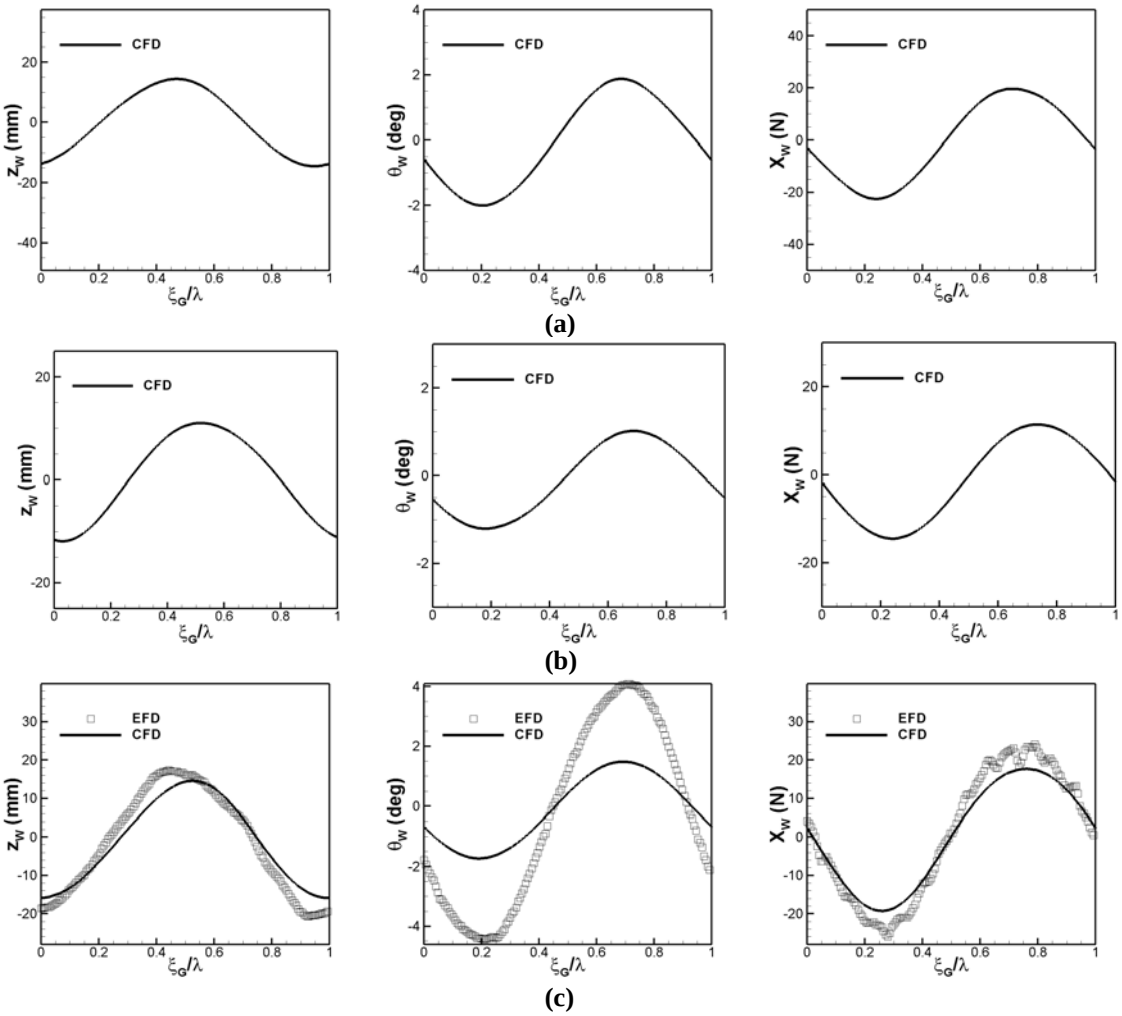

Figure 7-36: CFD and EFD of wave induced heave, pitch, and axial force vs. ξ_G/λ for zero deg static heel in following waves with H/λ=0.025 and λ/L=1.25: (a) Fr=0.15; (b) Fr=0.25; (c) Fr=0.35

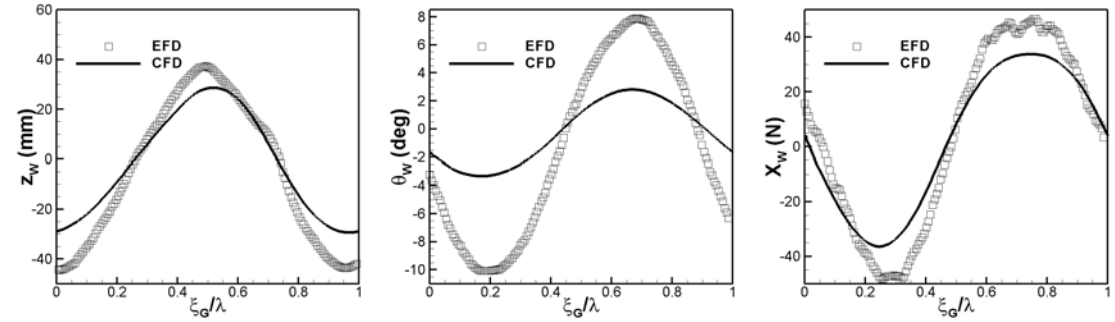

Figure 7-37: CFD and EFD of wave induced heave, pitch, and axial force vs. ξ_G/λ for zero deg static heel at Fr=0.35 in following waves with H/λ=0.025 and λ/L=1.25

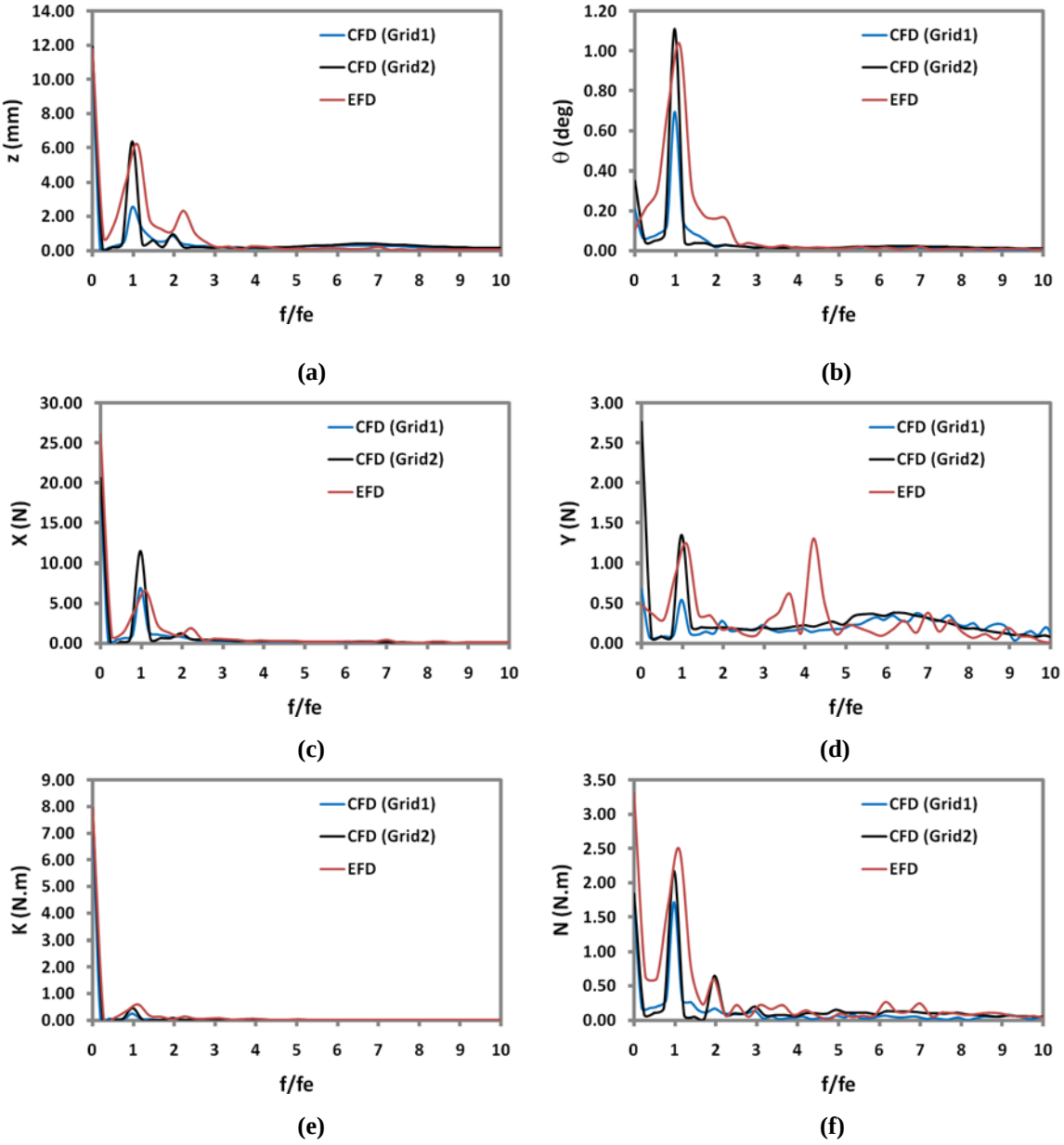

Figure 7-38: FFT results for 10 deg static heel at Fr=0.3 in following waves with H/λ=0.03 and λ/L=1: (a) heave; (b) pitch; (c) axial force; (d) side force; (e) roll moment; (f) yaw moment

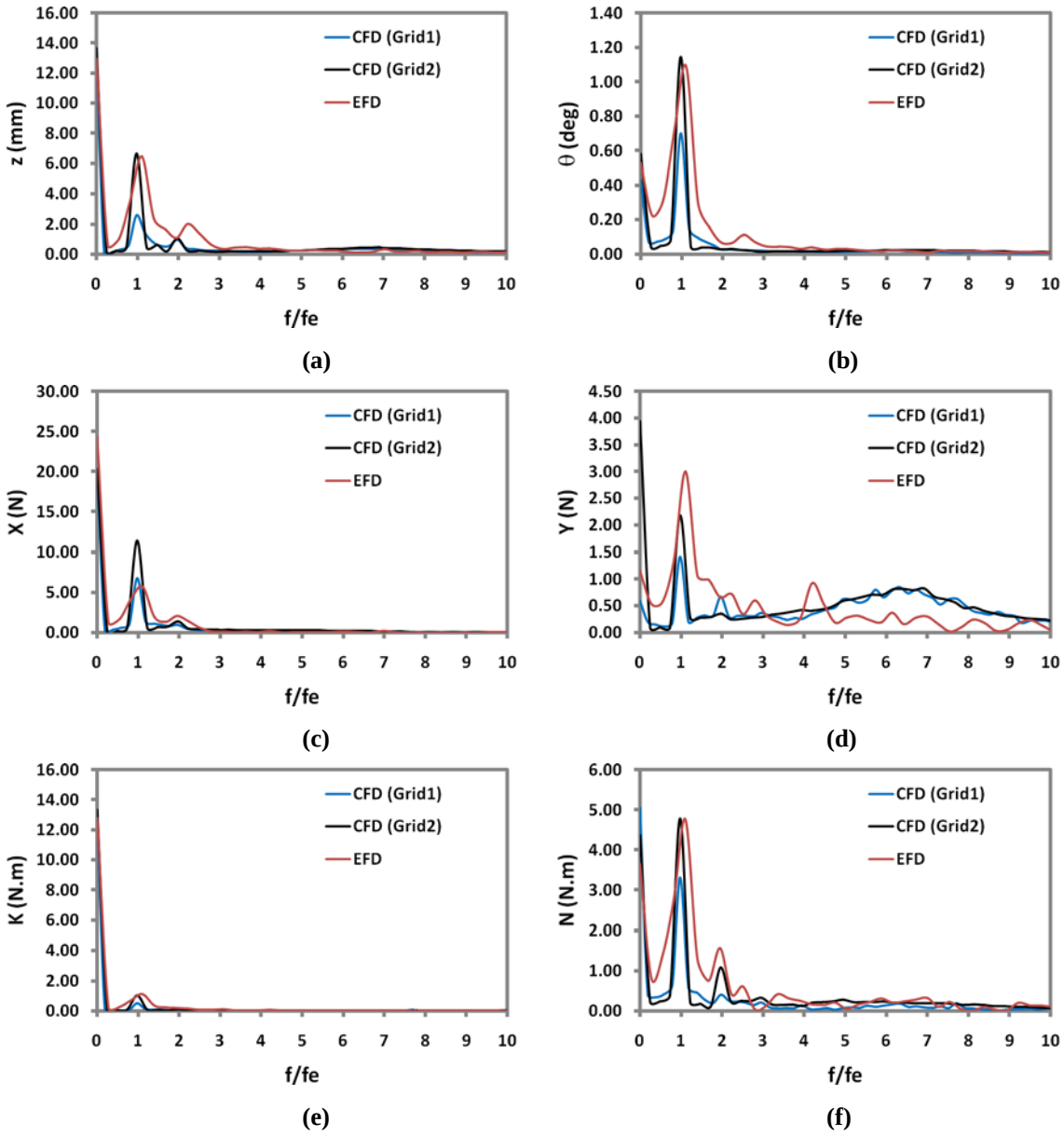

Figure 7-39: FFT results for 20 deg static heel at Fr=0.3 in following waves with H/λ=0.03 and λ/L=1: (a) heave; (b) pitch; (c) axial force; (d) side force; (e) roll moment; (f) yaw moment

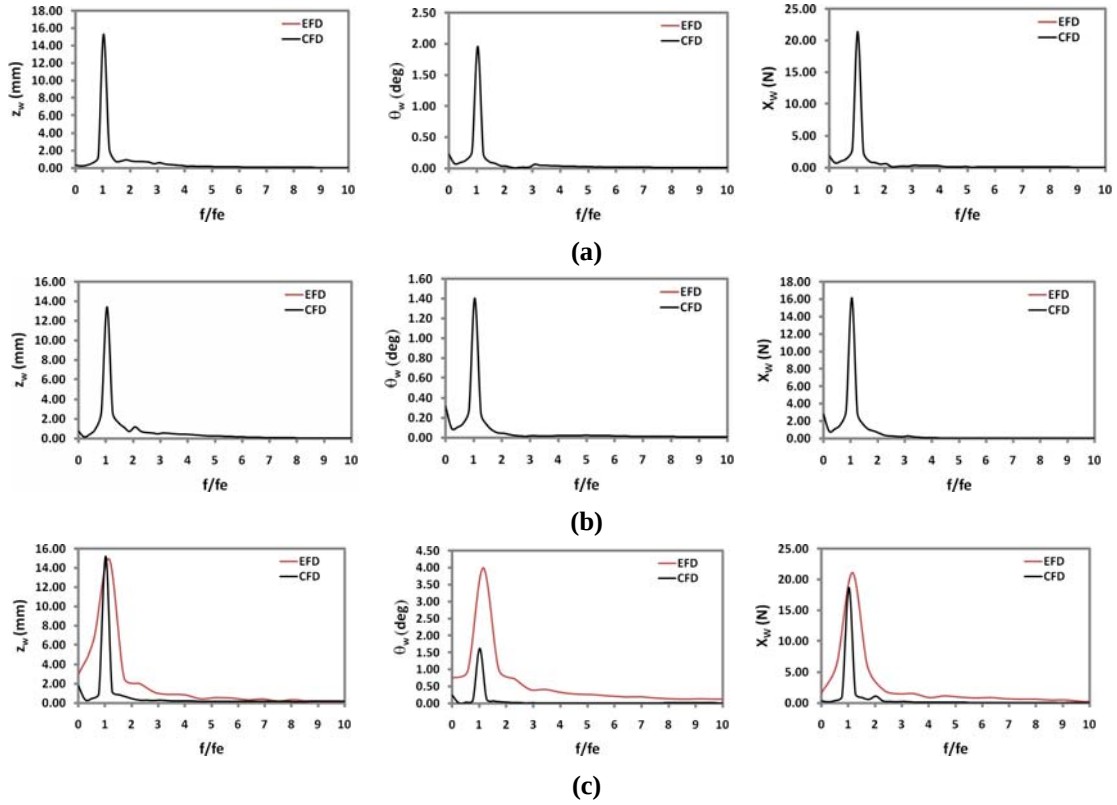

Figure 7-40: FFT of wave induced heave, pitch, and axial force (X_W=X_{total}-R) for zero deg static heel in following waves with H/λ=0.025 and λ/L=1.25: (a) Fr=0.15; (b) Fr=0.25; (c) Fr=0.35

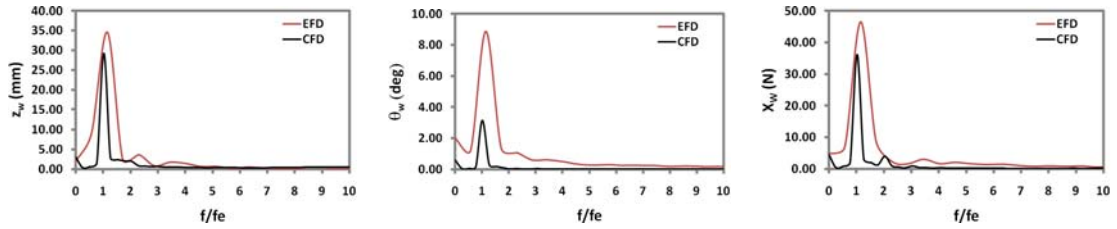

Figure 7-41: FFT of wave induced heave, pitch, and axial force for zero deg static heel at Fr=0.35 in following waves with H/λ=0.025 and λ/L=1.25

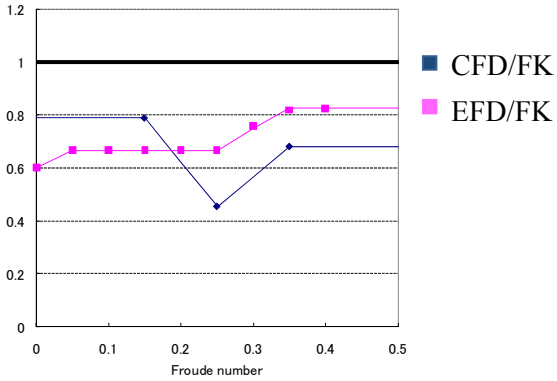

Figure 7-42: Comparison of EFD, CFD, and Potential Theory (Froude Krylov cal.) of wave-induced X force

CHAPTER 8. VALIDATION OF FREE MODEL SIMULATIONS

CFD free model simulations are performed with the same operational and environmental conditions used in the free model tests program 1 and 2 described in Chapter 6. The simulations are performed for series of control parameters (heading and Fr) to study and analyze the process of surf-riding, broaching, and periodic motion. The CFD results are compared with the results of NDA model which is based on the mathematical model described in Chapter 2. The inputs for the mathematical model are estimated from potential flow, EFD, and CFD, as shown in Chapter 7. Herein, the details of CFD simulation including computational domain and boundary conditions, grid, simulation design, 2DOF self-propulsion simulation in calm water, and free model simulation in following/quartering waves are presented and lastly the CFD and NDA results are compared with EFD.

8.1 Computational Domain, Boundary Conditions

The computational domains extend from $-0.6 < x < 1.8$, $-0.6 < y < 0.6$, $-0.8 < z < 0.8$, in dimensionless coordinates based on ship length, as shown in Fig. 8-1. The ship axis is aligned with the x-axis with the bow at x = 0 and the stern at x = 1. The free surface at rest lies at z = 0. The ship model is appended with skeg, bilge keels, and super structure. Twin rudders are included to steer the ship. The original rudders on OT model have a small trunk attached to the hull and a large spade. In this study the rudders are approximated as full spade rudders with no trunk, leaving a small gap between the hull and the rudder spade. This is done to simplify grid generation and overset design for the moving rudders.

Boundary conditions are shown in Table 8-1. Inlet, exit, and sides boundary conditions are imposed such that they follow linear wave theory equations:

$$p = \frac{A}{Fr^2} e^{kz} \cos(kx - 2\pi ft) - \frac{A^2}{2Fr^2 k} e^{2kz} \quad (8.1)$$

$$\phi = A\cos(kx - 2\pi ft) - z(x) \quad (8.2)$$

$$U(x,y,z,t) = U_0 + \frac{A}{Fr}\sqrt{k}e^{kz}\cos(kx - 2\pi ft) \quad (8.3)$$

$$W(x,y,z,t) = \frac{A}{Fr}\sqrt{k}e^{kz}\sin(kx - 2\pi ft) \quad (8.4)$$

Here, U_o is zero since all free model simulations are performed in earth coordinate system.

8.2 Grid

Computational grids are designed using overset technique in which independent grids are created for each appendage and then they are assembled to generate the total grid. The grid for each appendage essentially has to have enough overlap with other grids to communicate correctly with other blocks. Two double-O boundary-layer grids are generated with a hyperbolic grid generator of GRIDGEN to model the starboard and port sides of the hull such that starboard and portside grids are patched together at symmetric plate. Grid spacing at the hull is designed to yield y^+ <1 for wide range of Fr numbers. The superstructure grid oversets the boundary layer grids and is constructed with an H-type topology using hyperbolic grid generator. The superstructure grid allows computations with extreme motions such as capsizing. The skeg and bilge keels use H topology and overset the boundary layer grids. Double-O grids are used for each rudder such that inner side and outer side are patched at symmetric plate. Grid topology was selected so that a Cartesian grid (background block) is responsible to capture the flow far from the hull. Since there is a wave on the free surface, the background block was designed to have enough grid points near free surface. Table 8-2 summarize the grids and Figure 8-1 shows grid for the ship.

8.3 Simulation design

Free model simulations are carried out in earth-fixed inertial coordinate system in which velocity is not given to the flow but it is imposed on the ship. First, the model is simulated in calm water with self-propulsion condition using a speed controller to predict the propeller RPS to reach the target Fr number. The predicted RPS is then prescribed for the free model simulations at the same nominal Fr number to mimic EFD test design.

In free model simulations, propellers and rudders move and rotate with ship motions such as other appendages. However, they are capable of having relative motion respect to the hull. Propeller rotates around its shaft axis and is responsible to make enough thrust. Rudder rotates around z-axis making turning moment. This capability in the CFDShip-Iowa code is achieved by the concept of parent and child object in which propellers and rudders are considered as child object while the hull with other appendages are parent object, as discussed in Chapter 3.

8.3.1 Propellers

Propellers are modeled using actual rotating propeller or using a radial varying body force filed, which follows the variation of a theoretically derived circulation distribution. This body force field is prescribed by means of the ship speed based advance coefficient ($J=U/nD_p$) and open water curves i.e. thrust coefficient $K_T(J)$ and torque coefficient $K_Q(J)$ curves. The open-water curves are expressed as second-order polynomials, and the location and thickness of the actuator disk is prescribed with a vector going from point p1 to p2, with radius r_p and hub radius r_h. Details of the propellers used are provided in Table 8-3.

The propeller rotation speed (RPS) for each free model simulations can be prescribed or predicted. In this study, the propeller RPS is predicted in calm water for each Fr

number and then it is prescribed in free model simulations for the same Fr number to produce enough thrust. This is the same as EFD procedure for free model tests.

8.3.2 Rudders

Rudders are modeled as child object in which they can have relative motions respect to the ship. Rudder deflection can be controlled trough a PID controller as explained in Chapter 3. A PID controller with P=1 and I=D=0, the same as EFD, is used for rudders to change rudder deflection and turn the ship toward the target direction. This kind of controller would turn rudders exactly the same as course deviation since P=1 and other terms are zero. For each free running case, maximum rudder deflection and deflection rate are also specified as given by EFD to have the same behaviour for CFD and EFD rudder controller.

8.4 Self-Propulsion Simulations in Calm Water

As explained earlier, 2DOF self-propulsion simulations free to sink and trim in calm water are performed to indicate propeller RPS needed to push the ship to surge at target Fr number. This simulation is carried out for Fr=0.25, 0.3, 0.35, 0.4, and 0.45.

Figure 8-2 demonstrates CFD propeller RPS, thrust force, and ship motions calculated for all target Fr. As it is shown, the propeller RPS is changed by controller to reach the ship speed to the target Fr. After this point, the propeller RPS, thrust force, and ship motions are fairly constant. As shown in Fig.8-3, propeller RPS and sinkage increase linearly from low to high Fr whereas the thrust force and trim increase nonlinearly. The CFD and EFD comparison of propeller RPS demonstrates that CFD over predicts propeller RPS by E=5.8%D due to the fact that propeller model has some significant limitations. The most important issue is that the thrust and torque do not depend on the local flow field near the propellers, but on the total velocity of the ship. In addition, the body force is axisymmetric and side forces are neglected. In order to evaluate accuracy of

body force propeller model, CFD simulation is also carried out for actual dynamic propeller, as shown in Fig. 8-3, and indicated that RPS error drops to 1.7%D using actual propeller. This suggests the simplicity and efficiency of body force propeller model would cost about 4%D more error which is reasonable.

8.5 CFD Free Model Test Program 1

CFD studies are performed for $\lambda/L=1.25$, $H/\lambda=0.05$, GM=2.068 m and ψ_c = 5, 15, 30 deg, and GM=1.78 m and ψ_c = 15 deg. The simulation is carried out at Fr=0.4. The initial wave phase and surge velocity are not provided by experimental data and are estimated from EFD pitch history or/and trial and error method. Initial roll, pitch, yaw angle and rudder deflection are estimated from their experimental time histories. The propeller RPS is fixed during the simulation and a proportional heading controller with gain P=1 is used based on the deviation from the target heading. The propeller RPS at each nominal speed is obtained by running the self propulsion model in calm water, as explained earlier.

8.5.1 Fr=0.4 & GM=1.78 m

8.5.1.1 ψ_c = 15 deg

Figure 8-4 shows time histories of motions, forces, and moments on the hull, rudder, and propeller for the case of broaching where GM=1.78 m and ψ_c = 15 deg. Initial wave phase=264 deg and surge velocity=0.15, estimated from trial and error method, are used as shown in Table 8-4. The roll and pitch angles show that the model moves slightly slower than experiment, probably due to inaccurate initial conditions and/or variable EFD propeller RPS. The yaw shows that the initial heading is around 30 deg and controlled by rudder to reach desired course (ψ_c = 15). However, after about 5 seconds the ship starts turning broadside to the waves eventually broaching, with the rudder turned hard to port but unable to steer the ship. Figures 8-4b and 8-4c show active forces and moments.

Active forces and moments are those that voluntary or involuntarily modify the heading of the ship (hydrostatic forces/moments caused by the waves, and forces/moments caused by rudder action and by the propeller). Reactive moments are those that oppose the yaw motion, including dynamic pressure and friction moments. The yaw moments indicate that hydrostatic/wave yaw moment is about N_h=-100 N.m after t=5 sec while rudder reaction moment is about N_R=20 N.m which is not enough to resist to wave yaw moment. The ship stays in this condition for a while which causes reaching to 60 deg heading off from target and broaching. The propeller yaw moment is ten times smaller than rudder moment and it is negligible. In fact, propeller yaw moment and roll moment should be zero unless one of two propellers is temporally emerged out of water due to large roll angle as shown in Fig. 8-4c.

8.5.2 Fr=0.4 & GM=2.068 m

8.5.2.1 ψ_c = 5 deg

Figure 8-5 shows the case of stable surf-riding with GM=2.068 m and ψ_c = 5 deg. Initial wave phase=230 and surge velocity=0.2 are used based on trial and error method shown in Table 8-5. After an initial transition in which one wave overcomes the ship, the model reaches to enough forward speed to travel locked in waves. During the transition part, the rudder turns the model to the desired course very rapidly so that the ship travels with tight heading and is quickly captured by the wave down slope causing negative pitch angle at t=3 sec. After that, ship velocity reaches to wave velocity and ship is in surf-riding condition. Since relative ship position respect to waves is fixed during surf-riding, the motions, forces, and moments reach to the steady-state condition in which active and reactive forces/moments are balanced.

8.5.2.2 ψ_c = 15 deg

Figure 8-6 illustrates the broaching case where GM=2.068, ψ_c = 15 deg, and Fr=0.4. Initial conditions for wave phase and ship speed are 50 deg and 0.4, based on CFD simulations shown in Table 8-6. In overall, CFD model moves slower than experiment because EFD propeller RPS is 10% higher than CFD. This is due to the fact that EFD controller for propeller is not accurate enough to keep the propeller RPS constant. Pitch motion indicates the ship is captured by wave down slope ending up with surf-riding starting after t=2 sec and continuing for about 6 seconds. The surf-riding region can be seen from wave axial force and wave pitch moment time histories too. During surf-riding, the negative yaw angular velocity not only results in turning broadside to the wave but also induces a centrifugal force together with large forward velocity. This centrifugal force causes the roll angle of +50 deg. Also, the yaw moment originated by the wave becomes strong enough after t= 5 sec than any other active moment trying to counteract it, essentially the rudder moment, and results in broaching at t=9 sec.

8.5.2.3 ψ_c = 30 deg

Figure 8-7 shows the case of periodic motion with GM=2.068 m and ψ_c = 30 deg. Initial wave phase=20 deg and surge velocity=0.33 are applied, based on Table 8-7. The yaw angle shows that the model is released at 40 deg heading. At t=2 sec, wave induced yaw moment (N_h=-120 N.m) is stronger than rudder reaction moment (N_R= 20 N.m) so that the vessel turns hard causing 70 deg heading at t= 4 sec. At this time, ship is almost in beam waves inducing positive yaw moment and pushing the ship to turn toward the target heading. The ship reaches to target at t=8 sec where huge wave induced yaw moment turns the ship away from target heading and forms a periodic motion.

8.6 CFD Free Model Test Program 2

CFD studies are performed for λ/L=1.25, H/λ=0.05, Fr=0.3,0.35, 0.4, 0.45, GM=2.068 m and ψ_c = 5, 15, 22.5, 30 deg. The initial wave phase and surge velocity are not provided by experimental data and estimated from EFD pitch history or/and trial and error method.

8.6.1 Fr=0.4

8.6.1.1 ψ_c = 5 deg

Figure 8-8 shows the surf-riding case where ψ_c = 5. The pitch motion shows that the model is released at +4 deg and overtaken by waves very fast such that pitch reduces to -2 deg at t=1 sec. At this point, the bow is down and ship is locked in wave downslope so that pitch angle never returns to positive value and surf-riding happens. The roll motion indicates that the ship is almost at stable upright position during surf-riding. The rudder and yaw motion show that rudders turns to 20 deg right after releasing the model to turn the ship from 30 deg heading to the target heading (ψ_c = 5). However, it seems that the model stays at 10 deg heading and cannot reach to the target. This might be due to the type of PID controller (P=1, I=D=0) used for rudders. In fact, the controller would not react fast for small heading deviation so that rudders turn very slowly after t=8 sec. CFD is performed for several initial wave phase and ship speed, as shown in Table 8-8, and obtained initial wave phase and ship speed about 50 deg and 0.2, respectively. In overall, CFD predicts the trend of motions. However, CFD results show that CFD model moves slower than EFD and that is due to the difference between CFD and EFD propeller RPS as shown in Fig. 8-8a. CFD trajectory shows the surf-riding occurrence clearly. Figures 8-8b and 8-8c illustrate forces and moments due to waves, rudders, and propellers. Propeller forces and moments are very small compare with other forces and moments. Propeller thrust (X_P) shows that it is maximum at releasing condition (Fr=0.2) and

reduces by factor of ¼ after couple of seconds. This introduces that ship speed is increased by factor of about 2 during the simulation such that Fr reaches to 0.4 which is close to wave velocity. In other words, it is confirmed that the model is locked in waves and moves with it which results in surf-riding. Since the model is appended with twin counter rotating propellers, the total propellers roll and yaw moment are zero unless part of one propeller emerges out of water. Figure 8-8 indicates that propellers are partially out of water at the first couple of seconds due to large roll angle. The CFD prediction of forces and moments on hull and rudders could explain the process of surf-riding. Yaw moment indicates the N_H is very large up to t= 3 sec so that rudders cannot counteract it. After t=3 sec, the wave moment drops significantly since the ship speed is close to wave speed and the model is locked in waves. Consequently, rudders can work against waves moment such that N_R=+20 N.m and N_H=-20 N.m and turn the model toward the target while the model is seized in waves.

8.6.1.2 ψ_c = 15 deg

Figure 8-9 shows the surf-riding case where ψ_c = 15. Pitch motion shows that the ship is released while bow was down. However, the waves overtake the model and induce positive pitch at t=3 sec and negative pitch at t=4 sec. Then the model stays with negative pitch showing that it is locked in wave i.e. the model surf-rides. The yaw angle show clearly the surf-riding occurrence after t=7 sec. The turning speed of the model (rate of yaw angle) is very large between t=4 (right after overtaking by wave) and t=7 sec (before surf-riding). This produces very large centrifugal force causing fairly large roll angle during this time as shown in roll motion in Fig. 8-9a.The yaw motion is also indicates that initial heading is 10 deg whereas it reaches to 25 deg during surf-riding. Note that the target heading is 15 deg and the model passes the target heading around t= 5 sec. CFD is performed for the different initial conditions, as shown in Table 8-9, and 235 deg and 0.1 are used as the initial wave phase and ship speed, respectively. In overall, CFD predicts

the same phenomenon even though it shows small phase lag compare with EFD trend of motions. The yaw motion shows that the CFD model is at 25 deg heading during surf-riding similar to EFD but it oscillates more. The CFD drift angel indicates that during the time that ship turning speed is large, the model moves with 20 deg roll and about 3 deg drift angle. The prediction of propeller thrust shows that the model reaches to minimum speed/maximum thrust when the ship is going to be overtaken by waves and reaches to maximum speed/minimum thrust during surf-riding. Yaw moment indicates that rudders and waves moment are negative up to t=3 sec i.e. the model is even pushed by waves to move toward the target. After t=3 sec, the wave moment is still negative and much bigger than rudder counteracting moment such that the model reaches to 25 deg heading at t=6 sec. Later, the rudder yaw moment reaches roughly to wave moment amount such that ship stays relatively at 25 deg heading.

8.6.1.3 ψ_c = 22.5 deg

Figure 8-10 shows the case of broaching. The model is released at zero roll and pitch angle and 5 deg heading. The pitch angle indicates that the model is on the wave downslope for about 6 seconds in which pitch angle is negative. Basically, surf-riding is observed during this period. Then the model is surpassed by several waves causing oscillatory pitch motion. Yaw angle indicates that the model is released at 5 deg heading and reaches to 60 deg heading during surf-riding. After that, the rudders reach to their maximum deflection (35 deg) and are not able to control the model. The model continues turning up to 80 deg heading and broaches. The roll angle shows that the rate of yaw angle (turning rate) during surf-riding produces strong centrifugal force such that the model rolls up to 60 deg. However, the model is not involved in capsize process due to large roll restoring moment produced by its superstructure. Since initial conditions of wave phase and ship speed are unknown, they are estimated 200 deg and 0.55, based on Table 8-10. The CFD simulation predicts broaching and all other modes of motions. The

CFD model trajectory demonstrates broaching occurrence after surf-riding. It is observed that the model has about 15 deg drift angle during broaching. The propeller, rudder, and hull forces and moments provide more details of broaching process. The propellers thrust explain that the thrust is positive and the propellers produce resistant instead of thrust. According to Table 8-3, K_T would be negative for very large J or speed (J=U/nD). Herein, initial ship speed (Fr=0.55) is large such that K_T is negative and propellers produce resistant instead of thrust. After t=2 sec, the model speed reduces to wave speed and ship is locked in waves and surf-rides. During surf-riding, the wave yaw moment increases to N_H=-100 N.m and rudder moments reach to their maximum N_R=+40 N.m such that the rudders cannot counteract wave yaw moment and the model broaches.

8.6.1.4 ψ_c = 30 deg

Figure 8-11 shows the case of periodic motion. The model is released at +2 deg pitch and zero deg roll angle. The initial heading is 10 deg. The pitch motion shows that the model is overtaken by waves such that the bow moves up and down. The yaw angle shows that the model reaches to 60 heading at t=5 sec. However, the model is located on wave upslope at t=5 sec such that wave yaw moment would be positive and return the model to the target. More than that, rudders take the control of the model with 35 deg deflection. Then, the model moves toward the target such that the heading reduces to 45 deg (target heading is 30 deg) at t=7 sec. At this point, the bow is down and the model is located on the wave downslope such that wave yaw moment would be negative and turn the model to 60 deg heading at t=9 sec, similar to heading at t=5 sec. This introduces periodic motion with period of 4 sec which is basically encounter period at 60 deg heading respect to waves. During periodic motion, the large yaw rate produces large roll angle. The CFD simulation is performed for 144 deg initial wave phase and 0.2 ship speed, as shown in Table 8-11. CFD shows very good agreement with EFD in terms of the amplitude of motions and phase. CFD results indicate that the model reaches to about

10 deg drift angle after t=5 sec where periodic motion is started. The CFD forces and moments show periodic behaviour. The periodic change of ship speed causes periodic propeller thrust force. K_p and N_p clearly show that one propeller comes out of water during periodic motion. The wave yaw moment indicates that it is positive (N_H=80 N.m) at t=5 sec since it hits the model from portside as shown in Y_P and the model is turned toward the target. However, the yaw moment reaches to negative value N_H=-150 N.m at t=7 sec where the model is on the wave downslope and hit from starboard. This produces periodic motion.

8.6.2 Fr=0.45

8.6.2.1 ψ_c = 5 deg

Figure 8-12 shows the case of surf-riding. The yaw motion indicates that the model is released at 50 deg heading. The rudders turn hard to guide the model to the target heading which results in large yaw rate and consequently large roll angle due to centrifugal force. At t=6 sec, the rudders deflections are almost zero and the model is located at the target. However, surf-riding starts at t=9 sec after the model is overtaken by waves and locked in wave downslope. The EFD propeller RPS had to be fixed but it is well controlled by propeller controller. The reduction in RPS at t=9 sec explains that the ship speed is increased right before surf-riding and then decrease to wave speed during surf-riding. The CFD simulation is performed but with arbitrary initial conditions for roll, pitch, heading, rudder deflection, wave phase, and ship speed. The pitch motion shows that the CFD model is released at negative pitch angle and it keeps cruising at that situation. In other words, the model is locked in wave downslope right after it is released. Yaw motion and trajectory show that CFD model starts surf-riding at target heading from the beginning. The CFD yaw moment explains that the wave and rudders yaw moment are balanced

right after the releasing time such that rudders can take the control of the model and keep it in the target heading.

8.6.2.2 ψ_c = 15 deg

Figure 8-13 provides the results for surf-riding case where ψ_c = 15 deg. The pitch motion indicates that the model is at +4 deg pitch at t=0 sec and the pitch reduces to -2 deg at t=2 sec meaning that the model is overtaken by one wave. The pitch increases to about zero at t=6 sec and then drops to -2 deg at t=8 sec introducing the second wave overtakes the model too. Later, the model is seized in next wave downslope such that the bow is down for the rest of the test and surf-riding happens. The yaw and rudder motions illustrate the trend of surf-riding. The heading increases from 10 deg (initial heading) to 22 deg at t=8 sec exceeding the target heading. During this period, the rudders turn to 10 deg to guide the model toward the target. The model stays at 22 deg after t=8 sec and surf-riding starts. The CFD simulation is performed with different initial condition compare with EFD, as shown in Fig. 8-13. The initial pitch of CFD model is negative and the model stays at this situation for the rest of simulation. Yaw motion shows that CFD model turns to 25 deg heading with the same trend as EFD but with a phase lag due to initial condition issues. The trajectory shows surf-riding occurrence after the model travels 15 m which is about 5 times of ship length. The predicted propeller thrust shows that the thrust is minimum (ship speed is maximum) around t= 5 sec right before the model is involved in surf-riding process. The increased ship speed causes that the relative ship speed respect wave speed decreases and consequently wave yaw moment decreases after t=5 sec as shown in N_H. Consequently, rudders can counteract the wave yaw moment and take control of the model and put it at 25 deg heading.

8.6.2.3 ψ_c = 22.5 deg

Figure 8-14 shows the case of broaching in which ψ_c = 22.5 deg. The time history of pitch provides the details of ship position respect to waves. The ship is on wave crest at initial point and then located on wave trough around t=2 sec. Afterward, the ship is seized in wave downslope for about 4 sec. During this time, the model is involved in surf-riding situation and heading increases to 60 deg. At this point, rudders are at their maximum deflection such that the model continues turning to 80 deg heading without rudder counteracting moment and consequently the model broaches. EFD propeller RPS varies during the test which is due to the weakness of the propeller controller. CFD simulation is performed with different initial condition. In overall, CFD simulation shows similar trend for heading with a phase lag due to initial conditions. The CFD model starts surf-riding right after releasing and it lasts until the model is overtaken by waves at t=4 sec. The heading increases very fast to 70 deg during surf-riding and rudders reach to the deflection limit. On the other hand, the centrifugal force is very large due to large yaw rate and produces 50 deg roll angle. Consequently, the CFD model broaches at large roll angle. K_p and N_P show that one of the propellers emerges out of water during simulation. The CFD trajectory indicates broaching at x=13 m where the ship moves toward west. The model turns back to the target after broaching but another broaching could happen as shown in trajectory.

8.6.2.4 ψ_c = 30 deg

Figure 8-15 shows the case of broaching for ψ_c = 30 deg. The yaw motion shows that the model is released at zero heading and it turns to 80 deg heading after 6 sec. In fact, the heading exceeds the target since the yaw rate is very large. At t=6 sec, the rudders are at their maximum deflection and the model loses its control and broaches. After broaching, the model is roughly in beam waves such that wave yaw moment drops

significantly and rudders can counteract it and turn the model toward the target. The CFD simulation, performed for different initial condition, predicts broaching at t=13 sec. As shown in Fig. 8-15, the CFD model is released at 22 deg heading and oscillates around the target until the heading reaches to 80 deg at t =13 sec where rudders are at maximum angle and broaching happens. The pitch shows that CFD model is overtaken by second wave at t= 7 sec and then the model is involved in surf-riding for a while right before the broaching happens. The propeller moments show that one of the propellers emerges out of water during simulation. The rudder and wave yaw moment are positive during broaching which provide enough yaw moment to return the model to the target heading. The propeller thrust shows that the speed increases right before maximum headings at t=3 and 11 sec. At t=3 sec, rudders control the heading and prevent broaching. At t=11 sec, the rudders are at their maximum deflection and could not prevent broaching. The trajectory shows clearly the first and second maximum heading condition. The first one happens nearly at x=10 m and second occurs at x=25 m. The curvature of the trajectory shows the turning rate which is very large before broaching such that the model cannot stop turning and broaching happens.

8.6.3 Fr=0.35

8.6.3.1 ψ_c = 5 deg

Figure 8-16 shows the case of surf-riding where ψ_c = 5 deg. The model is released at relatively large roll, pitch, and heading. The model is overtaken by two waves in 7 seconds as shown in pitch motion. Afterward, the model is locked in wave downslope and surf-riding happens. The yaw motion indicates that the model turns fairly fast toward the heading before surf-riding and then the model stays at 5 deg heading (target heading) at t>7 sec. The rate of yaw angle induces large centrifugal force for t< 7 sec which causes 30 deg roll angle. The CFD simulation is carried out with different initial condition. The

CFD model is released at -2 deg pitch angle and stays roughly at this angle for the whole simulation. This introduces surf-riding occurrence right after releasing the model. The model rolls 5 deg during surf-riding and stays at 12 deg heading. The CFD trajectory approves that the model is involved in surf-riding since it is released. The propeller thrust shows that the ship speed increases (i.e. thrust reduces) during surf-riding. The wave and rudder yaw moment are at the same order during the surf-riding such that rudders can counteract wave yaw moment and take the control of the ship.

8.6.3.2 ψ_c = 15 deg

Figure 8-17 shows the case of broaching where ψ_c = 15 deg. The model is released on the wave crest so that the pitch angle is positive. Then, the model is overtaken by waves and pitch drops to -2 deg where the model is on the wave downslope. Later, the model is involved in surf-riding situation for about 5 sec. The heading shows that the model is at 10 deg heading at the beginning of the test. Then the model moves toward the target and oscillates around the target for 4 sec and lastly the model starts moving away from the target at t=7 sec. The turning rate is very large for t>7 sec such that the model reaches to 60 deg heading in less than 5 sec. For t>11 sec, the rudders are at their maximum deflection and cannot stop the ship turning such that the model reaches to 70 deg heading and broaching happens. During the broaching, the ship rolls 50 deg due to the created centrifugal force. The CFD simulation is performed for different initial condition. The model is released at bow down position and locked in wave downslope for 4 sec and surf-rides. During surf-riding, the heading exceeds the target heading and increases to 50 deg at t=5 sec where the rudders at their maximum deflection and broaching happens. The CFD simulation shows that the model is at large drift angle during broaching process. The trajectory shows that the model broaches nearly at x=12 m. The wave and rudder yaw moment provide the details of the broaching process. N_H is negative and it increases for t<4 sec. Consequently, heading increases even though rudder defecation increases to

turn the model toward the target and broaching happens. Note that during broaching, thrust is very low i.e. the model speed is very large.

8.6.3.3 ψ_c = 22.5 deg

Figure 8-18 provides the CFD and EFD results for ψ_c = 22.5 deg. The model is overtaken by several waves as shown in pitch motion. At t=10 sec, the model is locked in waves and surf-rides for a while. During this period, the heading increases to 60 deg where the rudders are at their maximum deflection. The large turning rate produces 50 deg roll angle. The CFD simulation is carried out for different initial condition. The model is released at 20 deg heading and moves toward the target. At t=2 sec, the model exceeds the heading and reaches to 60 deg heading (t=4 sec) where rudders are nearly at their maximum deflection and ship broaches. The trajectory shows broaching at x=8 m. Note that CFD and EFD show periodic trend before broaching. This suggests that this case is close to the boundary of broaching and periodic motion. In other words, increasing the target heading would change the broaching to period motion. The prediction of yaw moment show that wave yaw moment is about N_H=-100 N.m before broaching such that rudders cannot counteract it. After t> 4sec, the wave yaw moment increases to N_H=+80 N.m supporting rudders to turn the model toward the target. The propeller moment is 10 times smaller than rudder yaw moment and is negligible. In fact, propeller yaw moment should be zero due to symmetric behaviour of disk approach for twin counter-rotating propellers. However, one of two propellers can be emerged out of water temporally and making non-zero roll and yaw moments. For this case, a fraction of one of propellers comes out of water whenever roll angle is larger than 30 deg.

8.6.3.4 ψ_c = 30 deg

Figure 8-19 demonstrates the results for ψ_c = 30 deg. The pitch shows that the model is overtaken by waves and exhibits periodic trend. The heading shows that the model

reaches from 5 deg heading to the desired heading at t=4 sec. Afterward, the model oscillates a nit around the target and then turns to 50 deg heading. Lastly, the model oscillates around this heading and establishes periodic motion. The period of yaw is about the same as pitch and roll period i.e. encounter period. Also, the rudders show periodic trend due to periodic yaw motion. The CFD simulation shows similar condition. However, there is phase lag between CFD and EFD due to initial condition, as shown in pitch motion. The CFD simulation shows that the model has period drift suggesting that the bow oscillates when ship moves forward. The CFD yaw motion and trajectory show that the model oscillates at 40 deg heading and the period of oscillation is about the encounter period at that heading. The CFD forces and moments show periodic trend. The yaw moment shows that the wave yaw moment is N_H=-100 N.m for t<3 sec and it is larger than any other counteracting moment resulting in 55 deg heading. Then, the wave yaw moment increases to N_H=100 N.m and supports rudders at t=3 sec. Consequently, the model turns toward the desired heading. However, the yaw moment decreases again to N_H=-100 N.m at t=4 sec such that the model moves away from the target. This procedure provides periodic motion.

8.6.4 Fr=0.3

8.6.4.1 ψ_c = 5 deg

Figure 8-20 provides results for periodic motion case with ψ_c = 5 deg. The pitch motion shows that the model is at -2 deg pitch angle at the beginning of test. The model is overtaken by waves providing oscillatory pitch motion. The heading shows that the model is at 60 deg heading and then turns to the desired heading in 8 sec due to hard deflection of rudders. Afterward, the model oscillates around the target producing periodic motion. The period of oscillation is about 4 sec which is the wave encounter period at 5 deg heading. The roll angle shows that the model attains 60 deg roll during

turning to the target. The roll angle drops to less than 5 deg right after the model is at the target heading. The CFD simulation is performed for different initial condition. The model is released at very small heading and roll angle such that the model is located at the target heading in 2 sec and then oscillates around it producing periodic motion. The CFD simulation shows that the model has oscillatory drift angle. Also, The CFD indicates small oscillations on the trajectory due to periodic motion. More than that, all forces and moments show periodic trend. Since the model is overtaken by waves, the wave yaw moment oscillates between N_H=+5 and N_H=-10 N.m. If the heading is less than ψ_c, the wave and rudders yaw moment are negative (wave yaw moment supports rudders) and they attempt to increase heading to target value. If the heading is larger than ψ_c, the wave and rudders yaw moment are positive (wave yaw moment supports rudders) and they attempt to decrease heading. The contribution of rudders and wave causes the periodic motion trend.

8.6.4.2 ψ_c = 15 deg

Figure 8-21 shows the case of periodic motion for ψ_c = 15 deg. The model starts turning from 13 deg heading to the target right after releasing point. However, the heading exceeds the target such that 17 deg heading is observed at t=3 sec. Then the model turns back to the target and again passes the target and reaches to 10 deg heading at t=5 sec. This procedure repeats and exhibits periodic motion. The roll, pitch and rudders follow a periodic trend. The CFD simulation shows the same phenomenon for this case but with a phase lag due to dissimilarity of initial conditions. The period of CFD and EFD motions are 4.5 sec and they are the same as encounter period. The collaboration of rudders and wave yaw moment introduce a situation in which yaw moment supports the rudders yaw moment such that there is a strong yaw moment to turn the model toward the target all the time. For instance, the wave and yaw moment are N_H=20 and N_R=10 N.m at t=5 sec turning the model toward the heading. However, the

yaw moment is too strong such that the model passes the target at t=6 sec. At this time, both wave and rudders yaw moment drop to negative values N_H=-30 and N_R=-10 N.m producing enough yaw moment to turn back the model toward the target.

8.6.4.3 ψ_c = 22.5 deg

Figure 8-22 shows the case of periodic motion for ψ_c = 22.5 deg. The model is released at 15 deg heading and starts turning to the target at t=1 sec. The model passes the target at t=3 sec and reaches to 24 deg heading at t=3.5 sec. The model returns back to the desired heading at t=4 sec but again passes the target such that heading is 18 deg at t=5 sec. This procedure repeats and causes periodic motion. The roll and pitch angle increase up to 20 and 4 deg, respectively. The CFD simulation, performed for different initial condition, predicts periodic motion but with a phase lag respect to EFD results. The CFD trajectory, drift angle, and forces/moments show periodic trend in which the period of oscillation is about 4.5 sec and is the same as encounter period. The propeller forces and moments show that part of one propeller emerges out of water temporary during periodic motion where roll angle is large. The propeller thrust X_P shows oscillatory trend i.e. ship speed decreases and increases during periodic motion. In fact, the ship speed decreases/increases when the center of gravity is located on wave trough/crest. The wave and rudders yaw moment explain that their collaboration produces strong yaw moment such that the ship forces to move toward the target.

8.6.4.4 ψ_c = 30 deg

Figure 8-23 illustrates the results for periodic motion case where ψ_c = 30 deg. The model is released at 10 deg heading and moves toward the target quickly. At t=3 sec, the model passes the target and returns to target at t=5.5 sec. The model exceeds the target and reaches to 25 deg heading. At this point, the model turns back again to the target and produces periodic motion. The pitch and roll angle are about 25 deg and 4 deg during

periodic motion. The propeller RPS indicates that the propeller controller was unable to keep RPS constant such that RPS varies between 12.5 and 13.5 rps. The CFD simulation is performed for fixed RPS found in self-propulsion clam water at Fr=0.3. The CFD and EFD RPS difference is due to approximated propeller model used in CFD. The CFD trajectory and yaw motion show that CFD predicts periodic motion with a phase lag respect to EFD due to initial condition issues. The yaw moment shows that the collaboration of rudders and wave yaw moment produces periodic motion. In fact, wave yaw moment supports the rudders yaw moment all the time during the simulation such that there is a strong yaw moment to turn the model toward the target. For instance, the wave and yaw moment are N_H=50 and N_R=20 N.m at t=5 sec turning the model toward the heading. At t=6 sec, both wave and rudders yaw moment drop to negative values N_H=-50 and NR=-10 N.m producing enough yaw moment to turn the model away from the target.

8.6.5 Summary of CFD Free Model Test Program 2

The summary of CFD simulations are shown in Fig. 8-24. It is indicated that CFD can predict the boundary between surf-riding, broaching, and periodic motion. The CFD simulations follow exactly EFD trend with increasing Fr and heading. Figure 8-24 shows that there is a boundary between periodic motion and surf-riding/broaching at Fr=0.3 for heading<30 deg. For Fr<0.3, which is blow the boundary, CFD and EFD show periodic motion whereas surf-riding/broaching is observed for above the boundary. Therefore that CFD predicts the same boundary even though initial conditions for many cases are different from EFD. However, the maximum achieved roll angle is strongly function of initial condition such that CFD shows different diagram for roll angle. In overall, CFD shows outstanding prediction of instability boundary.

8.7 NDA Free Model Simulation

To compare with the free-running model experiments and CFD, the coupled surge-sway-yaw-roll maneuvering mathematical model described in Chapter 2 (Eq. (2.74)) is applied to the ship with the same operational and environmental conditions used in the free model tests program 2. The higher order terms are neglected but the mathematical model is still nonlinear since the wave forces are functions of the relative ship position to waves. The maneuvering and propulsion coefficients in calm water are estimated with the conventional captive model tests as described in Chapter 2. Wave induced forces are estimated from CFD, potential theory and EFD captive model in following waves.

8.7.1 NDA Based on Inputs from EFD

The result is shown with the experimental data in Fig. 8-25 (Umeda et al., 2008). When the auto pilot course is smaller, there is a boundary between the stable surf-riding and periodic motions near the nominal Froude number of 0.3. Below this boundary, periodic motions are simulated as they are identified in the experiments. Above this boundary, a stable surf-riding region exists, and includes the stable surf-riding identified in the experiment. However, this region also includes the case of broaching in the experiment. When the auto pilot course is larger, the simulated roll exceeds 90 degrees above the nominal Froude number of 0.3. On the other hand, in the experiment the maximum roll angle is 71 degrees. This means that the mathematical model overestimates the roll angle and underestimates the yaw deviation. It can be presumed that this is induced by the emergence of propeller and rudder out of water, which could reduce the yaw checking ability under the extreme roll angle. In the region categorized as "not identified", sub-harmonic motions often are obtained.

8.7.2 NDA Based on Inputs from CFD & Potential Theory

Since there are notable difference among the EFD and CFD, and the Froude-Krylov prediction, as explained in Chapter 7, it is important to examine their effects on system-based prediction of ship motions including surf-riding, broaching and periodic motion. For this purpose, system-based simulation using the mathematical model mentioned before was executed for the cases of free model tests of the ONR tumblehome vessel with inputs from CFD and potential theory.

Figure 8-26 shows comparison between the free model test and the system-based numerical simulation using the wave-induced surge force estimated by the Froude-Krylov prediction. Although notable discrepancy in the wave-induced surge force exists as shown in Chapter 7, the difference in the system-based simulation results between the two is not significant. One surf-riding- related broaching case in the free model test, where the auto-pilot course of 22.5 degrees and the nominal Froude number of 0.35, is categorized as a harmonic periodic motion in the system-based simulation with the wave-induced surge force measured from captive test, while it is done as stable surf-riding in the simulation shown in Fig. 8-26. This is because the wave-induced surge force is smaller in this system-based simulation. In case of the system-based simulation using the wave-induced surge force estimated by the CFD as shown in Fig. 8-27, the stable surf-riding zone further but slightly shrinks because of smaller wave-induced surge force at relevant speed. Other notable change is not found. As a whole, for this subject ship, the Froude-Krylov calculation for estimating the wave-induced surge force is satisfactory.

8.8 Summary of Free Model Simulations

CFD 2DOF self-propulsion simulation is carried out with propeller model and actual propeller to predict necessary RPS for several Fr. The prediction error of propeller RPS is about 5.8%D for propeller model while it drops to 1.7 %D for actual propeller. This

suggests the simplicity and efficiency of body force propeller model would cost about 4%D more error which is reasonable. CFD free model simulations show promising results for surf-riding, broaching and periodic motion. CFD predicts the instability boundary perfectly. For small heading (ψ_c < 30 deg), there is a boundary between surf-riding/broaching and periodic motion at Fr=0.3. CFD predicts surf-riding/broaching above the boundary and periodic motion below the boundary. CFD calculation of wave and rudders yaw moment explains the processes of surf-riding, broaching, and periodic motion. It is concluded that wave yaw moments is the major cause of broaching/periodic motion, with rudder and propeller moments much smaller in magnitude. The ship speed increases significantly before surf-riding/broaching which might produce large turning rate and consequently large centrifugal force and roll moment. The emergence of propeller out of water and water on deck occurrence are observed for many cases. It is shown that OT would not capsize due to large restoring moment of its superstructure. The comparison of CFD and EFD time history of motions show a phase difference between CFD and EFD, possibly due to inaccurate initial conditions and/or propeller modeling. The NDA simulation using EFD inputs predicts the boundary but the simulated roll exceeds 90 degrees for Fr>0.3 while EFD maximum roll angle is 71 degrees. This might be improved by considering emergence of propeller and rudder out of water in the mathematical model. The NDA simulation using CFD and potential flow (Froude-Krylov calculation) inputs predicts reasonably the boundary of instability and suggests that CFD/ potential flow can be considered as replacement for EFD inputs.

Table 8-1: Summary of boundary conditions

	ϕ	p	k	ω	U	V	W
Inlet	$A\cos(kx-2\pi ft)-z(x)$	$\frac{A}{Fr^2}e^{kz}\cos(kx-2\pi ft)-\frac{A^2}{2Fr^2k}e^{2kz}$	$k_{fs}=10^{-}$	$\omega_{fs}=9$	$U(x,y,z,t)=U_0+\frac{A}{Fr}\sqrt{k}e^{kz}\cos(kx-2\pi ft)$	$V=0$	$W(x,y,z,t)=\frac{A}{Fr}\sqrt{k}e^{kz}\sin(kx-2\pi ft)$
Exit	$A\cos(kx-2\pi ft)-z(x)$	$\frac{A}{Fr^2}e^{kz}\cos(kx-2\pi ft)-\frac{A^2}{2Fr^2k}e^{2kz}$	$k_{fs}=10^{-}$	$\omega_{fs}=9$	$U(x,y,z,t)=U_0+\frac{A}{Fr}\sqrt{k}e^{kz}\cos(kx-2\pi ft)$	$V=0$	$W(x,y,z,t)=\frac{A}{Fr}\sqrt{k}e^{kz}\sin(kx-2\pi ft)$
Sides	$A\cos(kx-2\pi ft)-z(x)$	$\frac{A}{Fr^2}e^{kz}\cos(kx-2\pi ft)-\frac{A^2}{2Fr^2k}e^{2kz}$	$k_{fs}=10^{-}$	$\omega_{fs}=9$	$U(x,y,z,t)=U_0+\frac{A}{Fr}\sqrt{k}e^{kz}\cos(kx-2\pi ft)$	$V=0$	$W(x,y,z,t)=\frac{A}{Fr}\sqrt{k}e^{kz}\sin(kx-2\pi ft)$
Bottom	$\frac{\partial\phi}{\partial n}=1$	$\frac{\partial p}{\partial n}=0$	$\frac{\partial k}{\partial n}=0$	$\frac{\partial\omega}{\partial n}=0$	$U=1$	$V=0$	$W=0$
Top	$\frac{\partial\phi}{\partial n}=-1$	$\frac{\partial p}{\partial n}=0$	$\frac{\partial k}{\partial n}=0$	$\frac{\partial\omega}{\partial n}=0$	$\frac{\partial U}{\partial n}=0$	$\frac{\partial V}{\partial n}=0$	$\frac{\partial W}{\partial n}=0$
Ship hull	$\frac{\partial\phi}{\partial n}=0$	Poisson Eq.	$k=0$	$\omega=\frac{60}{\mathrm{Re}\,\beta y^{+2}}$	$U=C_g$	$V=0$	$W=0$

Table 8-2: Grids and decomposition information

Grid	Points	Processors	Object	Child to
Boundary Layer starboard	351,616	3	Ship	None
Boundary Layer portside	351,616	3	Ship	None
superstructure	466,032	4	Ship	None
Skeg	118,188	1	Ship	None
Bilge keel Starboard	119,556	1	Ship	None
Bilge keel portside	119,556	1	Ship	None
Rudder starboard Outboard	120,048	1	Ship	Ship
Rudder Starboard Inboard	120,048	1	Ship	Ship
Rudder Portside Outboard	120,048	1	Ship	Ship
Rudder Portside Inboard	120,048	1	Ship	Ship
Background	1,759,755	15	None	None
Total	**3,766,511**	**32**		

Table 8-3: Principal dimensions of the propeller

	OT
	Starboard/Port
K_T	K_T= 0.62702-0.26467J-0.09665J^2/ 0.64111-0.27016J-0.09319J^2
K_Q	K_Q=0.15200-0.05676J-0.02075J^2/ 0.15546+0.05956J +0.01991J^2
r_p/L	0.016937
r_h/r_p	0.2
p1/L	(0.920929,0.026605,-0.035147)/ (0.920929,-0.026605,-0.035147)
p2/L	(0.932429,0.026605,-0.036153)/ (0.932429,-0.026605,-0.036153)

Table 8-4: Initial condition study for GM=1.78 m, Fr=0.4, and ψ_c=-15 deg (Test program 1)

	Wave Phase (deg)	Initial Fr	Target Fr	Initial heading (deg)	Target heading (deg)	Predicted heading (deg)	Predicted Phenomenon	Max Roll angle (deg)
EFD	?	?	0.4	-30	-15	-80	broaching	75
CFD	0	0.0	0.4	-30	-15	-60	broaching	50
	180	0.0	0.4	-30	-15	-70	broaching	55
	180	0.3	0.4	-30	-15	-67	broaching	60
	180	0.4	0.4	-30	-15	7	broaching	40
	200	0.3	0.4	-30	-15	-70	broaching	55
	220	0.3	0.4	-30	-15	-70	broaching	58
	240	0.3	0.4	-30	-15	-70	broaching	58
	260	0.3	0.4	-30	-15	-70	broaching	55
	264	0.15	0.4	-30	-15	-70	broaching	60
	264	0.2	0.4	-30	-15	-75	broaching	60
	264	0.25	0.4	-30	-15	-75	broaching	62
	280	0.3	0.4	-30	-15	-65	broaching	60

Table 8-5: Initial condition study for GM=2.068 m, Fr=0.4, and ψ_c=-5 deg (Test program 1)

	Wave Phase (deg)	Initial Fr	Target Fr	Initial heading (deg)	Target heading (deg)	Predicted heading (deg)	Predicted Phenomenon	Max Roll angle (deg)
EFD	?	?	0.4	-33	-5	-5	surf-riding	40
CFD	0	0.0	0.4	-33	-5	-5	surf-riding	15
	137	0.3	0.4	-33	-5	-5	surf-riding	37
	180	0.3	0.4	-33	-5	-5	surf-riding	47
	180	0.4	0.4	-33	-5	-5	surf-riding	42
	200	0.3	0.4	-33	-5	-5	surf-riding	44
	230	0.1	0.4	-33	-5	-5	surf-riding	23
	230	0.2	0.4	-33	-5	-5	surf-riding	35
	230	0.3	0.4	-33	-5	-5	surf-riding	32
	280	0.3	0.4	-33	-5	-5	surf-riding	30

Table 8-6: Initial condition study for GM=2.068 m, Fr=0.4, and ψ_c=-15 deg (Test program 1)

	Wave Phase (deg)	Initial Fr	Target Fr	Initial heading (deg)	Target heading (deg)	Predicted heading (deg)	Predicted Phenomenon	Max Roll angle (deg)
EFD	?	?	0.4	-13	-15	-60	broaching	60
CFD	30	0.1	0.4	-13	-15	oscillating	periodic	15
	30	0.15	0.4	-13	-15	oscillating	periodic	20
	30	0.3	0.4	-13	-15	-60	broaching	40
	30	0.4	0.4	-13	-15	-60	broaching	37
	50	0.4	0.4	-13	-15	-60	broaching	45
	50	0.45	0.4	-13	-15	-60	broaching	45
	80	0.1	0.4	-13	-15	oscillating	periodic	13
	80	0.15	0.4	-13	-15	oscillating	periodic	25
	80	0.16	0.4	-13	-15	oscillating	periodic	28
	80	0.17	0.4	-13	-15	oscillating	periodic	30
	80	0.18	0.4	-13	-15	oscillating	periodic	29
	80	0.19	0.4	-13	-15	oscillating	periodic	25
	80	0.2	0.4	-13	-15	oscillating	periodic	30
	80	0.3	0.4	-13	-15	-60	broaching	40
	80	0.4	0.4	-13	-15	-60	broaching	38
	120	0.2	0.4	-13	-15	-50	broaching	25
	130	0.1	0.4	-13	-15	oscillating	periodic	15
	130	0.3	0.4	-13	-15	-60	broaching	38

Table 8-7: Initial condition study for GM=2.068 m, Fr=0.4, and ψ_c=-30 deg (Test program 1)

	Wave Phase (deg)	Initial Fr	Target Fr	Initial heading (deg)	Target heading (deg)	Predicted heading (deg)	Predicted Phenomenon	Max Roll angle (deg)
EFD	?	?	0.4	-40	-30	oscillating	periodic	55
CFD	0	0.0	0.4	-40	-30	oscillating	periodic	35
	20	0.25	0.4	-40	-30	oscillating	periodic	50
	20	0.33	0.4	-40	-30	oscillating	periodic	50

Table 8-8: Initial condition study for GM=2.068 m, Fr=0.4, and ψ_c=-5 deg

	Wave Phase (deg)	Initial Fr	Target Fr	Initial heading (deg)	Target heading (deg)	Predicted heading (deg)	Predicted Phenomenon	Max Roll angle (deg)
EFD	?	?	0.4	-30	-5	-5	surf-riding	20
CFD	0	0.4	0.4	-30	-5	-5	surf-riding	10
	50	0.1	0.4	-30	-5	-5	surf-riding	30
	50	0.2	0.4	-30	-5	-5	surf-riding	20
	50	0.3	0.4	-30	-5	-5	surf-riding	10
	50	0.4	0.4	-30	-5	-5	surf-riding	10
	50	0.5	0.4	-30	-5	-5	surf-riding	20

Table 8-9: Initial condition study for GM=2.068 m, Fr=0.4, and ψ_c=-15 deg

	Wave Phase (deg)	Initial Fr	Target Fr	Initial heading (deg)	Target heading (deg)	Predicted heading (deg)	Predicted Phenomenon	Max Roll angle (deg)
EFD	?	?	0.4	-8.6	-15	-25	broaching	14
CFD	235	0.1	0.4	-8.6	-15	-28	broaching	17
	235	0.2	0.4	-8.6	-15	-70	broaching	45
	235	0.275	0.4	-8.6	-15	-42	broaching	27
	235	0.4	0.4	-8.6	-15	-71	broaching	47

Table 8-10: Initial condition study for GM=2.068 m, Fr=0.4, and ψ_c=-22.5 deg

	Wave Phase (deg)	Initial Fr	Target Fr	Initial heading (deg)	Target heading (deg)	Predicted heading (deg)	Predicted Phenomenon	Max Roll angle (deg)
EFD	?	?	0.4	-7	-22.5	-80	broaching	65
CFD	0	0.45	0.4	-7	-22.5	-65	broaching	40
	50	0.45	0.4	-7	-22.5	-65	broaching	40
	95	0.45	0.4	-7	-22.5	-60	broaching	45
	144	0.45	0.4	-7	-22.5	-60	broaching	40
	200	0.45	0.4	-7	-22.5	-65	broaching	50
	200	0.50	0.4	-7	-22.5	-65	broaching	48
	200	0.55	0.4	-7	-22.5	-65	broaching	46
	280	0.45	0.4	-7	-22.5	-65	broaching	47
	330	0.37	0.4	-7	-22.5	-65	broaching	45
	330	0.4	0.4	-7	-22.5	-65	broaching	43
	330	0.45	0.4	-7	-22.5	-65	broaching	45

Table 8-11: Initial condition study for GM=2.068 m, Fr=0.4, and ψ_c=-30 deg

	Wave Phase (deg)	Initial Fr	Target Fr	Initial heading (deg)	Target heading (deg)	Predicted heading (deg)	Predicted Phenomenon	Max Roll angle (deg)
EFD	?	?	0.4	-12	-30	oscillating	periodic	40
CFD	144	0.2	0.4	-12	-30	oscillating	periodic	50

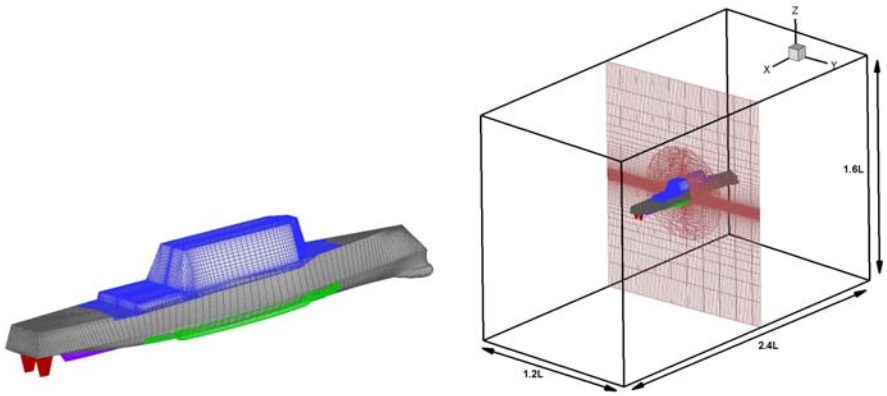

Figure 8-1: Grid and solution domain of free model simulations

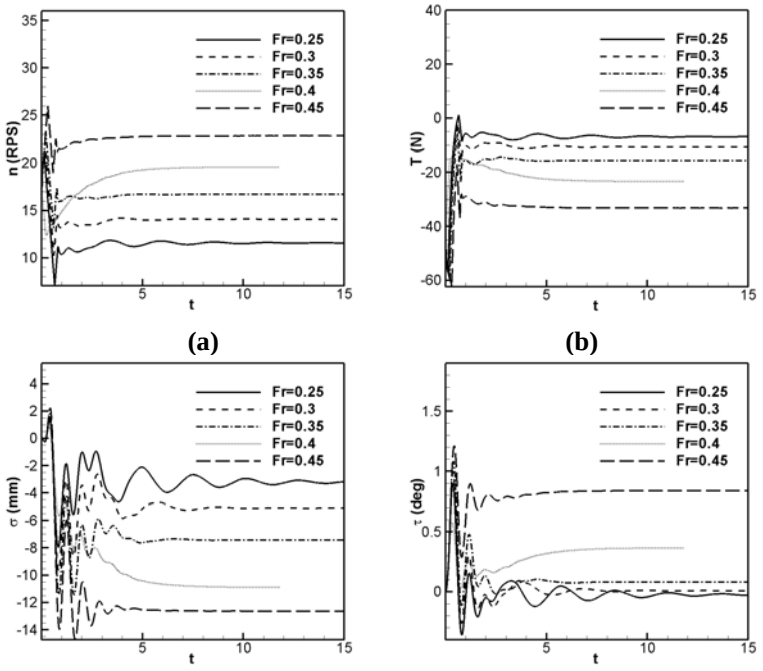

Figure 8-2: Self-propelled simulation in calm water: (a) RPS; (b) thrust; (c) σ; (d) τ

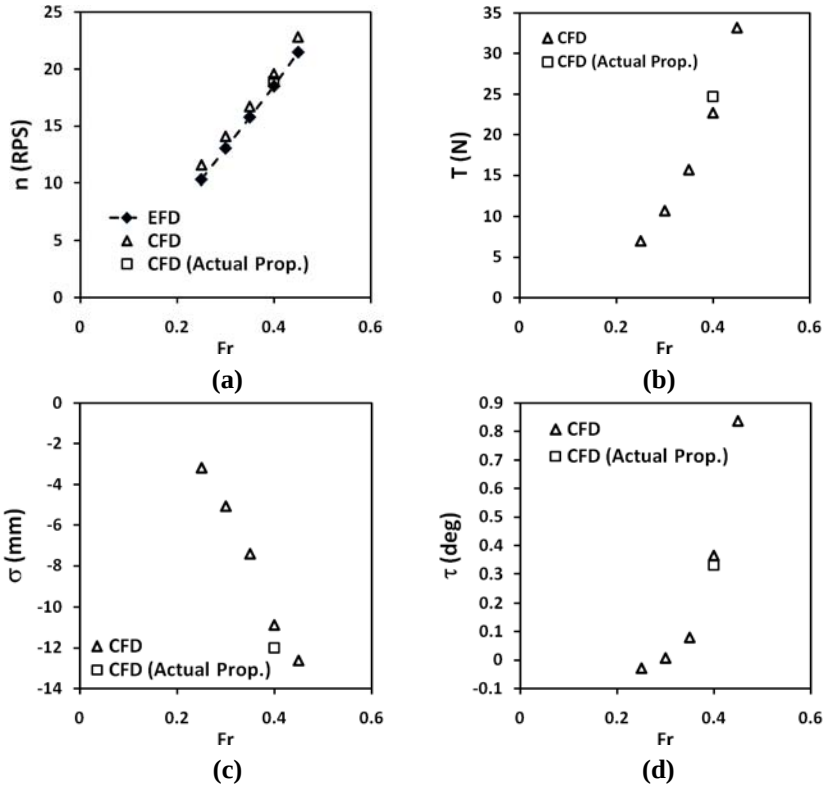

Figure 8-3: Comparison of self-propelled simulations in calm water using actual propeller and body force propeller: (a) RPS; (b) thrust; (c) σ; (d) τ

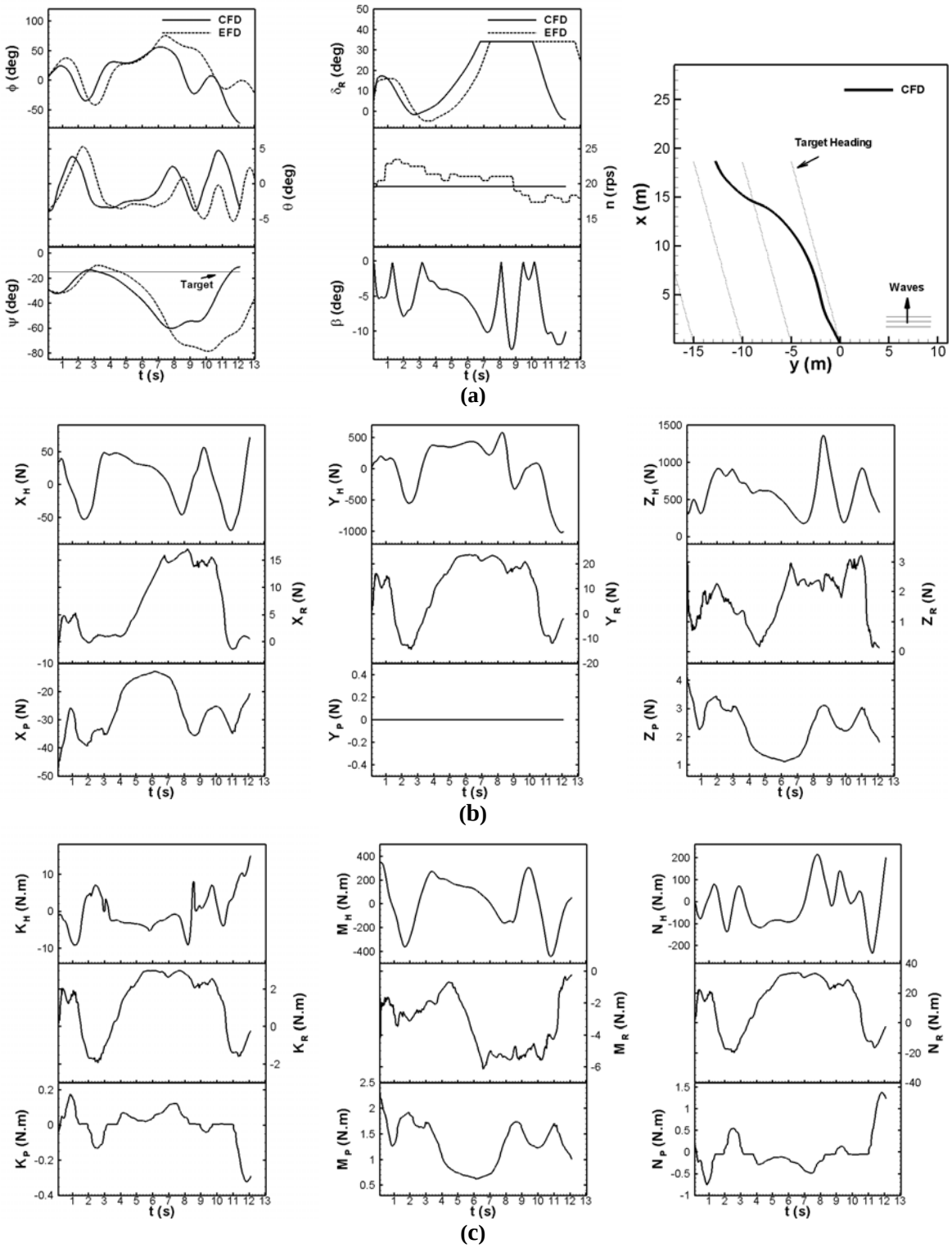

Figure 8-4: CFD (ε_0=264^o, $u_0/\hat{o}$ (Lg)=0.15) and EFD comparison for GM=1.78 m, Fr=0.4, and ψ_c=-15 deg: (a) motions; (b) forces; (c) moments

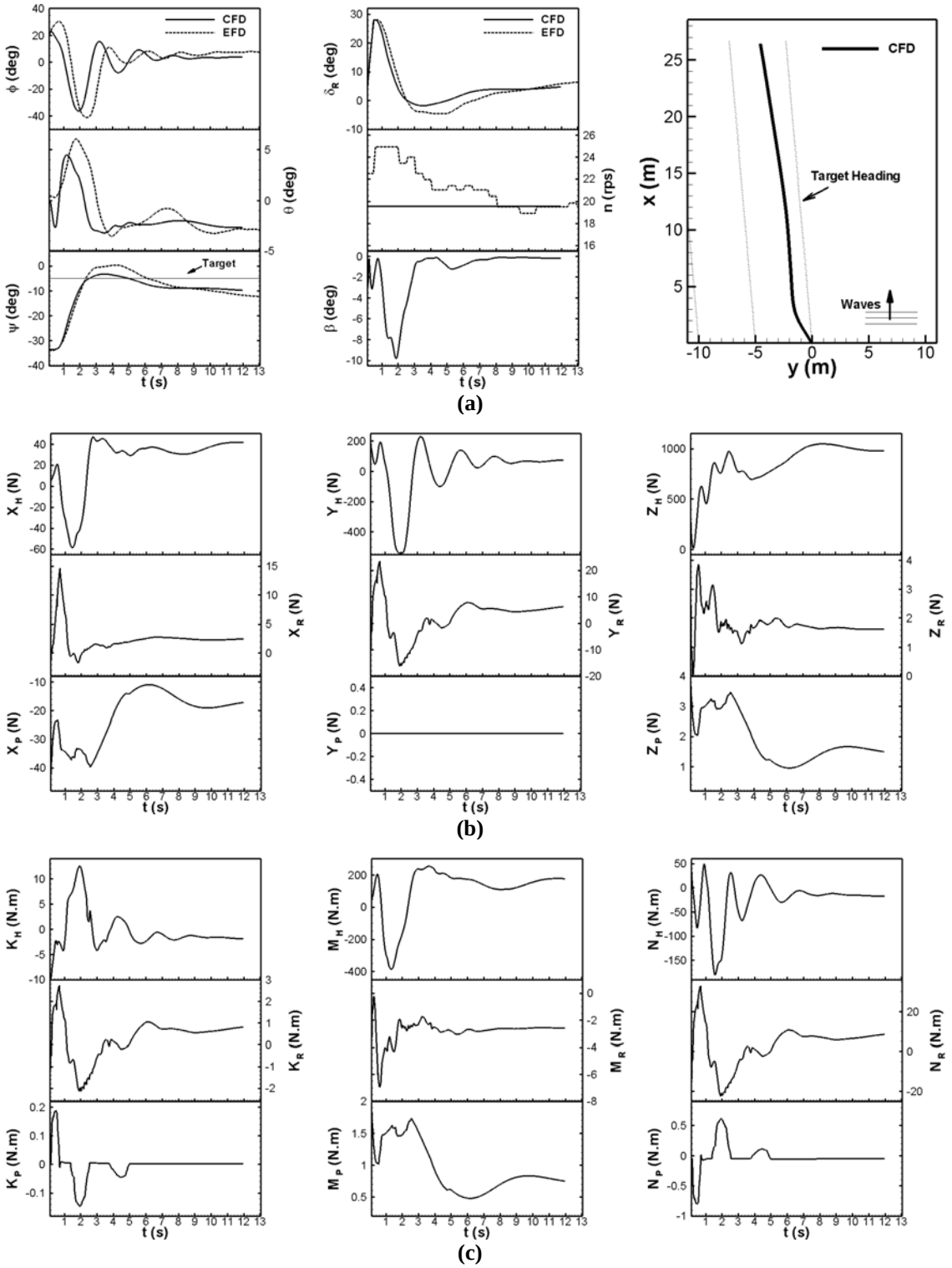

Figure 8-5: CFD (ε_0=230°, $u_0/\hat{o}$ (Lg)=0.2) and EFD comparison for GM=2.068 m, Fr=0.4, and ψ_c=-5 deg: (a) motions; (b) forces; (c) moments

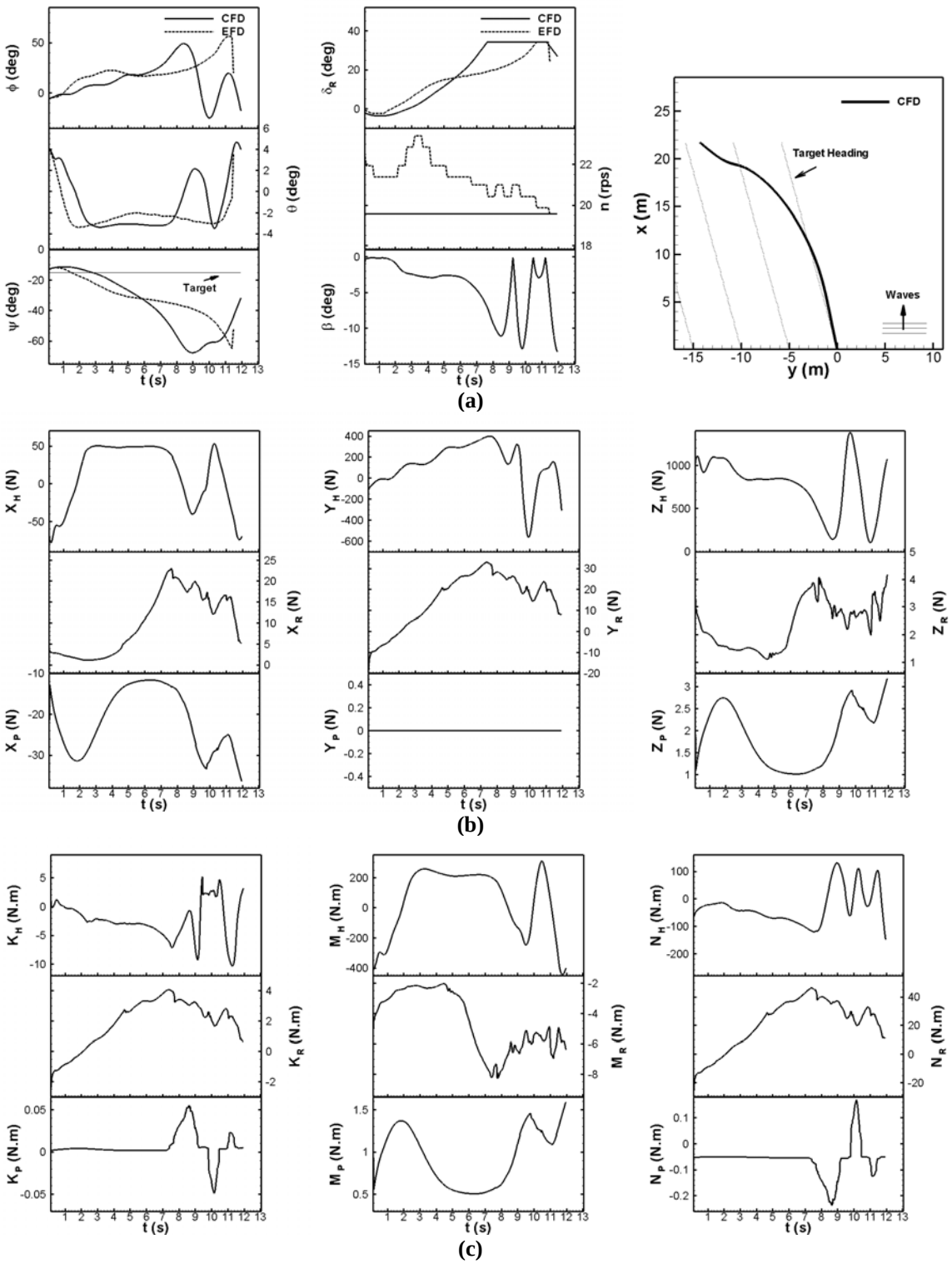

Figure 8-6: CFD (ε_0=50°, $u_0/\hat{o}$ (Lg)=0.4) and EFD comparison for GM=2.068 m, Fr=0.4, and ψ_c=-15 deg: (a) motions; (b) forces; (c) moments

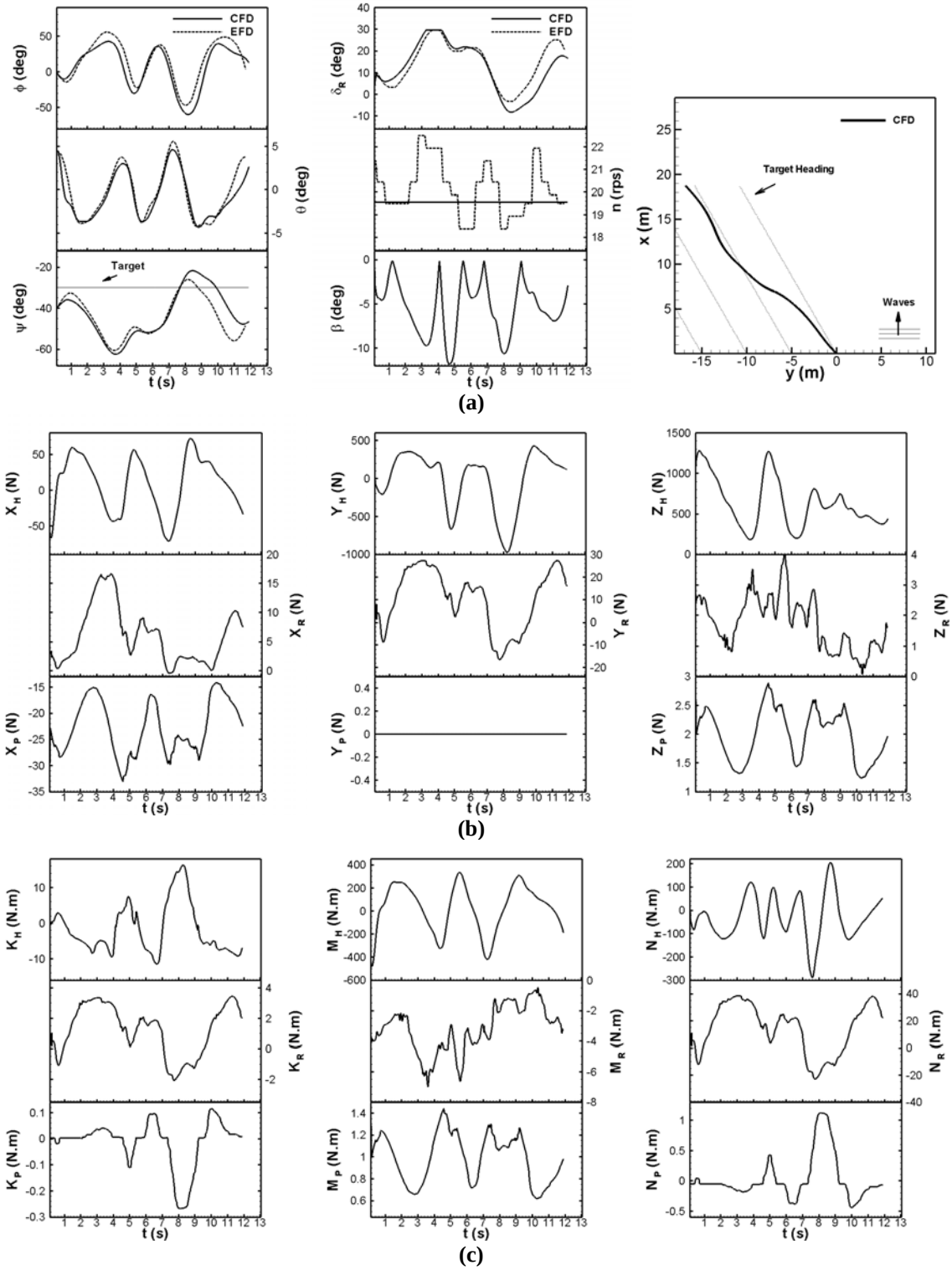

Figure 8-7: CFD (ε_0=20^o, $u_0/\hat{o}$ (Lg)=0.33) and EFD comparison for GM=2.068 m, Fr=0.4, and ψ_c=-30 deg: (a) motions; (b) forces; (c) moments

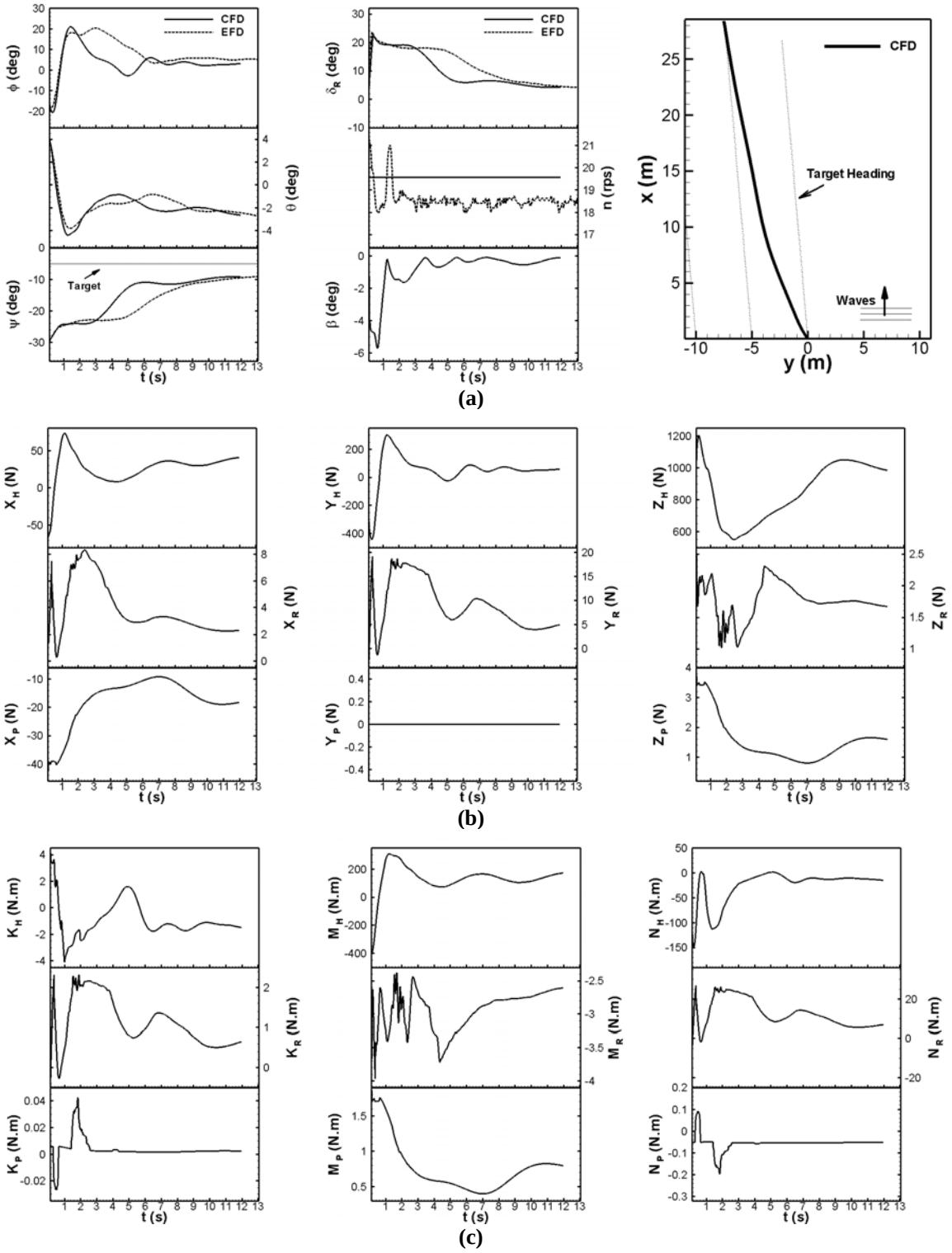

Figure 8-8: CFD (ε_0=50^o, $u_0/\hat{o}$ (Lg)=0.2) and EFD comparison for GM=2.068 m, Fr=0.4, and ψ_c=-5 deg: (a) motions; (b) forces; (c) moments

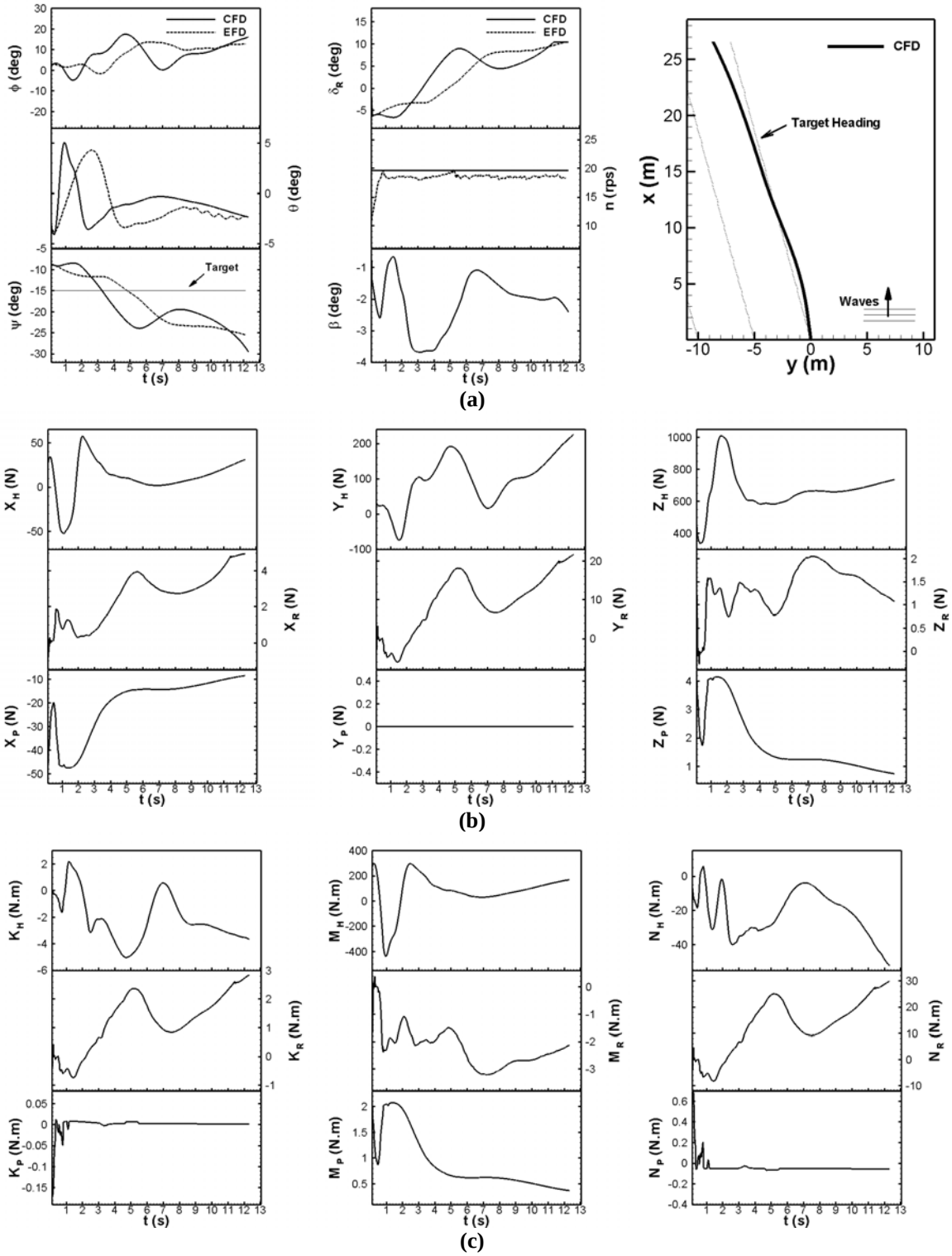

Figure 8-9: CFD (ε_0=235°, $u_0/\hat{o}$ (Lg)=0.1) and EFD comparison for GM=2.068 m, Fr=0.4, and ψ_c=-15 deg: (a) motions; (b) forces; (c) moments

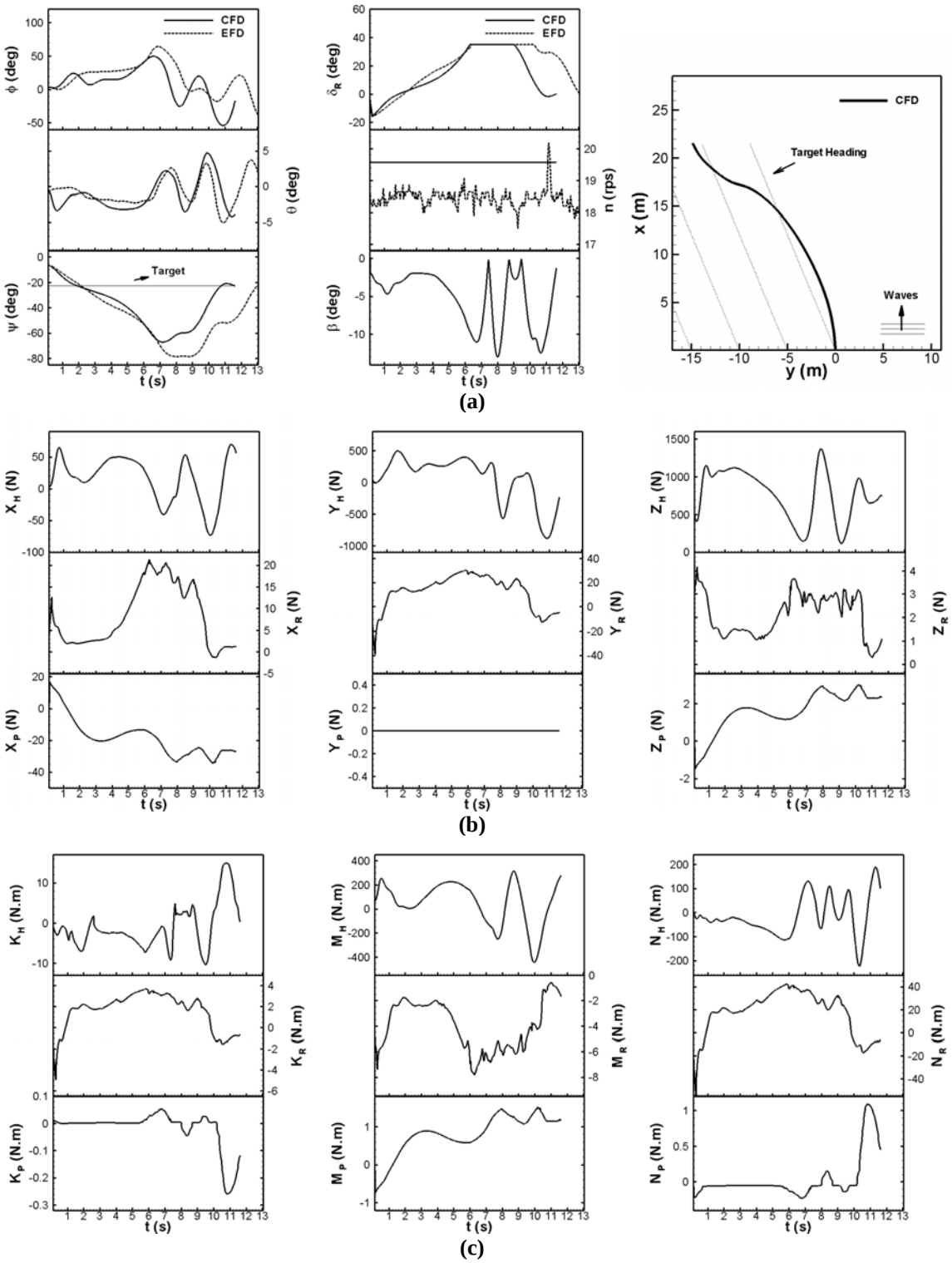

Figure 8-10: CFD (ε_0=200^o, $u_0/\hat{o}$ (Lg)=0.55) and EFD comparison for GM=2.068 m, Fr=0.4, and ψ_c=-22.5 deg: (a) motions; (b) forces; (c) moments

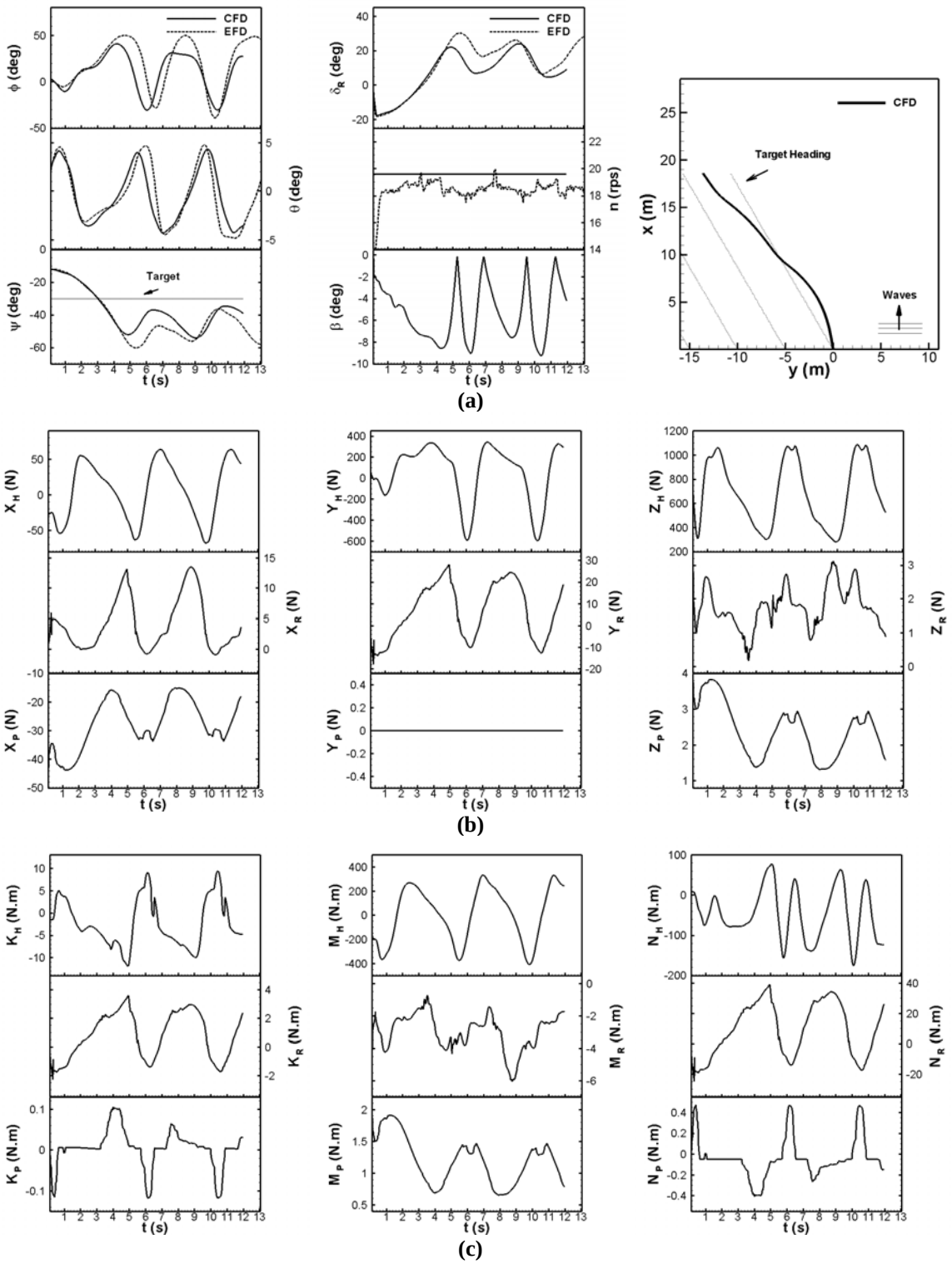

Figure 8-11: CFD (ε_0=144^o, $u_0/\hat{o}$ (Lg)=0.2) and EFD comparison for GM=2.068 m, Fr=0.4, and ψ_c=-30 deg: (a) motions; (b) forces; (c) moments

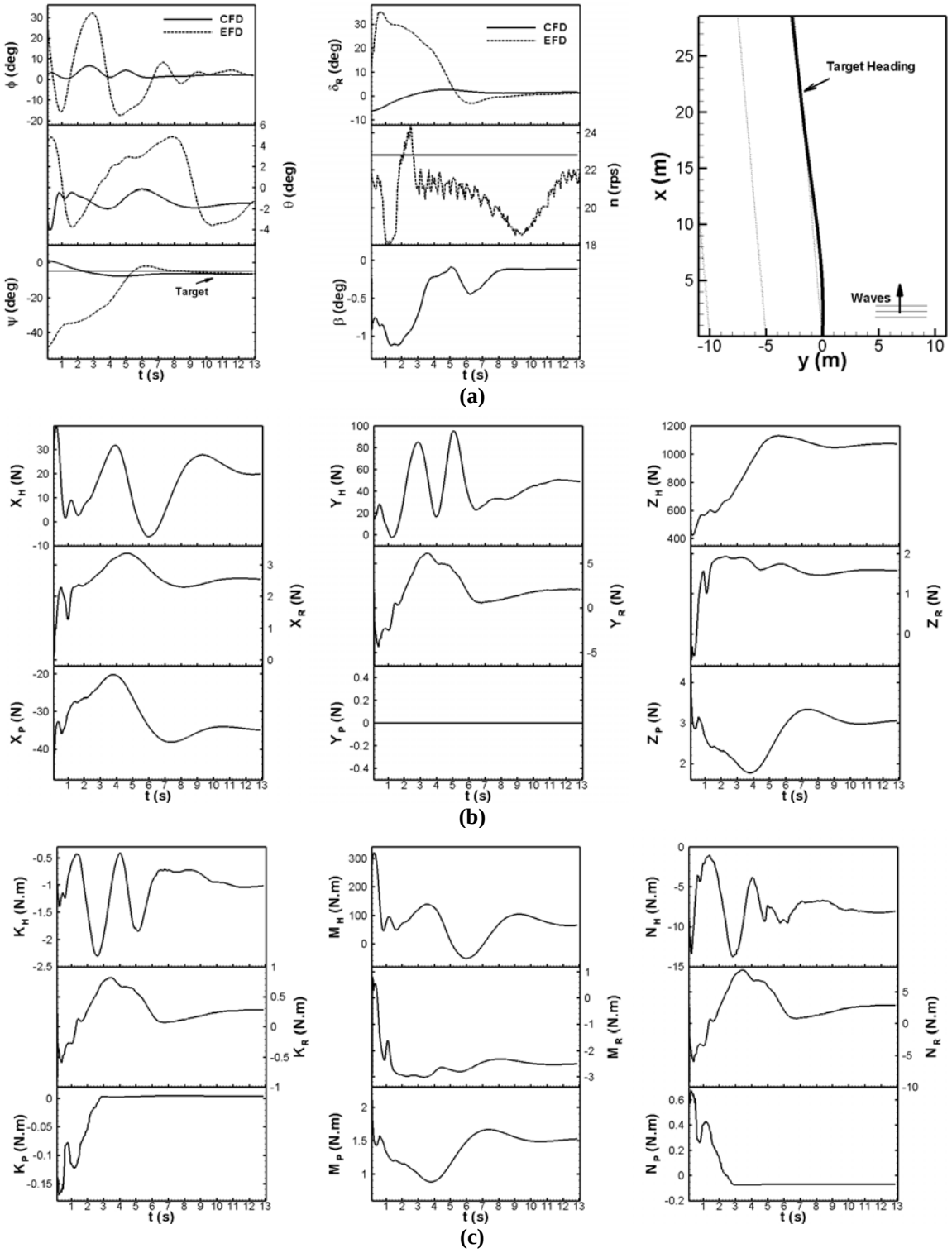

Figure 8-12: CFD (ε_0=235°, $u_0/\hat{o}$ (Lg)=0.275) and EFD comparison for GM=2.068 m, Fr=0.45, and ψ_c=-5 deg: (a) motions; (b) forces; (c) moments

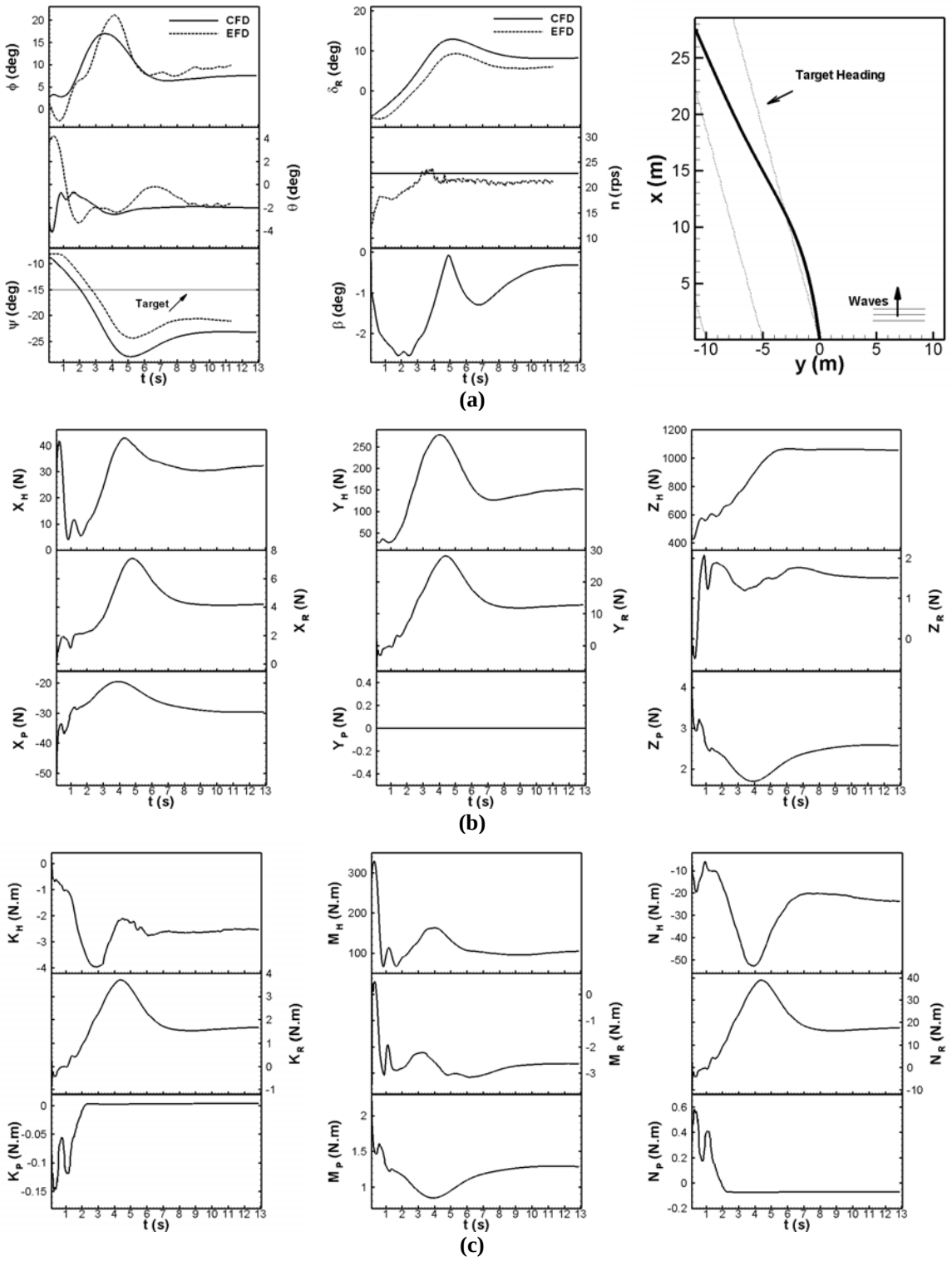

Figure 8-13: CFD (ε_0=235°, $u_0/\hat{o}$ (Lg)=0.275) and EFD comparison for GM=2.068 m, Fr=0.45, and ψ_c=-15 deg: (a) motions; (b) forces; (c) moments

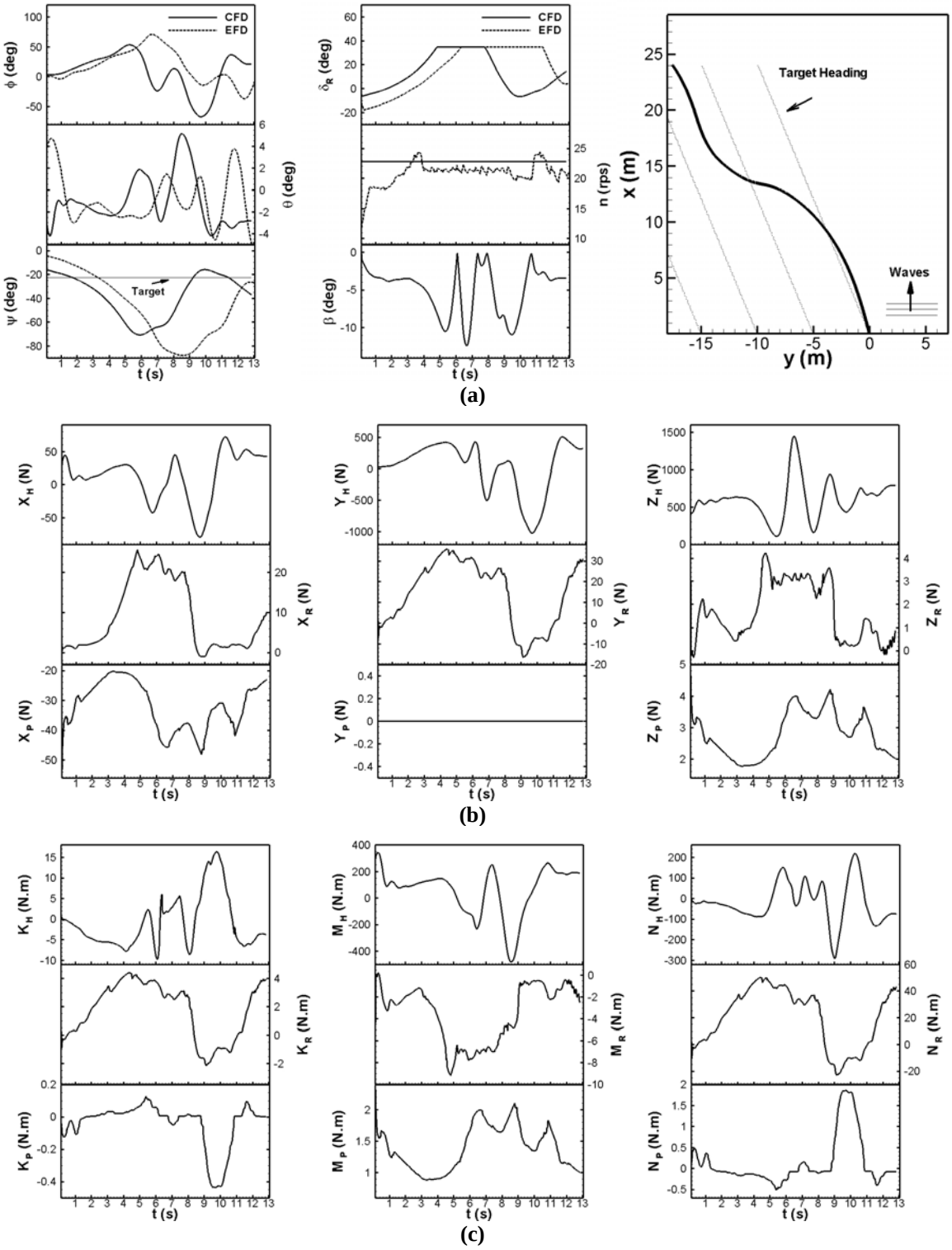

Figure 8-14: CFD (ε_0=235°, $u_0/\hat{o}$ (Lg)=0.275) and EFD comparison for GM=2.068 m, Fr=0.45, and ψ_c=-22.5 deg: (a) motions; (b) forces; (c) moments

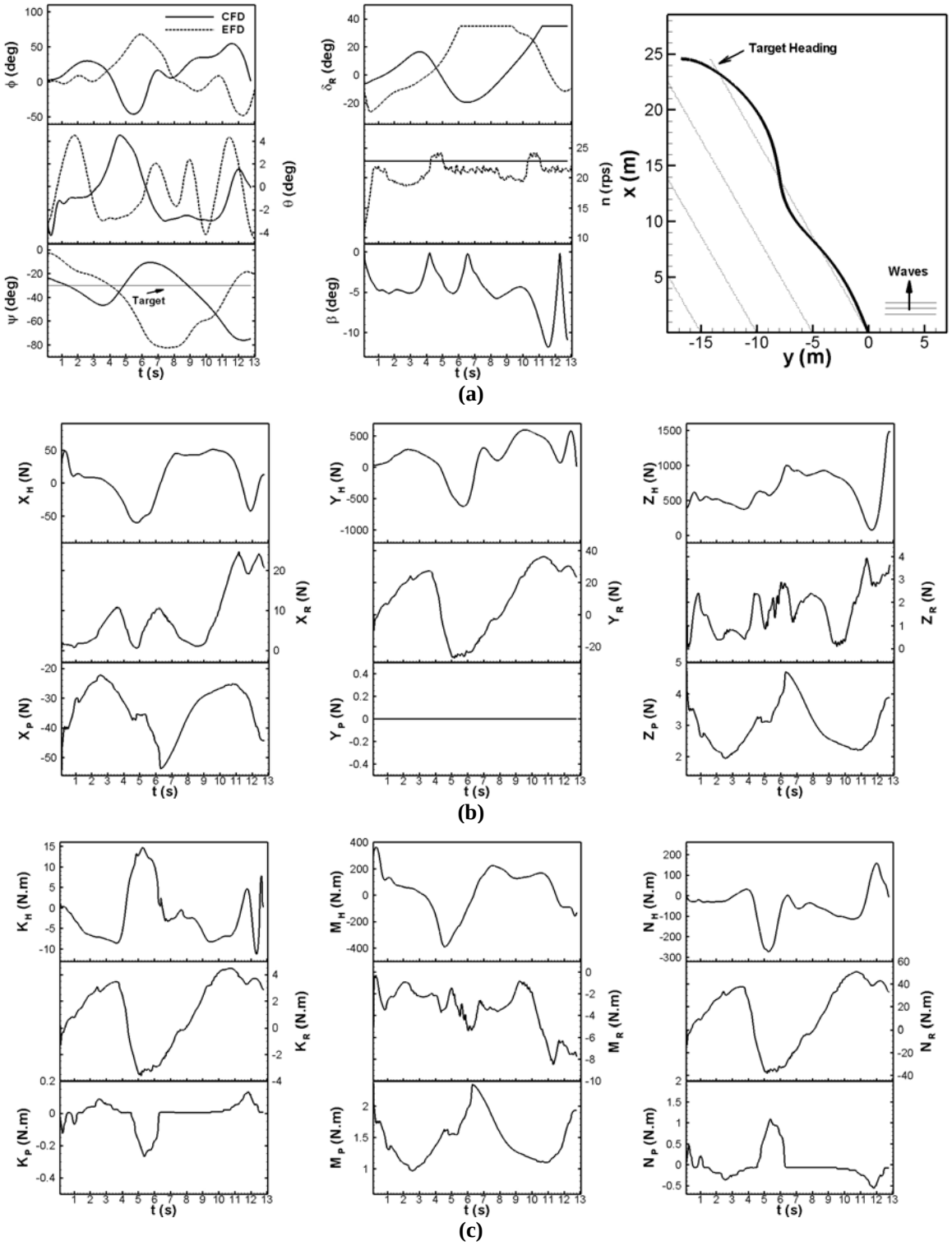

Figure 8-15: CFD (ε_0=235°, $u_0/\hat{o}$ (Lg)=0.275) and EFD comparison for GM=2.068 m, Fr=0.45, and ψ_c=-30 deg: (a) motions; (b) forces; (c) moments

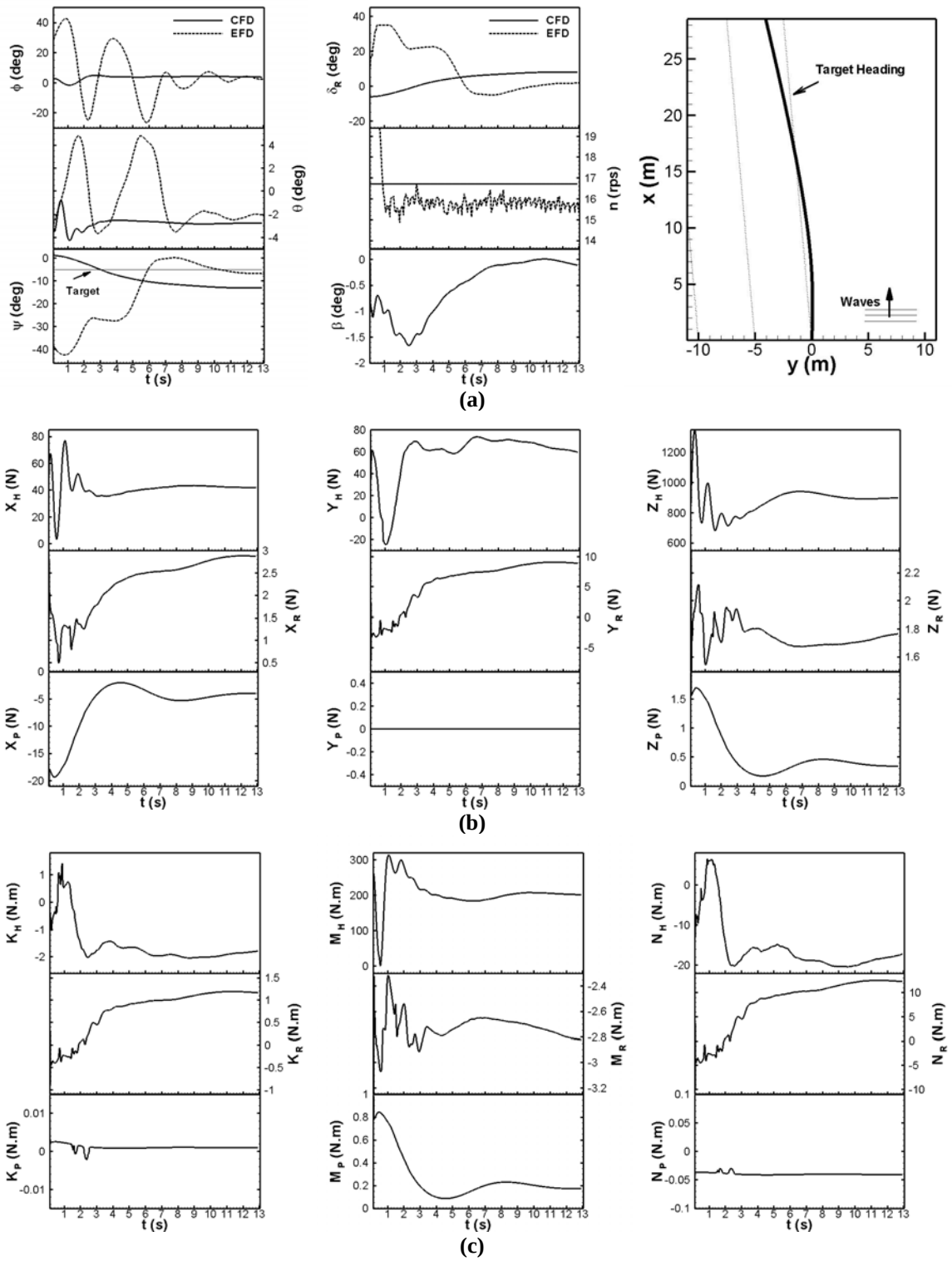

Figure 8-16: CFD (ε_0=235°, $u_0/\hat{o}$ (Lg)=0.275) and EFD comparison for GM=2.068 m, Fr=0.35, and ψ_c=-5 deg: (a) motions; (b) forces; (c) moments

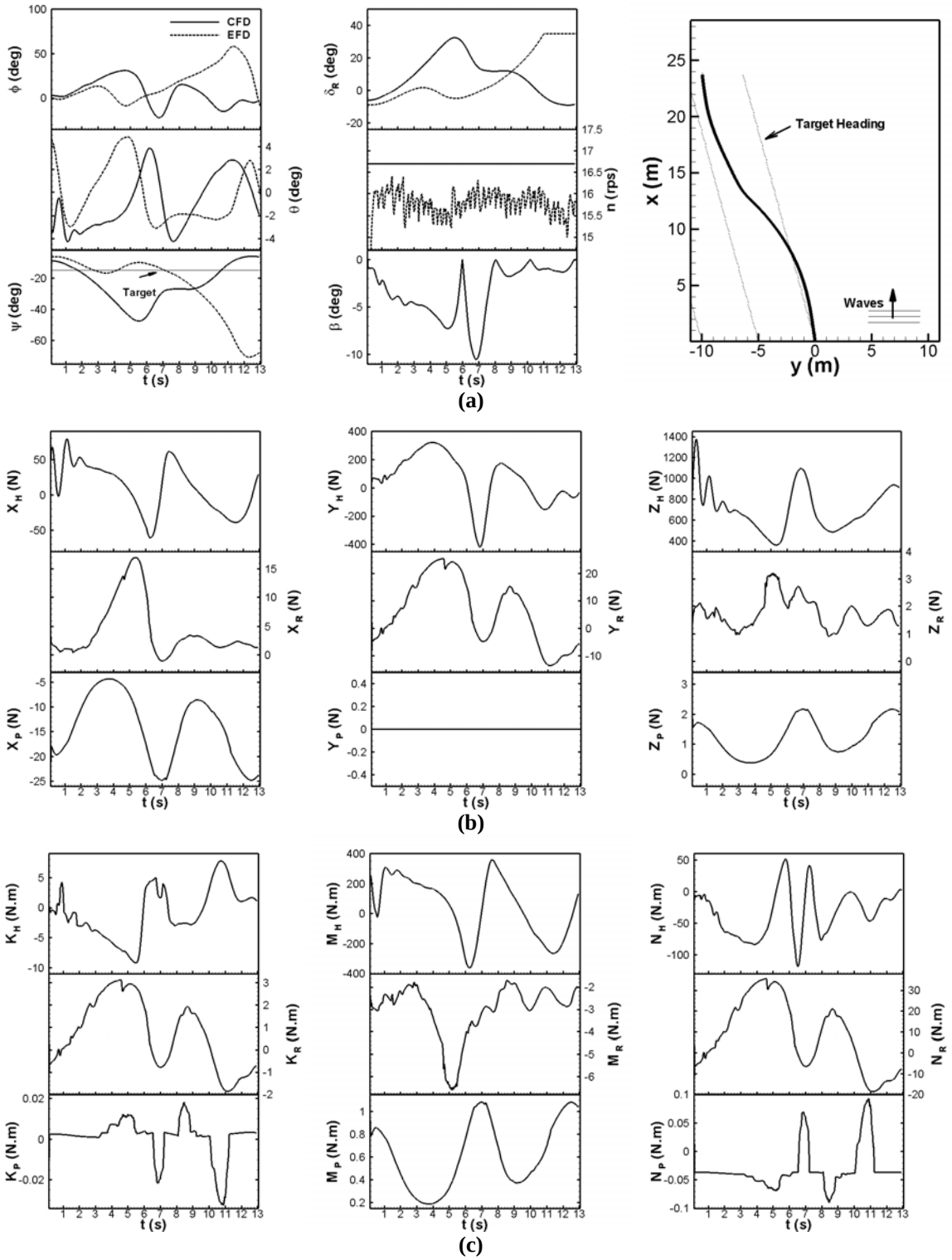

Figure 8-17: CFD (ε_0=0°, $u_0/\hat{o}$ (Lg)=0.275) and EFD comparison for GM=2.068 m, Fr=0.35, and ψ_c=-15 deg: (a) motions; (b) forces; (c) moments

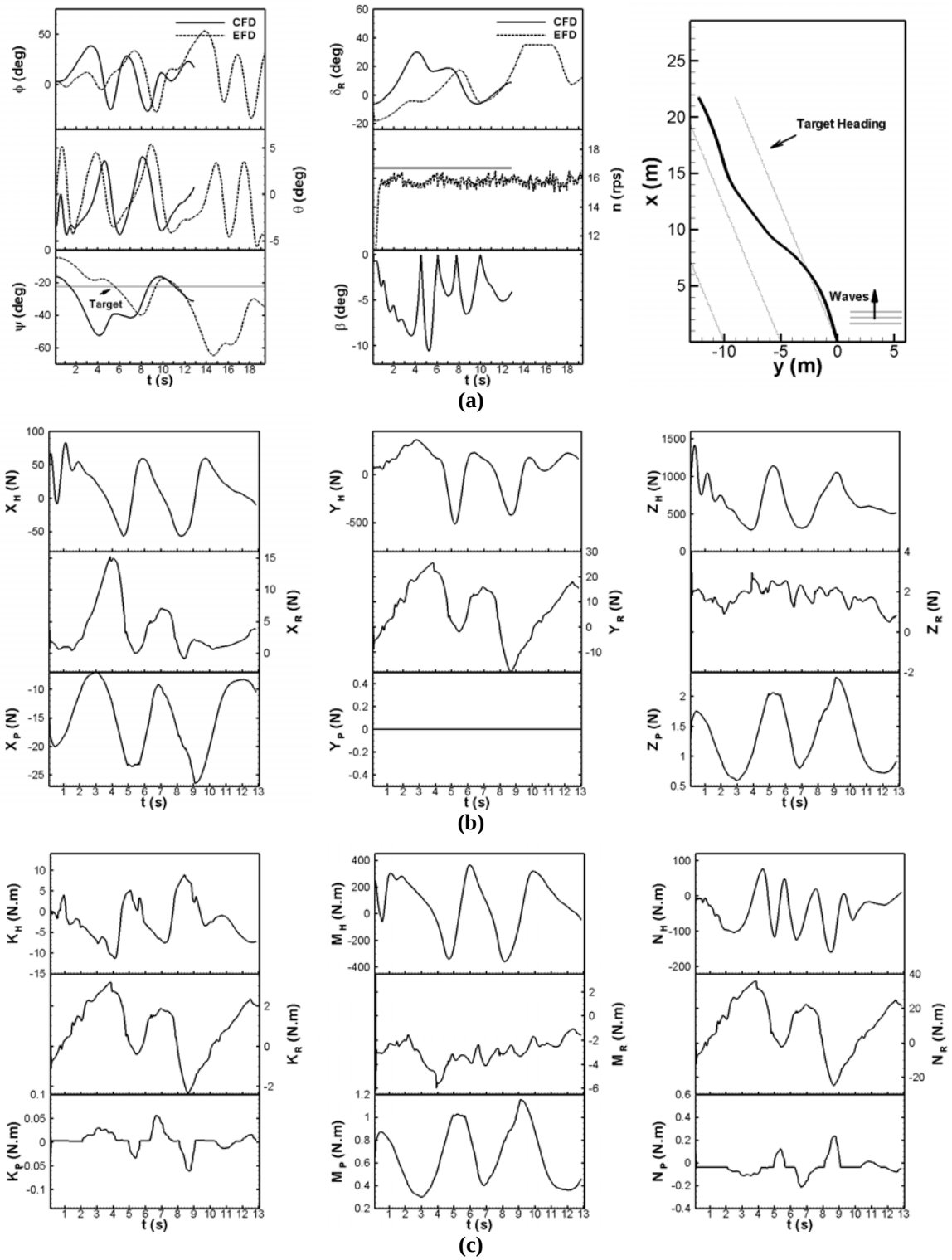

Figure 8-18: CFD (ε_0=0°, $u_0/\hat{o}$ (Lg)=0.275) and EFD comparison for GM=2.068 m, Fr=0.35, and ψ_c=-22.5 deg: (a) motions; (b) forces; (c) moments

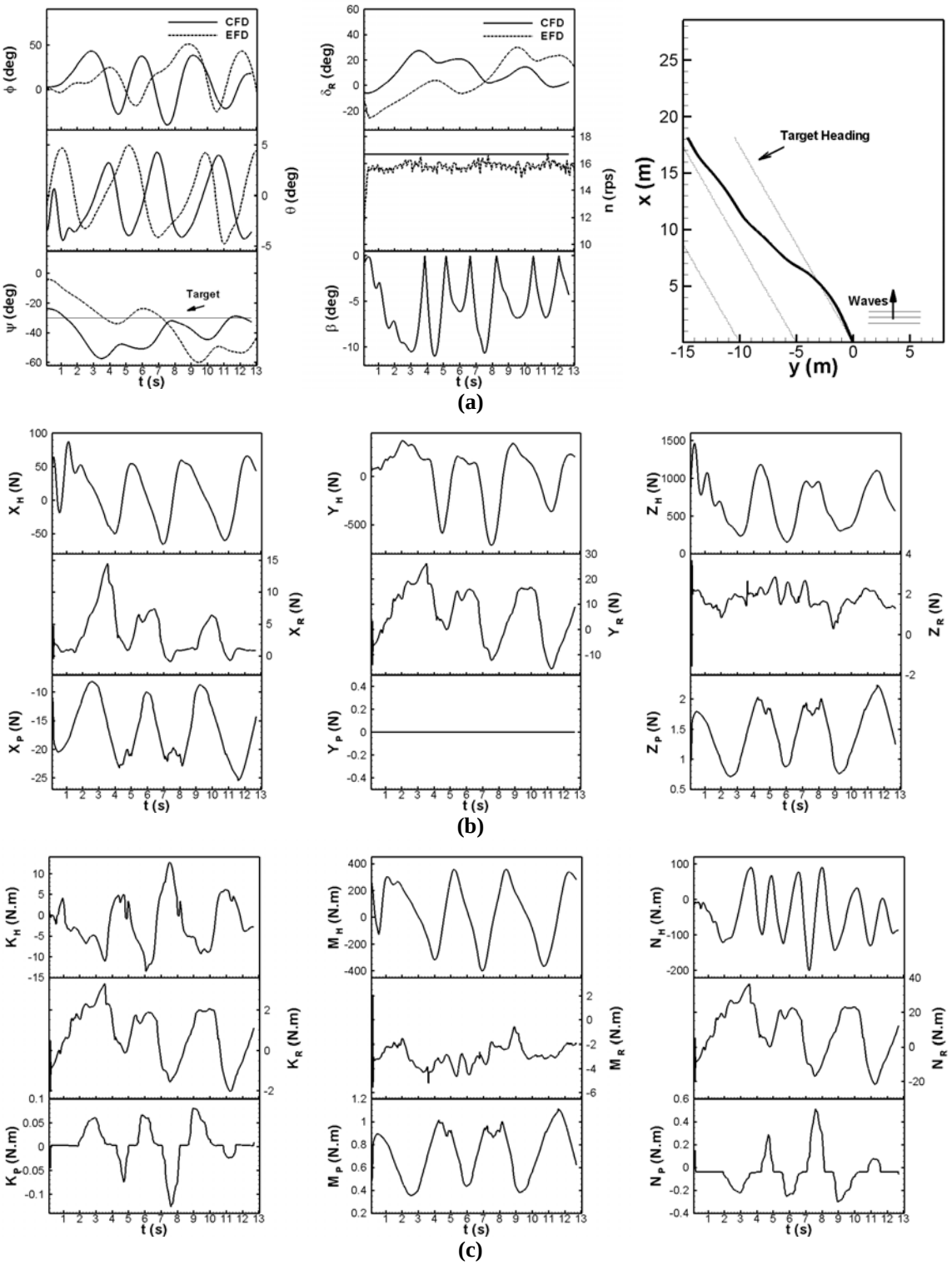

Figure 8-19: CFD (ε_0=0°, $u_0/\hat{o}$ (Lg)=0.275) and EFD comparison for GM=2.068 m, Fr=0.35, and ψ_c=-30 deg: (a) motions; (b) forces; (c) moments

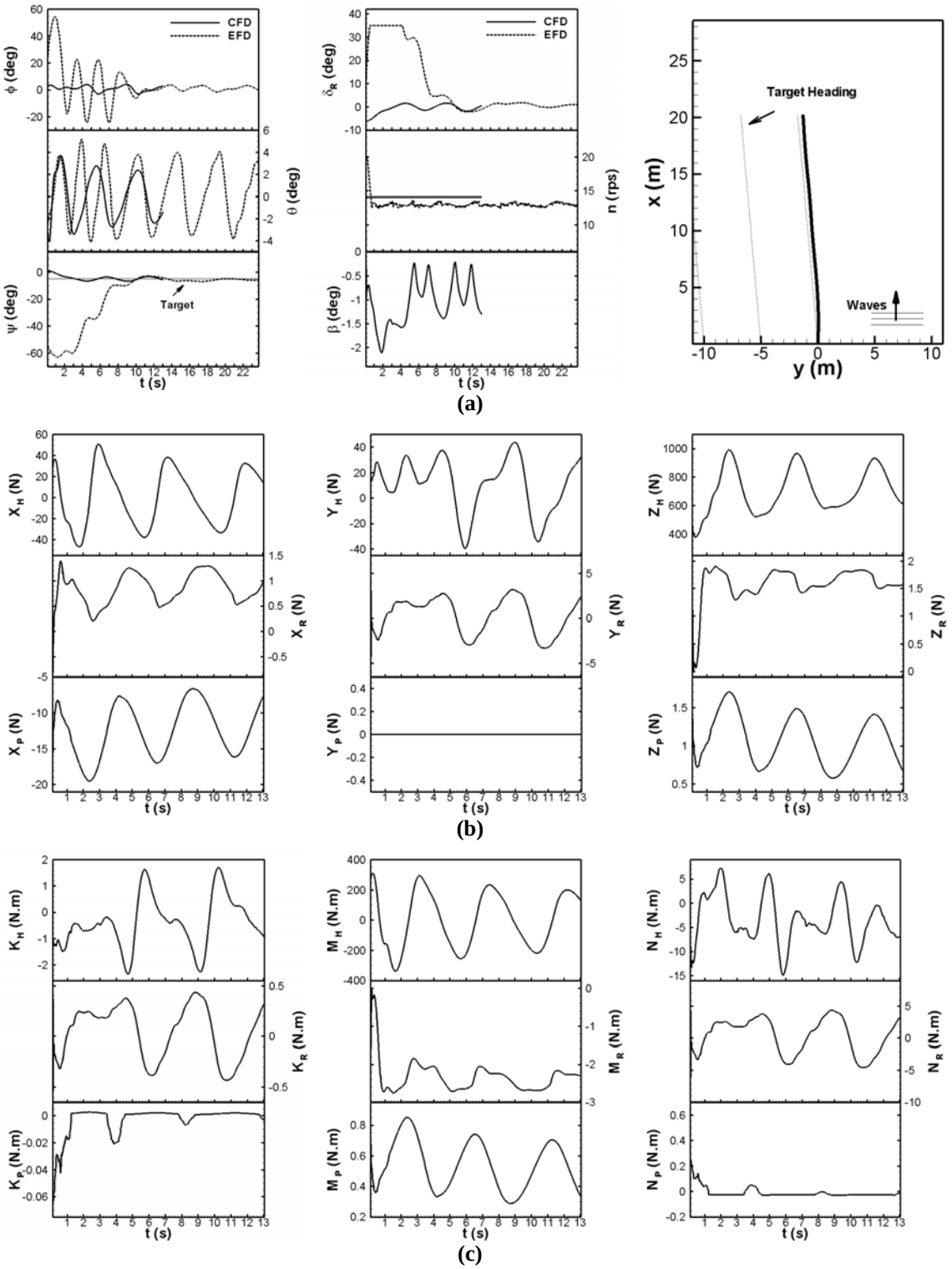

Figure 8-20: CFD (ε_0=235°, $u_0/\hat{o}$ (Lg)=0.2) and EFD comparison for GM=2.068 m, Fr=0.3, and ψ_c=-5 deg: (a) motions; (b) forces; (c) moments

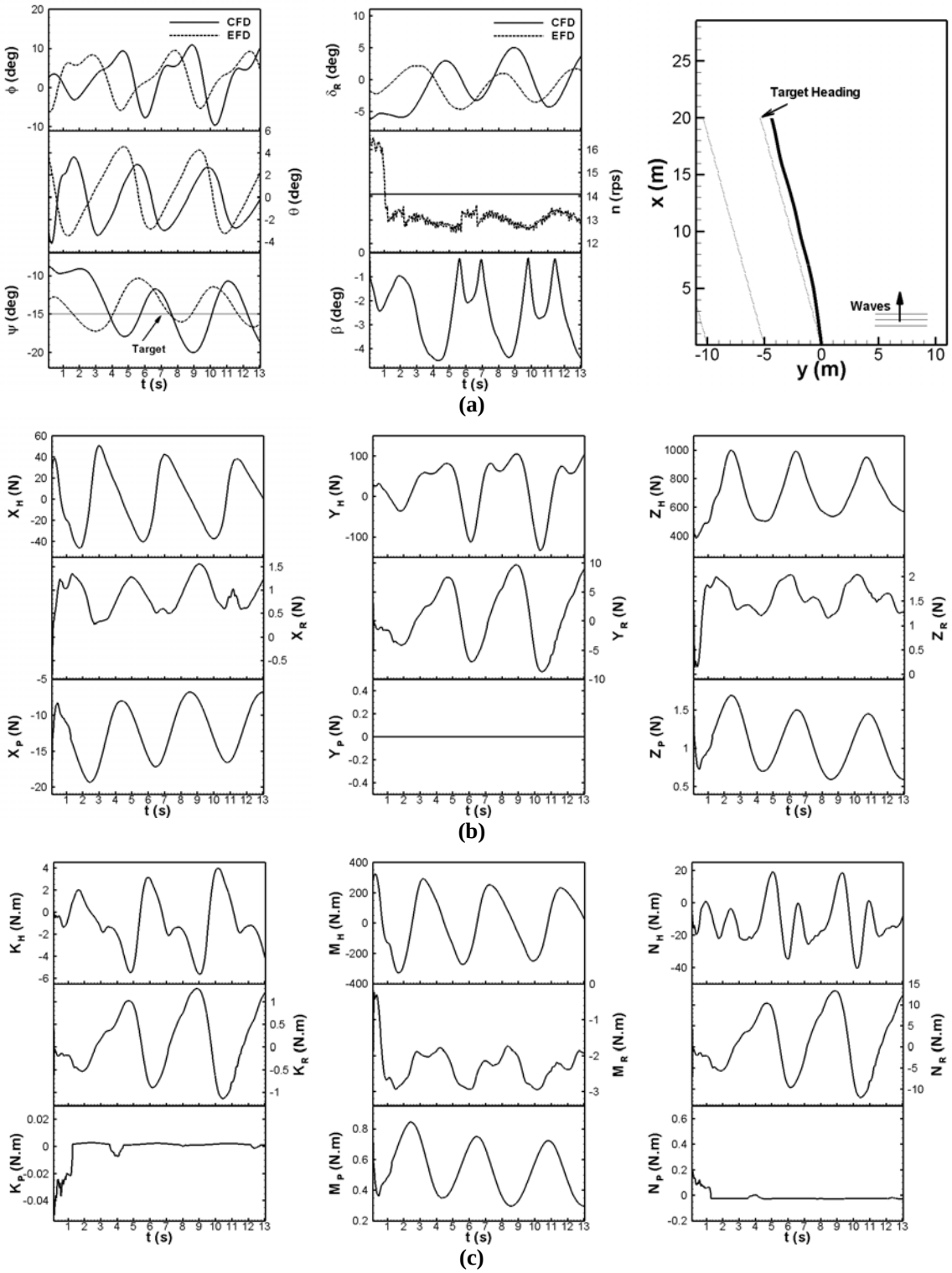

Figure 8-21: CFD (ε_0=235°, $u_0/\hat{o}$ (Lg)=0.2) and EFD comparison for GM=2.068 m, Fr=0.3, and ψ_c=-15 deg: (a) motions; (b) forces; (c) moments

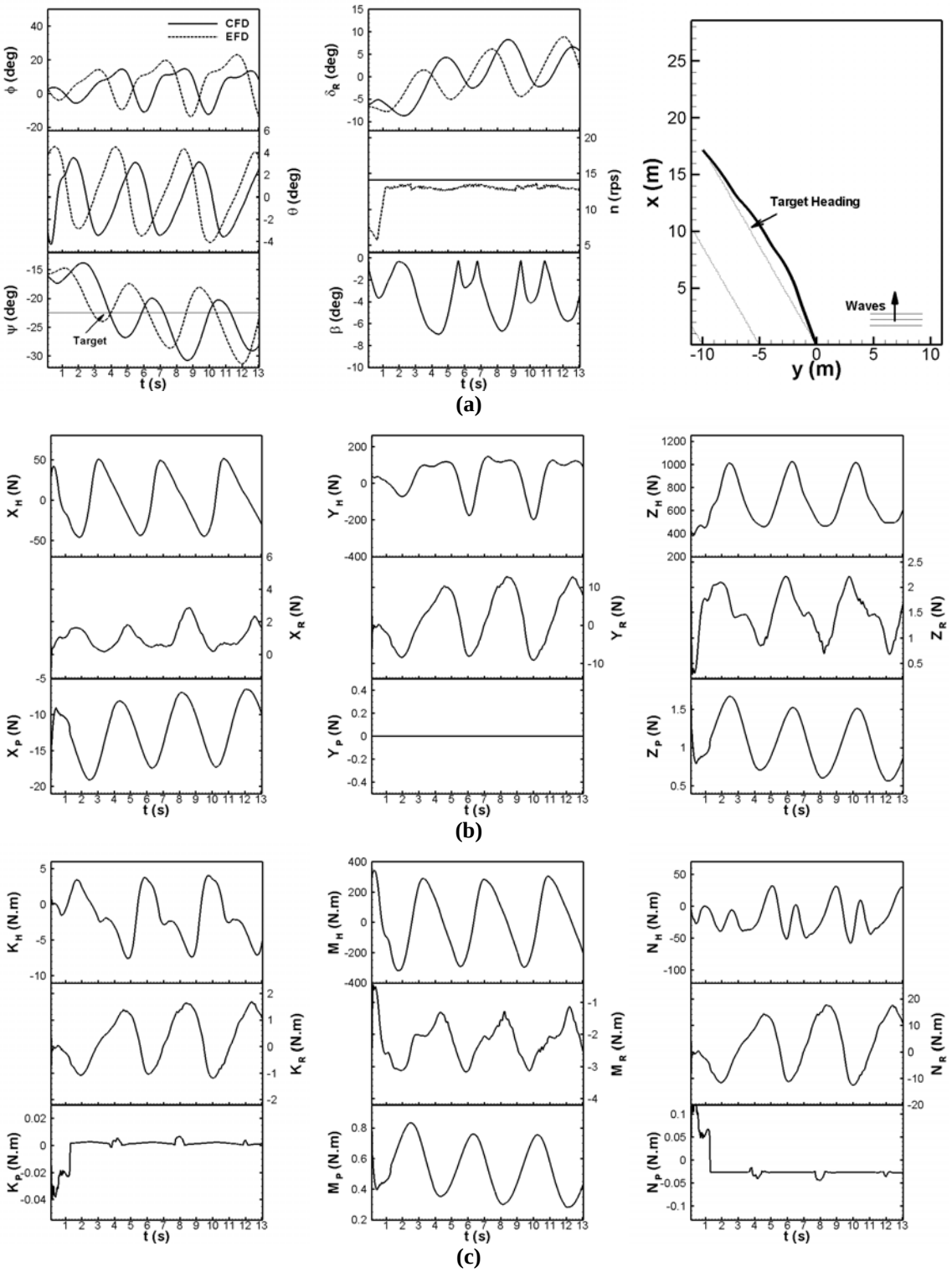

Figure 8-22: CFD (ε_0=235°, $u_0/\hat{o}$ (Lg)=0.2) and EFD comparison for GM=2.068 m, Fr=0.3, and ψ_c=-22.5 deg: (a) motions; (b) forces; (c) moments

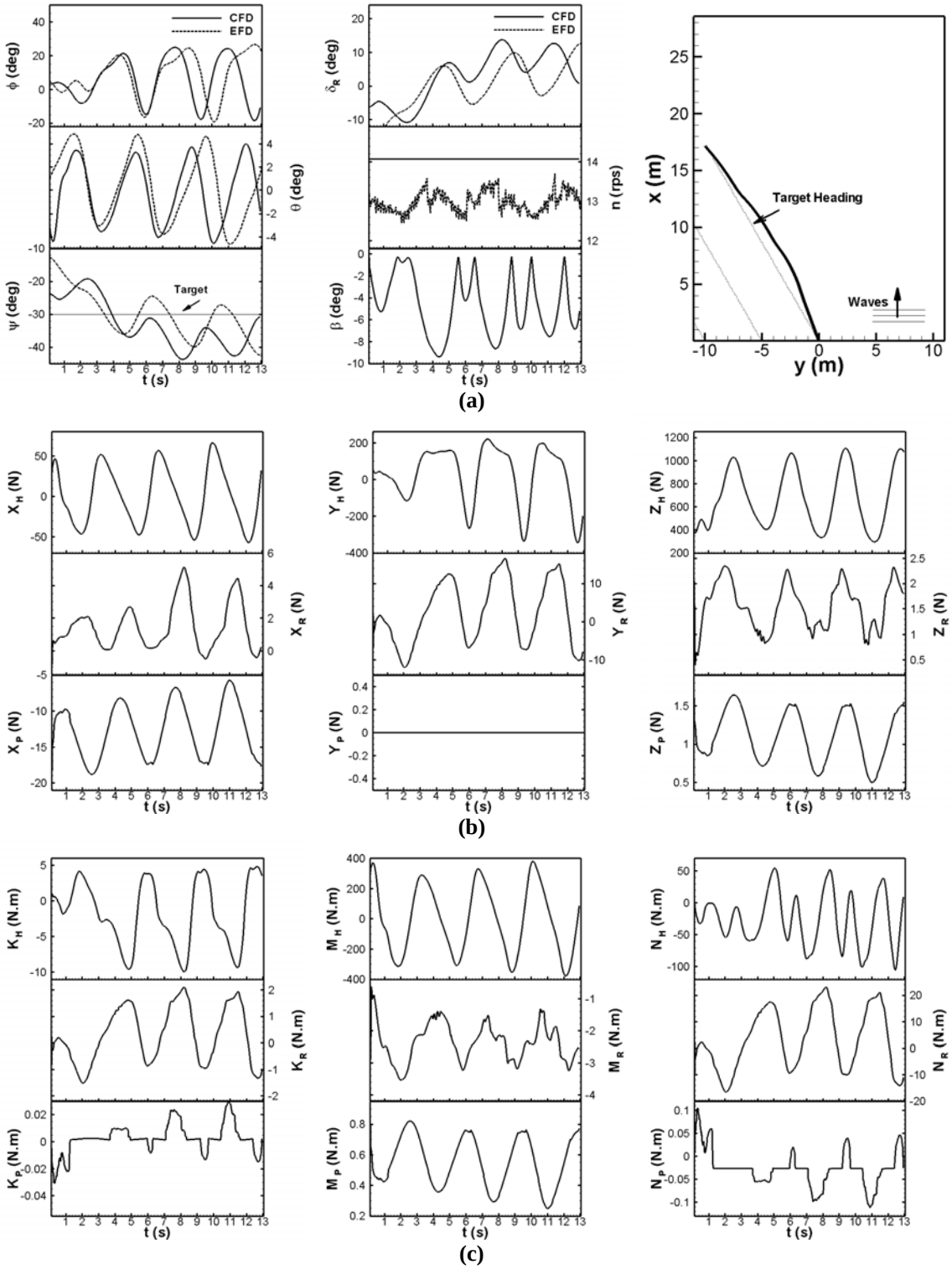

Figure 8-23: CFD (ε_0=235°, $u_0/\hat{o}$ (Lg)=0.2) and EFD comparison for GM=2.068 m, Fr=0.3, and ψ_c=-30 deg: (a) motions; (b) forces; (c) moments

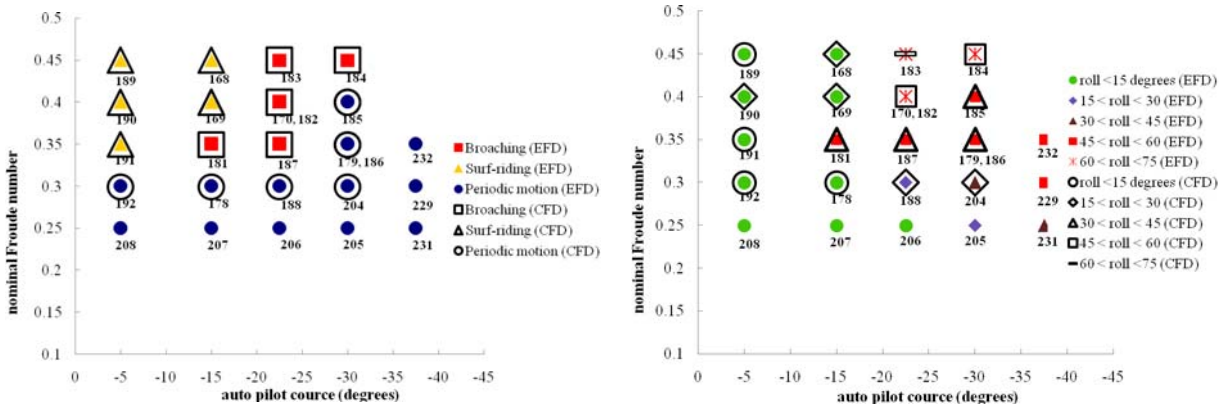

Figure 8-24: Summary of CFD simulations for Test Program 2

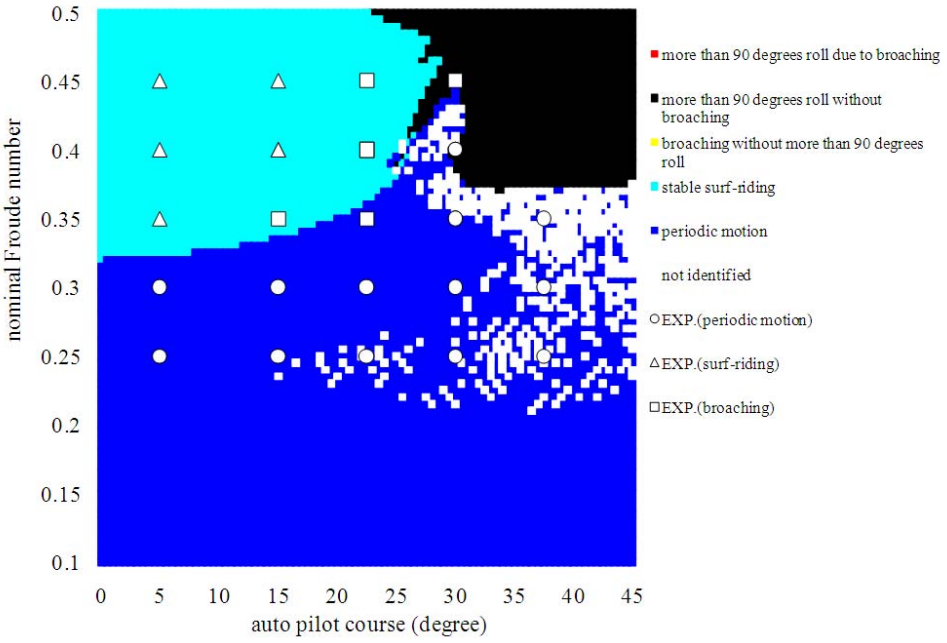

Figure 8-25: Comparison between the free model test and the system-based numerical simulation using the wave-induced surge force estimated by the captive model experiment

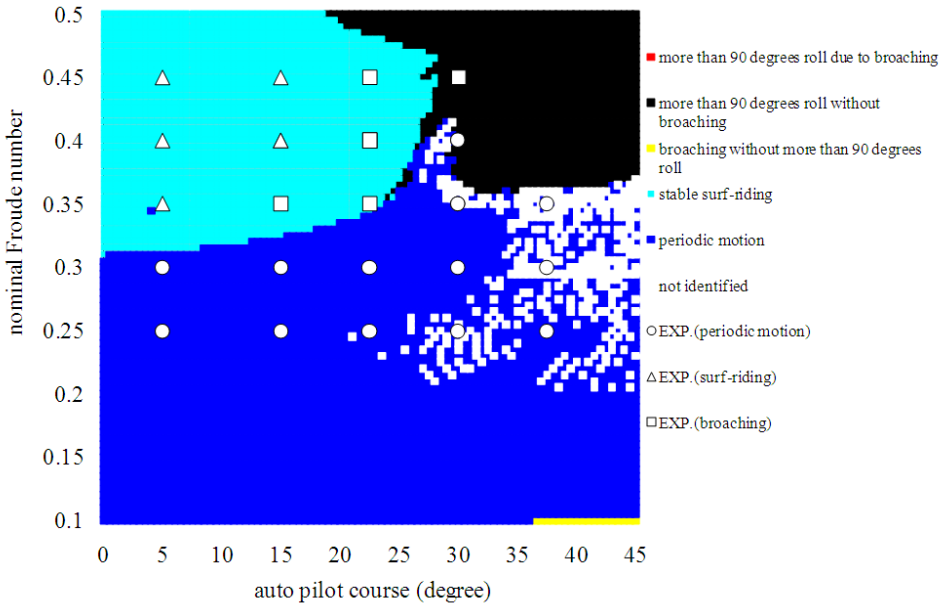

Figure 8-26: Comparison between the free model test and the system-based numerical simulation using the wave-induced surge force estimated by potential theory

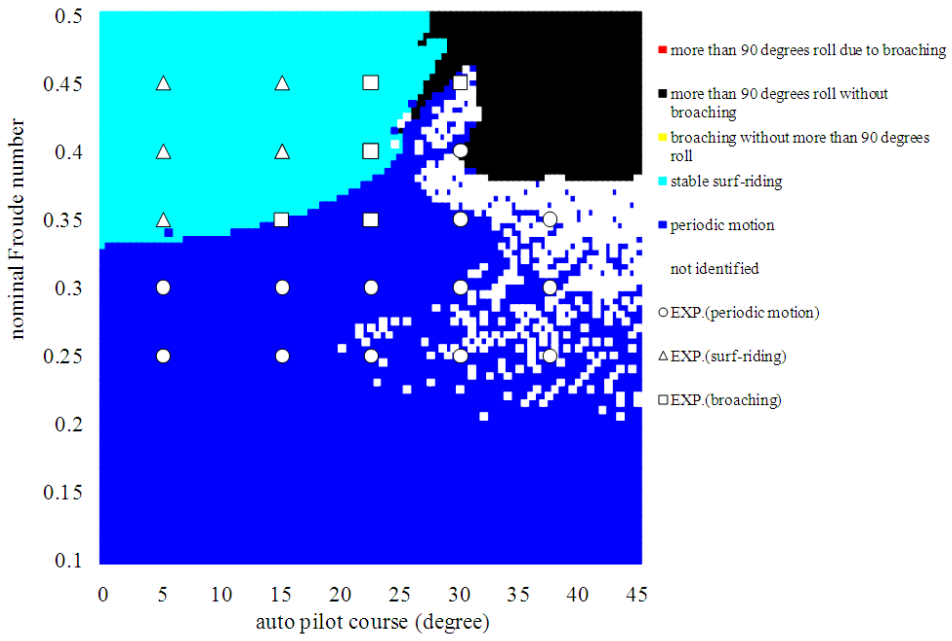

Figure 8-27: Comparison between the free model test and the system-based numerical simulation using the wave-induced surge force estimated by CFD

CHAPTER 9. CONCLUSIONS AND FUTURE WORK

For the first time, the CFD simulations and NDA predictions of ship instability are performed with focus on parametric rolling and broaching and compared with EFD.

The CFD and NDA parametric rolling studies for OT surface combatant include roll decay in calm water and roll decay/parametric rolling in head waves. CFD roll decay in calm water indicates good agreement with EFD, especially for GM=0.043 m and GM=0.038 m. CFD reasonably predicts the influence of mean roll angle and Fr on damped roll frequency. CFD predicts the speed effect on linear damping and shows similar values to EFD for GM=0.043 m, but under predicts for lower GM. CFD nonlinear damping shows good agreement with EFD for GM=0.043 m and under predicts for lower GM, especially GM=0.038 m and Fr=0.35. The NDA model of OT roll decay indicates that OT roll reconstruction requires nonlinear restoring coefficients with linear or nonlinear damping coefficient. Comparing NDA roll decay reconstruction with CFD indicates that E values are similar to those for CFD. OT is compared with 5415 surface combatant. Comparing 5415 and OT shows that effects of mean roll angle on roll decay characteristics are stronger for OT vs. 5415. The linear damping of 5415 is smaller than that of OT and the nonlinear damping is not observed for 5415 whereas it is significant for OT. Bert reconstruction for 5415 is for equivalent linear damping without requiring nonlinear restoring coefficients whereas best reconstruction for OT requires nonlinear damping and restoring coefficients. CFD parametric rolling simulations show remarkably close agreement with EFD. CFD predicts parametric roll in head waves for GM=0.038 and 0.033 m and roll decay for GM=0.043 m. The CFD stabilized roll angle is very close to those of EFD but CFD predicts larger instability zones. The CFD and EFD results are analyzed with consideration ship motion theory and compared with Mathieu equation and NDA. NDA predictions are in qualitative agreement with CFD and EFD. The CFD and

NDA results were blind in that the actual EFD radius of gyration k_{xx} was not known a priori.

The CFD studies of parametric rolling are extended for prediction of broaching both by using CFD as input to NDA in replacement of EFD or potential flow methods and by using CFD for broaching simulation. The CFD calm water captive resistance test, static heel, and static drift simulations are conducted to estimate inputs for NDA model of broaching and 6DOF simulation in following/quartering waves are conducted for complete simulation of broaching. For captive tests, the grid study is performed for calm water static heel which indicates the average RSS grid uncertainty is 3%D. CFD resistance test full Fr curve simulation in calm water shows close agreement with EFD with average RSS error of 3%D for X, σ, τ. CFD and EFD full Fr curve static heel results show fairly close agreement for σ, τ, X, K for the full Fr range, whereas Y and N were significantly under predicted for large Fr>.4. Forces and moment analyses support the mathematical model of static heel showing that heel angle has second order effect on X while it has first order effect on Y, K, and N such that increasing heel angle would change Y, K, and N except X. CFD shows fairly close agreement for static heel linear maneuvering derivatives, whereas large errors are indicated for nonlinear maneuvering derivatives. CFD and EFD static drift show good results of σ, τ, X, Y, N for the full Fr range, whereas K is over predicted for Fr>0.2. It is shown that drift angle has second order effect on X and first order effect on Y, K, and N. CFD shows reasonable agreement for static drift linear maneuvering derivatives, whereas large errors are indicated for nonlinear maneuvering derivatives. CFD non-zero static heel in following waves shows fairly close agreement for σ, τ, K, N, whereas X and Y show large errors. CFD zero static heel in following waves shows large errors for X and θ. The average error increases by factor of 2 for same increase in wave amplitude. Heave response shows 1st and 2nd harmonics and pitch show 1st harmonic. X indicates 1st and 2nd harmonics and Y and N show 1st, 2nd, and 4th harmonics. The surge force in following wave is estimated from

Potential Theory calculation (Froude-Krylov calculation) and compared with CFD and EFD. It is shown that CFD successfully reproduces the decrease of the wave-induced surge force near the Fr of 0.2 whereas Potential Theory fails probably because it cannot capture the 3D wave pattern.

The CFD broaching simulations are performed for series of control parameters (heading and Fr) to study and analyze the process of surf-riding, broaching, and periodic motion. The CFD results are compared with the results of NDA model based on CFD, EFD, and Potential Calculation inputs. CFD 2DOF self-propulsion simulation is carried out with propeller model and actual propeller to predict necessary RPS for several Fr. The prediction error of propeller RPS is about 5.8%D for propeller model while it drops to 1.7 %D for actual propeller. This suggests the simplicity and efficiency of body force propeller model would cost about 4%D more error which is reasonable. CFD free model simulations show promising results for surf-riding, broaching and periodic motion. CFD predicts the instability boundary perfectly. For small heading (ψ_c < 30 deg), there is a boundary between surf-riding/broaching and periodic motion at Fr=0.3. CFD predicts surf-riding/broaching above the boundary and periodic motion below the boundary. CFD calculation of wave and rudders yaw moment explains the processes of surf-riding, broaching, and periodic motion. It is concluded that wave yaw moments is the major cause of broaching/periodic motion, with rudder and propeller moments much smaller in magnitude. The ship speed increases significantly before surf-riding/broaching which might produce large turning rate and consequently large centrifugal force and roll moment. The emergence of propeller out of water and water on deck occurrence are observed for many cases. It is shown that OT would not capsize due to large restoring moment of its superstructure. The comparison of CFD and EFD time history of motions show a phase difference between CFD and EFD, possibly due to inaccurate initial conditions and/or propeller modeling. The NDA simulation using EFD inputs predicts the boundary but the simulated roll exceeds 90 degrees for Fr>0.3 while EFD maximum roll

angle is 71 degrees. This might be improved by considering emergence of propeller and rudder out of water in the mathematical model. The NDA simulation using CFD and Potential Flow (Froude-Krylov calculation) inputs predicts reasonably the boundary of instability and suggests that CFD/ Potential Flow can be considered as replacement for EFD inputs.

It is recommended that future work extends presented broaching simulations by replacing body force propeller model with actual propeller similar to reality. It is expected that the CFD and EFD agreement will be improved even though the role of the uncertainty on initial conditions would be still an issue. Also current 4DOF surge-sway-roll-yaw NDA model of broaching should be extended to 6DOF model including heave and pitch motion to improve NDA predictions and build a model to analyze 6DOF simulations.

REFERENCES

Balay, S., Buschelman, K., Gropp, W., Kaushik, D., Knepley, M., Curfman, L., Smith, B., and Zhang, H., 2002, "PETSc User Manual", ANL-95/11-Revision 2.1.5, Argonne National Laboratory.

Bensow, R.E., and Fureby, C., 2007, "Large Eddy Simulation of Viscous Flow around a Submarine during Maneuver", 9th Numerical Ship Hydrodynamics Conference, Vol. I, pp. 282-297.

Bhushan, S., Xing, T., Carrica, P., and Stern, F., 2007, "Model- and Full-Scale URANS/DES Simulations for Athena R/V Resistance, Powering, and Motions", 9th Numerical Ship Hydrodynamics Conference, Vol. II, pp. 122-142.

Boger, D.A., and Dreyer, J.J., 2006, "Prediction of Hydrodynamic Forces and Moments for Underwater Vehicles Using Overset Grids", AIAA Paper No. 2006-1148.

Bulian, G., 2004, "Approximate Analytical Response Curve for a Parametrically Excited Highly Nonlinear 1-DOF System with an Application to Ship Roll Motion Prediction", Nonlinear Analysis: Real World Applications, Vol. 5, No. 4, pp. 725-748.

Bulian, G., 2005, "Nonlinear Parametric Rolling in Regular Waves - A General Procedure for the Analytical Approximation of the GZ Curve and Its Use in Time Domain Simulations", Ocean Engineering, Vol. 32, No. 3-4, pp. 309-330.

Bulian, G., Francescutto, A., 2008, "Theoretical Prediction and Experimental Verification of Multiple Steady States for Parametric Roll", 10th International Workshop on Ship Stability and Operational Safety, Daejeon.

Bulian, G., Francescutto, A., and Lugni, C., 2003,"On the Non-linear Modeling of Parametric Rolling in Regular and Irregular Waves", Proceedings of 8th International Conference on the Stability of Ships and Ocean Vehicles (STAB 2003), Madrid, Spain, pp. 305-323.

Burcher, R.K., 1990, "Experiments into the Capsize of Ships in Head Seas", Proceedings of International Conference on the Stability of Ships and Ocean Vehicles (STAB 90), Naples, Vol.1, pp. 82–89.

Carrica, P.M., Ismail, F., Hyman, M., Bhushan, S., and Stern, F., 2008a, "Turn and Zigzag Manoeuvres of a Surface Combatant Using a URANS Approach with Dynamic Overset Grids", SIMMAN 2008, Copenhagen.

Carrica, P.M., Paik, K.J., Hosseini, H.S., and Stern, F., 2008b, "URANS Analysis of a Broaching Event in Irregular Quartering Seas", Journal of Marine Science and Technology, Vol.13, pp.395-407.

Carrica, P.M., Stern, F., 2008c, "DES Simulations of KVLCC1 in Turn and Zigzag Manoeuvring with Moving Propeller and Rudder", SIMMAN 2008, Copenhagen.

Carrica, P.M., Wilson, R.V., and Stern, F., 2007a, "An Unsteady Single-Phase Level Set Method for Viscous Free Surface Flows", International Journal Numerical Methods Fluids, Vol. 53, Issue 2, pp. 229-256.

Carrica, P.M., Wilson, R.V., Noack, R.W., and Stern, F., 2007b, "Ship Motions Using Single-Phase Level Set with Dynamic Overset Grids", Computers & Fluids, Vol. 36, No. 9, pp. 1415-1433.

Carrica, P.M., Wilson, R.V., Noack, R.W., Xing, T., Kandasamy, M., Shao, J., Sakamoto, N., Stern, F., 2006, "A Dynamic Overset Single Phase Level Set Approach for Viscous Ship Flows and Large Amplitude Motions and Maneuvering", 26th ONR Symposium on Naval Hydrodynamics, Rome, Vol. 1, pp. 97-116.

Das, S.N., Das, S.K., 2004, "Determination of Coupled Sway, Roll and Yaw Motions of a Floating Body in Regular Waves", International Journal of Mathematics and Mathematical Sciences, Vol. 41, pp. 2181-2197.

Das, S.N., Das, S.K., 2005, "Mathematical Model for Coupled Roll and Yaw Motions of a Floating Body in Regular Waves under Resonant and Non-Resonant Conditions", Applied Mathematical Modeling, Vol. 29 (1), pp. 19-34.

De Kat, J.O., and Thomas, W.L., 1998a, "Extreme Rolling, Broaching and Capsizing–Model Tests and Simulations of a Steered Ship in Waves", 22nd Symposium on Naval Hydrodynamics, Washington, D.C.

De Kat, J.O., and Thomas, W.L., 1998b, "Model Tests for Validation of Numerical Capsize Predictions", 4th Stability Workshop, Canada.

Eissa, M., and EI-Bassiouny, A., 2003, "Analytical and Numerical Solutions of a Nonlinear Ship Rolling Motion", Journal of Applied Mathematics and Computing, Vol. 134, pp. 234–270.

Fosson, T.I., 1999, "Guidance and Control of Ocean Vehicles", New York: John Willy & Sons Ltd.

France, W.N., Levadou, M., Treakle, T.W., Paulling, J.R., Michel, R.K. and Moore, C., 2003, "An Investigation of Head-Sea Parametric Rolling and its Influence on Container Lashing Systems", Marine Technology, Vol. 40(1), pp.1–19.

Francescutto, A., 2001, "An Experimental Investigation of Parametric Rolling in Head Waves", Journal of Offshore Mechanics and Arctic Engineering, Vol. 123, pp.65–69.

Francescutto, A., Bulian, G., and Lugni, C., 2004, "Nonlinear and Stochastic Aspects of Parametric Rolling", Marine Technology, Vol. 41(2), pp.74-81.

Hamamoto, M., Enomoto, T., Sera, W., Panjaitan, J., Ito, H., Takaishi, Y., Kan, M., Haraguchi, T., and Fujiwara, T., 1996, "Model Experiments of Ship Capsize in Astern Seas", JSNAJ, Vol. 179, pp. 77-87.

Hashimoto, H., Umeda, N., 2002 "Enhanced Approach for Broaching Prediction with Higher Order Terms taken into account", Proceedings of the 6th International Ship Stability Workshop.

Hashimoto, H., Umeda, N., 2004, "Nonlinear Analysis of Parametric Rolling in Longitudinal and Quartering seas with Realistic Modeling of Roll-Restoring Moment", Journal of Marine Science and Technology, Vol.9, No.3, pp.117-126.

Hashimoto, H., Umeda, N., Matsuda, A. and Nakamura, S., 2006, "Experimental and Numerical Studies on Parametric Roll of a Post-Panamax Container Ship in Irregular Waves", Proc. STAB 2006, Rio de Janeiro, pp.181–190.

Hashimoto, H., Umeda, N., Matsuda, A., 2004a "Importance of Several Nonlinear Factors on Broaching Prediction", Journal of Marine Science and Technology, Vol.9, pp.80-93.

Hashimoto, H., Umeda, N., Matsuda, A., 2004b, "Model Experiment on Heel-Induced Hydrodynamic Forces in Waves for Broaching Prediction", Proceedings of the 7th International Ship Stability Workshop, Shanghai Jiao Tong Univ., pp.144-155.

Himeno, Y., 1981, "Prediction of Ship Roll Damping – State of the Art", University of Michigan, Report No. 239.

Hochbaum, AC., Vogt, M., 2002, "Towards the Simulation of Seakeeping and Maneuvering Based Computation of the Free Surface Viscous Ship Flow," Proceedings of the 24th Symposium on Naval Hydrodynamics, Fukuoka, Japan.

Huang, J., Carrica, P., Stern, F., 2008, "Semi-coupled air/water immersed boundary approach for curvilinear dynamic overset grids with application to ship hydrodynamics," International Journal Numerical Methods Fluids, Volume 58, Issue 6, pp. 591-624.

Hyman, M.C., Moraga, F.J., Drew, D.A. and Lahey, R.T., 2006, "Computation of the Unsteady Two-Phase Flow around a Maneuvering Surface Ship", 26th ONR Symposium on Naval Hydrodynamic, Vol. 2, pp. 39-58.

IMO, 2006, "Japan Remarks of Numerical Modeling for Parametric Rolling", SLF49/5/7/Corr.1.

Irvine, M., Longo, J., Stern, F., 2004, "Towing Tank Tests for Surface Combatant for Free Roll Decay and Coupled Pitch and Heave Motions," Proc. 25th ONR Symposium on Naval Hydrodynamics, St. Johns, Canada.

Ishida, S., 1993, "Model Experiment on the Mechanism of Capsizing of a Small Ship in Beam Seas (Part2 On the Nonlinearity of Sway Damping and its Lever)", JSNAJ, Vol.174.

Ishida, S., Takaishi, Y., 1990, "A Capsizing Experiment of a Small Fishing Boat in Breaking Waves", STAB'90, Vol.1, Naples.

Kamel, M.M., 2007, "Bifurcation Analysis of a Nonlinear Coupled Pitch–Roll Ship", Mathematics and Computers in Simulation, Vol. 73, pp. 300–308.

Lilienthal, T., Matsuda, A., and Thomas, G., 2007 "Dynamic Stability in Following Seas: Predictive and Experimental Approaches", Journal of Marine Science and Technology, Vol. 12, No. 2.

Lin, W.M., Yue, D.KP., 1991, "Numerical Solutions for Large Amplitude Ship Motions in The Time Domain", Proc. 18th Symposium on Naval Hydrodynamics, Washington D.C., pp.41-66.

Matsuda, A., Hashimoto, H., and Umeda, N., 2006, "Experimental and Theoretical Study on Critical Condition of Bow-Diving", Proc. STAB 2006, Rio de Janeiro, pp.455-461.

Menter, F.R., 1994, "Two Equation Eddy Viscosity Turbulence Models for Engineering Applications", AIAA J., Vol. 32(8), pp. 1598-1605.

Mulvihill, L.P., and Yang, C., 2007, "Numerical Simulation of Flow over Fully Appended ONR Body-1 with Overset Grid Scheme", 9th Numerical Ship Hydrodynamics Conference, Vol. I, pp. 46-57.

Neves, M.A.S., Perez, N., and Lorca, O., 2002, "Experimental Analysis on Parametric Resonance for Two Fishing Vessels in Head Waves," Proc. 6th ISSW, New York.

Neves, M.A.S., Vivano, J.E.M, Rodriguez, C.A, 2009, "Numerical Dynamics on Parametric Rolling of Ships in Head Seas", Proc. STAB 2009, Russia, pp. 509-520.

Newman, J.N., 1977, "Marine Hydrodynamics", Cambridge, MA: MIT Press.

Noack, R., 2005, "SUGGAR: a General Capability for Moving Body Overset Grid Assembly", AIAA Paper No. 2005-5117.

Oakley, O.H., Paulling, J.R., and Wood, P.D., 1974, "Ship Motions and Capsizing in Astern Seas", 10th Naval Hydrodynamics Symp., MIT, IV-1, pp. 1-51.

Olivieri, A., Campana, E., Francescutto, A., and Stern, F., 2006a "Beam Seas Tests of Two Different Ship Models in Large Amplitude Regular Waves", Proceedings 9th International Conference on Stability of Ships and Ocean Vehicles.

Olivieri, A., Campana, E., Stern, F., and Francescutto, A., 2006b, "Capsize High-Quality Data for Validation of URANS Codes", Proc. 26th ONR Symposium on Naval Hydrodynamics, Rome, Italy.

Olivieri, A., Francescutto, A., Campana, E., and Stern, F., 2008, "Parametric Roll Highly Controlled Experiments for an Innovative Ship Design", 27th International Conference on Offshore Mechanics and Arctic Engineering, Estoril, Portugal 15-20.

Orihara, H., and Myata, H., 2003, "A Numerical Method for Arbitrary Ship Motions in Arbitrary Wave Conditions using Overlapping Grid Systems", 8th Int. Conf. Numerical Ship Hydrodynamics, Busan, S. Korea.

Paulling, J.R., and Rosenberg, R.M., 1959, "On Unstable Ship Motions Resulting from Nonlinear Coupling", Journal of Ship Research, Vol. 3, No. 1.

Queutey, P., and Visonneau, M., 2007, "An Interface Capturing Method for Free-Surface Hydrodynamic Flows", Computers and Fluids, Vol. 36-9, pp. 1481-1510.

Sadat-Hosseini, H., Carrica, P., Stern, F., Umeda, N., Hashimoto, H., Matsuda, A., 2009a, "Comparison CFD, System-Based Approach and EFD of Surf-riding, Periodic Motion, and Broaching for ONR Tumblehome", 10th International Conference on Stability of Ships and Ocean Vehicles (STAB2009), St Petersburg, Russia.

Sadat-Hosseini, H., Park, I., Stern, F., Olivieri, A., Campana, E., Francescutto, A., 2007, "Complementary URANS CFD and EFD for Validation Extreme Motions Predictions", 9th ICNSH, Ann Arbor, MI.

Sadat-Hosseini, H., Stern, F., Olivieri, A., Campana, E., Hashimoto, H., Umeda, N., Bulian, G., Francescutto, A., 2009b, "Head-Waves Parametric Rolling of Surface Combatant", Journal of Ocean Engineering, submitted for review.

Sakamoto, N., 2009, "URANS and DES Simulation of Static and Dynamic Maneuvering for Surface Combatant", University of Iowa: Thesis and Dissertation.

Sarchin, T.H., and Goldberg, L.L., 1962, "Stability and Buoyancy Criteria for US Naval Ships", Transaction of the Society of Naval Architects and Marine Engineers, Vol. 70, pp. 418-458.

Sato, Y., Miyata, H., Sato, T., 1999, "CFD Simulation of 3-Dimensional Motion of a Ship in Waves: Application to an Advancing Ship in Regular Head Waves", Journal of Marine Science and Technology, 1999, Vol. 4, pp.108–116.

Shin Y.S., Belenky, V.L., Paulling, J.R, Weems, K.M., Lin, W.M., 2004," Criteria for Parametric Roll of Large Containerships in Longitudinal Seas", SNAME Annual meeting, Washington D.C.

Skomedal, S.G., 1982, "Parametric Excitation of Roll Motion and Its Influence on Stability", Proc. STAB 82, Tokyo, pp. 113–125.

Stern F., Ismail, F., Xing, T., and Carrica, P.M, 2008, "Vortical and Turbulent Structures using Various Convection Schemes with Algebraic Reynolds Stress-DES Model for the KVLCC2 at Large Drift Angles", Proceedings 27th Symposium Naval Hydrodynamics, Seoul, Korea.

Stern, F., Kim, H.T., Patel, V.C., and Chen, H.C., 1998, "A Viscous-Flow Approach to the Computation of Propeller-Hull Interaction", J. of Ship Research, Vol. 32(4), pp.246-262.

Surendran, S., and Reddy, J.V.R., 2002, "Roll Dynamics of a Ro–Ro Ship", International Shipbuilding Progress, Vol. 49, pp. 301-320.

Surendran, S., and Reddy, J.V.R., 2003, "Numerical Simulation of Ship Stability for Dynamic Environment", Ocean Eng., Vol. 30, pp. 1305-1317.

Umeda, N., 1998, "New Remarks on Methodologies for Intact Stability Assessment", 4th Stability Workshop, Canada.

Umeda, N., 1999, "Nonlinear Dynamics of Ship Capsizing Due to Broaching in Following and Quartering Seas", Journal of Marine Science and Technology, Vol. 4, pp.16–26.

Umeda, N., and Hamamoto, M., 2000, "Capsize of Ship Models in Following/ Quartering Waves -Physical Experiments and Nonlinear Dynamics-", Philosophical Transactions of the Royal Society of London, Series A, Vol. 358, pp.1883-1904.

Umeda, N., and Hashimoto, H., 2006, "Recent Development of Capsizing Prediction Techniques of Intact Ships Running in Waves", 26th Symposium on Naval Hydrodynamics, Rome, Italy.

Umeda, N., Hamamoto, M., Takaishi, Y., et al., 1995, "Model Experiment of Ship Capsize in Astern Seas", Journal of Society of Naval Architects of Japan, Vol. 177, pp. 207-217.

Umeda, N., Hashimoto, H., Matsuda, A., 2003, "Broaching Prediction in the Light of an Enhanced Mathematical Model with Higher-Order Terms Taken into Account", Journal of Marine Science and Technology, Vol. 7, pp.145–155.

Umeda, N., Hashimoto, H., Vassalos, D, Urano, S., and Okou, K., 2004, "Nonlinear Dynamics on Parametric Roll Resonance with Realistic Numerical Modeling", International Shipbuilding Progress, Vol. 51, No 2/3, pp. 205-220.

Umeda, N., Maki, A., and Hashimoto, H. 2006, "Manoeuvring and Control of a High-Speed Slender Vessel with Twin Screws and Twin Rudders in Following and Quartering Seas", Journal of the Japan Society of Naval Architects and Ocean Engineers, Vol. 4, pp.155-164, (in Japanese).

Umeda, N., Matsuda, A., Hamamoto, M., and Suzuki, S., 1999, "Stability Assessment for Intact Ships in the Light of Model Experiments", Journal of Marine Science and Technology, SNAJ, Japan, Vol. 4, pp.45-57.

Umeda, N., Matsuda, A., Hashimoto, H., Yamamura, S., and Maki, A., 2008, "Model Experiments on Extreme Motions of a Wave-Piercing Tumblehome Vessel in Following and Quartering Waves", Journal of the Japan Society of Naval Architects and Ocean Engineers, Vol. 8, pp.123-129.

Umeda, N., Munif, A., Hashimoto, H., 2000, "Numerical Prediction of Extreme Motions and Capsizing for Intact Ships in Following/Quartering Seas", Proceedings of the 4th Osaka Colloquium on Seakeeping Performance of Ships, Osaka Pref. Univ., Osaka, pp.368–373.

Weymouth, G., Wilson, R., Stern, F., 2005, "RANS CFD Predictions of Pitch and Heave Ship Motions in Head Seas", Journal of Ship Research, Vol. 49(2), pp.80–97.

Wilson, R.V., Carrica, P.M., Stern, F., 2005, "Unsteady RANS Method for Ship Motions with Application to Roll for a Surface Combatant", Journal of Computer and Fluids, Vol. 35, pp. 419-451.

Wilson, R.V., Nichols, D.S., Mitchell, B., Karman Jr., S.L., Betro, V.C., Hyams, D.G., Sreenivas, K., Taylor, L.K., Briley, W.R., and Whitfield, D.L., 2007, "Simulation of a Surface Combatant with Dynamic Ship Maneuvers", 9th Numerical Ship Hydrodynamics Conference, Vol. I, pp. 208-223.

Xing, T., Carrica, P.M, and Stern, F., 2008, "Computational Towing Tank Procedures for Single Run Curves of Resistance and Propulsion," ASME J. Fluids Eng, Vol. 130, pp. 101-114.

Xing, T., Shao, J., and Stern, F., 2007, "BKWRS- DES of Unsteady Vortical Flow for KVLCC2 at Large Drift Angles", 9th Numerical Ship Hydrodynamics Conference, Vol. I, pp.172-190.

Zhou, L., Chena, F., 2008, "Stability and Bifurcation Analysis for a Model of a Nonlinear Coupled Pitch–Roll Ship", Journal of Mathematics and Computers in Simulation, Vol. 79(2), pp.149-166.